Imperial College
London

Blockage tolerant wind tunnel testing of aerofoils at angles of incidence from 0° to 360°, with respect to the self-start of vertical-axis wind turbines

John M. Rainbird

Supervised by Dr. Joaquim Peiro
and Prof. J. Michael R. Graham

Imperial College London
Department of Aeronautics

This thesis is submitted for the degree of Doctor of Philosophy
and the Diploma of Imperial College London

2015

Declaration

I hereby declare that this thesis, and the research to which it refers, are the product of my own work, and has not been submitted for any other reward. Ideas and quotations from the work of other people, published or otherwise, are fully acknowledged.

The copyright of this thesis rests with the author and is made available under a Creative Commons Attribution Non-Commercial No Derivatives licence. Researchers are free to copy, distribute or transmit the thesis on the condition that they attribute it, that they do not use it for commercial purposes and that they do not alter, transform or build upon it. For any reuse or redistribution, researchers must make clear to others the licence terms of this work.

John M. Rainbird

For my parents, Mel and Jim, who have given me everything I needed to get this far.

Acknowledgements

I would like to thank my supervisors, Dr. Joaquim Perió and Prof. J. Michael R. Graham, for the support and advice they have provided throughout my research. They believed in my ideas when I came to them with an as yet unfunded proposal, and have given me the guidance I needed to develop them into the document you are about to read.

The work described here would not have been possible without the financial support of the Environmental Services Association Education Trust (ESAET), to whom I am very grateful. In particular, ESAET board member Roger Hewitt was instrumental in arranging formalities between Imperial College and the Trust. I would like to thank my examiners, Prof. Peter W. Bearman and Prof. Frank Coton, in advance for taking the time to read this thesis.

The whole of the technical services and administrative teams in the Department of Aeronautics provided an enormous amount of help to me throughout the project. A great deal of manufacturing was required over its course, including the construction of an entire new wind tunnel test section, I would not have managed it without them. Special thanks goes to Ian James for help in building the test section and for reconfiguring the 3×3 lab for experiments, to Roland Hutchins for advice on the design of parts for manufacture, and for fabrication of the test aerofoil hubs and test section support, Jon Cole for water-jet cutting of sheet metal parts and advice on epoxy resin casting, Ian Pardew for manufacture of the slat aerofoil cast, Mark Grant for his advice on designing parts for three-dimensional printing and Alan Smith for manufacture of the test section frame. Molly Ip and Susan Avery helped with the management of the project's finances, and with the procurement of apparatus from external contractors.

I have been fortunate enough to work with a number of vertical-axis wind turbine researchers on collaborative projects. Dr. Esteban Ferrer of the Universidad Politécnica de Madrid allowed me to use his VAWT-specific Discontinuous-Galerkin CFD solver and gave practical guidance on making best use of it. Dr. Alessandro Bianchini, Dr. Francesco Balduzzi, Prof. Giovanni Ferrara and Dr. Lorenzo Ferrari of the REASE Group at the University of Florence were responsible for the computational side of a fruitful numerical and experimental study on flow curvature effects in VAWTs. I've also benefitted from the input of my fellow researchers at Imperial College, particularly all those I have shared an office with. Whether

suggesting improvements to my work, or helping in the search for new and ever more inventive ways to procrastinate, the last four years would have been far less enjoyable without them.

My family and friends have given me a lot of love, and numerous welcome distractions, over the course of my research, I am very lucky to have them. Last but by no means least, thank you to my girlfriend Kate, for pushing me to get this finished so we can have our weekends back, and for covering more than her fair share of bar tabs while I've been an impoverished student.

Abstract

The need for better quality aerofoil data, extending to incidences well beyond stall, for the modelling of vertical-axis wind turbine (VAWT) start-up is established through blade element-momentum modelling. The model is used to show that differences between existing post-stall data are large enough to impact on turbine performance. The differences between the existing aerofoil data are found to result primarily from inconsistencies introduced by wind tunnel blockage and the potential flow-derived formulae used to correct for it.

A blockage tolerant wind tunnel test section has been constructed and calibrated for aerofoil testing. The tunnel has two semi-permeable walls made up of an array of transverse aerofoil-shaped slats. It produces free-air equivalent data without the need for blockage corrections. The ratio of slat to open area in the permeable walls that best minimises blockage has been obtained through testing of five different-sized NACA 0015 aerofoils.

In free-air, results for the five aerofoils would be identical. The open area ratio that produces the most consistent results for the five aerofoils, based on a standard deviation analysis of the results, is therefore judged to be the best. The aerofoils are tested in a solid-walled wind tunnel, and the data processed using a selection of blockage corrections. The corrections are also judged using a standard deviation analysis.

The tolerant tunnel, configured with the best open area ratio, outperforms the best corrections. Comparisons are made between results from the tolerant and solid-walled tunnels for the smallest (least blocked) aerofoil, with the latter corrected for blockage. Results are equal to within experimental error.

Three additional aerofoils (a symmetrical NACA 0018 and two cambered versions of it) are tested in the tunnel. Results are used in a numerical study of virtual camber effects on VAWT blades. The effect is found to be significant in turbines with large blade chord to

turbine radius ratios. Assessments of Reynolds number effects between 20 000 and 300 000 and camber, for attached and detached blade flows, on forces are presented for all four profiles. A critical Reynolds number is established, above which a laminar separation bubble is able to form on the aerofoil's suction surface. Lift generation before stall improves greatly at supercritical Reynolds numbers.

VAWT start-up is modelled using a blade-element momentum method and the new experimental results. A conclusion is reached on the causes of characteristic VAWT start-up behaviour. The turbines enter an idling phase and either get stuck in it due to the presence of a "dead band" of negative torque production at low tip-speed ratios, or exit it into a rapid acceleration to final highest speeds. The behaviour results from blade Reynolds number effects, specifically the large jump in aerofoil performance at the critical Reynolds number. When turbines successfully self-start, blades are able to operate in local flows with supercritical Reynolds number for a sufficient portion of their rotation to slowly accelerate through the idling phase. When they encounter a "dead band" this is not the case.

Contents

Acknowledgements iii

Abstract v

Table of Contents vii

List of Figures xiii

List of Tables xxiv

Nomenclature xxv

1 Introduction 1

1.1 Vertical-axis wind turbine start-up . . . 2

1.2 VAWT Aerodynamics . . . 4

1.3 Modelled start-up . . . 6

1.4 Phenomena governing start-up behaviour . . . 7

1.5 Stall and attached flow aerofoil behaviour . . . 10

1.5.1 Trailing edge stall . . . 10

1.5.2 Leading edge stall . . . 11

1.5.3 Thin aerofoil stall . . . 12

1.5.4 Carmichael's lift curve and polar types . . . 13

1.5.5 Laminar separation bubbles . . . 13

1.6 Post-stall aerofoil data for VAWT modelling . . . 14

1.7 Existing aerofoil studies . . . 15

1.7.1 Post-stall studies . . . 15
1.7.2 Low-Reynolds number aerofoil experiments . . . 17
1.7.3 Inconsistencies between data from the literature . . . 17
1.8 Wind tunnel blockage . . . 19
1.9 The blockage tolerant tunnel . . . 20
1.10 Summary of research objectives . . . 20
1.11 List of publications . . . 21

2 Wind tunnel blockage and methods used to limit its impact 24
2.1 Blockage corrections . . . 24
2.1.1 Lift interference . . . 25
2.1.2 Solid Blockage . . . 26
2.1.3 Wake blockage . . . 28
2.1.4 Horizontal buoyancy . . . 28
2.1.5 Application of corrections . . . 29
2.1.6 Maskell's corrections for bluff bodies and stalled wings . . . 30
2.1.7 Boundary measurement methods . . . 31
2.1.8 Turbulence factor . . . 32
2.1.9 Limitations to correction regimes . . . 33
2.1.10 Analysis of different corrections regimes . . . 34
2.2 Blockage tolerant wind tunnels . . . 41
2.2.1 Adaptive walls . . . 41
2.2.2 Open jet tunnels . . . 41
2.2.3 Large conventional tunnels . . . 42
2.2.4 Porous walls . . . 43
2.3 The Parkinson tolerant tunnel . . . 43

3 The blockage tolerant wind tunnel: preliminary work 46
3.1 Experiments in the 18" Flow Control wind tunnel . . . 46
3.1.1 Aerofoils . . . 47
3.1.2 Model mounting and data acquisition . . . 47
3.1.3 Results . . . 49

3.2 Numerical modelling . . . 55
3.3 Parkinson tunnel blockage reduction . . . 57

4 The blockage tolerant wind tunnel: design, build and commissioning 60
4.1 The Imperial College 3' × 3' wind tunnel . . . 60
4.1.1 3' × 3' tolerant test section construction . . . 61
4.1.2 Test section support . . . 61
4.1.3 Slat aerofoils . . . 62
4.2 Test aerofoils . . . 64
4.2.1 NACA 0015 . . . 64
4.2.2 NACA 0018 and similar profiles with camber . . . 65
4.2.3 Aerofoil construction . . . 66
4.2.4 Profile accuracy and surface roughness . . . 67
4.2.5 Test aerofoil mounting . . . 69
4.3 Data acquisition and experiment control . . . 71
4.4 Tunnel speed measurement and calibration . . . 72
4.4.1 Tunnel contraction to centreline pitot-static . . . 72
4.4.2 "Contraction velocity" to tunnel controller voltage input . . . 73
4.5 Experimental methods . . . 74
4.5.1 Angles of attack . . . 74
4.5.2 Settling times, sampling times and frequencies . . . 75
4.5.3 Data processing . . . 76
4.5.4 Force and pressure transducer zeroing . . . 77
4.6 Cross-flow uniformity of the new 3' × 3' test section . . . 78
4.7 Errors, accuracy and repeatability . . . 80
4.8 Tolerant tunnel OAR calibrations . . . 84
4.8.1 Parkinson's calibration techniques . . . 85
4.8.2 Force measurements for the five NACA 0015 aerofoils with various tolerant tunnel OARs and solid tunnel walls . . . 86
4.8.3 Surface pressures for the two tapped NACA 0015 aerofoils with various tolerant tunnel OARs and solid tunnel walls . . . 90

4.8.4 Hameury's methods: C_d and C_p measurements at $\alpha = 90°$ 94
4.8.5 Standard deviation of forces and moments 97
4.8.6 Surface pressure distribution similarity 106
4.9 Discussion on OAR calibrations 108

5 Force and surface pressure experiments: results, validation and analysis 113
5.1 Surface pressure distributions 113
5.2 Force transducer measurements, tolerant tunnel with OAR = 71% 117
5.2.1 Pre-offset settling times 117
5.2.2 Sampling times 119
5.2.3 NACA 0015 119
5.2.4 NACA 0018 135
5.2.5 NACA 0018 cambered transforms 141
5.3 Force transducer measurements, solid walled tunnel 145
5.3.1 NACA 0015 154
5.4 Reynolds number effects 158
5.4.1 Maximum C_l/C_d 158
5.4.2 Attached flow $C_{l\,\mathrm{MAX}}$ and $C_{d\,\mathrm{MIN}}$ 160
5.4.3 Stall angle 162
5.4.4 Detached flow lift and drag peaks 162
5.5 Thickness and camber effects 166

6 VAWT modelling and application of new aerofoil data to VAWT analyses 168
6.1 Blade element-momentum method 168
6.1.1 The double-multiple streamtube model 172
6.1.2 Limitations of BEM models 174
6.2 Unsteady aerodynamics 175
6.2.1 Dynamic stall 176
6.2.2 Dynamic stall model of the current study 178
6.2.3 Attached flow unsteady aerodynamics 185
6.3 Blade Reynolds number effects 187
6.4 Blade-wake interactions 188

6.5 Migliore's virtual camber and incidence effects . . . 190
6.5.1 Imperial BEM code results . . . 191
6.5.2 Collaborative project with the University of Florence . . . 194
6.6 Three-dimensional effects . . . 196
6.6.1 Finite blade effects . . . 197
6.6.2 Stall smoothing . . . 199
6.7 Full turbine modelling . . . 200
6.7.1 Parasitic drag . . . 200
6.7.2 Power and torque modelling . . . 201
6.7.3 Start-up modelling . . . 204

7 Research achievements 210
7.1 The provision of a highly accurate set of post-stall aerofoil data . . . 210
7.1.1 Further work . . . 212
7.2 An explanation of VAWT start-up behaviour . . . 213
7.2.1 Further work . . . 214
7.3 Impact and beneficiaries of the research . . . 215

References 217

Appendices 229

A Aerofoil studies referenced in the thesis 230
A.1 Aerofoil experiments covering a wide range of incidences . . . 230
A.1.1 The NACA 0012 . . . 230
A.1.2 The NACA 0015 . . . 233
A.1.3 The NACA 0018 . . . 234
A.2 Low-Reynolds number aerofoil experiments . . . 235
A.2.1 Althaus . . . 235
A.2.2 Dong-Ha et al. . . . 235
A.2.3 Jacobs and Sherman . . . 236

B Method of images **238**

B.1 Lift interference . . . 238

B.2 Solid blockage . . . 239

B.3 Wake blockage . . . 241

C Derivation of a formula for calculating the required c/H ratio for blockage corrections to be less than 5% **243**

D Additional plots **245**

D.1 Force measurements for the five NACA 0015 aerofoils with various tolerant tunnel OARs at $Re = 150\,000$ . . . 245

D.1.1 Single slatted wall . . . 245

D.1.2 Double slatted walls . . . 248

D.2 Force measurements for the five NACA 0015 aerofoils with various tolerant tunnel OARs at $Re = 60\,000$ . . . 251

D.3 Force measurements for the five NACA 0015 aerofoils with various tolerant tunnel OARs at $Re = 250\,000$ . . . 253

D.4 Force measurements for the five NACA 0015 aerofoils with solid tunnel walls at $Re = 60\,000$ . . . 255

D.5 Force measurements for the five NACA 0015 aerofoils with solid tunnel walls at $Re = 250\,000$ . . . 257

D.6 Surface pressures for the two tapped NACA 0015 aerofoils with various tolerant tunnel OARs and solid tunnel walls, at $Re = 150\,000$ . . . 259

D.7 Surface pressures for the two tapped NACA 0015 aerofoils with various tolerant tunnel OARs and solid tunnel walls, at $Re = 60\,000$ . . . 261

D.8 Surface pressures for the two tapped NACA 0015 aerofoils with various tolerant tunnel OARs and solid tunnel walls, at $Re = 250\,000$ . . . 265

List of Figures

1.1 TSR development with time from the transient start-up experiments of Hill et al., Rainbird, Bianchini et al. and Chua. 3
1.2 VAWT velocity triangle. 5
1.3 Lift, drag and tangential coefficients against incidence, with limits in VAWT blade incidence at different TSRs highlighted. 6
1.4 Effects of small changes in post-stall lift on VAWT performance. 7
1.5 Typical lift curve slopes for different types of stall. 11
1.6 Stall types according to Khoo. 12
1.7 Typical lift curve slopes and polars for different types of stall. 13
1.8 C_l and C_d vs α for selected NACA 00XX studies. 16

2.1 Effects of wind tunnel walls on streamlines around an aerofoil. 25
2.2 Variation of Maskell's blockage factor ϵ_q with incidence for two-dimensional plates and the $c/H = 0.15$ aerofoil of the current study. 32
2.3 Variation of turbulence factor with turbulence intensity. 33
2.4 C_l, C_d and C_m vs α for $c/H = 0.1$, 0.15, 0.2, 0.25 and 0.3 NACA 0015 aerofoils taken in the solid walled tunnel at $Re = 150\,000$, raw data. 35
2.5 C_l, C_d and C_m vs α for $c/H = 0.1$, 0.15, 0.2, 0.25 and 0.3 NACA 0015 aerofoils taken in the solid walled tunnel at $Re = 150\,000$, ESDU corrections. 36
2.6 C_l, C_d and C_m vs α for $c/H = 0.1$, 0.15, 0.2, 0.25 and 0.3 NACA 0015 aerofoils taken in the solid walled tunnel at $Re = 150\,000$, Rae et al. corrections. 36
2.7 C_l, C_d and C_m vs α for $c/H = 0.1$, 0.15, 0.2, 0.25 and 0.3 NACA 0015 aerofoils taken in the solid walled tunnel at $Re = 150\,000$, Maskell's corrections. 37

2.8 C_l, C_d and C_m vs α for $c/H = 0.1$, 0.15, 0.2, 0.25 and 0.3 NACA 0015 aerofoils taken in the solid walled tunnel at $Re = 150\,000$, Maskell's corrections with recalculated ϵ_q. 38
2.9 Summations of standard deviations for C_l, C_d and C_m for all NACA 0015 aerofoils, processed with selected bockage corrections 38
2.10 C_l, C_d and C_m vs α for the $c/H = 0.1$ NACA 0015 aerofoil using the blockage corrections of ESDU, Rae et al, Maskell and Maskell with recalculated ϵ_q . . . 39
2.11 Parkinson's slatted-walled tolerant tunnel configured with double slatted walls. 44

3.1 Aerofoil mounting in the wind tunnel, front-on (top) and side-on (bottom) views. 48
3.2 Experimental set-up in and around the wind tunnel. 49
3.3 C_l and C_d vs α alongside the studies of Althaus and Sheldahl and Klimas. . . . 51
3.4 Results alongside the NACA 0012 post-stall studies of Sheldahl and Klimas and Critzos et al., and output of the AERODAS model. 52
3.5 C_l and C_d vs α for $c/H = 0.27$ and $c/H = 0.32$ aerofoils taken in the solid walled test section: raw uncorrected data (u) and corrected data (c). 54
3.6 C_l and C_d vs α for $c/H = 0.27$ and $c/H = 0.32$ aerofoils taken in the SS-0.59 tolerant tunnel. 55
3.7 C_l and C_d vs α for $c/H = 0.27$ and $c/H = 0.32$ aerofoils taken in the DS-0.43 tolerant tunnel. 56
3.8 C_l and C_d vs α for $c/H = 0.27$ and $c/H = 0.32$ aerofoils taken in the DS-0.59 tolerant tunnel. 56
3.9 Effect of aerofoil size on ratio of lift coefficients (theory)/ratio of lift curve slopes (experiments). 57

4.1 Streamwise cutaway view of the Imperial College Parkinson tunnel. 62
4.2 The Imperial College Parkinson test section under construction. 63
4.3 Slat aerofoil production process. 64
4.4 Symmetrical NACA 0018 and similar cambered profile sharing a quarter chord. 65
4.5 The two cambered aerofoils during construction. 67
4.6 Results of profile accuracy measurements of the NACA 0015. 68

4.7 The $c/H = 0.2$ aerofoil mounted in the wind tunnel with double slatted walls, OAR = 0.55. 69
4.8 The top assembly of the apparatus, showing end plate, adapter, force transducer, bearing mount and attachments to the timber framework of the test section. 70
4.9 The bottom assembly of the apparatus, with tunnel floor removed, showing end plate, adapter, force transducer, bearing mount and the cooling unit of the stepper motor. 71
4.10 Flow velocity variation from mean stream-wise velocity across the test section, for the solid walled tunnel. 78
4.11 Flow velocity variation from mean stream-wise velocity across the test section, for the tolerant tunnel, DS-71 configuration. 79
4.12 Estimated and actual maximum errors for C_d (top) and C_m (bottom) vs Re. . 81
4.13 C_l, C_d and C_m vs α for the NACA 0015 from the tolerant tunnel at $Re = 150\,000$, raw runs and averages. 83
4.14 C_l, C_d and C_m vs α for $c/H = 0.1$, 0.15, 0.2, 0.25 and 0.3 NACA 0015 aerofoils taken in the tolerant tunnel, DS-67 configuration at $Re = 150\,000$. 87
4.15 C_l, C_d and C_m vs α for $c/H = 0.1$, 0.15, 0.2, 0.25 and 0.3 NACA 0015 aerofoils taken in the tolerant tunnel, DS-71 configuration at $Re = 150\,000$. 88
4.16 C_l, C_d and C_m vs α for $c/H = 0.1$, 0.15, 0.2, 0.25 and 0.3 NACA 0015 aerofoils taken in the tolerant tunnel, DS-75 configuration at $Re = 150\,000$. 88
4.17 C_l, C_d and C_m vs α for $c/H = 0.1$, 0.15, 0.2, 0.25 and 0.3 NACA 0015 aerofoils taken in the solid walled tunnel at $Re = 150\,000$. 89
4.18 C_l, C_d and C_m vs α for $c/H = 0.1$, 0.15, 0.2, 0.25 and 0.3 NACA 0015 aerofoils taken in the solid walled tunnel at $Re = 150\,000$, ESDU corrections. 89
4.19 C_p plotted against normalised chord-wise position for the $c/H = 0.15$ and $c/H = 0.25$ NACA 0015 aerofoils at $Re = 150\,000$ in the DS-71 tolerant tunnel. 92
4.20 C_p plotted against normalised chord-wise position for the $c/H = 0.15$ and $c/H = 0.25$ NACA 0015 aerofoils at $Re = 150\,000$ in the solid walled tunnel. . . 93

4.21 Variation of C_d at 90° as a function of OAR for five NACA 0015 aerofoils, Re = 150 000, double slatted wall tunnel configurations (corrected solid-walled results are also shown, with unfilled markers, at OAR = 0.3), alongside Hameury's results for normal flat plates. 95

4.22 Variation of suction surface C_p at $\alpha = 90°$ as a function of OAR for the two pressure tapped NACA 0015 aerofoils, Re = 150 000, double slatted wall tunnel configurations, alongside Hameury's results for normal flat plates. 96

4.23 Summations of standard deviations for C_l, C_d and C_m for all NACA 0015 aerofoils, plotted against OAR for double slatted wall tunnel configurations. Note that while corrected solid-walled data has an OAR of 0, it is shown plotted at OAR = 0.775. 99

4.24 Summations of standard deviations for C_l, C_d and C_m for all NACA 0015 aerofoils, plotted against OAR for single slatted wall tunnel configurations. Note that while corrected solid-walled data has an OAR of 0, it is shown plotted at OAR = 0.925. 100

4.25 Flow pattern in tolerant tunnel plenum chamber under extreme blockage. . . . 103

4.26 Summations of standard deviations for C_l, C_d and C_m for NACA 0015 aerofoils with $c/H < 0.3$, plotted against OAR for double slatted wall tunnel configurations. Note that while corrected solid-walled data has an OAR of 0, it is shown plotted at OAR = 0.775. 104

4.27 Variation of sums of difference in C_p for $-2° \leq \alpha \leq 8°$ (Re = 60 000) and $-2°$ - $10°$ (Re = 150 000, 250 000), as a function of OAR for the two pressure tapped NACA 0015 aerofoils, double slatted wall tunnel configurations. 107

4.28 Variation of sums of difference in C_p for $20° \leq \alpha \leq 160°$, as a function of OAR for the two pressure tapped NACA 0015 aerofoils, double slatted wall tunnel configurations. 107

4.29 C_l, C_d and C_m vs α for the $c/H = 0.1$ NACA 0015 aerofoil taken in the tolerant tunnel, DS-67, DS-71 and DS-75 configurations, at Re = 60 000. 109

4.30 C_l, C_d and C_m vs α for the $c/H = 0.1$ NACA 0015 aerofoil taken in the tolerant tunnel, DS-67, DS-71 and DS-75 configurations, at Re = 150 000. 109

4.31 C_l, C_d and C_m vs α for the $c/H = 0.1$ NACA 0015 aerofoil taken in the tolerant tunnel, DS-67, DS-71 and DS-75 configurations, at $Re = 250\,000$. 110
4.32 C_p plotted against normalised chord-wise position for the $c/H = 0.15$ NACA 0015 aerofoil at $\alpha = 90°$ taken tolerant tunnel, DS-67, DS-71 and DS-75 configurations. 111
4.33 Modelled streamline behaviour in free air, a solid-walled tunnel and the DS-71 tolerant tunnel. 112

5.1 C_p plotted against normalised chord-wise position for the $c/H = 0.25$ NACA 0015 aerofoil at various Reynolds numbers at (a) 20°, (b) 0°, (c) 2°, (d) 4°, (e) 6°, (f) 10° 115
5.2 C_p plotted against normalised chord-wise position for the $c/H = 0.25$ NACA 0015 aerofoil compared to other studies at (a) 30°, (b) 50°, (c) 90°, (d) 150°, (e) 170°, (e) 180° 116
5.3 C_l vs α for the $c/H = 0.1$ NACA 0015 aerofoil taken in the tolerant tunnel, DS-71 configuration at various Re. (a) $-4° \leq \alpha \leq 184°$, (b) $-4° \leq \alpha \leq 15°$. . . 121
5.4 C_d vs α for the $c/H = 0.1$ NACA 0015 aerofoil taken in the tolerant tunnel, DS-71 configuration at various Re. (a) $-4° \leq \alpha \leq 184°$, (b) $-4° \leq \alpha \leq 15°$. . . 122
5.5 C_m vs α for the $c/H = 0.1$ NACA 0015 aerofoil taken in the tolerant tunnel, DS-71 configuration at various Re. (a) $-4° \leq \alpha \leq 184°$, (b) $-4° \leq \alpha \leq 15°$. . . 123
5.6 C_l vs C_d polar for the $c/H = 0.1$ NACA 0015 aerofoil taken in the tolerant tunnel, DS-71 configuration at various Re. (a) $-4° \leq \alpha \leq 184°$, (b) $-4° \leq \alpha \leq$ stall. 124
5.7 C_l vs α from various NACA 0015 and NACA 0012 studies. (a) $-4° \leq \alpha \leq 184°$, (b) $-4° \leq \alpha \leq 15°$. 126
5.8 C_d vs α from various NACA 0015 and NACA 0012 studies. (a) $-4° \leq \alpha \leq 184°$, (b) $-4° \leq \alpha \leq 15°$. 127
5.9 C_m vs α from various NACA 0015 and NACA 0012 studies. (a) $-4° \leq \alpha \leq 184°$, (b) $-4° \leq \alpha \leq 15°$. 128
5.10 Pressure distributions and laminar separation bubbles 132
5.11 Smoke stream flow visualisation for a low incidence, low Reynolds number NACA 0012. 133

5.12 Pressure distributions at incidences around stall angle for the $c/H = 0.25$ aerofoil at $Re = 150\,000$. 135
5.13 C_l vs α for the $c/H = 0.2$ NACA 0018 aerofoil taken in the tolerant tunnel, DS-71 configuration at various Re. (a) $-4° \leq \alpha \leq 184°$, (b) $-4° \leq \alpha \leq 22°$. . . 137
5.14 C_d vs α for the $c/H = 0.2$ NACA 0018 aerofoil taken in the tolerant tunnel, DS-71 configuration at various Re. (a) $-4° \leq \alpha \leq 184°$, (b) $-4° \leq \alpha \leq 22°$. . . 138
5.15 C_m vs α for the $c/H = 0.2$ NACA 0018 aerofoil taken in the tolerant tunnel, DS-71 configuration at various Re. (a) $-4° \leq \alpha \leq 184°$, (b) $-4° \leq \alpha \leq 22°$. . . 139
5.16 C_l vs C_d polar for the $c/H = 0.2$ NACA 0018 aerofoil taken in the tolerant tunnel, DS-71 configuration at various Re. (a) $-4° \leq \alpha \leq 184°$, (b) $-4° \leq \alpha \leq$ stall. 140
5.17 C_l vs α from various NACA 0018 studies. (a) $-4° \leq \alpha \leq 184°$, (b) $-4° \leq \alpha \leq 22°$. 142
5.18 (a) C_d vs. α for incidences of $-4°$ to $184°$ and (b) C_l vs. C_d for attached flow, from various NACA 0018 studies. 143
5.19 C_m vs α from various NACA 0018 studies. 144
5.20 C_l vs α for the $c/H = 0.2$ transformed NACA 0018 aerofoil with $c/R = 0.114$, taken in the tolerant tunnel, DS-71 configuration at various Re. (a) $-184° \leq \alpha \leq 184°$, (b) $-16° \leq \alpha \leq 22°$. 146
5.21 C_d vs α for the $c/H = 0.2$ transformed NACA 0018 aerofoil with $c/R = 0.114$, taken in the tolerant tunnel, DS-71 configuration at various Re. (a) $-184° \leq \alpha \leq 184°$, (b) $-16° \leq \alpha \leq 22°$. 147
5.22 C_m vs α for the $c/H = 0.2$ transformed NACA 0018 aerofoil with $c/R = 0.114$, taken in the tolerant tunnel, DS-71 configuration at various Re. (a) $-184° \leq \alpha \leq 184°$, (b) $-16° \leq \alpha \leq 22°$. 148
5.23 C_l vs C_d polar for the $c/H = 0.2$ transformed NACA 0018 aerofoil with $c/R = 0.114$ taken in the tolerant tunnel, DS-71 configuration at various Re. (a) $-184° \leq \alpha \leq 184°$, (b) incidences at which flow is attached. 149
5.24 C_l vs α for the $c/H = 0.2$ transformed NACA 0018 aerofoil with $c/R = 0.25$, taken in the tolerant tunnel, DS-71 configuration at various Re. (a) $-184° \leq \alpha \leq 184°$, (b) $-16° \leq \alpha \leq 22°$. 150

5.25 C_d vs α for the $c/H = 0.2$ transformed NACA 0018 aerofoil with $c/R = 0.25$, taken in the tolerant tunnel, DS-71 configuration at various Re. (a) $-184° \leq \alpha \leq 184°$, (b) $-16° \leq \alpha \leq 22°$. 151

5.26 C_m vs α for the $c/H = 0.2$ transformed NACA 0018 aerofoil with $c/R = 0.25$, taken in the tolerant tunnel, DS-71 configuration at various Re. (a) $-184° \leq \alpha \leq 184°$, (b) $-16° \leq \alpha \leq 22°$. 152

5.27 C_l vs C_d polar for the $c/H = 0.2$ transformed NACA 0018 aerofoil with $c/R = 0.25$ taken in the tolerant tunnel, DS-71 configuration at various Re. (a) $-184° \leq \alpha \leq 184°$, (b) incidences at which flow is attached. 153

5.28 C_l vs α for the $c/H = 0.1$ NACA 0015 aerofoil taken in the solid walled tunnel, at various Re, with blockage corrections applied. (a) $-4° \leq \alpha \leq 184°$, (b) $-4° \leq \alpha \leq 15°$. 155

5.29 C_d vs α for the $c/H = 0.1$ NACA 0015 aerofoil taken in the solid walled tunnel, at various Re, with blockage corrections applied. (a) $-4° \leq \alpha \leq 184°$, (b) $-4° \leq \alpha \leq 15°$. 156

5.30 C_m vs α for the $c/H = 0.1$ NACA 0015 aerofoil taken in the solid walled tunnel, at various Re, with blockage corrections applied. (a) $-4° \leq \alpha \leq 184°$, (b) $-4° \leq \alpha \leq 15°$. 157

5.31 Maximum C_l/C_d vs Re for the four aerofoils tested in the tolerant tunnel, compared to trends from Lissaman's review. 159

5.32 Variations with Re for the four aerofoils tested in the tolerant tunnel, compared to Timmer and Jacobs and Sherman 161

5.33 Stall angle and flow reattachment angle vs Re for the four aerofoils tested in the tolerant tunnel. White filled data points are for readings taken for flow reattachment (with reducing incidence). 163

5.34 Maximum detached flow (a) C_l and (b) C_d vs Re for the four aerofoils tested in the tolerant tunnel, with maximum error bars. 164

5.35 Maximum detached flow (a) C_l and (b) C_d vs Re for the studies of Critzos et al, Du et al, Sheldahl and Klimas, and Zhou et al. 165

6.1 An actuator disk in a stream of velocity V_1 169

6.2 Force and velocity diagram for a VAWT blade element 170
6.3 VAWT streamtube and actuator arrangements, actuators shown in red 173
6.4 C_T vs a relationship per BEM theory and Sharpe's empirical extension, and experiments on which the latter is based. 175
6.5 Dynamic stall model C_n against α compared to McCroskey et al's test data taken at $Re = 490\,000$ and $M = 0.035$. 180
6.6 $F_n{}^*$ vs θ at TSR = 2.5, models compared to test data of (a) Strickland et al. and (b) Vittecoq and Laneville. 182
6.7 $F_t{}^*$ vs θ at TSR = 2.5, models compared to test data of (a) Strickland et al. and (b) Vittecoq and Laneville. 183
6.8 Theodorsen's F and G functions against k 186
6.9 $F_n{}^*$ vs θ at TSR = 2.5, models with and without variable Re_b, compared to test data of (a) Strickland et al. and (b) Vittecoq and Laneville. 188
6.10 $F_t{}^*$ vs θ at TSR = 2.5, models with and without variable Re_b, compared to test data of (a) Strickland et al. and (b) Vittecoq and Laneville. 189
6.11 (a) $F_n{}^*$ and (b) $F_t{}^*$ vs θ at TSR = 2.5, models with and without virtual camber and incidence effects, compared to test data of Vittecoq and Laneville. 192
6.12 (a) $F_n{}^*$ and (b) $F_t{}^*$ vs θ at various TSRs compared to test data of Maeda et al. 193
6.13 Pressure distribution comparisons between XFOIL and Fluent outputs at $\theta = 32.8°$. 196
6.14 C_l vs. incidence - reconstructed results from Fluent VAWT simulations compared to aerofoil experiment: (a) $c/R = 0.114$ Trans. expt. NACA 0018 CFD (b) $c/R = 0.114$ NACA 0018 expt. trans. CFD (c) $c/R = 0.25$ Trans. expt. NACA 0018 CFD (d) $c/R = 0.25$ NACA 0018 expt. trans. CFD. 197
6.15 Turbine power curves from Fluent simulations and the University of Florence BEM code: (a) $c/R = 0.114$, (b) $c/R = 0.25$. 198
6.16 C_l and C_d vs α for the NACA 0018, $c/R = 0.25$ aerofoil at $Re = 200\,000$ with smoothed stall. 200
6.17 C_P vs TSR compared to the test data of Bravo et al. 202
6.18 C_P vs TSR compared to the test data of Maeda et al. 204

6.19 TSR development with time for the Durham turbine compared to the author's earlier experiments 205
6.20 Modelled α_b development with time for the Durham turbine. 207
6.21 Modelled Re_b development with time for the Durham turbine. 207
6.22 C_T vs TSR for the Durham turbine. 208

D.1 C_l, C_d and C_m vs α for $c/H = 0.1$, 0.15, 0.2, 0.25 and 0.3 NACA 0015 aerofoils taken in the tolerant tunnel, SS-71 configuration at $Re = 150\,000$. 245
D.2 C_l, C_d and C_m vs α for $c/H = 0.1$, 0.15, 0.2, 0.25 and 0.3 NACA 0015 aerofoils taken in the tolerant tunnel, SS-79 configuration at $Re = 150\,000$. 246
D.3 C_l, C_d and C_m vs α for $c/H = 0.1$, 0.15, 0.2, 0.25 and 0.3 NACA 0015 aerofoils taken in the tolerant tunnel, SS-83 configuration at $Re = 150\,000$. 246
D.4 C_l, C_d and C_m vs α for $c/H = 0.1$, 0.15, 0.2, 0.25 and 0.3 NACA 0015 aerofoils taken in the tolerant tunnel, SS-88 configuration at $Re = 150\,000$. 247
D.5 C_l, C_d and C_m vs α for $c/H = 0.1$, 0.15, 0.2, 0.25 and 0.3 NACA 0015 aerofoils taken in the tolerant tunnel, DS-50 configuration at $Re = 150\,000$. 248
D.6 C_l, C_d and C_m vs α for $c/H = 0.1$, 0.15, 0.2, 0.25 and 0.3 NACA 0015 aerofoils taken in the tolerant tunnel, DS-55 configuration at $Re = 150\,000$. 249
D.7 C_l, C_d and C_m vs α for $c/H = 0.1$, 0.15, 0.2, 0.25 and 0.3 NACA 0015 aerofoils taken in the tolerant tunnel, DS-59 configuration at $Re = 150\,000$. 249
D.8 C_l, C_d and C_m vs α for $c/H = 0.1$, 0.15, 0.2, 0.25 and 0.3 NACA 0015 aerofoils taken in the tolerant tunnel, DS-63 configuration at $Re = 150\,000$. 250
D.9 C_l, C_d and C_m vs α for $c/H = 0.1$, 0.15, 0.2, 0.25 and 0.3 NACA 0015 aerofoils taken in the tolerant tunnel, DS-67 configuration at $Re = 60\,000$. 251
D.10 C_l, C_d and C_m vs α for $c/H = 0.1$, 0.15, 0.2, 0.25 and 0.3 NACA 0015 aerofoils taken in the tolerant tunnel, DS-71 configuration at $Re = 60\,000$. 252
D.11 C_l, C_d and C_m vs α for $c/H = 0.1$, 0.15, 0.2, 0.25 and 0.3 NACA 0015 aerofoils taken in the tolerant tunnel, DS-75 configuration at $Re = 60\,000$. 252
D.12 C_l, C_d and C_m vs α for $c/H = 0.1$, 0.15, 0.2, 0.25 and 0.3 NACA 0015 aerofoils taken in the tolerant tunnel, DS-67 configuration at $Re = 250\,000$. 253

D.13 C_l, C_d and C_m vs α for $c/H = 0.1$, 0.15, 0.2, 0.25 and 0.3 NACA 0015 aerofoils taken in the tolerant tunnel, DS-71 configuration at $Re = 250\,000$. 254
D.14 C_l, C_d and C_m vs α for $c/H = 0.1$, 0.15, 0.2, 0.25 and 0.3 NACA 0015 aerofoils taken in the tolerant tunnel, DS-75 configuration at $Re = 250\,000$. 254
D.15 C_l, C_d and C_m vs α for $c/H = 0.1$, 0.15, 0.2, 0.25 and 0.3 NACA 0015 aerofoils taken in the solid walled tunnel at $Re = 60\,000$. 255
D.16 C_l, C_d and C_m vs α for $c/H = 0.1$, 0.15, 0.2, 0.25 and 0.3 NACA 0015 aerofoils taken in the solid walled tunnel at $Re = 60\,000$, ESDU corrections. 256
D.17 C_l, C_d and C_m vs α for $c/H = 0.1$, 0.15, 0.2, 0.25 and 0.3 NACA 0015 aerofoils taken in the solid walled tunnel at $Re = 60\,000$, Maskell's corrections. 256
D.18 C_l, C_d and C_m vs α for $c/H = 0.1$, 0.15, 0.2, 0.25 and 0.3 NACA 0015 aerofoils taken in the solid walled tunnel at $Re = 250\,000$. 257
D.19 C_l, C_d and C_m vs α for $c/H = 0.1$, 0.15, 0.2, 0.25 and 0.3 NACA 0015 aerofoils taken in the solid walled tunnel at $Re = 250\,000$, ESDU corrections. 258
D.20 C_l, C_d and C_m vs α for $c/H = 0.1$, 0.15, 0.2, 0.25 and 0.3 NACA 0015 aerofoils taken in the solid walled tunnel at $Re = 250\,000$, Maskell's corrections. 258
D.21 C_p plotted against normalised chord-wise position for the $c/H = 0.15$ and $c/H = 0.25$ NACA 0015 aerofoils at $Re = 150\,000$ in the DS-67 tolerant tunnel. 259
D.22 C_p plotted against normalised chord-wise position for the $c/H = 0.15$ and $c/H = 0.25$ NACA 0015 aerofoils at $Re = 150\,000$ in the DS-75 tolerant tunnel. 260
D.23 C_p plotted against normalised chord-wise position for the $c/H = 0.15$ and $c/H = 0.25$ NACA 0015 aerofoils at $Re = 60\,000$ in the DS-67 tolerant tunnel. . 261
D.24 C_p plotted against normalised chord-wise position for the $c/H = 0.15$ and $c/H = 0.25$ NACA 0015 aerofoils at $Re = 60\,000$ in the DS-71 tolerant tunnel. . 262
D.25 C_p plotted against normalised chord-wise position for the $c/H = 0.15$ and $c/H = 0.25$ NACA 0015 aerofoils at $Re = 60\,000$ in the DS-75 tolerant tunnel. . 263
D.26 C_p plotted against normalised chord-wise position for the $c/H = 0.15$ and $c/H = 0.25$ NACA 0015 aerofoils at $Re = 60\,000$ in the solid walled tunnel. . . 264
D.27 C_p plotted against normalised chord-wise position for the $c/H = 0.15$ and $c/H = 0.25$ NACA 0015 aerofoils at $Re = 250\,000$ in the DS-67 tolerant tunnel. 265

D.28 C_p plotted against normalised chord-wise position for the $c/H = 0.15$ and $c/H = 0.25$ NACA 0015 aerofoils at $Re = 250\,000$ in the DS-71 tolerant tunnel. 266

D.29 C_p plotted against normalised chord-wise position for the $c/H = 0.15$ and $c/H = 0.25$ NACA 0015 aerofoils at $Re = 250\,000$ in the DS-75 tolerant tunnel. 267

D.30 C_p plotted against normalised chord-wise position for the $c/H = 0.15$ and $c/H = 0.25$ NACA 0015 aerofoils at $Re = 250\,000$ in the solid walled tunnel. . . 268

List of Tables

1.1 Summary of aerofoil studies referenced in this paper. Where a range of Reynolds numbers is given, peaks are for $Re = 150\,000$ or the nearest alternative. 18

3.1 Absolute differences between $c/H = 0.27$ and $c/H = 0.32$ data for selected tunnel configurations. 58

4.1 Maximum deviation of aerofoil surfaces from intended profile shape. 68
4.2 Incidence ranges tested in different sessions of experimentation. 74
4.3 Sampling times for force and pressure experiments. 76
4.4 Estimated maximum percentage error for force and moment readings. 82
4.5 Summary of tunnel configuration performance based on standard deviation summations for all NACA 0015 aerofoils 101
4.6 Summary of tunnel configuration performance based on standard deviation summations for NACA 0015 aerofoils with $c/H < 0.3$ 105

5.1 Sampling times for force and pressure experiments 119

6.1 Summary of turbines referenced in this paper. 181

Nomenclature

a	Cylinder radius (m)
a	Lift curve slope
c	Aerofoil chord length (m)
k_{aero}	Aerofoil cross-sectional area parameter
p	Wind tunnel plenum chamber depth (m)
p	Pressure (Pa)
r	Pearson product-moment correlation coefficient
t	Aerofoil thickness (m)
A_{aero}	Aerofoil cross-sectional area (m^2)
$\mathcal{AR}$	Aspect ratio
C_d	Drag coefficient
C_l	Lift coefficient
C_m	Coefficient of moment about quarter chord
C_p	Pressure coefficient
C_P	power coefficient
C_Q	Torque coefficient
D	Drag force (N)
H	Wind tunnel height (m)
K_1	Empirical constant for the Gormont dynamic stall model
K_{wc}	Wake blockage factor
L	Wind tunnel test section length (m)
L	Lift force (N)
M	Mach number

Q	Source/sink strength
R	Turbine radius (m)
Re	Reynolds number
Re_{crit}	Critical Reynolds number
V	Velocity (m/s)
α	Angle of incidence (rad)
β	Prandtl-Glauert compressibility factor $\beta = \left(\sqrt{1 - {M_\infty}^2}\right)^{-1}$
γ	Empirical constant for the Gormont dynamic stall model
ϵ	Blockage factor
ζ	c/h quartic coefficient, see Eqn. (C.6)
θ	Azimuth angle (rad)
λ	Tip-speed ratio $= \frac{\omega R}{V_\infty}$
λ_2	Solid blockage body shape factor
μ	Point doublet strength
ρ	Density of air (kg/m^3)
τ	Aerofoil thickness ratio $\tau = t/c$
ϕ	Velocity potential
ω	Rotational velocity/circular frequency (rad/s)
Γ	Vortex strength

Subscripts

b	Relating to a turbine blade
c	Corrected value
sc	Due to solid blockage
u	Uncorrected value; raw experimental data
wc	Due to wake blockage
B	Due to total (solid + wake) blockage
FA	Free air value
R	Due to flow rotation
∞	Free-stream value

Abbreviations

HAWT	Horizontal axis wind turbine
OAR	Open area ratio
TSR	Tip-speed ratio
VAWT	Vertical axis wind turbine

Chapter 1

Introduction

Vertical-axis wind turbines (VAWTs) rotate about an axis perpendicular to the flow, causing torques produced to vary over the course of a rotation, with negative torque production in some sectors. The ability of fixed-blade Darrieus VAWTs to self-start is doubted by some, due to a predicted "dead band" of negative net torque production at certain low tip-speed ratios (TSRs) [1], though self-starting has been observed in controlled conditions [2, 3, 4, 5] and in field tests. In this study, self-starting ability is defined, following Bianchini et al. [6], as when a turbine accelerates through its entire power curve to its fastest equilibrium state unaided. The power curve is the plot of power coefficient, C_P, against TSR, refer to Figs 6.17 and 6.18 for some example curves. TSR is defined as:

$$\text{TSR} = \frac{\omega R}{V} \tag{1.1}$$

where ω is the turbine's angular velocity, R its radius and V the wind speed.

Where successful start-up is observed, turbines encounter an idling period of very low acceleration, indicating that while the negative torque "dead band" may not exist, a region of TSRs where torques are at least very low certainly does. The start-up phase of operation is fundamental to the design of smaller turbines. The majority of commercially available VAWTs are small to medium scale (< 15 kW). Moderate improvements to starting capability can improve a turbine's annual energy yields greatly [7] by allowing useful energy extraction in lower winds.

For most applications, aerofoils are not expected to encounter deep stall, which typically

starts at an incidence, α, of approximately 20°, so testing rarely extends beyond the range $-20° \leq \alpha \leq +20°$ (see, for example, [8]). Post-stall operation is expected of wind turbine blades during start-up, with the inboard regions of horizontal-axis wind turbine (HAWT) blades and the full length of VAWT blades experiencing angles deep into stall at low TSRs [9]. VAWT performance, particularly during start-up, is sensitive to small changes in aerofoil characteristics at certain post-stall angles [2], making accurate post-stall data desirable for the study of these machines.

This study aims to explain observed non-linear VAWT acceleration patterns and the "dead band" through analysis of all the main aerodynamic phenomena at play during turbine start-up. The primary focus is on post-stall aerofoil performance and how best to obtain good quality experimental aerofoil data when flow is separated. Wind tunnel blockage is an important consideration in such experiments. Even small aerofoils can heavily block a tunnel when stalled, and blockage corrections are not suited for use with extensively separated flows [10].

Aerofoil experiments have been conducted in a blockage tolerant wind tunnel design [11] that produces free-air equivalent data without the need for blockage corrections. Prior use has been made of the tunnel for aerofoil testing with attached flows [12], for moderately stalled aerofoils [13], for unsteady aerofoils [14] and for bluff bodies [15] but this study represents the first application of the design to deeply stalled aerofoils.

1.1 Vertical-axis wind turbine start-up

The 1970s and 1980s saw a burst of VAWT development precipitated by the OPEC oil crisis [16]. A number of large turbines were designed configured with troposkein-shaped blades, curved after the shape a spinning rope held at both ends naturally takes, in an effort to minimise non-tensional structural forces acting on them. Today's typically smaller VAWTs endure lower structural forces and primarily use either straight or helical blades. With improvements in material technologies even larger contemporary VAWTs under development use straight blades. One example is the Nenuphar Twinfloat, a 5MW prototype floating VAWT design [17]. Straight-bladed turbines are also the most common configuration used in experimental studies (refer to Table 6.1 for VAWT studies from the literature), so there is a body of data against which to validate numerical analyses. This study therefore focuses on small,

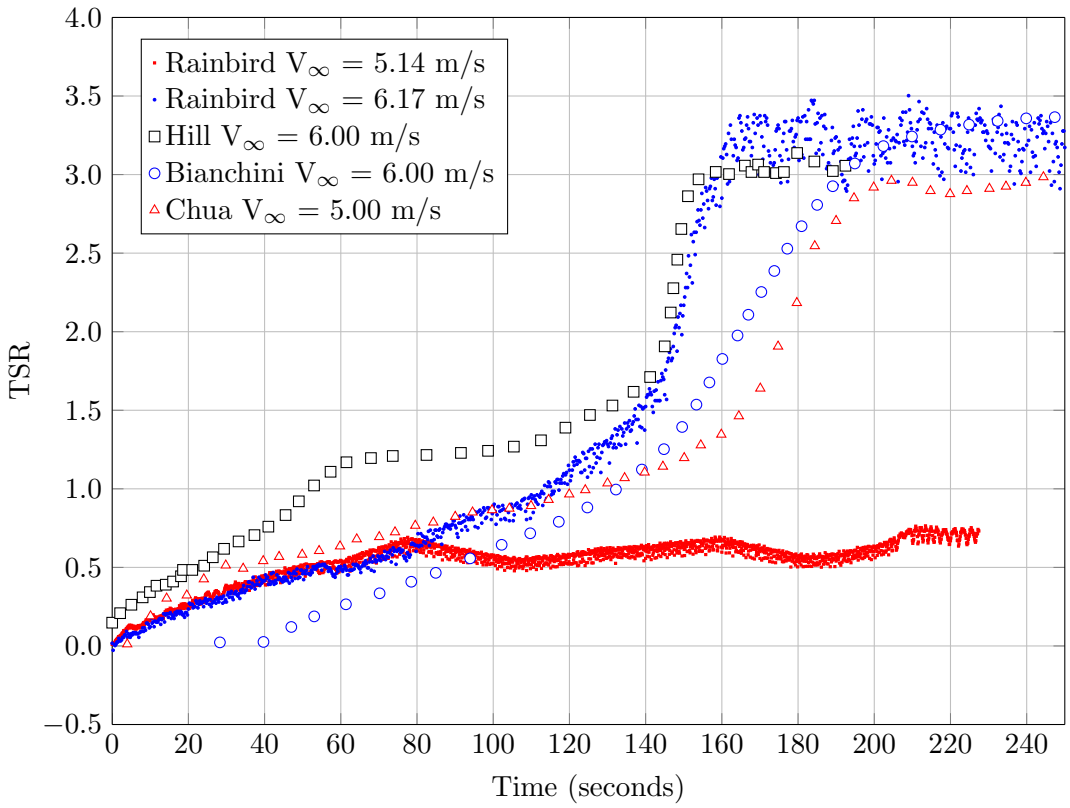


Figure 1.1: TSR development with time from the transient start-up experiments of Hill et al. [2], Rainbird [3], Bianchini et al. [4] and Chua [5].

straight-bladed VAWTs, see Fig. 1.2.

A limited number of studies have produced time-dependent VAWT start-up data. Fig. 1.1 shows experimental results for TSR against time taken at Durham University (those of Rainbird [3] and Hill et al. [2]) at a selection of wind speeds, alongside results of other similar studies. In all experiments the turbines rotate under their own power and are allowed to free spin, with no electrical generation equipment or other loading connected to them. For turbines dimensions, see Table 6.1.

Durham experiments [2, 3] were conducted in a large wind tunnel (1.7 m × 1.15 m cross section). Rainbird's results [3] produce a successful self-start at 6.17 m/s and a failure at 5.14 m/s, highlighting the sensitivity of VAWTs to flow conditions: a difference in flow velocity of 1 m/s results in very different turbine performance. A turbine point of equilibrium is a condition at which the average torque generated around a full rotation is zero. The turbine tends therefore to maintain a steady rotation when a point of equilibrium is reached. Should

its speed dip but all other conditions remain equal, a positive torque is produced and the turbine accelerates back to equilibrium. Should it speed up a negative torque is produced and it decelerates back to equilibrium.

The successful self-starting Durham runs exhibit an idling period of slow acceleration until a TSR of approximately 1.6 has been reached after 140 seconds, at which point the turbine rapidly accelerates to its highest equilibrium state at a TSR just above 3. The unsuccessful 5.14 m/s run is unable to overcome the idling phase, getting stuck at an earlier equilibrium TSR of 0.6 that is not encountered in the other runs. The "dead band" typically starts at TSRs around this point [1].

Bianchini et al. also conducted start-up experiments in a large wind tunnel (3 m × 3 m) [4, 6], their turbine successfully self starts at $V_\infty = 6$ m/s displaying a similar two-stage acceleration pattern to the Durham turbine. A 140 seconds idling period is followed by rapid acceleration to the highest equilibrium state at a TSR of 3.4. The turbine was also tested at 3 m/s and was able to self-start to a TSR of 3.9, but with a longer idling period of 325 seconds.

Chua conducted experiments with three large fans providing a wind speed near to the turbine of approximately 5 m/s (measured with an anemometer) [5], his turbine again demonstrates an idling period, of 160 seconds, followed by rapid acceleration to a TSR of 3.

South and Rangi [18, 19] tested two small rotors in a wind tunnel at 5.2 m/s: a three-bladed turbine with straight blades and another with troposkein-shaped blades, where the blade number was varied between one and six. During self-start tests of the troposkein turbine it achieved a maximum TSR of 0.5, but if assisted to a TSR of 2.6, would accelerate rapidly to its highest equilibrium state at a TSR of 8.6, suggesting a "dead band" of negative torque production exists at TSRs in the range 0.5 - 2.6 for this particular turbine at this flow speed. They did not publish transient results from the turbine.

1.2 VAWT Aerodynamics

Due to the arrangement of the turbine's axis of rotation perpendicular to flow, the apparent velocity experienced by a VAWT blade, V_b, and its incidence angle, α, are dependent on its position during rotation, defined by the azimuth angle θ, see Fig. 1.2 for a blade velocity triangle. It can be seen that V_b and α are functions of the rotational velocity, ωR, and the

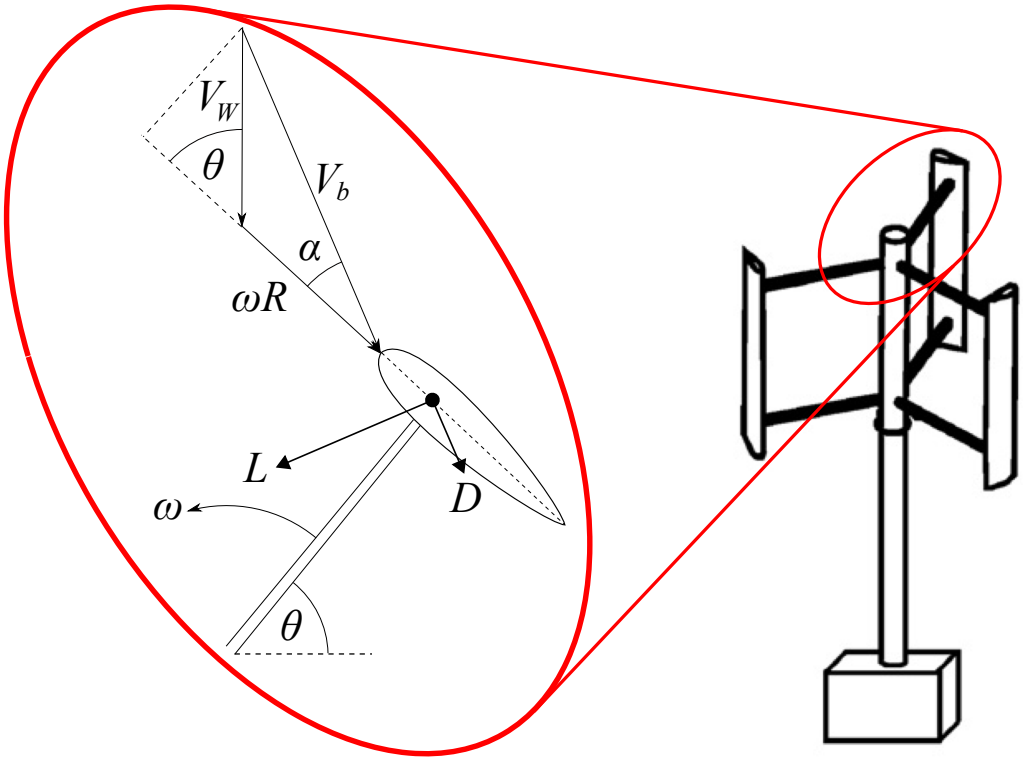


Figure 1.2: VAWT velocity triangle.

component of the flow through the turbine, V_W, resolved into a blade chord-wise direction using the azimuth, together with the blade-normal component of V_W. Note that by comparison, V_b and α are defined only by ωR and V_W in a HAWT.

Dependence on azimuth means that blade effective angle of incidence is varying, even at a constant wind speed and TSR. At higher TSRs where the rotational velocity component comes to dominate the velocity triangle there is less incidence variation, but during start-up a wide range of incidences is present. Fig. 1.3 shows lift, drag and tangential coefficients against incidence for the NACA 0015 [20], a profile commonly used in VAWTs. The incidence extremes experienced by VAWT blades at different TSRs have been highlighted: at a TSR of 4, it can be seen that these do not extend much past stall points, but at TSR = 1, angles as high as $\pm 90°$ are encountered. At this TSR, the tangential coefficient (which provides turbine torque) looks to be close to zero if integrated around a full rotation of the turbine, hence the low acceleration shown in Fig. 1.1.

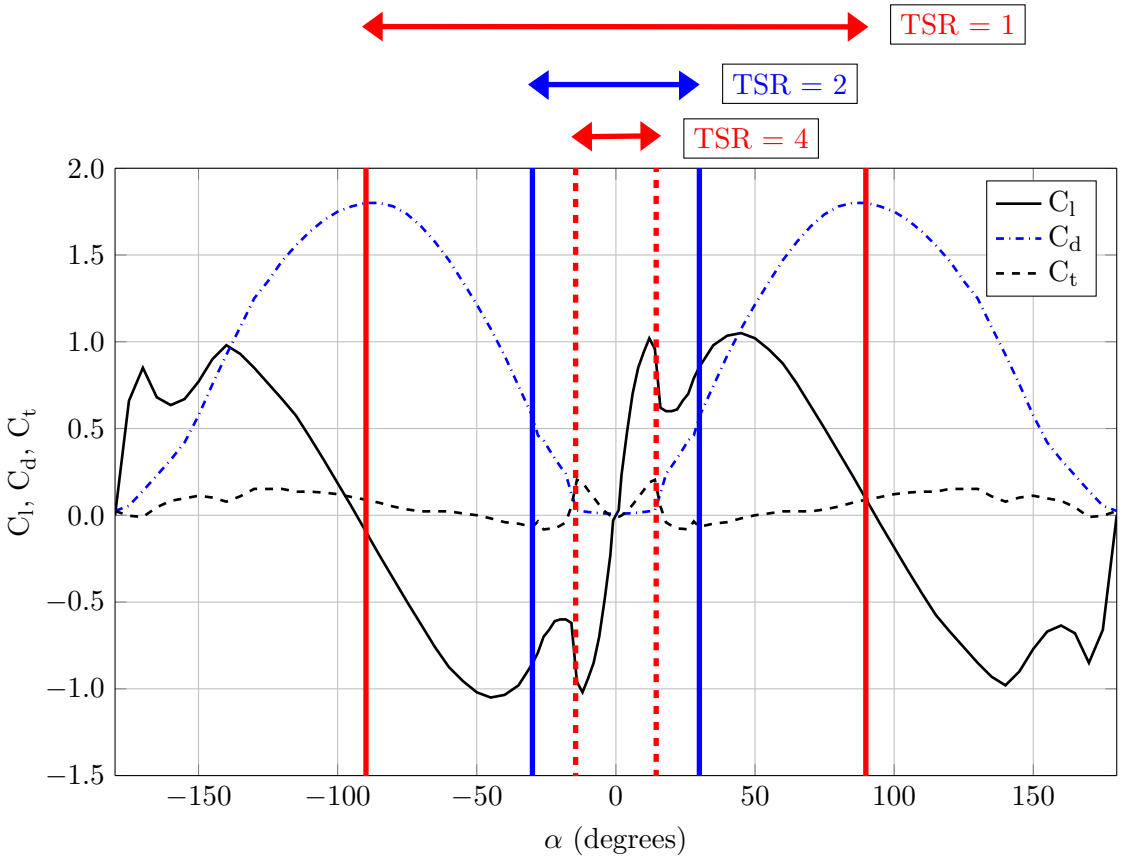
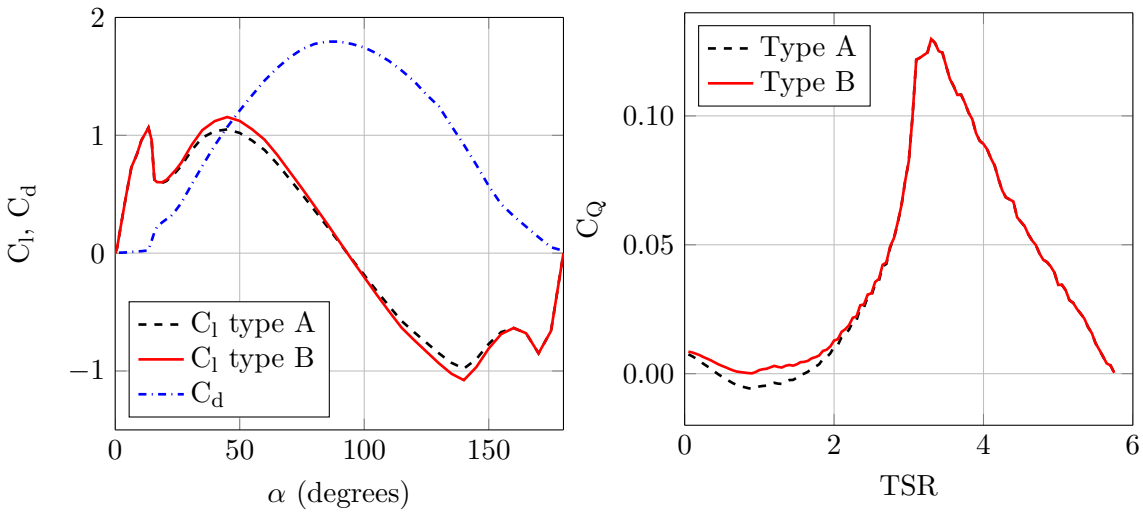


Figure 1.3: Lift, drag and tangential coefficients against incidence [20], with limits in VAWT blade incidence at different TSRs highlighted.

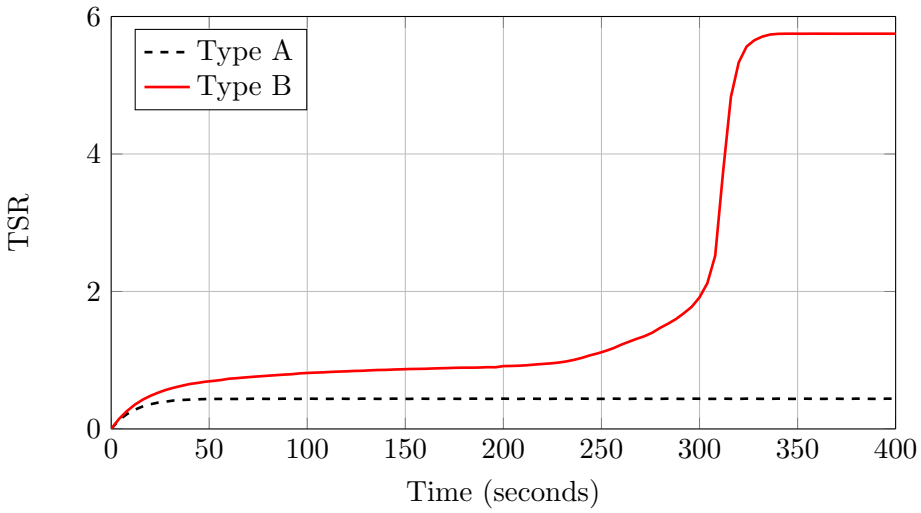
1.3 Modelled start-up

To demonstrate the sensitivity of VAWTs to post-stall aerofoil performance, the start-up of a turbine has been modelled using a blade-element momentum (BEM) model with aerofoil coefficients based on Sheldahl and Klimas's post-stall study [20]. This BEM model is described in Ch. 6 of this thesis. Fig. 1.4a shows lift and drag coefficients, C_l and C_d, against α for the NACA 0015 aerofoil. The C_l designated as type A is that of the reference [20], while type B is a lift characteristic modified to exhibit 10% higher post-stall peaks in C_l at incidences of 45° and 140°. Fig. 1.4b shows the resulting turbine torque coefficient C_Q against TSR from the BEM code using C_l types A and B (the same C_d was used for both runs). Fig. 1.4c shows the development of TSR with time from a standing start. The 10% increase in post-stall lift peaks is sufficient to impact on the prediction of successful self-starting, the Type A turbine



(a) Aerofoil coefficients [20]

(b) Turbine C_Q



(c) Turbine start-up behaviour

Figure 1.4: Effects of small changes in post-stall lift on VAWT performance.

failing to accelerate along its entire power curve due to a "dead band" of negative torque in the range 0.4 <TSR< 1.6.

1.4 Phenomena governing start-up behaviour

The characteristic start-up performance of a VAWT, resulting in either non-linear acceleration or a stagnation due to presence of a "dead band", could result from a number of aerodynamic effects. As well as post-stall aerofoil performance, those most likely to significantly influence

behaviour of the turbines during start-up are briefly introduced below and discussed in more detail in Ch. 6. All of the effects are considered to varying degrees in the code used to produce Fig. 1.4.

Unsteady aerodynamics

When an aerofoil is undergoing motions that result in time-dependent variations of the effective angle of attack, the instantaneous forces generated by it are different to those generated at similar, static incidences. Where the variation takes the incidence above the static stall angle, the aerofoil will experience dynamic stall [21].

Dynamic stall results in an overshoot of static stall angle and maximum lift when effective incidence is ramping up, but when the stall does occur a vortex is shed from the leading edge of the aerofoil. Lift is enhanced as long as the vortex is above the suction surface of the aerofoil, but it is soon carried along the surface downstream of it by the prevailing flow. The centre of pressure moves downstream rapidly, resulting in generation of large pitching moments [22].

Forces generated by aerofoils demonstrate significant hysteresis depending on whether or not incidence is increasing or decreasing, with an undershoot of static stall and maximum lift when effective incidence is decreasing. The influence of the dynamic effects is proportional to the reduced frequency k of a system

$$k = \frac{\omega c}{2V} \tag{1.2}$$

where c is the aerofoil chord and ω is the circular frequency of the oscillation. At $k < 0.05$, a system can be considered quasi-steady, at $0.05 < k < 0.2$ unsteady effects should be considered in any analysis. At $k > 0.2$ the system is highly unsteady and dynamic effects come to dominate performance [22]. For the Durham VAWT, these limits equate to TSRs of 0.48 and 1.90, putting the vast majority of the start-up process within a range of k where dynamic effects are significant. Crucially, this includes the key TSR of approximately 0.6 where successful and failed start-up paths diverge (see Fig. 1.1).

Blade Reynolds number effects

Large variations in VAWT blade apparent velocity, particularly at low TSRs, mean that the blades experience a wide range of Reynolds numbers, Re. At a TSR of 1, in a windspeed of 5m/s, the blades of the Durham turbine will experience Reynolds numbers from approximately 0 to 50 000. See the following Section 1.5 for more on aerofoil behaviour in attached flows and aerodynamic stall, as affected by the Reynolds number.

There is very little post-stall aerofoil data available at any Reynolds numbers and a lack of even pre-stall data at Reynolds numbers below around 300 000, see Section 1.7, making quasi-steady analysis of turbine start-up a challenge unless using an aerofoil for which such data exists. New experimental results covering Reynolds numbers of 20 000 - 300 000 for the NACA 0015, NACA 0018 and two transforms of the NACA 0018 are presented in Ch. 5.

Blade-wake interactions

Due to the vertical axis of rotation, blade-wake interactions occur in VAWTs, with blades on the downstream half of the rotation encountering the wakes of those on the upstream half of the rotation. Interactions have a particularly significant impact at TSRs of 0.5 to 1.6 [23], a region covering most of the start-up process.

Flow curvature

VAWT blades experience an apparent curvilinear flow due to the path of their rotation, while aerofoil lift and drag data is obtained in rectilinear flow in wind tunnels. This curved flow imparts virtual camber and incidence effects onto the blades [24], meaning that blade lift and drag data must be modified to account for these, or data for aerofoils with real camber and incidence used when analysing the turbines. The effects are more pronounced in turbines with higher c/R ratios and at higher TSRs [24]. The two transforms of the NACA 0018 presented in Ch. 5 are cambered following virtual camber theory, in order to study the effect on VAWTs numerically.

Some modelling of turbine start-ups has applied virtual camber to blades only once a certain TSR is reached, or for the start-up, or not at all, with self-start success or failure dependant on application of the camber effect [4].

1.5 Stall and attached flow aerofoil behaviour

Stall is the process by which a lifting body suffers a drop in the lift force it generates due to the separation of flow from its suction surface. Whether separation occurs or not is a function of phenomena occurring in the shear layer surrounding the body. In aerofoils, with rounded leading edges, separation is dependent on pressure gradient (itself dependent of the curvature and orientation of the aerofoil) and the Reynolds number of the flow.

In the range of Reynolds numbers assessed in this study, if the boundary layer on the aerofoil is laminar, as the adverse pressure gradient on the suction surface is increased (i.e. by increasing incidence) it will either separate or could briefly separate, transition to turbulent flow, then reattach, forming a separation bubble, see Section 1.5.5. At higher Reynolds numbers, the boundary layer could transition to turbulence without any separation. Turbulent boundary layers resist separation better than their laminar equivalents due the better mixing in the layer giving better momentum transfer and a fuller velocity profile.

McCulloch and Gault define three types of stall for low speed flows: trailing edge, leading edge and thin aerofoil stall [25], described in the following sections and shown in Fig. 1.5, along with some combined stall types. Their experiments were conducted at $Re = 5.8 \times 10^6$. Later work extended the Reynolds numbers considered to the range 700 000 - 25×10^6 through a review of the literature available at the time [26]. Relationships between Reynolds number, aerofoil thickness and stall type were established in this Reynolds number range, which is well above the range considered here.

Carmichael's review covers a wider range of Reynolds numbers, from fractional values up to 10^9, but the focus is on the lower end of the range, at 20 000 - 200 000, almost coincident with this study [28]. He defines five lift curve and polar types, based solely on lift curve and polar shapes from the literature. Limited attempts are made to formulate relationships between behaviours and aerofoil shape or Reynolds number. See Section 1.5.4 for more on Carmichael's stall types.

1.5.1 Trailing edge stall

Usually affecting thicker aerofoils, particularly at higher Reynolds numbers, this stall sees separation occurring first near the trailing edge of the suction surface, see Fig. 1.6. The point

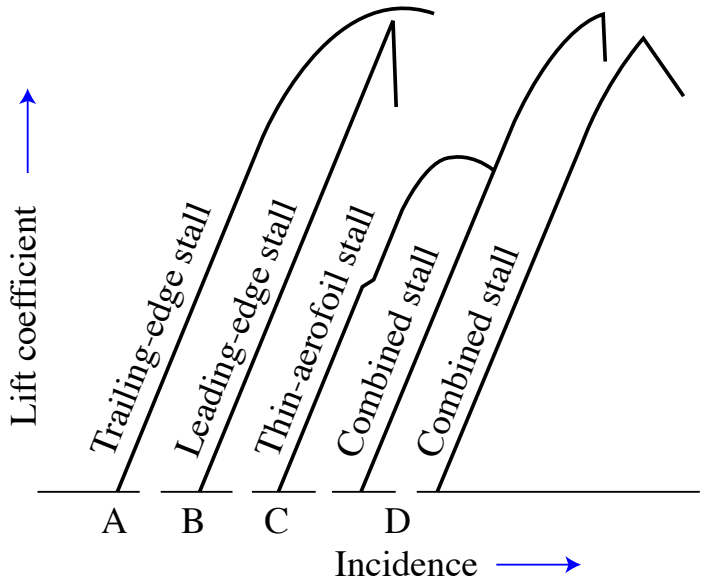


Figure 1.5: Typical lift curve slopes for different types of stall [27] (after [26]).

of separation gets progressively nearer the leading edge as incidence is increased until finally flow is completely separated across all of the surface. At the point of maximum lift, separation is across approximately half of the surface. It is characterised by a smooth, gradual change in the gradient of the lift curve slope as stall is approached and passed.

1.5.2 Leading edge stall

The sharp, sudden drop in lift associated with leading edge stall, as seen in Fig. 1.5 (curve B), is caused by the bursting of a laminar separation bubble. It primarily affects sections with moderate thickness of 9 - 15%. At angles below stall, a laminar separation bubble is present on the aerofoil's suction surface. Peak pressure occurs near the leading edge, aft of which is a region of pressure recovery with an adverse pressure gradient. As incidence is increased, the pressure gradient increases in strength, pulling the point of separation, and with it the bubble, forward. Just before stall, the bubble is near to the peak pressure point, see Fig. 1.6. At the stall angle, the pressure gradient becomes too large for the bubble to sustain and it suddenly bursts, with instantaneous separation across the whole pressure surface occurring. The stall is very sharp, with little or no change in the lift/incidence slope before the sudden drop in lift.

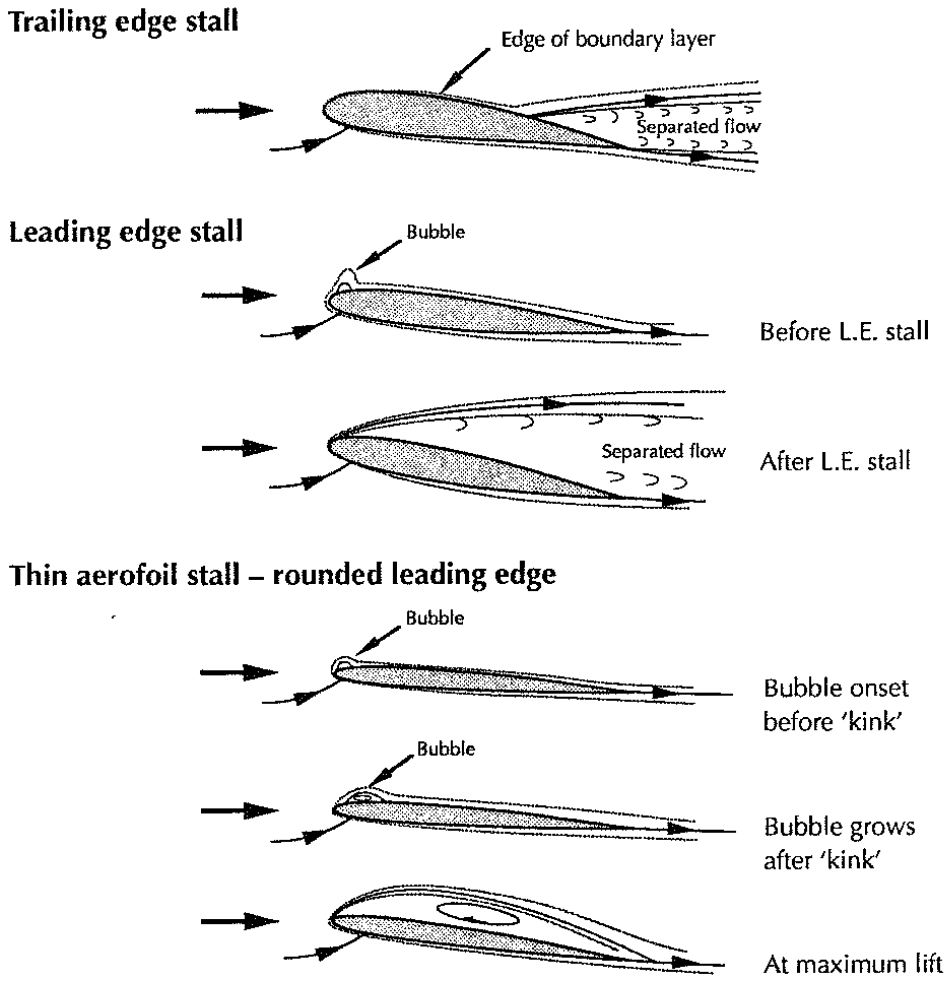


Figure 1.6: Stall types according to Khoo [29].

1.5.3 Thin aerofoil stall

Typical of sharp-leading edged profiles and thin, rounded profiles (with thicknesses below 9% of chord), thin aerofoil stall is smooth and gradual like trailing edge stall, but features lower values of maximum lift coefficient, $C_{l\,\mathrm{MAX}}$. At some incidence a certain point before the maximum lift and stall, the lift curve has a characteristic "kink". At angles below this incidence, there is a bubble on the suction surface, positioned near the leading edge. After the kink, it begins to increase in size with increasing incidence, see Fig. 1.6, until at the point of maximum lift it stretches across the suction surface. Beyond this, stall occurs and flow is fully separated.

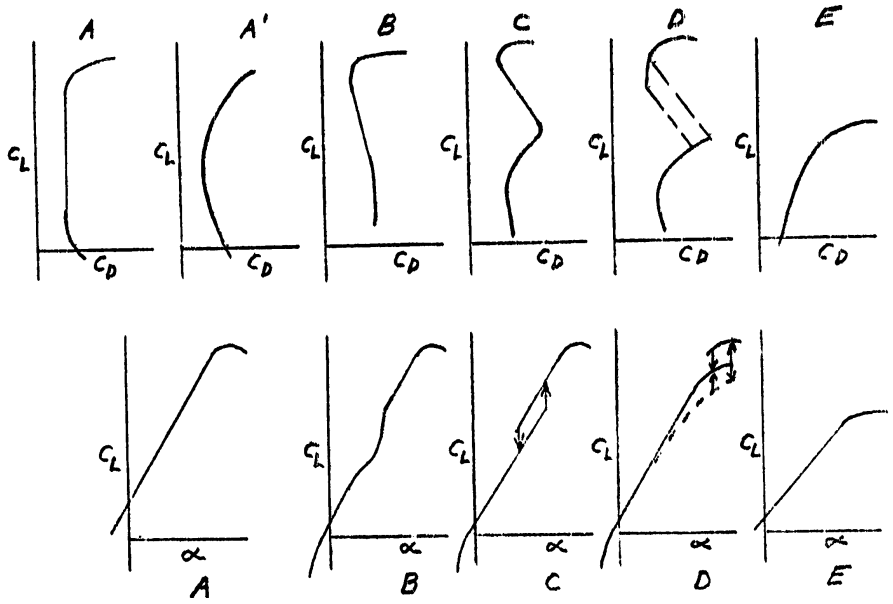


Figure 1.7: Typical lift curve slopes and polars for different types of stall [28].

1.5.4 Carmichael's lift curve and polar types

Carmichael classifies a number of different lift curve and lift/drag polar characteristics, shown in Fig. 1.7. He states that generally, a given aerofoil will perform following either A or B type behaviours at higher Reynolds numbers, regressing to the C, D or E types as Reynolds number is decreased. Aerofoils with B and C type curves tend to provide the best performance in terms of L/D ratios.

Aerofoils with excessive thickness or camber are more likely to exhibit the distorted curve shapes of C or D at a given Reynolds number. E type behaviour is generally associated with aerofoils with minimal thickness and camber, or with very thick aerofoils. Note that McCulloch and Gault's stall types would be classified as type A (leading edge or trailing edge) or type B (thin aerofoil) under Carmichael's classification.

1.5.5 Laminar separation bubbles

Laminar boundary layers are susceptible to separation, particularly in the pressure recovery region of the suction surface, due to their inability to sustain much of an adverse pressure gradient [30]. Separated shear layers are more susceptible to transition to turbulence, and when laminar boundary layers separate they rapidly do so. Once turbulent, the shear layer

will reattach to the aerofoil surface due to the greater entrainment of flow, forming a laminar separation bubble, enclosing an area of recirculating flow [30]. See Fig. 5.10b for a diagram of a bubble showing the separation point, transition and reattachment, alongside a typical pressure distribution across a bubble.

The length required for the separated shear layer to transition and reattach is defined by a Reynolds number of around 50 000 [28] (referred to as the "critical Reynolds number" Re_{crit}, the specific value is dependent on profile shape and surface roughness among other variables), so bubbles are shorter in higher Reynolds number flows. In flows with $Re < Re_{\text{crit}}$, the transition occurs downstream of the trailing edge of the aerofoil so the flow is unable to reattach and form a bubble, with separation occurring across the whole suction surface at even moderate incidences.

The laminar separation bubble has a significant impact on aerofoil performance at $Re_{\text{crit}} < Re < 700\,000$ and continues to have measurable effect on characteristics up to $Re = 4 \times 10^6$ [28]. It has a bigger effect at lower Reynolds numbers due to the larger size of the bubble. Presence of a bubble can lead to a hysteresis in lift and drag behaviour with incidence where stall is caused by a sudden bursting of a bubble. Flow may not reattach until the incidence is decreased some way below the stall angle, due to a discrepancy between the pressure gradient that can be tolerated by a bubble and that at which a bubble can reform.

1.6 Post-stall aerofoil data for VAWT modelling

The modelled start-ups presented in Section 1.3 have established that variations in post-stall aerofoil performance can have a large impact on the model output. Throughout this thesis, the term "post-stall" refers to aerodynamic characteristics in the range of incidences between stall angles, approximately $10° < \alpha < 170°$ (and the corresponding negative incidences). The term "deep stall" refers to the range of incidences $20° < \alpha < 160°$ (and the corresponding negative incidences) and "the immediate vicinity of stall" to $10° < \alpha < 20°$ (and the corresponding negative incidences).

Low-order models, such as the BEM code used for the start-ups, still represent an industry standard for the analysis of wind turbines. Whether used as a first step in the design process, or in coupled codes for the analysis of aerodynamics, hydrodynamics, structural and control

dynamics simultaneously [16], they are used ahead of more advanced analyses due to their robustness and speed. Reasonably accurate results have been produced by other researchers using BEM codes for studies on VAWT acceleration [6] and for power and operating range calculations [31].

Until such time as advanced computational methods become cheaper and more reliable, low order methods will remain an important tool in wind turbine design. For VAWT start-up, where stall is encountered, BEM codes are preferable to potential flow methods as they can provide results where flow is separated. Unlike potential flow methods, BEM codes require two-dimensional aerofoil data as inputs, making high quality post-stall aerofoil data vitally important to the design of VAWTs for better self-start.

1.7 Existing aerofoil studies

Little aerofoil data exists covering a full range of incidences (0° to 180° for symmetrical aerofoils, 0° to 360° for others) and, in particular, there is a lack of data taken at the low Reynolds numbers at which typical VAWT blades operate. For example, the commercially available Urban Green Energy Visionair 3 turbine [32] has a 1.8 m diameter and 0.38 m blade chord. In accelerating from standing to TSR = 2 in a wind speed of 6 m/s, it will experience a maximum blade Reynolds number of only 450 000.

1.7.1 Post-stall studies

Existing aerofoil studies that cover a wide range of incidences in the post-stall region do not show strong agreement. Fig. 1.8 reproduces C_l and C_d from the studies of Bergeles et al. [33], Critzos et al. [34] and Massini et al. [35] for the NACA 0012, Sheldahl and Klimas [20] and Pope [36] for the NACA 0015 and those of Du et al. [37] and Timmer [38] for the NACA 0018. The differences in thickness between the NACA 0012, 0015 and 0018 should have a limited impact on results where flow is separated. Sheldahl and Klimas presented results for the NACA 0009, 0012 and 0015 with performance in deep stall shown to be largely independent of thickness [20].

At the second lift peak at $\alpha \approx 45°$, values of C_l vary between 0.98 and 1.18, a difference of 20%. At peak drag at $\alpha \approx 90°$, C_d is between 1.75 and 2.07, an 18% variation. The variation

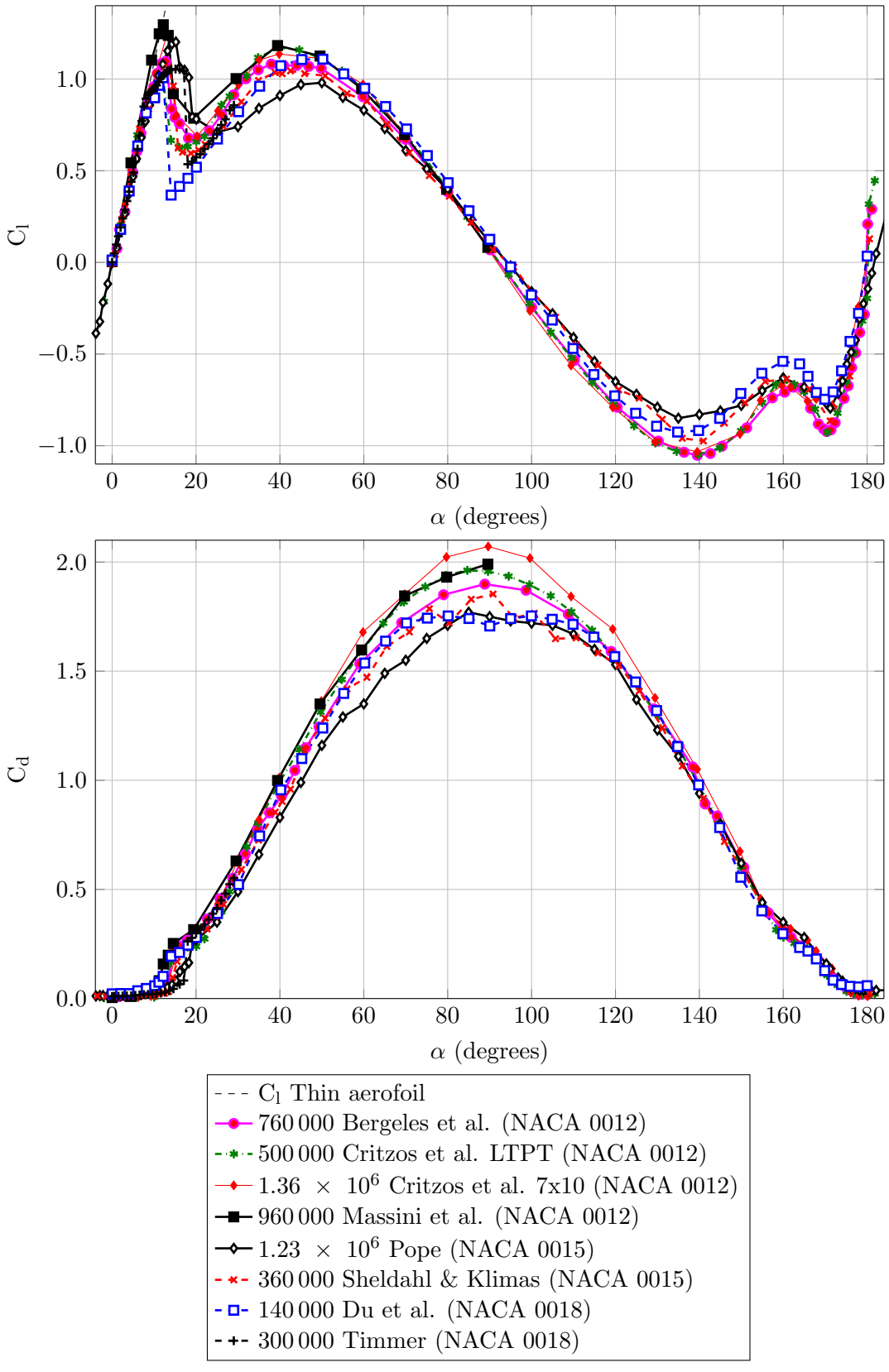


Figure 1.8: C_l and C_d vs α for selected NACA 00XX studies (see Table 1.1 for references).

in the lift peak is more than sufficient to impact on accurate modelling of VAWT start-up, as shown in Section 1.3, suggesting more accurate post-stall data is required to simulate start-up with confidence. These uncertainties in aerofoil characteristics are perhaps the reason that, in spite of experimental studies showing that VAWTs with straight, symmetrical blades are capable of self-starting (see Fig. 1.1), accurate modelling of successful start-up can be impossible without modification of the input aerofoil coefficient data: Bianchini et al. switch off "virtual camber" effects at low TSRs [6] while Rossetti and Pavesi [39] apply the post-stall model of Viterna and Corrigan [40] to their blades.

The selected studies shown in Fig. 1.8 represent all investigations of symmetrical aerofoils post-stall that the authors could find, other than Zhou's work at very low Reynolds numbers [42] and Poisson-Quinton and de Sievers's study [48], for which no information about experimental configuration could be found (see Timmer [49] for a review of NACA 0012 data and Lindenberg [50] for a more comprehensive review including cambered aerofoils). The studies are summarised in Table 1.1.

1.7.2 Low-Reynolds number aerofoil experiments

Also included in Table 1.1 are the low Reynolds number studies of Althaus [8, 51] and Jacobs and Sherman [43] that do not extend to deep stall, and are referenced later in this thesis. Studies taken at low Reynolds numbers are rare, much like post-stall data, though interest from the UAV and wind turbine industries mean such experiments are becoming more common. Though data has not been directly referenced from them, the low Reynolds number experimental reviews of Miley [30] and the numerous original low Reynolds number works of Selig, particularly on wind tunnel testing methodology [52] have proved invaluable to this study.

1.7.3 Inconsistencies between data from the literature

Table 1.1 contains information on factors that can affect aerofoil force measurements taken in wind tunnels, namely the Reynolds number of the flow, the aspect ratio of the wing under test (a relevant consideration even when trying to reproduce two-dimensional flows), the chord-to-height ratio, c/H, of the aerofoil and tunnel and the methods used to combat wind

Source	Post-stall peak C_l	Post-stall peak C_d	Re ($\times 10^6$)	c/H	$\mathcal{AR}$	Corrections (see below)
NACA 0012 studies						
Althaus [8]	-	-	0.15	0.33	1.85	a, e
Bergeles et al. [33]	1.08	1.90	0.76	0.14	1.70	a, b, d, f
Critzos et al. LTPT [34]	1.13	2.08	1.80	0.07	6.00	a, e
Critzos et al. LTPT [34]	1.15	1.96	0.50	0.07	6.00	
Critzos et al. Langley 7×10 [34]	1.14	2.07	1.36	0.10	7.00	
Dong-Ha et al. [41]	-	-	0.02 - 0.05	0.36	2.78	none
Massini et al. [35]	1.18	1.99	0.96	0.13	2.00	a, d, f
Sheldahl and Klimas [20]	1.10	1.83	0.36	0.07	6.00	a, c, f
Zhou et al. [42]	0.98	1.45	0.005 - 0.05	0.17	2.70	d
NACA 0015 studies						
$c/H = 0.10$ (this study)	1.10	1.92	0.02 - 0.25	0.10	10.00	b[2]
$c/H = 0.15$ (this study)	1.04	1.87	0.06 - 0.25	0.15	6.67	
$c/H = 0.20$ (this study)	1.10	1.92	0.06 - 0.25	0.20	5.00	
$c/H = 0.25$ (this study)	1.13	1.85	0.06 - 0.25	0.25	4.00	
$c/H = 0.30$ (this study)	1.19	1.85	0.06 - 0.25	0.30	3.33	
Jacobs and Sherman [43]	-	-	0.17	0.08[1]	6.00[1]	h
Pope [36]	0.98	1.77	1.23	0.17	1.67	a, g
Sheldahl and Klimas [20]	1.05	1.86	0.36-0.70	0.07	6.00	a, c, f
NACA 0018 studies						
Du et al. [37]	1.11	1.75	0.06 - 0.14	0.28	3.54	b
Timmer [38]	-	-	0.15 - 1.00	0.20	7.20	b, d

a. Rae et al. [44], see § 2.1.10
b. AGARD [45, 46]/ESDU [10], see § 2.1.5
c. Horizontal buoyancy [44], see § 2.1.4
d. Maskell [47], see § 2.1.6 and 2.1.10
e. Boundary measurements, see § 2.1.7
f. Turbulence factor [44], see § 2.1.8
g. "Breather" section in wind tunnel [36]
h. Apparatus-specific correction regime [43]

1. Jacobs and Sherman's study uses finite wings. c/H is not a good indicator of blockage for these experiments (See § A.2.3).
2. a and d also assessed, see § 2.1.10, c found to produce insignificant adjustments (§ 2.1.4) and not applied, f assessed but not applied (§ 2.1.8).

Table 1.1: Summary of aerofoil studies referenced in this paper. Where a range of Reynolds numbers is given, peaks are for $Re = 150\,000$ or the nearest alternative.

tunnel blockage (see Section 1.8). Other factors can affect performance, such as model surface roughness and turbulence, but these are not routinely given in papers.

Where flow is attached, poor agreement between studies conducted at low Reynolds num-

bers is well established [53, 28, 30], due to the impact of experimental inconsistencies including flow quality, measurement methods, measurement accuracy and model accuracy. Small errors and inconsistencies that would not be significant in higher Reynolds number experiments are magnified at low Re.

For studies that have varied the Reynolds number in deep stall (where flow is separated), findings on Reynolds number influence on post-stall aerofoil performance are inconclusive, suggesting variations between existing studies also result from experimental inconsistencies. In addition to the inconsistencies associated with attached flows, different blockage reduction techniques can be responsible for large variations between studies.

For the reader's convenience, the studies referenced in Table 1.1 are summarised in greater detail in in Appendix A.

1.8 Wind tunnel blockage

Provided the area blockage ratio is within reasonable bounds, wind tunnel blockage is not an important consideration for conventional aerofoil studies at moderate angles of attack. Corrections to account for the blockage of models under test and that of their wakes, along with the constriction to curvature imparted on flows by tunnel walls, are derived from classical potential flow theory and are well established [10]. Where blockage is low and flow is attached, corrections rarely have a significant effect on data and they are seldom discussed in reviews of experimental inconsistencies [53, 28, 30].

There are a number of alternative correction methodologies that can be applied to data, with no established best practice, particularly where flow is separated. Ch. 2 contains a review of corrections and derivations of them from potential flow and empirical means. Evidence is presented of the significant impact a researcher's choice of corrections has on results. An assessment of the correction methodologies is given based on their ability to correct raw data from five different sized NACA 0015 aerofoils to a common set of free-air equivalents.

The majority of correction methods are not designed for use with extensive separated flows. As such, a review of alternative means of minimising blockage that are better suited to separated flows is also presented.

1.9 The blockage tolerant tunnel

The tunnel design settled on for use in the study reduces blockage through physical means. It uses a passive blockage tolerant design, with transversely slatted walls replacing the conventional solid tunnel walls on the wall opposite the test aerofoil's suction surface, or the walls opposite both the suction and pressure surfaces, see Fig. 2.11. The slotted gaps between the slats allow flow to exit and re-enter the main channel of the tunnel, avoiding the model under test and reducing blockage. The open area ratio, OAR, of slotted gaps in the walls to total wall area, must be set to a certain level which is model and tunnel dependent.

If the OAR is properly calibrated, the tunnel can provide near-blockage free data for a wide range of model sizes and model types [54], with no need for blockage corrections. The downside of the tunnel's use is the extensive preparatory experiments required before main testing can take place. Ch. 4 documents the design and build of the new test section, a process that would not need to be repeated by future tunnel users, but also the lengthy calibration experiments required to ensure the tunnel's OAR is appropriately set. These would need to be repeated for any non-aerofoil models to ensure the best levels of blockage reduction.

1.10 Summary of research objectives

The first primary objective of this work is the study of VAWT start-up. The aim is to provide:

An explanation of VAWT start-up behaviour

The causes of the characteristic non-linear acceleration pattern of the turbines, with a long period of idling followed my rapid increases in speed, or the encountering of a "dead band" of negative torques preventing self-start, will be established. This will be achieved through the development of a BEM method tailored to model VAWTs at the low TSRs encountered at start-up. Code development is covered in Ch. 6, along with validation to experimental studies on blade forces and start-up.

The code considers all the main effects influencing behaviour during start-up (listed above in Section 1.4). Work to quantify their impacts on the forces generated by turbine blades is presented, again with comparisons made to experimental studies. Finally, a conclusion is

drawn on the main cause of VAWT acceleration patterns and the "dead band", in Ch. 6.

Aside from the inherent approximations necessary in low-order modelling, BEM codes are limited primarily by the quality of aerofoil data input to them. At low TSRs, VAWT blades experience effective incidence well into deep stall, making good quality post-stall data key to the accurate modelling of start-up with BEM codes. The review of the literature, presented in Section 1.7.1, has revealed large uncertainties in aerofoil forces where flow is separated. Work to establish the causes of these are presented in Ch. 2. Wind tunnel blockage and the steps taken to counter it are found to be the largest contributor. As such, the the second primary objective of this study is:

The provision of a highly accurate set of post-stall aerofoil data

New experimental data is presented for four aerofoils, over a full range of incidences (0° to 180° for symmetrical aerofoils, 0° to 360° for others). A blockage tolerant tunnel was built and calibrated for the collection of data, requiring no blockage corrections, see Chapters 3-4. A conventional, solid-walled tunnel was also used in conjunction with blockage corrections, and comparisons made between the two blockage reduction techniques. Results from both tunnels, and the comparison between them are presented in Ch. 5. There is good agreement between corrected data from the solid-walled tunnel and the data from the tolerant wall tunnel. This gives confidence in the use of the tolerant tunnel to measure datasets of this type.

Blockage is the main source of experimental inconsistencies in wind tunnel experiments on aerofoils and different blockage reduction techniques can provide very different results from the same raw experimental data. As such, the agreement between the two different blockage reduction techniques suggests that blockage has been suitably minimised in both and that the datasets are highly accurate.

1.11 List of publications

Journal articles

J. Rainbird, J. Peiro and M. Graham, "Blockage-tolerant wind tunnel measurements for a NACA 0012 at high angles of attack", *J. Wind Engineering and Industrial Aerodynamics*,

Vol. 145, pp. 209-218, 2015.

A. Bianchini, J. Rainbird, J. Peiro, J.M.R. Graham, F. Balduzzi, G. Ferrara and L. Ferrari, "An Experimental and Numerical Assessment of Airfoil Polars for Use in Darrieus Wind Turbines. Part 1 - Flow Curvature Effects," *Journal of Engineering for Gas Turbines and Power*, Vol. 138, pp. 032602-1:032602-10, 2016.

A. Bianchini, J. Rainbird, J. Peiro, J.M.R. Graham, F. Balduzzi, G. Ferrara and L. Ferrari, "An Experimental and Numerical Assessment of Airfoil Polars for Use in Darrieus Wind Turbines. Part 2 - Post-stall data extrapolation methods," *Journal of Engineering for Gas Turbines and Power*, Vol. 138, pp. 032603-1:032603-10, 2016.

J. Rainbird, J. Peiro, J.M.R. Graham, A. Bianchini, F. Balduzzi, G. Ferrara and L. Ferrari, "On the Influence of Virtual Camber Effect on the Airfoil Polars for Use in Simulations of Darrieus Wind Turbines", *Energy Conversion and Management*, Vol. 106, pp. 373 384, 2015.

J. Rainbird, J. Peiro and M. Graham, Post-stall airfoil performance and vertical-axis wind turbines, *AIAA Journal of Propulsion and Power*, 2016 (in press).

Book chapter

J. Rainbird, J. Peiro, M. Graham and E. Ferrer, "Vertical-Axis Wind Turbine start-up modelled with a high-order numerical solver" In: E. Ferrer and A. Montlaur, *CFD for Wind and Tidal Offshore Turbines*, Springer, 2015.

Conferences

A. Bianchini, J. Rainbird, J. Peiro, J.M.R. Graham, F. Balduzzi, G. Ferrara and L. Ferrari, "An Experimental and Numerical Assessment of Airfoil Polars for Use in Darrieus Wind Turbines. Part 1 - Flow Curvature Effects," in ASME Turbo Expo 2015, Montreal, Quebec, Canada, June 15-19 2015.

A. Bianchini, J. Rainbird, J. Peiro, J.M.R. Graham, F. Balduzzi, G. Ferrara and L. Ferrari, "An Experimental and Numerical Assessment of Airfoil Polars for Use in Darrieus Wind Turbines. Part 2 - Post-stall data extrapolation methods," in ASME Turbo Expo 2015, Montreal, Quebec, Canada, June 15-19 2015.

J. Rainbird, J. Peiro, M. Graham and E. Ferrer, "Vertical-Axis Wind Turbine start-up modelled with a high-order numerical solver", presented at ECFD VI, Barcelona, Spain, Jul 20-25, 2014.

J. Rainbird, J. Peiro and M. Graham, "Post-stall airfoil performance and vertical-axis wind turbines, in 33rd ASME wind energy symposium, AIAA SciTech 2015, Kissimmee, Florida, USA, Jan 5-9, 2015.

J. Rainbird, J. Peiro and M. Graham, "Post-stall aerofoils and vertical-axis wind turbines, presented at SUPERGEN Wind Hub General Assembly, Loughborough, UK, Apr 14, 2015. Prize winner: best technical content.

J. Rainbird, J. Peiro and M. Graham, "Vertical-axis wind turbine analysis using blockage tolerant wind tunnel results for post-stall aerofoils, presented at EWEA 2015, Paris, France, Nov 17-20, 2015

Chapter 2

Wind tunnel blockage and methods used to limit its impact

Conventional wind tunnels, with solid-walled test sections, do not provide an accurate reproduction of unconstrained steady flow. Their walls constrain any streamline curvature induced by the model and together with the model block the flow through the tunnel, causing it to speed up. Fig. 2.1 shows a comparison of streamline development around an aerofoil in a wind tunnel and in free air. The figure was prepared using the panel method described in Section 3.2. The streamlines in both cases start from the same points. Those constrained by the tunnel show less curvature than the free air equivalents and are forced closer together by the blockage of the aerofoil and tunnel walls. Forces generated by the aerofoil under test and surface pressures on it are therefore different to those in free air.

This chapter covers some of the methods used to limit the effects of blockage on data obtained from wind tunnel experiments, both through correcting formulae and apparatus modifications.

2.1 Blockage corrections

By far the most common approach is to apply blockage corrections to data taken in solid-walled wind tunnels. These are composed of elements to correct for the blockage due to the model, due to the model's wake, and to streamline curvature. They are derived using

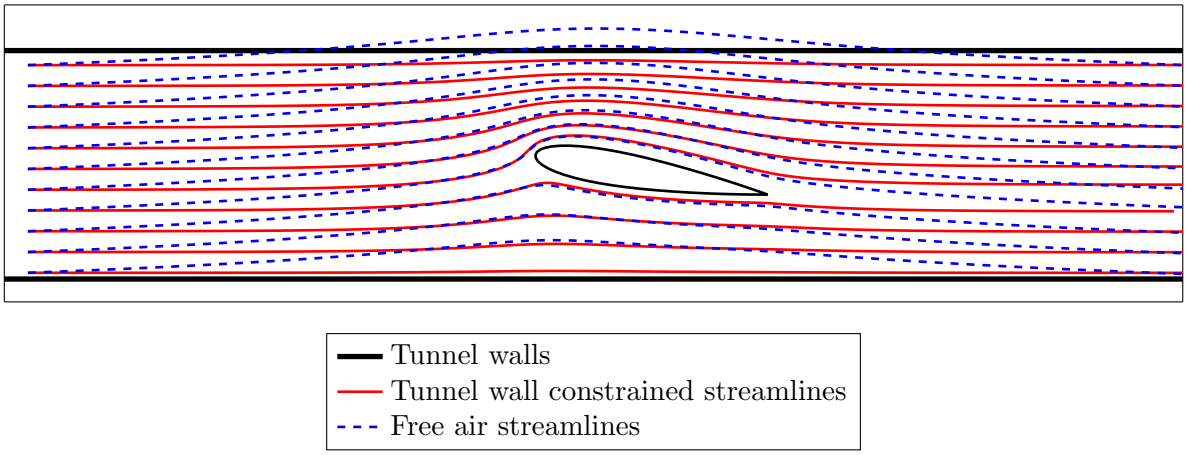


Figure 2.1: Effects of wind tunnel walls on streamlines around an aerofoil.

potential flow theory for streamline constraints and wake blockage, and through potential flow and empirical methods for solid blockage, or through wholly empirical means for solid and wake blockage components together. A number of correction regimes exist, producing different effective free air results from the same raw data. This section provides derivations of the corrections used in the current research, a comparison with other corrections used in studies referenced in this thesis, and a general critique of correction formulae.

2.1.1 Lift interference

Lift interference is caused by the limitations placed on streamline curvature by the tunnel walls, i.e. the part of the wall interference due to circulation generated by the model. Corrections for it were by first derived by Glauert, who proposed a correction to the angle of incidence, $\Delta\alpha$, obtained by modelling the aerofoil under test as a point vortex at its quarter chord [55]. The vortex has strength $\Gamma = \frac{1}{2}C_l U_u c$, where C_l is the lift coefficient, U_u the measured flow velocity in the wind tunnel (i.e. uncorrected for blockage effects, denoted by the subscript u) and c is the aerofoil chord. The tunnel walls are modelled using a method of images (see Appendix B) and can be shown to induce an upwash at the half-chord of the aerofoil. The induced incidence $\Delta\alpha$ can be obtained from the angle between the free-stream and the velocity vector equating to the free stream plus this upwash, in terms of uncorrected lift coefficient C_{lu}, chord and tunnel height, H, as

$$\Delta\alpha = \frac{\pi}{96}\left(\frac{c}{H}\right)^2 C_{lu} \tag{2.1}$$

See Appendix B.1 for a full derivation of this correction.

Allen and Vincenti [56] show that if the aerofoil is modelled as a distribution of vorticity along its chord, Eqn. (2.1) becomes

$$\Delta\alpha = \frac{\pi}{96}\left(\frac{c}{H}\right)^2 (C_{lu} + 4C_{mu}) \tag{2.2}$$

taking account of the actual centre of lift of the model through the inclusion of the uncorrected coefficient of moment, C_{mu}, term. Using thin aerofoil theory and assuming that $\mathrm{d}C_l/\mathrm{d}\alpha \approx 2\pi$, the induced lift, ΔC_l, and moment, ΔC_m, can be calculated from $\Delta\alpha$ as

$$\Delta C_l = -\frac{\pi^2}{48}\left(\frac{c}{H}\right)^2 C_{lu} \tag{2.3}$$

and

$$\Delta C_m = \frac{\Delta C_l}{4} \tag{2.4}$$

2.1.2 Solid Blockage

Solid blockage is caused by the constraints placed on the flow by the volume of the model itself, resulting in an increase in local velocity. It is corrected for by taking a ratio of a representative cross-sectional area of the model to that of the tunnel and adjusting the flow velocity using Bernoulli's equation and conservation of mass.

Lock derived a correction for solid blockage of symmetrical bodies by considering the model as a cylinder, represented by a point source-sink doublet of strength $\mu = 2\pi a^2 U_u$ where a is the cylinder radius [57]. Using a method of images he derived a formula for the solid blockage factor, ϵ_{sb}, the ratio of velocity change caused by the effects of solid blockage to uncorrected free stream velocity in the wind tunnel, of

$$\epsilon_{sb} = \frac{\pi^2}{3}\left(\frac{a}{H}\right)^2 \tag{2.5}$$

See Appendix B.2 for a full derivation of this correction.

Glauert extended the scope of the correction by representing aerofoils as equivalent cylinders of diameter $t\sqrt{\lambda_2}$ [58], where t is the aerofoil thickness and λ_2 is a solid blockage body shape factor:

$$\epsilon_{sb} = \frac{\pi^2 \lambda_2 t^2}{12 H^2} \tag{2.6}$$

A plot of λ_2 against thickness ratio, t/c is provided by Glauert for Rankine ovals, ellipses and Joukowski aerofoils [58], allowing the factor to be obtained from model dimensions for these specific model shapes. Allen and Vincenti give a similar correction of

$$\epsilon_{sb} = \frac{\pi^2}{48} \left(\frac{c}{H}\right)^2 \Lambda \tag{2.7}$$

where

$$\Lambda = 4 \left(\frac{t}{c}\right)^2 \lambda_2 \tag{2.8}$$

and provide look-up tables for Λ for Rankine ovals, ellipses, Joukowski aerofoils and several NACA aerofoil families [56]. The parameters Λ and λ_2 can be calculated but this requires a complicated integration of an expression that depends on the aerofoil surface shape and velocity distribution around it.

By modelling the test aerofoil as a series of doublets along its chord rather than a single doublet, Thom derived a correction in terms of the aerofoil cross-sectional area A_{aero} that requires no use of look-ups from plots or tables

$$\epsilon_{sb} = \frac{\pi}{6} \left(\frac{A_{aero}}{H^2}\right) \tag{2.9}$$

but this is only valid for thin aerofoils [59]. Thompson used empirical methods to improve the correction for use with aerofoils of different thicknesses [1]

$$\epsilon_{sb} = \frac{\pi A_{aero}}{6h^2} \left[1 + 1.2 \left(\frac{t}{c}\right)\right] \tag{2.10}$$

Also through empirical means, Batchelor accounted for the effects of incidence on the solid blockage factor [61]

$$\epsilon_{sb}(\alpha) = \epsilon_{sb} \left[1 + 1.1 \left(\frac{c}{t}\right) {\alpha_u}^2\right] \tag{2.11}$$

Since testing extends beyond $\alpha = 90°$, Batchelor's formula has been modified to better

[1] Thompson's work is in an unpublished 1948 Aeronautics Research Council report [60] that could not be sourced. An AGARD review of blockage corrections contains details of the correction [45].

correct incidences greater than 90° in this study ($\alpha = \frac{\pi}{2}$ radians for the purpose of the formula).

$$\epsilon_{sb}(\alpha) = \epsilon_{sb}\left[1 + 1.1\left(\frac{c}{t}\right)\left(\frac{\pi}{2} - \left|\frac{\pi}{2} - \alpha_u\right|\right)^2\right] \tag{2.12}$$

The modification ensures that the correction accounts for the inverse relationship between the incidence angle α and the area the aerofoil projects normal to the flow at $90° < \alpha < 180°$.

2.1.3 Wake blockage

Wake blockage is caused by the constraints placed on the flow by the model wake, resulting in an increase in local velocity, similarly to solid blockage. The model wake is represented as a point source with strength $m = \frac{1}{2}C_{du}U_u c$, with the tunnel walls again represented using a method of images [46]. A wake blockage ratio, ϵ_{wb}, the ratio of velocity change caused by the effects of wake blockage to uncorrected free stream velocity in the wind tunnel, is established by calculating the impact of the wake on the velocity far upstream of the model. This and the velocity at the model are used to establish the ratio

$$\epsilon_{wb} = \frac{1}{4}C_{du}\frac{c}{H} \tag{2.13}$$

In order to account for the non-zero interference far upstream of the wake caused by its modelling as a source, a sink and corresponding system of images is introduced far upstream. These are sufficiently far from the point upstream at which the wake influence is calculated to be ignored in the analysis. See Appendix B.3 for a full derivation of this correction.

2.1.4 Horizontal buoyancy

Rae et al. [44] recommend the use of an additional correction to drag, ΔD_{BL}, in the form of a horizontal buoyancy adjustment due to the pressure gradient caused by boundary layer growth in the wind tunnel, proposed by Glauert [58] or Allen and Vincenti [56]. The latter reference gives:

$$\Delta D_{BL} = \frac{6H^2}{\pi}\Lambda\frac{\pi^2}{48}\left(\frac{c}{H}\right)^2\frac{\mathrm{d}p}{\mathrm{d}x} \tag{2.14}$$

where Λ is the shape factor defined in Eqn. (2.8), and $\mathrm{d}p/\mathrm{d}x$ is the static pressure gradient caused by the boundary layer on the tunnel walls. Note that the correction is to drag rather than its coefficient. Glauert states that this correction is most important for streamlined bodies so is of limited importance post-stall, while Allen and Vincenti state that in most tunnels the pressure gradient is sensibly zero, so the correction is unnecessary in most cases. An analysis was conducted for the experiments run in this study, using Glauert's formula for the static pressure gradient [58]:

$$\frac{\mathrm{d}p}{\mathrm{d}x} = -k\frac{\frac{1}{2}\rho {U_u}^2}{H} \tag{2.15}$$

where k is a constant between 0.016 and 0.04 which should be established experimentally for a given tunnel. Here, with k set to 0.04, the correction only approached significance for the larger aerofoils when flow is attached, but remained in the order of experimental error. The correction is not included in AGARD [45, 46] or ESDU [10] corrections and has not been used in this study.

2.1.5 Application of corrections

Since all experiments in the research described in this thesis were conducted at low Mach numbers ($M < 0.09$), all compressibility factors have been omitted from correction formulae. Corrections used in this study are those recommended by both AGARD [45, 46] and ESDU [10], modified as described above. Correction terms $\Delta\alpha$, ΔC_l and ΔC_m are obtained using Eqns (2.2) - (2.4). A total solid blockage factor is obtained using Eqns (2.10) and (2.12):

$$\epsilon_{sb}(\alpha) = \frac{\pi A_{\text{aero}}}{6h^2}\left[1 + 1.2\left(\frac{t}{c}\right)\right]\left[1 + 1.1\left(\frac{c}{t}\right)\left(\frac{\pi}{2} - \left|\frac{\pi}{2} - \alpha_u\right|\right)^2\right] \tag{2.16}$$

and combined with wake blockage, Eqn. (2.13), to give a total blockage, ϵ_B:

$$\epsilon_B = \epsilon_{sb}(\alpha) + \epsilon_{wb} \tag{2.17}$$

A drag adjustment ΔC_d is calculated as the product of the solid blockage factor and uncorrected drag coefficient:

$$\Delta C_d = -C_{du}\epsilon_{sb}(\alpha) \tag{2.18}$$

and a flow velocity adjustment is obtained using the total blockage factor:

$$\Delta U = \epsilon_B U_u \tag{2.19}$$

Full corrections to force and moment coefficients therefore take the form:

$$C_{\text{force}\,c} = \frac{C_{\text{force}\,u} + \Delta C_{\text{force}}}{(1+\epsilon_B)^2} \tag{2.20}$$

where C_{force} is any force or moment coefficient and the subscript c denotes effective free air values that have been corrected for blockage. Most sources of blockage corrections assume a small overall blockage ϵ_B and so omit terms of ${\epsilon_B}^2$ and higher [45, 44, 10, 46]. These have been included in formulae here since $c/H = 0.3$ for the largest aerofoil tested. Terms of $(c/H)^4$ and higher have been ignored.

2.1.6 Maskell's corrections for bluff bodies and stalled wings

After finding theoretical corrections to be inaccurate for bluff bodies and stalled wings and aerofoils, Maskell produced an alternative methodology based on a single correction to dynamic pressure [47], applicable where flow is fully separated. It should be noted that the theoretical corrections assessed by Maskell were those of Glauert [58] and Pankhurst and Holder [62], neither of which feature the empirical thickness and incidence adjustments used in this study, see Eqns (2.10) and (2.12) respectively, though thickness is accounted for through shape factors.

Maskell established a relationship that provides an estimate of the effective increase in the dynamic pressure of the stream in a wind tunnel due to a constraint. The derivation used a momentum analysis and results in a formula in terms of measured drag coefficient, a "base pressure parameter" k and the ratio of model area to wind tunnel cross-sectional area (for two-dimensional experiments, this is equivalent to c/H):

$$\frac{q_c}{q_u} = \frac{{k_u}^2}{{k_c}^2} = 1 + \frac{C_{du}}{{k_c}^2 - 1}\frac{c}{H} \tag{2.21}$$

The base pressure parameter is defined as:

$${k_u}^2 = 1 - C_{pb\,u} \tag{2.22}$$

where $C_{pb\,u}$ is the measured base pressure coefficient, i.e. that pressure coefficient experienced across the majority of the downwind face of a bluff body, where flow is entirely separated. It is taken as an average of the pressures across the surface.

Using Eqn. (2.21), either by iteration or by rearranging for a quadratic equation and solving, a value for ${k_c}^2$ can be established from measured C_{du} and $C_{pb\,u}$. A simplified formula for the required adjustment to dynamic pressure is given by

$$\frac{\Delta q}{q_u} = \epsilon_q C_{d\,u} \frac{c}{H} \tag{2.23}$$

where $\Delta q = q_c - q_u$ and

$$\epsilon_q = \frac{1}{{k_c}^2 - 1} \tag{2.24}$$

This adjustment is then used to correct forces and moments (note that Maskell does not explicitly provide moment corrections) according to

$$C_{\text{force}\,c} = \frac{C_{\text{force}\,u}}{1 + \Delta q/q_u} \tag{2.25}$$

Maskell conducted tests on a variety of three-dimensional square plates to confirm his findings experimentally. Using the studies of Fage and Johansen, who took force and pressure readings for a two-dimensional flat plate at incidences in the range 0° - 90° [63, 64] and Eqn. (2.21), Maskell provides a relationship between ϵ_q and incidence (for 20° to 90°) for two-dimensional experiments, reproduced here in Fig. 2.2. Also included in the figure is an equivalent ϵ_q calculated from drag and base pressure measurements on a $c/H = 0.15$ NACA 0015 aerofoil taken during this study, detailed in Chapters 4-5. This equivalent ϵ_q is discussed in Section 2.1.10.

2.1.7 Boundary measurement methods

In their derivations, the corrections assessed in this chapter, other than Maskell, use potential flow theory and the method of images to calculate strengths of the singularities that model the test aerofoil, its wake and the wind tunnel walls, see Appendix B. Alternative methods make use of boundary flow measurements to calculate singularity strengths tailored to the specifics of the test conditions. The method of Hackett et al. [65] provides excellent correction of drag

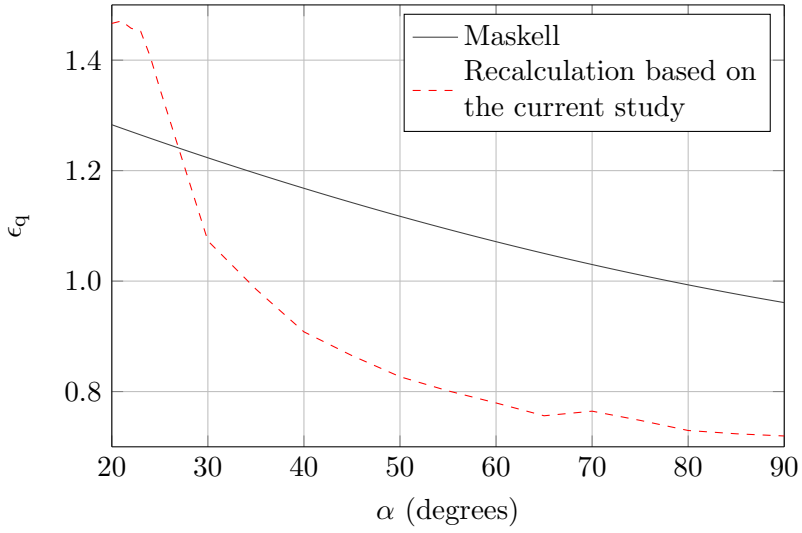


Figure 2.2: Variation of Maskell's blockage factor ϵ_q with incidence for two-dimensional plates and the $c/H = 0.15$ aerofoil of the current study.

forces for finite flat plates at extreme incidence but the corresponding performance for lift is no better than purely theoretical methods. Given the marginal gains in correction performance and significant additions required to experimental apparatus, boundary measurement methods will not be used in this study.

2.1.8 Turbulence factor

Rae et al. [44] provide a correction for the Reynolds number of experiments, based on the turbulence intensity of the flow in the wind tunnel used. The higher the turbulence in a wind tunnel, the higher the effective Reynolds number of the flow, since turbulence in the free-stream will promote premature transition to turbulence in boundary layers. This can have a significant impact on free-transition experiments at low Reynolds numbers, where extensive laminar flow is expected. The effective Reynolds number can be obtained by multiplying the measured value by a turbulence factor. The relationship between the required turbulence factor and turbulence intensity is reproduced in Fig. 2.3. Note that neither ESDU or AGARD provide a turbulence factor correction. The turbulence intensity in the 3×3 tunnel used for the experiments of Ch. 5 has been measured at less than 0.1%, giving a maximum turbulence factor of 1.08. No Reynolds number corrections have been applied in this study.

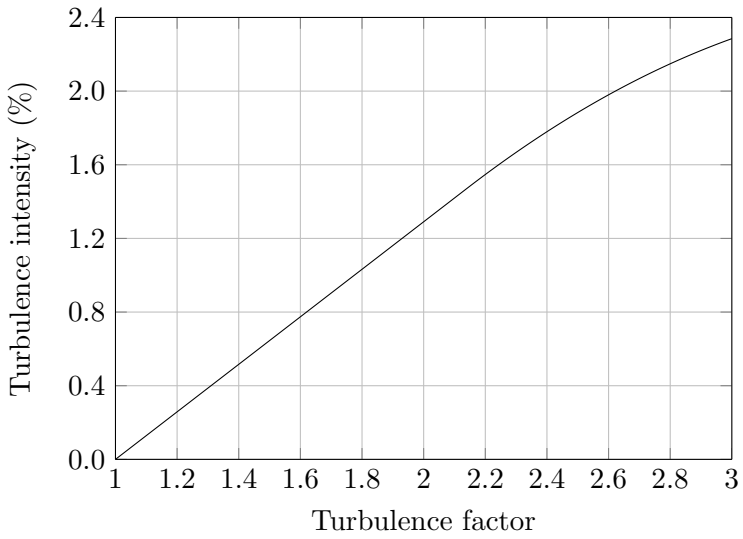


Figure 2.3: Variation of turbulence factor with turbulence intensity.

2.1.9 Limitations to correction regimes

Both the ESDU[10]/AGARD[45, 46] and Rae et al.'s [44] corrections are based on the following assumptions:

- Flow is inviscid, a reasonable assumption for flows in the range of Reynolds numbers used in this study away from boundary layers. Viscous-inviscid interactions in the flows over models and at tunnel walls can lead to uncertainties in the corrections but these are usually insignificant [46].

- Flow is incompressible, acceptable for low Mach number flows.

- Flow is fully attached, appropriate only to the point at which a separation bubble starts to form, or flow fully detaches. Practically, corrections can be applied to flows with "some degree of separation ... with caution" [10]. Though it is inappropriate to use such corrections for fully separated flows, they are used in most of the post-stall studies referenced in this thesis in the absence of any better alternatives.

- The wind tunnel test section is sufficiently long for flows far upstream and downstream of the model to be parallel to tunnel walls. Suitability is obviously apparatus dependent. The upstream distance between tunnel contraction and model is $1.17H$ for the 18-inch tunnel used for experiments described in Ch. 3 and $1.31H$ for the 3×3 wind

tunnel (see Chapters 4-5). These are possibly insufficient for this assumption to hold at extreme incidences, where the accuracy of calculated induced angles of incidence could be impeded.

- The model is a thin aerofoil, a suitable assumption for aerofoils where thickness is less than 10% of chord. Here, use is made of Thompson's empirical thickness adjustment to solid blockage corrections [60], see Eqn. (2.10), extending the applicability of the theory to the NACA 0012, 0015 and 0018 aerofoils.

- The aerofoil is modelled as a single vortex, source or doublet, so it must be small in comparison to the tunnel. This is inappropriate for larger c/H ratios at incidences near 90°. ESDU state that corrections have been used with c/H ratios of up to 0.35 [10] (the largest in this study is 0.3). AGARD recommend a maximum c/H of 0.25 [45] for the same corrections. Allen and Vincenti [56] contend that their corrections (on which Rae et al's [44] are based) can be used post-stall with c/H up to 0.4, though they accept there is no experimental evidence to support this and it is doubtful the contention applies where incidences as high as 90°.

2.1.10 Analysis of different corrections regimes

Another major limitation of corrections is that significant differences in final, effective free-air data can result from the experimenter's choice of corrections. There is little in the way of a consensus on which to use, particularly where the model under test encounters separated flow.

In order to judge which corrections work best, experimental data from this study for five different sized NACA 0015 aerofoils, tested at a Reynolds number of 150 000 in a solid walled test section (see Ch. 4 for details on the experiments), have been processed with a variety of correction formulae. The corrections have been chosen because they are commonly used in the studies referenced in Section 1.7.1.

The aerofoils have c/H ratios of 0.1, 0.15, 0.2, 0.25 and 0.3, so are affected to different extents by wind tunnel blockage. Fig. 2.4 shows measured coefficients of lift, drag and moment about the quarter chord plotted against incidence. The results for the smallest aerofoil are presented with thicker and more solid lines than the others. The plot clearly demonstrates

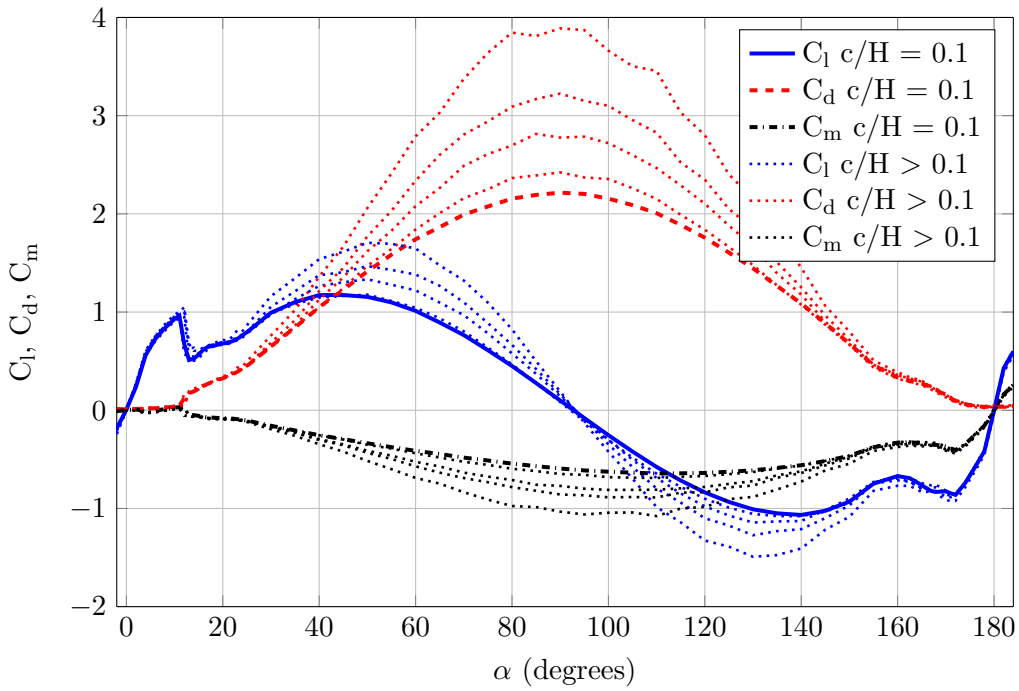


Figure 2.4: C_l, C_d and C_m vs α for $c/H = 0.1$, 0.15, 0.2, 0.25 and 0.3 NACA 0015 aerofoils taken in the solid walled tunnel at $Re = 150\,000$, raw data.

the impact of blockage on wind tunnel results. The larger the c/H ratio, the greater the magnitude of readings post-stall. For lift, drag and moment, the $c/H = 0.1$ aerofoil has the lowest peaks, followed by the $c/H = 0.15$ and so on to the $c/H = 0.3$ aerofoil which has the largest peaks. In a theoretically ideal experiment, with no impact of blockage and no variations in roughness or profile accuracy between the models, results for the five aerofoils would be identical when tested at a constant Reynolds number.

Figs 2.5 and 2.6 show the same data processed with the corrections of ESDU [10] and Rae et al. [44] respectively. Figs 2.7 and 2.8 show the data processed with Maskell's correction where it is applicable (at incidences in the range $20° \leq \alpha \leq 160°$). Fig. 2.7 uses Maskell's ϵ_q, while Fig. 2.8 uses an ϵ_q calculated using results from the current study.

All of the corrections significantly reduce the spread between the data of the five aerofoils, with the ESDU and Maskell (with original ϵ_q) corrections performing particularly well. In order to compare the performances of the corrections methodically, Fig. 2.9 has been prepared. It shows results of a regression analysis that measures the similarity of corrected coefficients given by each of the sets of corrections. At each incidence at which readings were taken, a

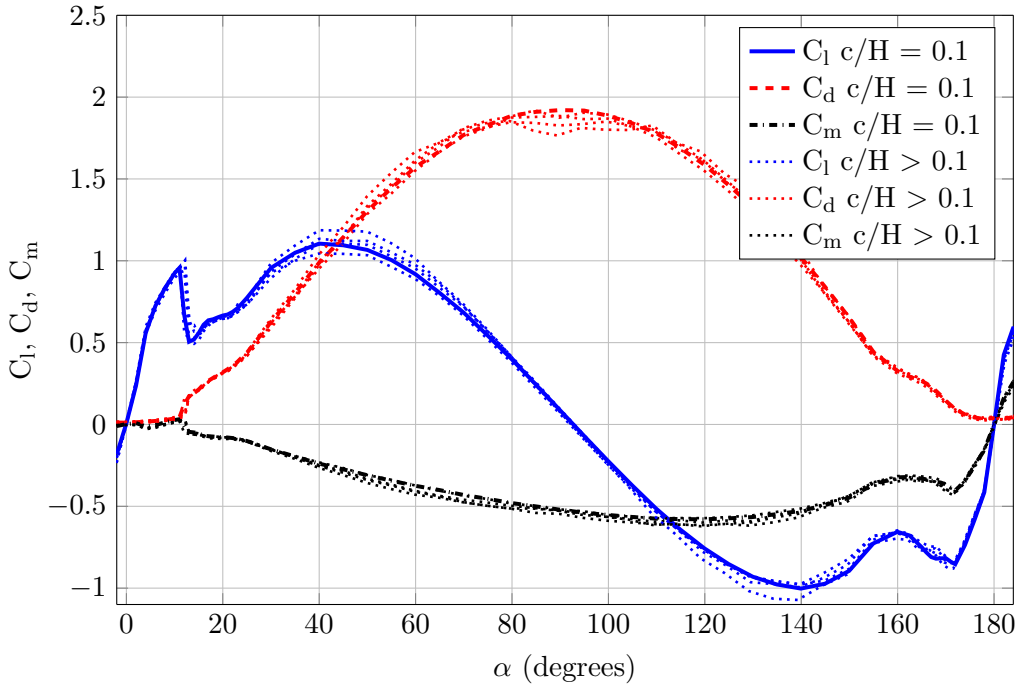


Figure 2.5: C_l, C_d and C_m vs α for $c/H = 0.1$, 0.15, 0.2, 0.25 and 0.3 NACA 0015 aerofoils taken in the solid walled tunnel at $Re = 150\,000$, ESDU corrections.

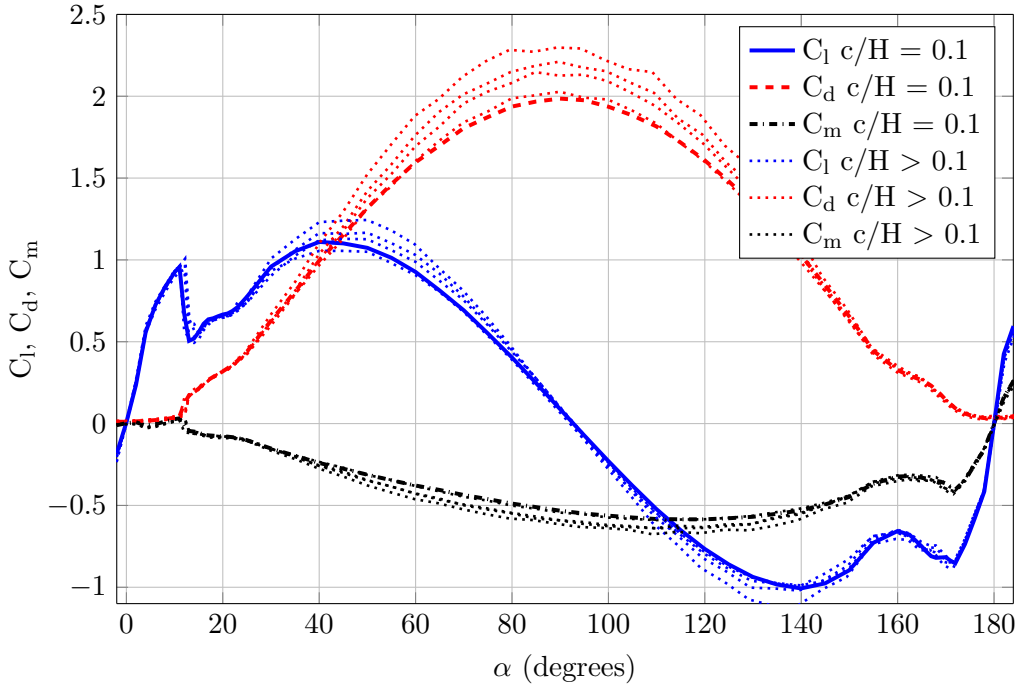


Figure 2.6: C_l, C_d and C_m vs α for $c/H = 0.1$, 0.15, 0.2, 0.25 and 0.3 NACA 0015 aerofoils taken in the solid walled tunnel at $Re = 150\,000$, Rae et al. corrections.

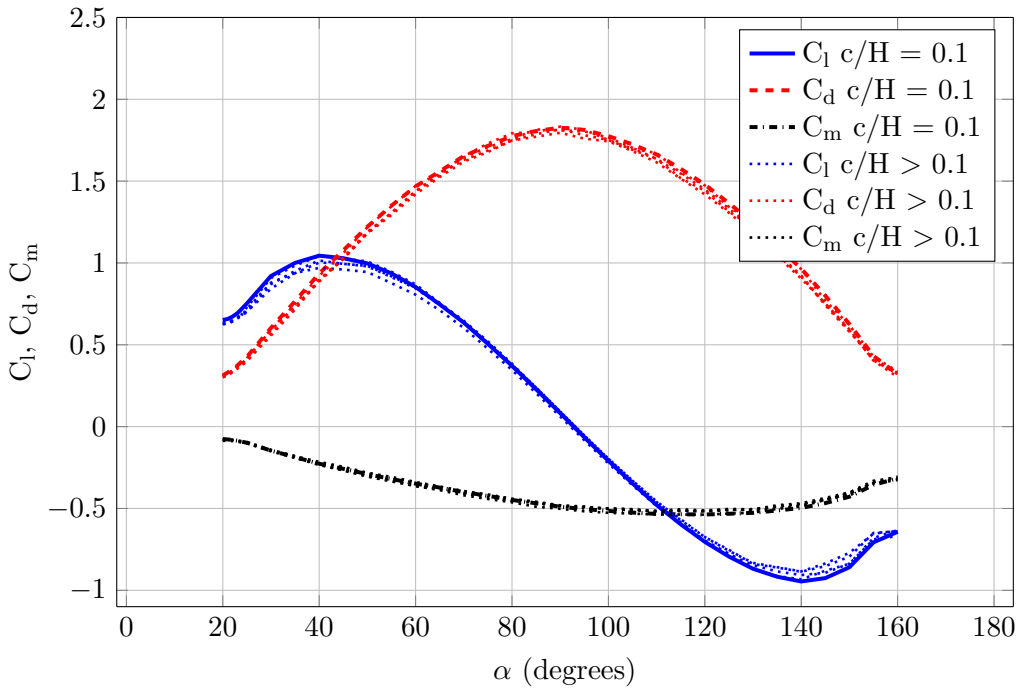


Figure 2.7: C_l, C_d and C_m vs α for $c/H = 0.1$, 0.15, 0.2, 0.25 and 0.3 NACA 0015 aerofoils taken in the solid walled tunnel at $Re = 150\,000$, Maskell's corrections.

standard deviation of the results for the five aerofoils is calculated. This is then added over a range of incidences to give a sum of standard deviations $\sum$SD. Here the range at which Maskell's correction is applicable ($20° \leq \alpha \leq 160°$) has been used to allow a fair comparison between the corrections. The smaller $\sum$SD is, the better the corrections are are collapsing the data. See Section 4.8.5 for more on the $\sum$SD method.

The analysis confirms that of the classical, potential flow theory corrections, ESDU outperforms Rae et al. The two sets of corrections differ only in their handling of solid blockage, Rae et al. use Eqn. (2.7) while ESDU use (2.16). The former makes no account of incidence, while thickness is accounted for through the shape factor Λ rather than Thompson's empirical method, Eqn. (2.10).

Maskell's correction performs better still, but gives over-corrected coefficients that are significantly lower than those of the other methods. Fig. 2.10 shows corrected results for the $c/H = 0.1$ aerofoil from all methods, plotted on the same axes, demonstrating the large difference between Maskell and the others.

The Maskell correction was developed theoretically, then modified empirically for infinite

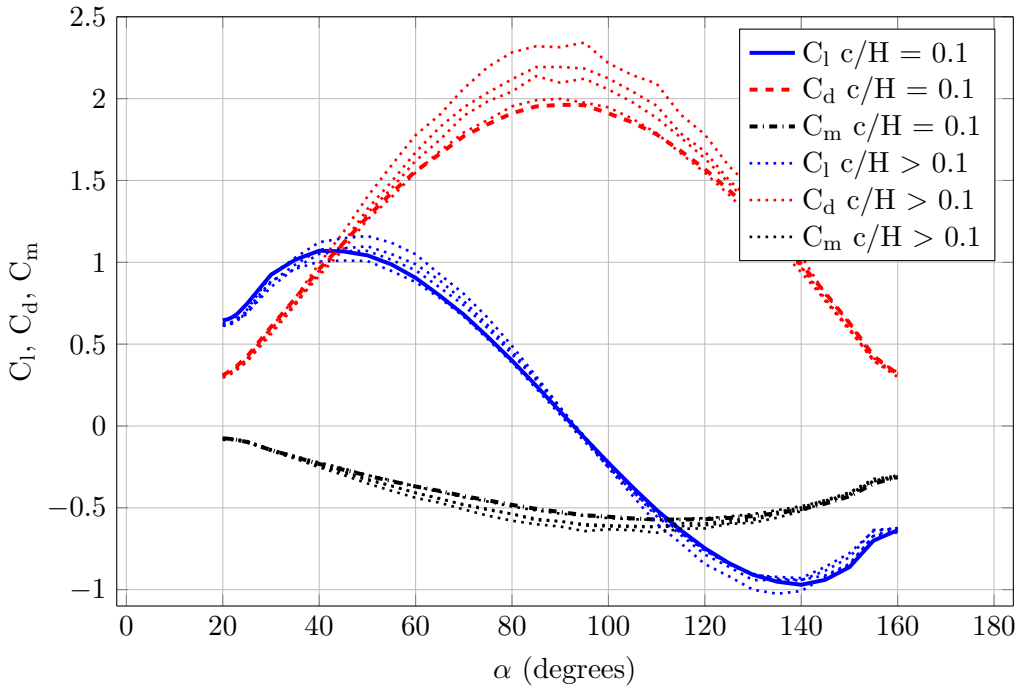


Figure 2.8: C_l, C_d and C_m vs α for $c/H = 0.1$, 0.15, 0.2, 0.25 and 0.3 NACA 0015 aerofoils taken in the solid walled tunnel at $Re = 150\,000$, Maskell's corrections with recalculated ϵ_q.

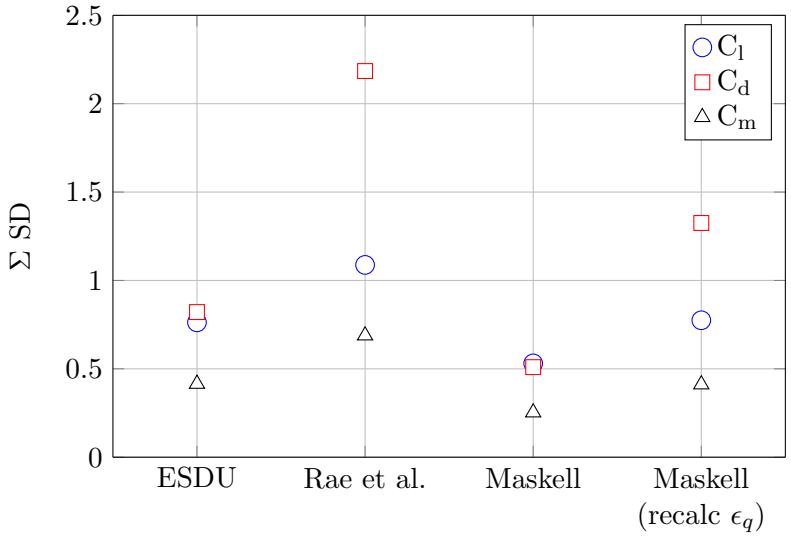


Figure 2.9: Summations of standard deviations for C_l, C_d and C_m for all NACA 0015 aerofoils, processed with selected bockage corrections

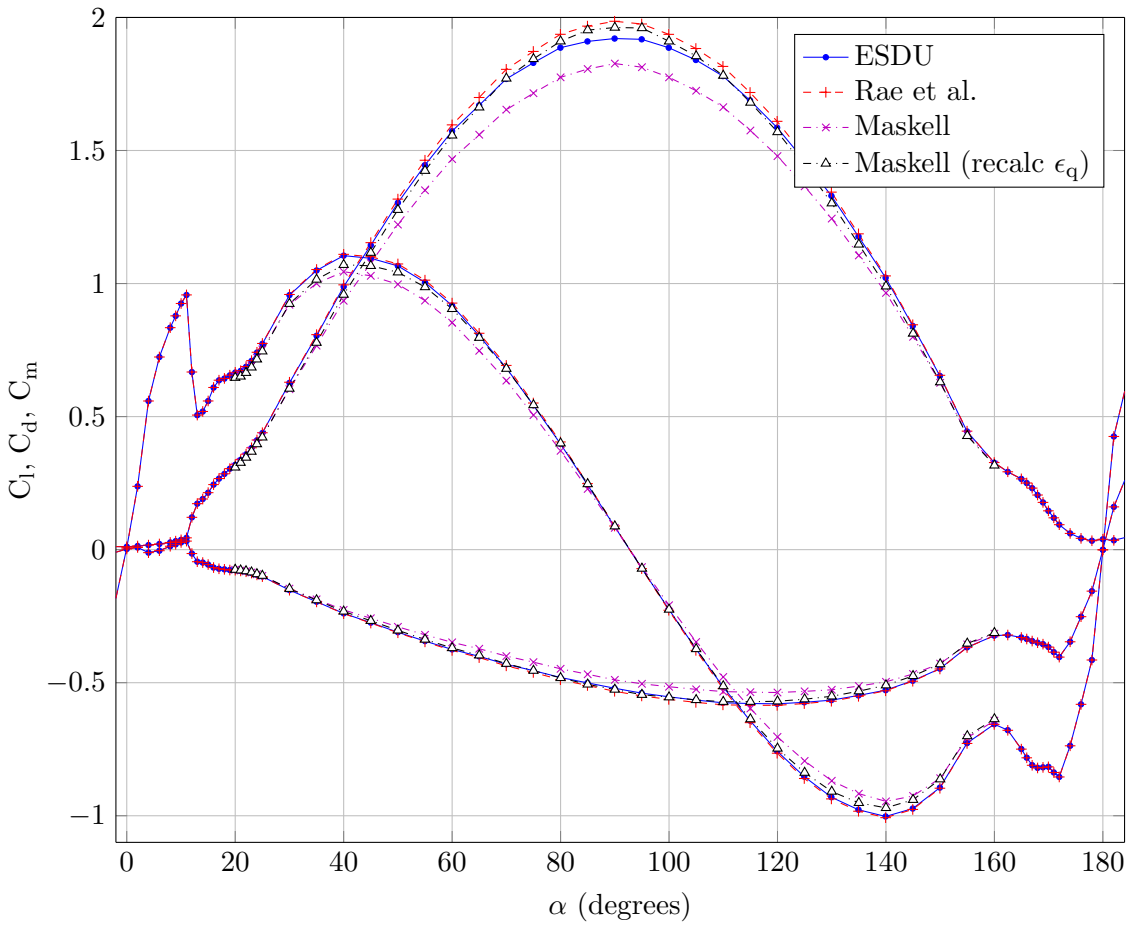


Figure 2.10: C_l, C_d and C_m vs α for the $c/H = 0.1$ NACA 0015 aerofoil using the blockage corrections of ESDU [10], Rae et al. [44], Maskell [47]and Maskell with recalculated ϵ_q

plates using existing data from the 1920s studies of Fage and Johansen [63, 64]. The studies provide the pairing of base pressure and drag force readings, necessary to calculate ϵ_q, at four incidences: 30°, 50°, 70° and 90°.

For models with uniform base pressure (a constant pressure across the upwind face of the bluff body, where flow is completely separated), ϵ_q can be calculated from a single pressure measurement on the base. For models with a non-uniform C_{pb}, it is necessary to measure pressure distributions over the base of the body and also on the surface of the wake. Maskell notes that for most practical purposes it is "probably sufficient" to take $\epsilon_q \approx 1$ for two-dimensional flow, whether the base pressure is uniform or not [47]. Most users of the correction do just that.

In this study, ϵ_q has been recalculated using results for the $c/h = 0.15$ aerofoil. Aerofoil C_{pb} was found to be near uniform in the incidence range $20° \leq \alpha \leq 160°$, see Figs 4.19 and 5.2, so no wake surface measurements were deemed necessary. C_{pb} has been taken as an average of all suction surface tappings. See Fig. 2.2 for the recalculated ϵ_q plotted against incidence, alongside Maskell's original. The original's near-linear relationship is the result of extrapolating from the four Fage and Johansen data points, note that both the ϵ_q plots are near parallel in the range these points cover ($30° \leq \alpha \leq 90°$). Differences between the plots result from the different blockages of the models used, Fage and Johansen's flat plate having $c/H = 0.071$.

Using this recalculated ϵ_q, Maskell's correction gives results far closer to the other methods for the $c/H = 0.1$ aerofoil. The ϵ_q is for the $c/H = 0.15$ aerofoil rather than the $c/H = 0.1$ as the smaller aerofoil is not pressure tapped so couldn't provide the $C_{bp\,u}$ data necessary for the calculation. The larger blockage results in a lower ϵ_q, which in turn provides a slight under-correction of blockage when applied to the $c/H = 0.1$ aerofoil using Eqn. (2.25).

The corrections provided for the other aerofoils is not good with the recalculated ϵ_q, with the under-corrections getting progressively worse the larger the c/H. Original derivation of the correction used square, finite flat plates, with area ratios (plate area to wind tunnel cross-sectional area) of 0.003, 0.0150, 0.0301 and 0.0451. Even the largest of these area ratios is less than half that of the smallest aerofoil in this study (0.1 for the $c/H = 0.1$ aerofoil). Other researchers have found that Maskell's correction is unsuitable for use with blockages higher than 10% [66].

ESDU corrections have been chosen for use in this study based on the regression analysis illustrated in Fig. 2.9, and have been used to correct data taken in solid walled tunnels in the experiments described later in this thesis. The corrected coefficients they provide have been used as a bench-mark against which to measure the blockage reduction capabilities of the tolerant tunnel developed during this study. While Maskell's correction performs better than ESDU in the regression analysis, doubt remains as to the accuracy of the correction provided using Maskell's original ϵ_q, due to the lower blockage models used in deriving the original correction. Recalculated using data from the current study, corrections for the $c/h = 0.1$ aerofoil are closer to those of other methods but performance over the range of aerofoil sizes tested is worse than that of ESDU.

Fig. 2.10 shows how significant the choice of corrections is to the effective free-air data provided from an experiment. ESDU, Rae at al. and Maskell, with the original ϵ_q, are all in common use, yet there is a spread of 9% between the corrected drag peaks at 90°, and a spread of 7% between the lift peaks at 40°. Comparing to Fig. 1.8, where spreads between existing studies are shown to be 20% for lift and 18% for drag (or 13% for lift and 18% for drag, ignoring the unusual study of Pope), it can be posited that blockage, and the steps taken to limit it, are the most significant sources of inconstencies in the literature.

2.2 Blockage tolerant wind tunnels

With blockage corrections providing such a wide spread of results at extreme incidences, and their application being unsuited where flow is detached or tunnel blockages are high, numerous alternatives have been proposed. Most methods make use of specialised apparatuses that limit blockage through physical means, with a number requiring some form of residual correction to achieve effective blockage-free data.

2.2.1 Adaptive walls

Adaptive wall tunnels have adjustable boundaries that can be shaped either manually or by a control system to approximate the free-air streamlines around the model under test at an appropriate distance. Such tunnels should provide near blockage-free data if the approximation to the streamlines is good enough. The hardware required is costly and complex compared to a conventional wind tunnel. Productivity is much lower due to the time required to adjust the tunnel walls and refine them to the correct shape in preliminary experiments [67]. For aerofoil testing over a range of incidences, walls would require reshaping at each change of incidence, significantly increasing the amount of time required for (and so costs of) experiments.

2.2.2 Open jet tunnels

Open jet studies of aerofoils, taken in tunnels without a floor or ceiling, are much less common than those using solid walled tunnels. The tunnel configuration is more commonly used with larger, more complex models such as full wind turbines. Maintaining mass flow conservation in such a tunnel is difficult, hindering the quality of non-dimensionalised data obtained from

the facilities. Some researchers have provided aerofoil data using open jet wind tunnels [3, 68] but agreement to solid-walled studies is poor. Blockage corrections must still be applied to open jet data. Negative solid blockage and streamline curvature corrections are prescribed by ESDU, along with a flow direction adjustment [10]. The overall correction is lower in magnitude than those required for a comparable solid walled tunnel, with no wake blockage correction needed.

2.2.3 Large conventional tunnels

Given the limitations of correcting for separated flows, the possibility of conducting experiments in large conventional tunnels has been investigated. Accurate free-air equivalent readings can be obtained without the need for corrections in a suitably large tunnel. A data set was judged to be sufficiently accurate here if the maximum correction to any coefficient reading was smaller than 5%. The adjustment to drag at $\alpha = 90°$ is typically the largest, both in magnitude and by percentage, so by limiting this to 5%, all other adjustments can be judged to be at least similarly limited. In planning the experiments detailed in this paper, a quartic inequality[2] in c/H, given by

$$0.95\zeta^2\left(\frac{c}{H}\right)^4 + 1.9K_{wb}C_{du}\zeta\left(\frac{c}{H}\right)^3 + (2.9\zeta + 0.95{K_{wb}}^2{C_{du}}^2)\left(\frac{c}{H}\right)^2 + 1.9K_{wb}C_{du}\left(\frac{c}{H}\right) < 0.05 \tag{2.26}$$

was established, where

$$\zeta = \frac{\pi k_e \tau}{6}(1 + 1.2\tau)\left(1 + \frac{1.1}{\tau}\alpha^2\right) \tag{2.27}$$

$\tau = t/c$, K_{wb} is the wake blockage ratio factor, a constant specified as 0.25 by ESDU [10] (the factor in Eqn. (2.13)), C_{du} is the uncorrected drag coefficient and k_e is a constant for a given profile such that $A_e = k_{aero}\tau c^2$. The value of k_e has been calculated as 0.68 for the NACA 0012.

The inequality can be solved for c/H for given values of τ and k_{aero}, $\alpha = \pi/2$ radians and a measured or estimated C_{du} at this α. For a NACA 0012 aerofoil with $C_{du} = 2$ at $\alpha = \pi/2$ the result is $c/H < 4.5\%$. This is prohibitively small, the wind tunnel used in the experiments detailed in this paper has a 915 mm square cross section, so would require an aerofoil chord of

[2] See Appendix C for a full derivation.

less than 41.2 mm to achieve a ratio within the acceptable range. Small aerofoils are harder to profile accurately and are a limiting factor on the maximum Reynolds number achievable with a given wind tunnel. As such, in the current study it is impossible to obtain effective free-air data from conventional closed jet tunnels without the use of blockage corrections.

2.2.4 Porous walls

Porous walled test sections offer an alternative means of minimising blockage effects physically without the need for very large tunnels or small aerofoils. The simplest designs use passive techniques where wall porosity is fixed before running an experiment. Since corrections for closed and open jets are of opposite signs [10], one would expect that free-air conditions can be approximated using semi-permeable walls. Longitudinally slotted walls have been used for the purpose [69], but such tunnels often require application of some empirical factor that is dependent on both wall configuration and test model [70]. An alternative design using transverse slots, which can accommodate a variety of model sizes and shapes with no empirical factor required, is described in the following section.

2.3 The Parkinson tolerant tunnel

Parkinson's tolerant section design [11] has slots perpendicular to the flow in certain sections of the tunnel walls that allow flow to exit and enter the main channel, with the walls made up of a regular array of evenly spaced aerofoils. The shape of the array components avoids flow separation around them. Plenums of stagnant air outside the slotted walls, enclosed from the external environment, ensure mass conservation in the flow along the tunnel. The design is versatile, significantly reducing blockage for a wide range of model sizes in a given tunnel with an appropriate open area ratio [54] (OAR, a measure of open to slatted wall areas, defined as g/s using the notation in Fig. 2.11 where g is the gap between slat aerofoils and s is the spacing between them). Appropriate OARs are determined through experiments on models of different sizes but with like shapes, and may be specific to model shape rather than tunnel. This makes experiments more costly and time consuming than for the equivalent solid-walled tunnel experiments, as the tunnel must be configured before main experiments can be run. The two-dimensionality of the design prevents development of significant transverse flows,

which can impede the quality of readings taken from a experiment attempting to reproduce two-dimensional flows.

Parkinson's design was originally developed with a slatted ceiling and solid floor for the testing of aerofoils pre-stall (by his student Williams) [12]. The floor was left solid as otherwise it was thought that the aerofoil under test would draw the shear layer from a bottom plenum chamber into the main test section upstream of the aerofoil, degrading the flow around it [12]. An OAR of 0.6 was judged best for unstalled aerofoils, see Section 4.8 for the OAR calibration methodology used. Preliminary work on stalled aerofoils at $\alpha = 20°$ used an OAR of 0.7 [13].

A slatted floor and ceiling configuration (as illustrated in Fig. 2.11) with an OAR of 0.59 was later used with aerofoils [71], following potential flow modelling that suggested the quality of blockage reduction was better than for the original design. Limited experimental results were presented to support this prediction, with no comparisons made to Williams' single slatted wall work.

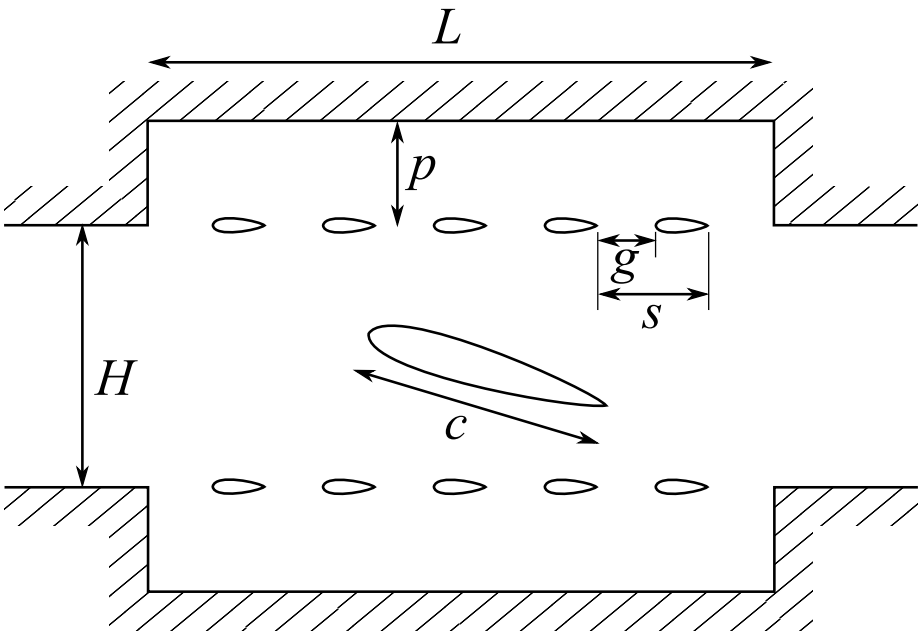


Figure 2.11: Parkinson's slatted-walled tolerant tunnel configured with double slatted walls.

A slatted floor and ceiling design was also utilised for bluff body testing [54] of circular cylinders, circular cylinders with splitter plates and flat plates normal to the flow, with promising results for a variety of sizes of all three models taken using OARs in the range

0.5-0.7.

The strong performance of the tunnel design at reducing blockage where flow is separated, without reliance on blockage corrections, could make it an ideal candidate for stalled aerofoil studies. An AGARD review of corrections for high angle of attack models highlights Parkinson's tunnel as suitable for the purpose [70]. Imperial College owns a 0.457 m $\times$ 0.457 m double slatted wall Parkinson tunnel. It was decided to run some aerofoil experiments in the tunnel over a wide range of incidences to assess how well it reduces blockage.

Chapter 3

The blockage tolerant wind tunnel: preliminary work

Parkinson's tolerant tunnel design was chosen for further investigation, its potential for blockage reduction of high incidence aerofoils where flow is separated having been noted by Parkinson himself and other researchers. Imperial College's small-scale test section, built to the design a number of years ago for the testing of bluff bodies, has been used for proof-of-concept experiments. These have been conducted to judge whether or not the tunnel design is suitable for post-stall aerofoil testing and are described in this chapter.

3.1 Experiments in the 18" Flow Control wind tunnel

The Imperial College 18" Flow Control wind tunnel has an open circuit design and a square cross section with side length of 0.457 m. Turbulence intensity in the working section has recently been measured at 0.15%, while the flow uniformity is within 0.5% of the centreline flow across the central half of the tunnel's cross section. The small-scale Parkinson test section has been built for use with the 18" tunnel, with an identical 0.457 m $\times$ 0.457 m cross-section. It has a slatted floor and ceiling configuration, see Fig. 2.11, with a L/H ratio of 2.14, a plenum depth to tunnel height ratio, p/H, of 0.39 and NACA 0015 slat aerofoils with 80 mm chords. It can be modified to a solely slatted ceiling configuration or to a conventional closed section by replacing the slatted floor, or both floor and ceiling, with solid panels.

3.1.1 Aerofoils

The NACA 0012 profile was chosen for testing as there is more existing data at extreme incidence angles for it than for any other section, in spite of the sharp leading edge stall it experiences at the Reynolds number used in this preliminary work ($Re = 1.5 \times 10^5$). A number of existing NACA 0012 models were available for use with the tolerant test section. Leading edge stall can be unpredictable, potentially occurring at different angles of attack on different runs of the same experiment, but no such repeatability issues were encountered in this study. The larger of the two aerofoils used has a chord of 147 mm, giving a c/H ratio of 0.32 and has a hollow resin construction. The smaller has a 124 mm chord ($c/H = 0.27$) and is made of wood. Both aerofoils have a span of 435 mm and are fitted with small end plates, primarily intended to inhibit leakage from the tunnel at the aerofoil mounting points. See Fig. 3.1 for a diagram of the aerofoil mounting.

3.1.2 Model mounting and data acquisition

The aerofoils were mounted at the half chord to a hub assembly that allowed for rapid adjustment of the angle of incidence. The hub in turn connected to a pair of struts mounted on a cross-beam, itself bolted to a Nutem Model 528 three-component force balance, see Fig. 3.2 for a diagram of the experimental set-up. Using the original force balance struts and cross-beam, the balance is rated to an accuracy of ± 0.15 N for lift and ± 0.05 N for drag. New extended struts and beam were manufactured to provide sufficient clearance around the bottom plenum chamber. These allow larger vibrations to develop in unsteady flow than did with the original shorter struts and beam.

Care has been taken with data acquisition to limit the effects of these vibrations. Readings were taken at 100 Hz (a much higher rate than the highest frequencies of the main vibrations induced) for 10 s after a period of settling. This was sufficient to capture approximately four periods of the lowest frequency of fluctuating force induced in any reading (occurring at $\alpha = 90^\circ$ for drag). The data was digitised using a National Instruments NI USB-6229 data acquisition board.

Aerofoil incidence was adjusted manually at the hub assembly. Tunnel velocity was also adjusted manually before each reading, measured across the contraction of the tunnel using

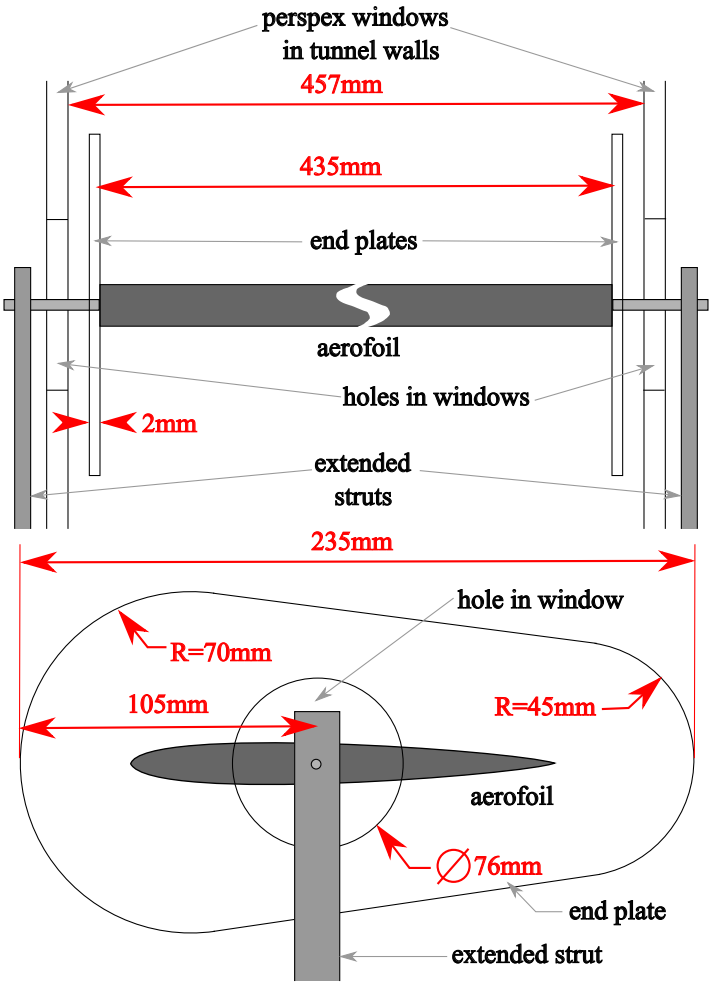


Figure 3.1: Aerofoil mounting in the wind tunnel, front-on (top) and side-on (bottom) views.

a Furness Controls FCO510 micromanometer.

The force balance was calibrated before experiments using weights applied in the directions of expected lift and drag forces. Due to significant drift in the load cells, unloaded readings for the balance were taken before and after each run of the tunnel. Unloaded values for each incidence were calculated by time apportioning the difference between the start and end unloaded readings. This drift is the largest source of potential error in readings taken from the apparatus. Total potential error in the system is estimated at a maximum of approximately 3%, based on the typical load cell drift and the maximum differences between repeated runs for the same aerofoil and tunnel configuration. Other than in the immediate post-stall region between stall and $\alpha = 15°$, where stall cells can cause inconsistencies in force measurements

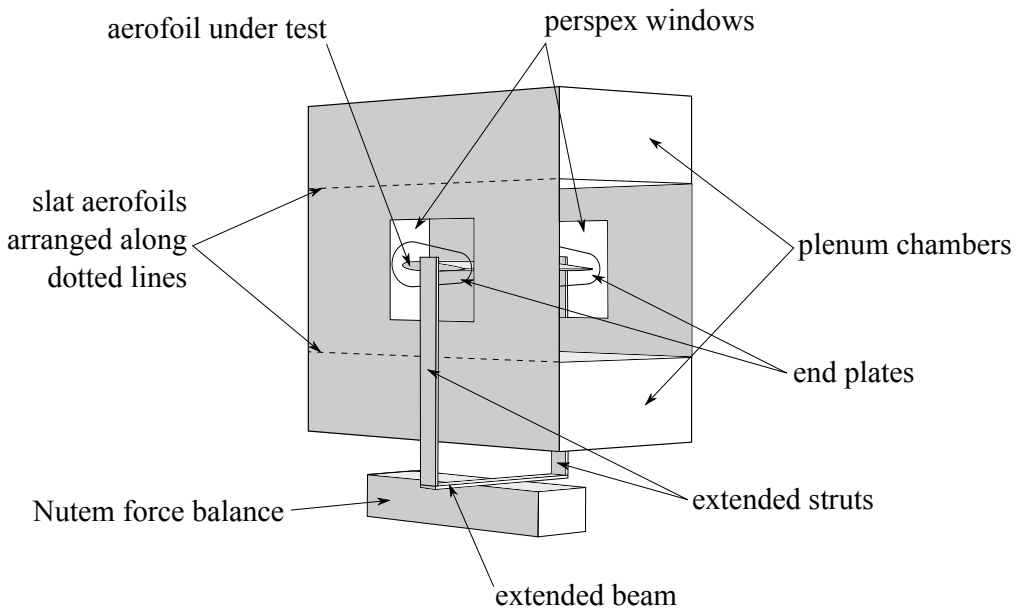


Figure 3.2: Experimental set-up in and around the wind tunnel.

and differences between runs were as high as 8%, differences between repeated runs of the same experiment were within this maximum.

3.1.3 Results

Measurements of lift and drag were taken for the $c/H = 0.27$ and $c/H = 0.32$ aerofoils for $0^\circ < \alpha < 180^\circ$, the test section configured with a slatted ceiling with OARs of 0.43, 0.51, 0.59, 0.67 and 0.84 (tunnel configurations denoted SS-0.43, SS-0.51, SS-0.59, SS-0.67 and SS-0.84 respectively); with a slatted floor and ceiling with OARs of 0.43, 0.51, 0.59, and 0.67 (denoted DS-0.43, DS-0.51, DS-0.59, and DS-0.67) and with conventional solid walls (where blockage corrections are applied to data).

Selection of data for inclusion in this report

Results are presented for the solid-walled tunnel (raw data and with corrections applied) and for the SS-0.59, DS-0.43 and DS-0.59 configurations. Solid-walled data is included to allow direct comparisons to existing studies. The SS-0.59 and DS-0.43 configurations were chosen for inclusion as the best of the SS and DS configurations, based on experimental results (see Section 3.3 for methodology used in this judgement) and through use of a numerical simulation

of the tolerant tunnel, see Section 3.2.

Since the simulation is based on a potential flow method, it is unsuitable for judging performance in the post-stall range of incidences. As mentioned, Parkinson's bluff body tunnel with slated floor and ceiling was found to work best with OARs of 0.5 to 0.7. An OAR of 0.563 was judged to be the best overall for flat plates with c/H of up to 0.33 in [54]. A similar tunnel should be capable of handling similar sized aerofoils at extreme angles of incidence, so results from the DS-0.59 arrangement are also presented here as this is the nearest OAR achievable with the current apparatus.

Comparisons to existing data

The apparatus has been validated by comparing results from the solid-walled test section configuration to existing data taken in similar conventional tunnels. Fig. 3.3 shows results for the $c/H = 0.32$ aerofoil taken in the solid walled tunnel, corrected for blockage using the methods of Section 2.1. Also included are the data of Sheldahl and Klimas [20] (as before, taken at $Re = 3.6 \times 10^5$) and Althaus's study taken at $Re = 1.5 \times 10^5$ [8]. As well as the same Reynolds number, it also shares similar c/H and aspect ratios (see Table 1.1) to the larger aerofoil of the current study.

Lift of the $Re = 1.5 \times 10^5$ studies is in close agreement pre-stall, with a gradient steeper than 2π up to $\alpha \approx 2°$, then a shallower gradient between there and stall, occurring at $\alpha = 11°$, with a Cl_{MAX} of approximately 0.9. The value of Cl_{MAX} is consistent with the trends established with Reynolds number in McCroskey's review of wind tunnel results for the NACA 0012 [72]. The steep gradient at $\alpha < 2°$ is caused by a laminar separation bubble on the suction surface of the aerofoil which moves towards the leading edge with increasing incidence. This is a feature of the NACA 0012's performance at low Reynolds numbers (none of the steeper gradient is exhibited by Sheldahl and Klimas's data taken at $Re = 7.0 \times 10^5$ [20]). See Sections 1.5.5 and Ch. 5 for more on laminar separation bubbles.

The agreement in the region $10° < \alpha < 15°$ is reasonable; the leading edge stall behaviour of the NACA 0012 makes small differences here unsurprising. The agreement between Sheldahl and Klimas and the others is surprising given the much larger Reynolds number used [20] and is likely due to the compensatory effect of the difference in blockage, with a c/H of 0.07 compared to 0.32-0.33 for the current study and that of Althaus [8].

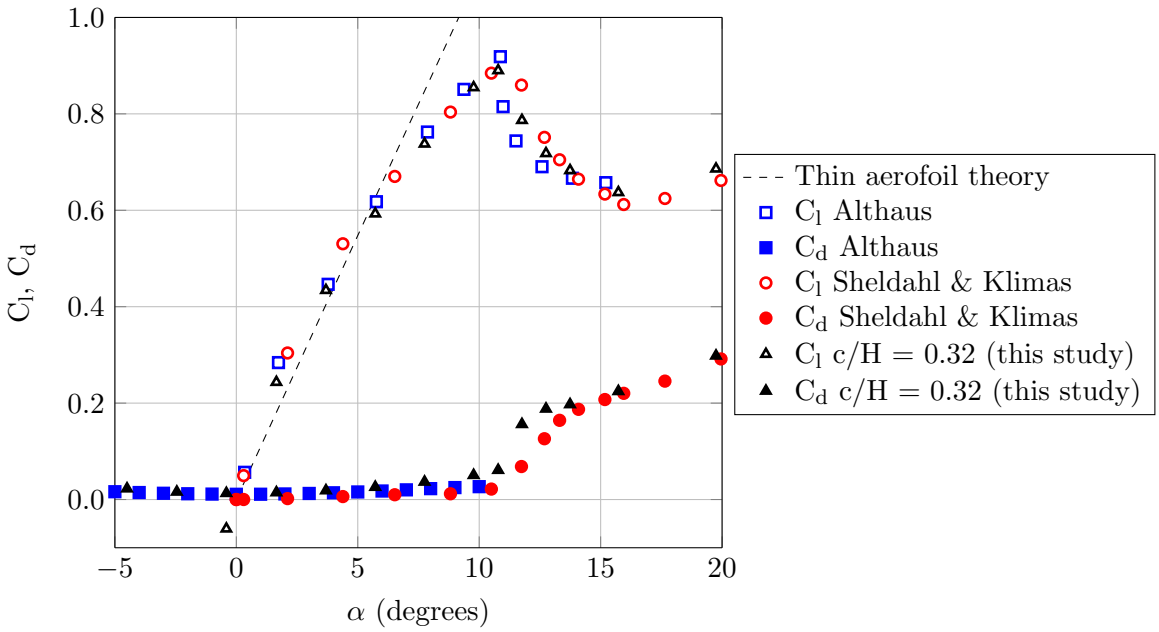
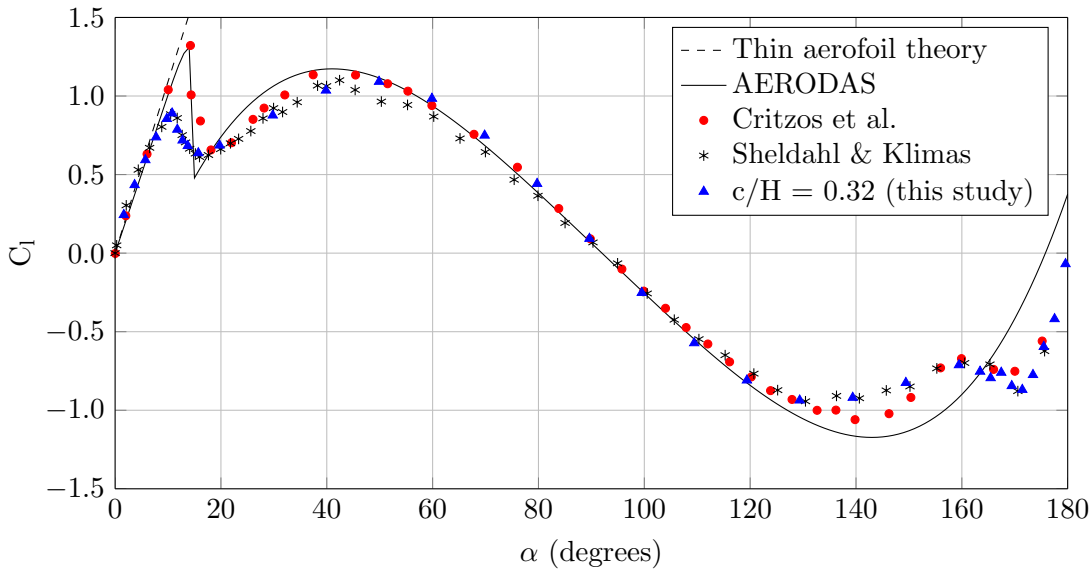


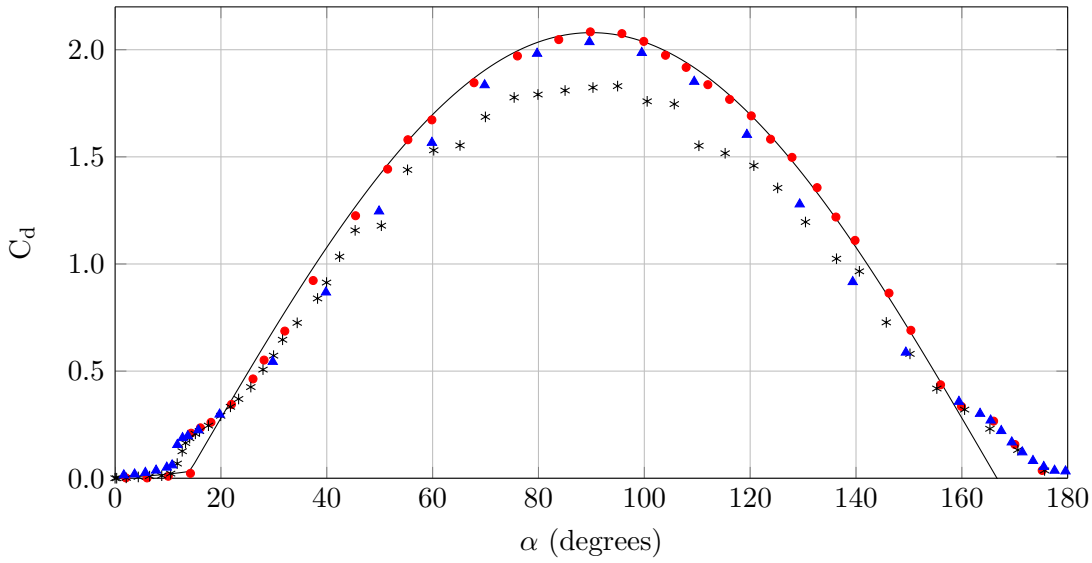
Figure 3.3: C_l and C_d vs α alongside the studies of Althaus [8] and Sheldahl and Klimas [20].

Figs 3.4a and 3.4b show plots of lift and drag, respectively, covering 0° to 180° of incidence. Included are results for the $c/H = 0.32$ aerofoil, alongside Sheldahl and Klimas [20] (as in Fig. 3.3) and Critzos et al's $Re = 1.8 \times 10^6$ study [34]. The second lift peak of the current study at $\alpha \approx 45°$ is similar in magnitude to that of Critzos et al. but higher than that of Sheldahl and Klimas. The two earlier studies share a common c/H of 0.07 so the differences between them are surprising. Reynolds number effects could be responsible, Critzos et al. completed experiments at $Re = 5 \times 10^5$ as well as 1.8×10^6 in the same tunnel [34] (the Langley LTPT, see Table 1.1), finding a slight positive correlation between Reynolds number and post-stall lift and drag peak magnitude, but Sheldahl and Klimas completed experiments at three Reynolds numbers (5×10^5 and 7×10^5 alongside the 3.6×10^5 reproduced here) and found post-stall performance to be independent of it [20]. Section 5.4 contains an analysis of Reynolds number effects on results from this study and the literature.

Results for drag are similar to lift: pre-stall all studies are in reasonable agreement while post-stall, results for the $c/H = 0.32$ aerofoil are similar to those of Critzos et al. but higher than Sheldahl and Klimas's.



(a) C_l vs α.



(b) C_d vs α.

Figure 3.4: Results alongside the NACA 0012 post-stall studies of Sheldahl and Klimas [20] and Critzos et al. [34], and output of the AERODAS model [73].

Solid walled tunnel

Fig. 3.5a shows results from the solid walled tunnel for the $c/H = 0.27$ and $c/H = 0.32$ aerofoils, both raw uncorrected and corrected, labelled "u" and "c" respectively. There is a divergence in the characteristics of the two aerofoils at incidences below 15.5°, particularly in the region $3.5° < \alpha < 15.5°$. Fig. 3.5b shows details from the lower incidence end of the

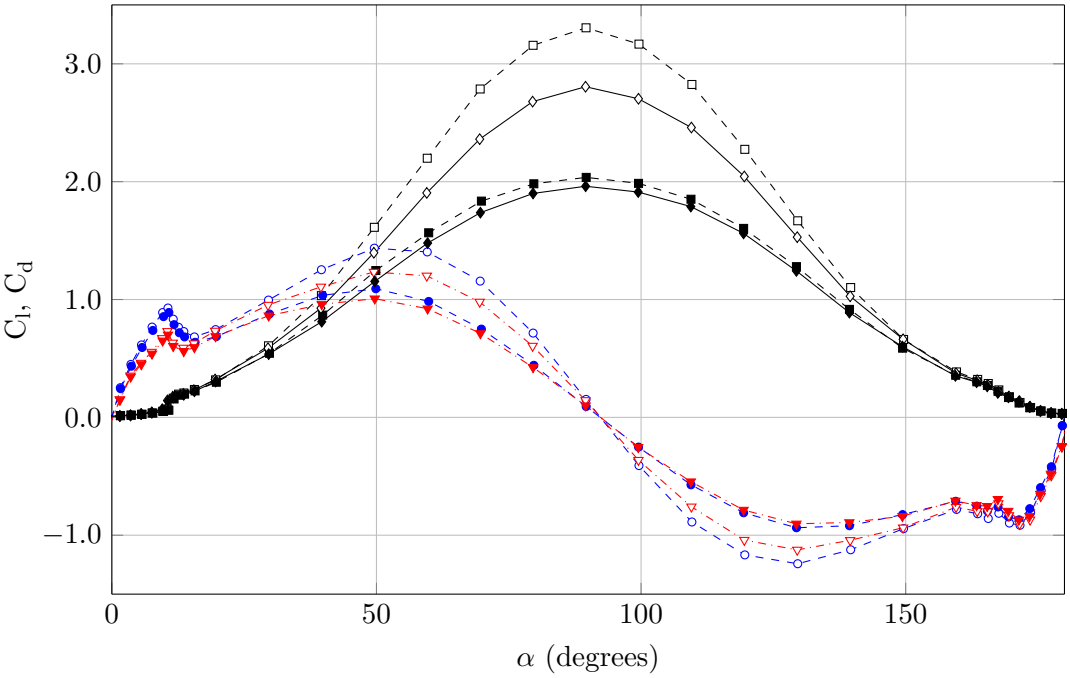
plots up to $\alpha = 30°$. The smaller aerofoil has a rougher surface finish, the differences in the performance at low incidence are consistent with those between smooth and rough aerofoils [74]. The unusual behaviour of the $c/H = 0.27$ aerofoil persisted in all tunnel configurations; pre-stall results for it are therefore not analysed further. Post-stall data for the two aerofoils is comparable since surface roughness has little impact on separated flow.

Blockage corrections collapse the data from the two aerofoils well in the post-stall region. The raw drag peak is 18% larger for the larger aerofoil, this difference reduces to 4% for the corrected peaks. As the studies presented in Fig. 1.8 and Table 1.1 suggest, post-stall lift and drag peaks are higher for the higher blockage experiment even after corrections have been applied.

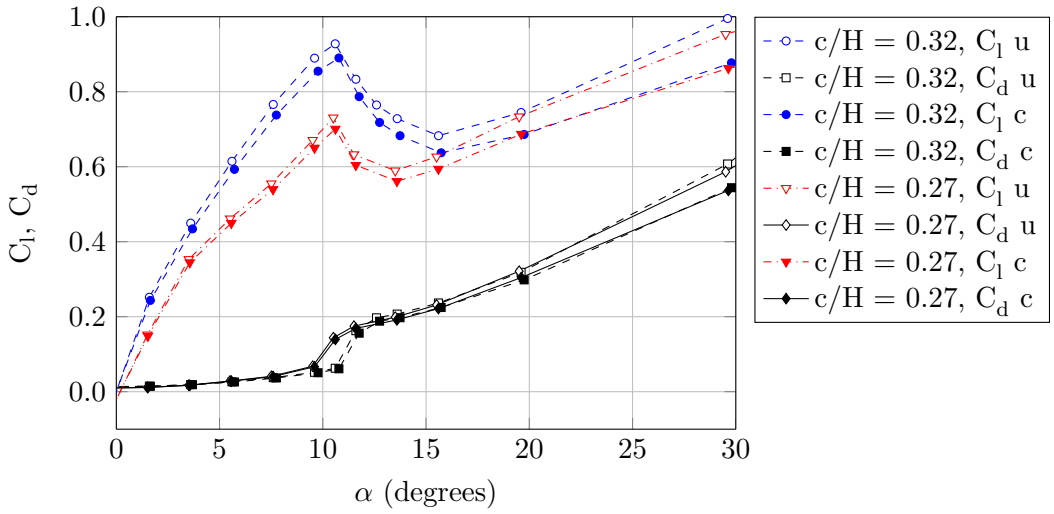
Tolerant tunnel

Fig. 3.6 contains results from the SS-0.59 configured tolerant tunnel, alongside the corrected results from the solid-walled tunnel for the $c/H = 0.32$ aerofoil to allow comparison with earlier figures. The plots are similar to the corrected solid-walled tunnel; the spread of data for the two aerofoils is far less than for the raw solid-walled data, with higher post-stall peaks (4% higher at the drag peak) for the larger aerofoil. Pre-stall results for the large aerofoil are very similar to the corrected data, the gradient of the curve being slightly lower, with stall occurring earlier (at 10.3°opposed to 10.8°) and at a lower peak (0.85 versus 0.89). Both aerofoils exhibit lower post-stall lift peaks than the corrected solid-walled data. There is strong agreement between the two tunnel configurations for drag of the $c/H = 0.32$ aerofoil, with identical drag coefficient peaks of 2.04 at $\alpha = 90°$.

Figs 3.7 and 3.8 show results for the DS-0.43 and DS-0.59 double slotted wall configurations. There is striking data collapse for the DS-0.43 tunnel, with results nearly identical for the two aerofoils for post-stall lift and for drag, other than for $60° < \alpha < 110°$ where the larger aerofoil exhibits a 5% higher drag peak. Hameury [54] found that a 33% blockage normal flat plate diverted flow to such an extent that it caused some of the slat aerofoils of his tunnel to stall, suggesting this is beyond the limit of tolerance of the tunnel. At these extreme incidences, the largest aerofoil could be similarly affecting the slats of the tunnel used in these experiments. Though agreement between the aerofoils is excellent, post-stall peaks are significantly lower than for the data from conventional tunnels, the $c/H = 0.32$ lift peak



(a) Full range of incidence tested, $0 \leq \alpha \leq 180°$



(b) Detail in the range $0 \leq \alpha \leq 30°$

Figure 3.5: C_l and C_d vs α for $c/H = 0.27$ and $c/H = 0.32$ aerofoils taken in the solid walled test section: raw uncorrected data (u) and corrected data (c).

is 21% higher for the corrected solid-walled data while drag peak is 23% higher. Pre-stall results for the larger aerofoil are close to those from the corrected solid-walled tunnel and the SS-0.59 configuration, with a $C_{l_{\text{MAX}}}$ of 0.85 at 10.5°

The collapse of data for the DS-0.59 tunnel is less impressive, with a greater spread between

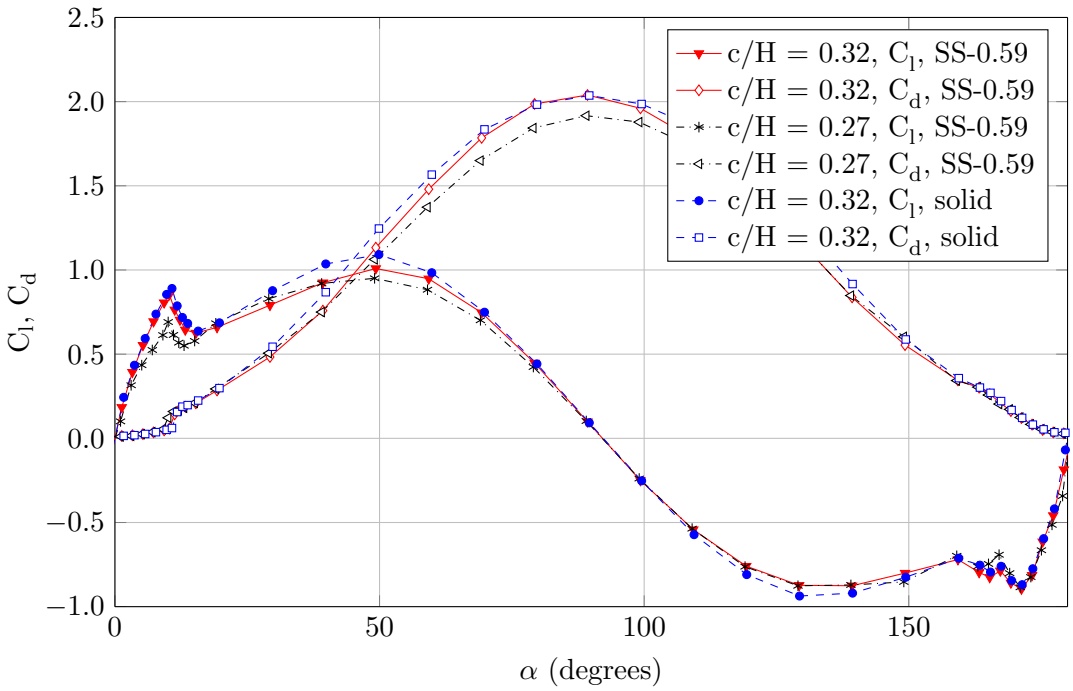


Figure 3.6: C_l and C_d vs α for $c/H = 0.27$ and $c/H = 0.32$ aerofoils taken in the SS-0.59 tolerant tunnel.

post-stall lift and drag, and a lower stall point ($C_{l_{\text{MAX}}} = 0.82$ at $\alpha = 10.20°$) than for the other configurations.

3.2 Numerical modelling

A potential flow model has been used to represent the tolerant tunnel numerically, based on the source/vortex panel method of Smith and Hess [75]. The decision to develop a new code was taken as no suitable software could be found capable of modelling the slatted tunnel walls. The code models the aerofoil under test using distributed source and vortices across the panels representing it, with a Kutta condition applied to the trailing edge panels of the upper and lower surfaces. It can also model the slat aerofoils using the same technique, applying any number of Kutta conditions in a given simulation. Results presented here use a simpler version of the code, with the tunnel walls and slat aerofoils modelled as flat panels using point vortices.

Fig. 3.9 shows the code output for the 18" Flow Control tunnel test section, with solid walls and with the SS-0.59 and DS-0.43 slatted wall configurations, in the form of a plot of

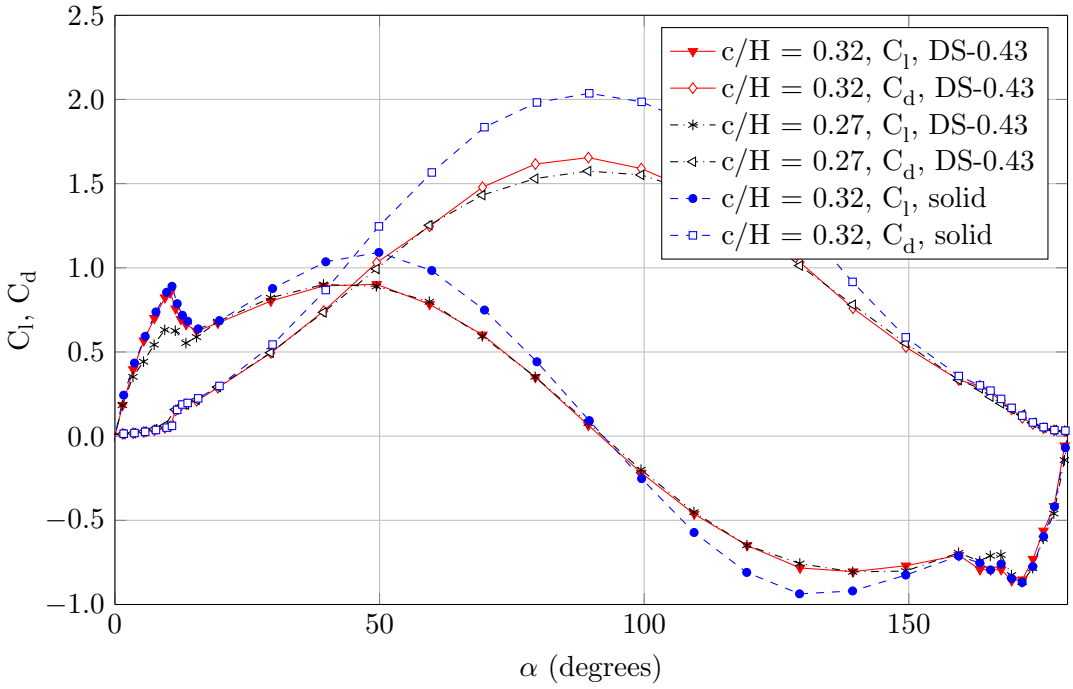


Figure 3.7: C_l and C_d vs α for $c/H = 0.27$ and $c/H = 0.32$ aerofoils taken in the DS-0.43 tolerant tunnel.

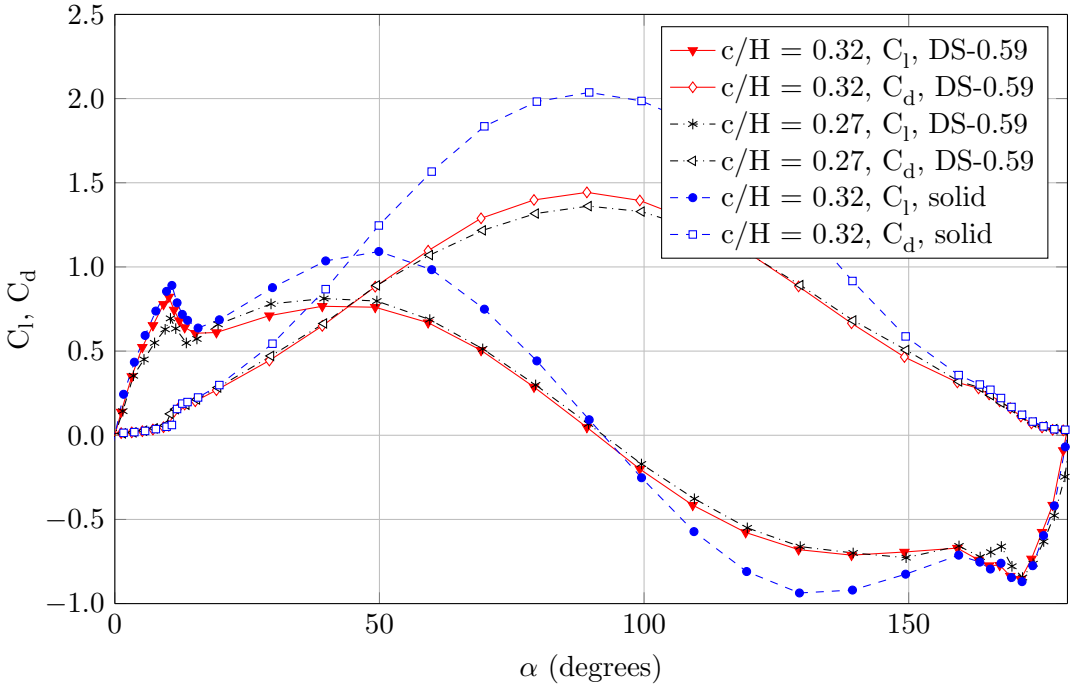


Figure 3.8: C_l and C_d vs α for $c/H = 0.27$ and $c/H = 0.32$ aerofoils taken in the DS-0.59 tolerant tunnel.

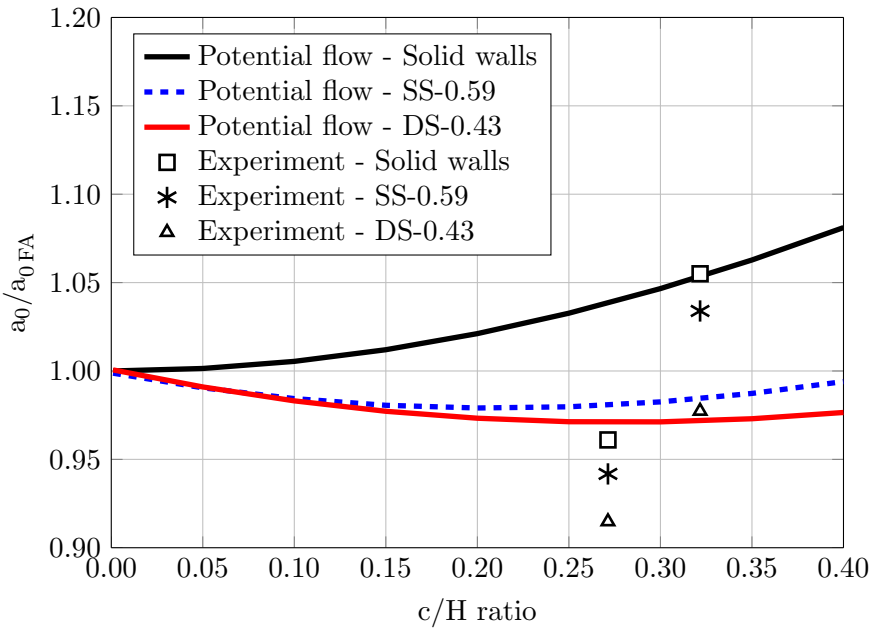


Figure 3.9: Effect of aerofoil size on ratio of lift coefficients (theory)/ratio of lift curve slopes (experiments).

normalised lift curve slope against c/H. The normalised lift curve slope is the gradient of the attached flow C_l vs. α curve from a given tunnel type, divided by the same gradient for unconstrained flow:

$$\frac{a_0}{a_{0_{\mathrm{FA}}}} = \frac{C_l/\alpha}{C_{l_{\mathrm{FA}}}/\alpha_{\mathrm{FA}}} \tag{3.1}$$

Unconstrained flow variables are given the subscript "FA" for "free air".

Simulations corresponding to SS-0.59 and DS-0.43 configurations give values of $a_0/a_{0_{\mathrm{FA}}}$ near to unity for $c/H < 0.4$ for the slatted ceiling and slatted floor and ceiling arrangements of the tunnel respectively. This implies that they replicate the free stream behaviour well for pairings of aerofoil and tunnel sizes of the order used in the experiments detailed in this thesis.

3.3 Parkinson tunnel blockage reduction

Hameury selected a DS-0.563 tunnel configuration by testing three pressure tapped flat plates with c/H of 0.083, 0.194 and 0.333 normal to the flow [54]. Various parameters, including base pressure coefficients, drag coefficients, Strouhal number and required blockage corrections,

were plotted against OAR and the tunnel providing the most consistent results for the range of model sizes was judged to be the best. In free air, results would be identical regardless of model size, so the tunnel providing this consistency can be taken as providing the nearest approximation of free-air conditions. Standard deviation of pressure distributions from a reference were assessed to see which tunnel provided the minimum deviation. Section 4.8 gives a more detailed look at Hameury's work.

Here, the focus is on force measurements of lift and drag and tunnels must be judged on their performance over the full range of post-stall incidences, not just at $\alpha = 90°$. Since only two aerofoils have been tested, there is no need for a standard deviation analysis, differences between the two are a sufficient measure of data spread. As such, Table 3.1 has been compiled, containing sums of the absolute differences between readings of lift and drag for the two aerofoils at each data point in the range $20° < \alpha < 160°$. The DS-0.43 configuration is shown to give the most consistent results for the two aerofoils over the range of incidences.

Tunnel configuration	Sum of differences, $20° < \alpha < 160°$		
	C_l	C_d	Total
Solid walled	3.77	6.13	9.89
SS-0.59	0.37	0.80	1.17
DS-0.43	0.19	0.37	0.56
DS-0.59	0.43	0.52	0.95

Table 3.1: Absolute differences between $c/H = 0.27$ and $c/H = 0.32$ data for selected tunnel configurations.

For attached flows, an experimental equivalent of the $a_0/a_{0_{\mathrm{FA}}}$ output of the tunnel panel code has been calculated with a_0 obtained from a linear regression analysis of results in the range of incidences $-2° \leq \alpha \leq 6°$ and $a_{0_{\mathrm{FA}}}$ approximated using thin aerofoil theory. Results for solid-walled, SS-0.59 and DS-0.43 tunnels are shown in Fig. 3.9. Due to surface roughness inducing shallow pre-stall gradients for the $c/H = 0.27$ aerofoil, its results are lower than theory for all tunnel configurations. The results for the $c/H = 0.32$ aerofoil are nearly identical for the solid walled and DS-0.43 tunnels, but the SS-0.59 does not correct the lift curve gradient as much as predicted.

The short L/H ratio of the test section used for these experiments (2.14, compared to 2.67

for Parkinson's original) is a possible cause of this less-than-expected reduction of blockage. When building tunnels to Parkinson's design, others have found an insufficiently long slatted section to cause similar problems [76], see Section 4.8.4 for more on tolerant tunnel L/H ratios.

Parkinson's tolerant tunnel design has been applied to aerofoils in the deep stall region of incidences for the first time. The results from the proof-of-concept tolerant tunnel experiments suggest its use is valid for the testing of post-stall aerofoils, the SS-0.59 configuration providing results very close to those achieved using current best practice, without reliance on correction methodologies that are not strictly applicable in the post-stall region. Current best practice is well established for unstalled aerofoils where flow is attached and corrections can be used with confidence. The tolerant tunnel provides results comparable to the corrected conventional tunnel data in this region of incidences, with no need for corrections.

The experiments support the findings of Parkinson and others that OARs of 0.5 to 0.7 are best for proving free-air like conditions. The findings, and the limitations encountered during the work with the 18" test section (namely its low L/H ratio and small cross-section) have been considered in the design of a new test section for further experimentation, described in the following chapter.

Chapter 4

The blockage tolerant wind tunnel: design, build and commissioning

Following the successful modelling and experimental campaign presented in Ch. 3, the suitability of Parkinson's design for post-stall aerofoil testing was confirmed. Tunnel dimension limits for effective blockage reduction (for example, a minimum L/H ratio) were established, using the results of the experiments and reviews of other studies conducted in Parkinson tunnels. The tunnel used for the proof-of-concept work is too small for the requirements of this study, due to limitations on aerofoil size at extreme incidences (and so profile accuracy and flow Reynolds number). As such, a larger test section was developed to Parkinson's design, for use with the Imperial College 3' $\times$ 3' wind tunnel. This chapter documents the design and build of the tunnel and the calibration of the tunnel OAR, through testing of five NACA 0015 aerofoils with different c/H ratios.

4.1 The Imperial College 3' $\times$ 3' wind tunnel

Experiments were conducted in Imperial College's 3' $\times$ 3' low speed, low turbulence wind tunnel. It has a closed return design, and a maximum flow speed of 45 m/s. The 7.5:1 contraction ratio ahead of the test section, and honeycomb screens help to give a reasonably low turbulence intensity of less than 0.1% when empty, making it suitable for low Reynolds number aerofoil testing [52]. The tunnel has three existing test sections, only two of which

are fitted in the tunnel loop at any one time, so that one can be prepared for experiments while the other two are in use. The test sections are mounted on steel trolleys with castor wheels.

4.1.1 3' × 3' tolerant test section construction

A new Parkinson-style test section was fabricated for the tunnel, which has a 915 mm × 915 mm test section with a length of 2390 mm. The Parkinson section has a plenum depth of 350 mm and a length of 2178 mm. Slats have a NACA 0015 profile and a chord of 90 mm. These dimensions are similar to those of Parkinson's original tunnel, which had an identical tunnel height, 92 mm chord NACA 0015 slats and a plenum of length 2440 mm and depth of 300 mm.

The test section can be configured with a single slatted wall, double slatted walls or as a conventional closed jet section. Slats are mounted between steel runners and can be slid along the test section and added or removed at will, enabling its OAR to be adjusted. They are bolted to the tunnel walls through mounting holes once in their desired locations. The slatted walls can be replaced with solid walls to replicate a conventional test section.

Fig. 4.1 shows a cutaway view of the facility. The aerofoil under test is mounted vertically between endplates which sit flush with the tunnel walls. Force transducers are mounted at both ends of the aerofoil to measure aerodynamic forces and moments, with the upper transducer mounted to a bearing unit that allows free rotation. The lower transducer is attached to a stepper motor to control incidence.

The body of the main tunnel and plenum chambers is constructed from MDF panels with a timber framework for strength. MDF parts were laser cut to order, including mounting holes for slat aerofoils at a variety of OARs. Doors in the ceiling and floor of the tunnel give access to the rig and the mounting points for slat aerofoils or solid wall panels. See Fig. 4.2 for a photograph of the test section under construction in the middle of the tunnel loop.

4.1.2 Test section support

A trolley was manufactured from steel box section to support the new tolerant test section. The trolley has the same dimensions as the original test section trolleys and like them is fitted

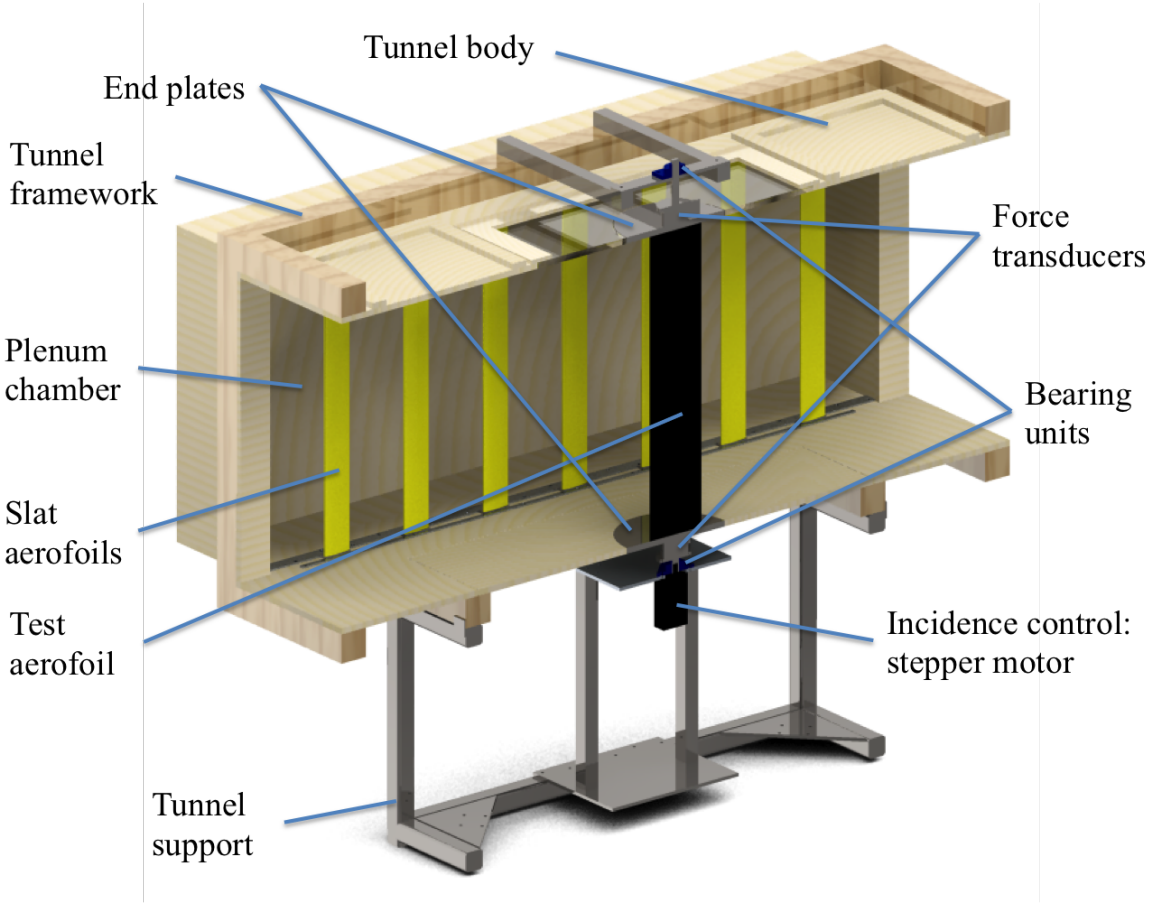


Figure 4.1: Streamwise cutaway view of the Imperial College Parkinson tunnel.

with castors, allowing easy movement of the assembly's considerable mass, and adjustable feet to support it when in use.

A steel plate is welded to the bottom of the trolley, providing a mounting point for a Minitec assembly that holds the bottom hub of the test aerofoil and a stepper motor to control aerofoil incidence. The top of the test aerofoil is supported by a smaller Minitec frame that is bolted to the test section's timber framework. Section 4.2.5 describes the test aerofoil mounting in more detail.

4.1.3 Slat aerofoils

For the experiment requiring the most slat aerofoils (the tunnel configured with two slatted walls, OAR = 50%), 24 are needed, amounting to a total length of almost 22 m of aerofoil. A method of manufacturing such a large amount of aerofoils in a cost-effective manner was

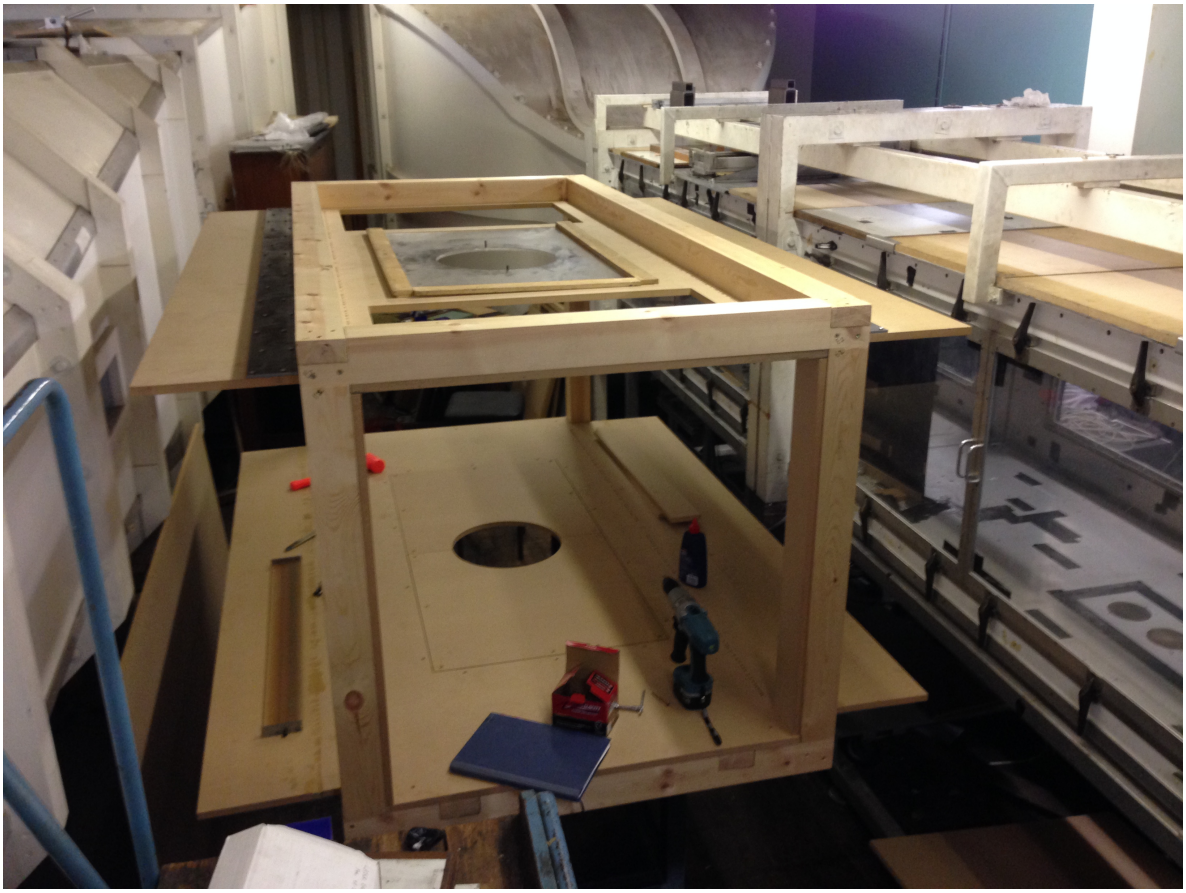


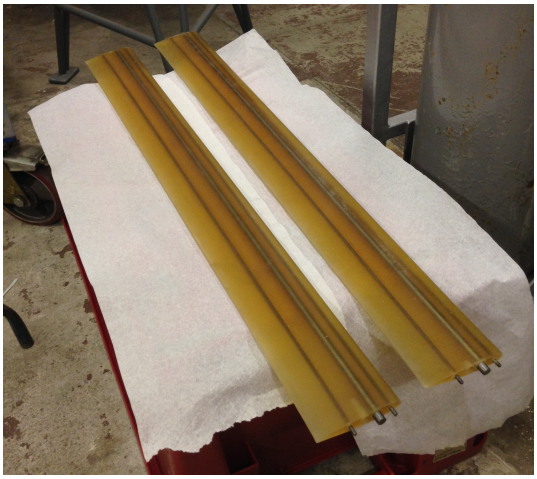
Figure 4.2: The Imperial College Parkinson test section under construction.

developed. See Fig. 4.3 for photographs of the slat aerofoils under construction. The NACA 0015 shape of the profile was cast in resin, using a four-part cast machined from SikaBlock and sealed with varnish. Beeswax was used as a release agent and applied to the cast before each use.

The aerofoils are cast around a core of one 8 mm steel rod for strength and two M4 threaded rods for the attachment of small steel end plates, allowing the slats to be slid along the steel runners with ease, see Fig. 4.3 for a profile shot of the slats showing the construction. The total length of the aerofoil and end plate assembly is 0.915 m, spanning the full height of the test section.



(a) The cast in use.



(b) Aerofoils curing.



(c) Profile view of slat.

Figure 4.3: Slat aerofoil production process.

4.2 Test aerofoils

The NACA 0015 and 0018 profiles were chosen as they are frequently used in experimental and numerical VAWT research, see Table 6.1 for a summary of experimental VAWT research referenced in this thesis. There are also some existing post-stall studies for the profiles against which to validate results (see Ch. 5 for validation and Table 1.1 for a summary of the aerofoil experiments referenced in this thesis).

4.2.1 NACA 0015

Five NACA 0015 aerofoils of different sizes were tested in order to assess wind tunnel blockage reduction techniques. All five aerofoils have a span of 915 mm and chords such that their c/H ratios are 0.1, 0.15, 0.2, 0.25 and 0.3. They are referred to by their c/H ratios throughout this thesis. The 0.15 and 0.25 aerofoils are tapped for surface pressure measurements at the

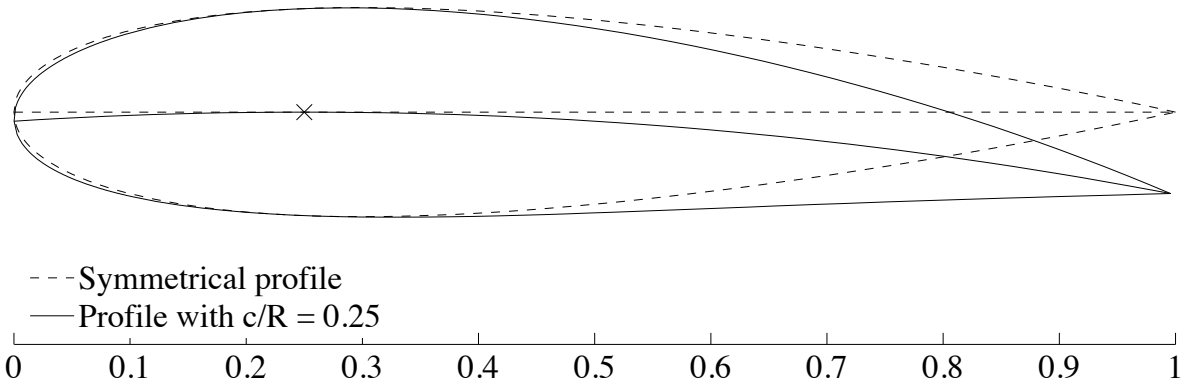


Figure 4.4: Symmetrical NACA 0018 and similar cambered profile sharing a quarter chord.

midspan, with limited numbers of tappings at each quarter-span for detection of any flow three-dimensionality.

4.2.2 NACA 0018 and similar profiles with camber

The NACA 0018, and two 18%-thick NACA 4-digit profiles with camber, were manufactured to study Migliore's virtual camber theory [24]. The results of this study are presented in Section 6.5. This research was, in part, jointly conducted with the University of Florence. For the collaboration, the aerofoil shapes and flow conditions were strictly defined ahead of work commencing. Imperial College were responsible for wind tunnel testing of the profiles, and Florence for modelling using CFD and BEM codes.

Testing was required to be conducted at Reynolds numbers of up to 300 000 for attached flow and 250 000 for separated flow. In order to conduct these tests within the limits imposed by the 3' × 3' tunnel's 45 m/s maximum velocity and the force transducer saturation limits (nominally 130N for lift and drag, but in reality lower than this once mounted in the apparatus and subject to moments and forces from the rig itself) the aerofoils needed chords longer than 0.18 m. Chords were set at 0.183 m, giving a c/H ratio of 0.2.

The cambered profiles are modified from the symmetrical NACA 0018 such that their camber line follows an arc of the circumference of a circle. The ratio of the aerofoil chord length to circle radius, c/R, is set to 0.114 for the first cambered profile and 0.25 for the other. Fig. 4.4 shows a symmetrical NACA 0018 profile and the cambered profile with $c/R = 0.25$.

Should Migliore's theory be correct, the profiles should perform in the wind tunnel as the

symmetrical NACA 0018 profile would in turbines with similar c/R ratios. The c/R were chosen for comparability to those used in Migliore's original paper of 0.114 and 0.26 [24]. The larger c/R ratio was modified slightly based on the turbines in Table 6.1 to help in modelling their performance (The average c/R of the Vittecoq and Laneville [77], Durham [2, 3], Bravo et al. [78] and Maeda et al. [79, 80] turbines is 0.25). The aerofoil with c/R of 0.114 has a maximum camber of 1.42% at 50% of chord, while the c/R of 0.25 has 3.11% maximum camber at 50% of chord.

4.2.3 Aerofoil construction

The aerofoils were manufactured using Nylon selective laser sintering (SLS) 3D printing technology. Each consists of 4 separate printed parts with a 228.75 mm span (the print chamber of the printer limits the size of parts), with a core of two 915 mm long steel rods. Printed Nylon parts can shrink and deform as they cool - steps were taken to minimise the risk of this happening by limiting wall thickness in the parts to 3 mm, ensuring heat dissipates quickly. Ribbing and span-wise struts were printed into the parts to give them sufficient stiffness. The Nylon sections were assembled around the steel cores using epoxy resin, with a final smooth surface and accurate profile achieved using filler, sand paper and paints. While sanding and filling the aerofoils, profile accuracy was checked against female profile templates, produced using a laser cutter with a rated accuracy of better than 100 μm which compares favourably to the typical accuracy of Nylon SLS printers, around 0.35 mm for parts of the size used here. Fig. 4.5 shows the aerofoils at two steps of the construction process. On the left, they have been assembled and glued together with epoxy. Daylight shining through them reveals the printed structure and steel rods within. On the right, the aerofoils have been filled and painted, showing the surface finish quality that can be achieved with these manufacturing techniques.

Two aerofoils, the $c/H = 0.15$ and $c/H = 0.25$ NACA 0015s, were tapped for pressure readings. Small copper taps were fitted flush to the aerofoil surface, with thin plastic piping attached to them, passing through the aerofoil and exiting at the top end of it when mounted in the wind tunnel.

The larger aerofoil had 50 taps in total, 30 at the midspan and 10 at each of the quarter spans for assessing the two-dimensionality of the flow. The smaller aerofoil had 37 taps in

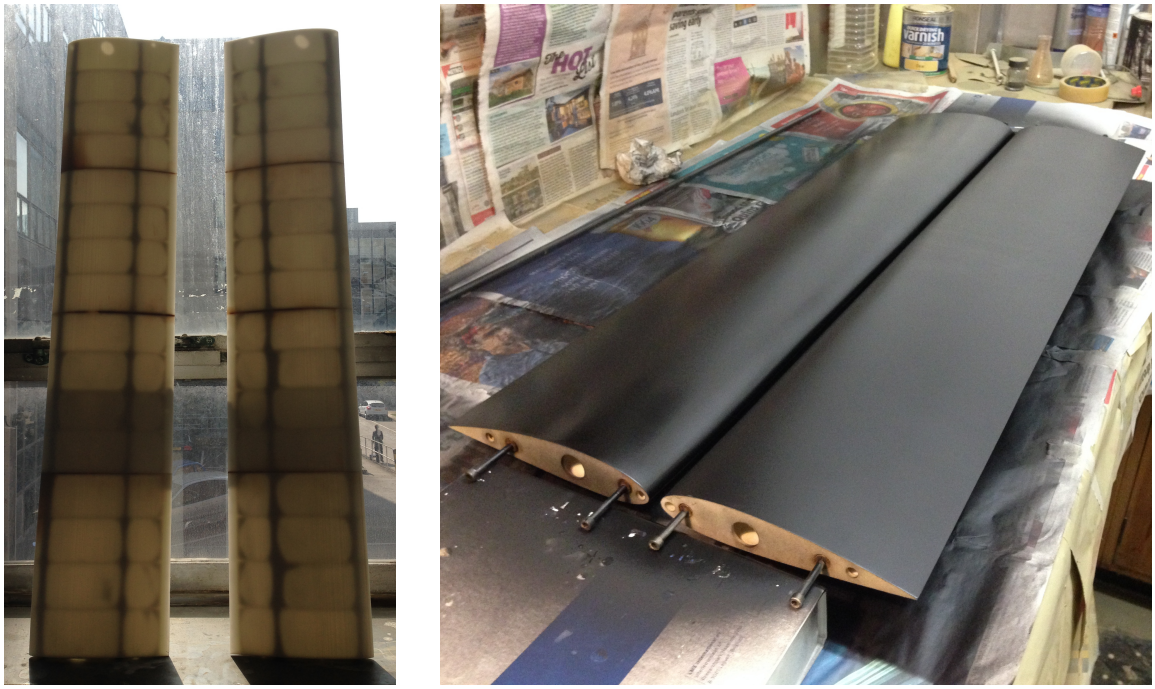


Figure 4.5: The two cambered aerofoils during construction.

total, 25 at the midspan and 6 at each quarter span. Unfortunately, a number of taps were lost during the manufacturing of the aerofoils, either due to the plastic piping becoming removed from the copper taps, or becoming kinked inside the aerofoils as they were assembled. In the $c/H = 0.25$ aerofoil, two taps were lost at the midspan and five across the two quarter spans. For the $c/H = 0.15$ aerofoil seven were lost at the midspan and one at one of the quarter spans. A large number of tappings in a small aerofoil meant the midspan of the $c/H = 0.15$ aerofoil was particularly cramped, leading to the significant loss of tappings there.

All aerofoils were machined square at the ends as accurately as possible as a final step of the manufacturing process to ensure good alignment with force measurement equipment.

4.2.4 Profile accuracy and surface roughness

Finished model profile accuracies have been measured using a Faro Edge ScanArm 3D coordinate measuring machine. The device has an articulated arm fitted with a high definition Laser line scanner. The aerofoils have uniform profiles across their spans, so measurements were taken across a randomly selected 10 cm span-wise strip (avoiding the joins between aerofoil segments at the half and quarter spans) for each of the aerofoils presented in Ch. 5 (the

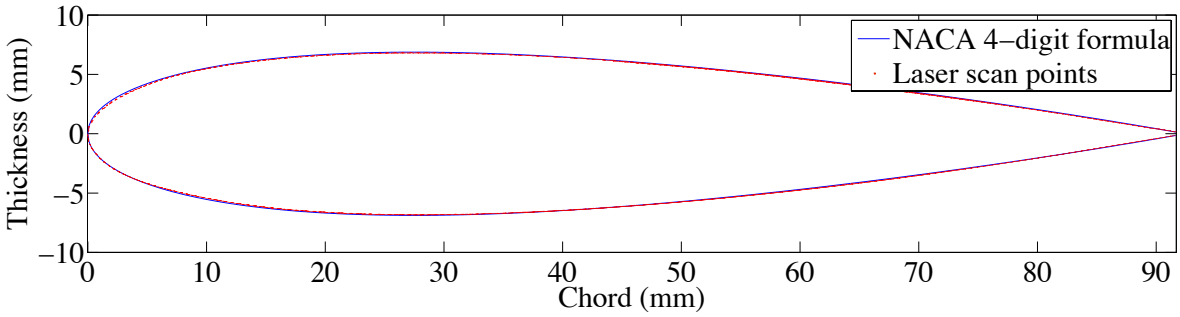


Figure 4.6: Results of profile accuracy measurements of the NACA 0015.

$c/H = 0.1$ NACA 0015 and the $c/H = 0.2$ NACA 0018 and cambered aerofoils).

The maximum deviation from the intended profile shape, measured normal to aerofoil surface, is 0.13 mm for the NACA 0015, or 0.14% of chord and 0.95% of maximum thickness. Fig. 4.6 contains the results of the scan for the NACA 0015, alongside the profile per the NACA 4-digit formula. Note that the plot is a two-dimensional representation of the scan. Data for the whole 10 cm span-wise strip is included, there being over 45 000 laser scan points on the figure. Maximum deviations for the other aerofoils are given in Table 4.1.

	Maximum deviations (normal to surface)		
Aerofoil	mm	% c	% t
NACA 0015	0.13	0.14	0.95
NACA 0018	0.33	0.18	1.00
NACA 0018 $c/R = 0.114$	0.27	0.15	0.82
NACA 0018 $c/R = 0.25$	0.35	0.19	1.06

Table 4.1: Maximum deviation of aerofoil surfaces from intended profile shape.

Surface roughness of the models was estimated by reference to a set of Rubert & Co. reference specimens at 0.4 μm Ra, sufficiently smooth for the roughness to have negligible impact on aerofoil performance.

These measurements are comparable to those taken by Selig and his team at the University of Illinois, responsible for the largest available body of low Reynolds number aerofoil research [81]. They routinely provide data on model accuracy, measured using a contact probe

coordinate measuring machine at model mid-spans. All their models have 305 mm chords. Most have maximum deviations of 0.25 to 0.76 mm, or 0.08% to 0.25% of chord (the profiles have various thicknesses). No surface roughness measurements are provided.

4.2.5 Test aerofoil mounting

The aerofoils were mounted vertically in the wind tunnel between two end plates that sit flush with the tunnel floor and ceiling, see Fig. 4.7. They are mounted such that incidence can be adjusted about the half chord, to avoid uneven blocking of the tunnel at extreme incidences. It was decided not to isolate the aerofoils from the wind tunnel boundary layer due to their insignificant displacement thickness at the model mounting point. Results presented in Figs 4.14 to 4.18 show little impact of aerofoil aspect ratio on readings around stall, suggesting any end wall effects caused by the boundary layers are minimal.



Figure 4.7: The $c/H = 0.2$ aerofoil mounted in the wind tunnel with double slatted walls, OAR = 0.55.

When forces are being measured, each end plate is attached to an adapter plate which in turn attaches to an ATI Industrial Automation Gamma IP65 6-component force and torque transducer. The upper transducer is mounted to the the framework of the tunnel via an axle assembly in a bearing unit, see Fig. 4.8, while the bottom is mounted to a stepper motor that controls aerofoil incidence, again via a bearing, see Fig. 4.9.

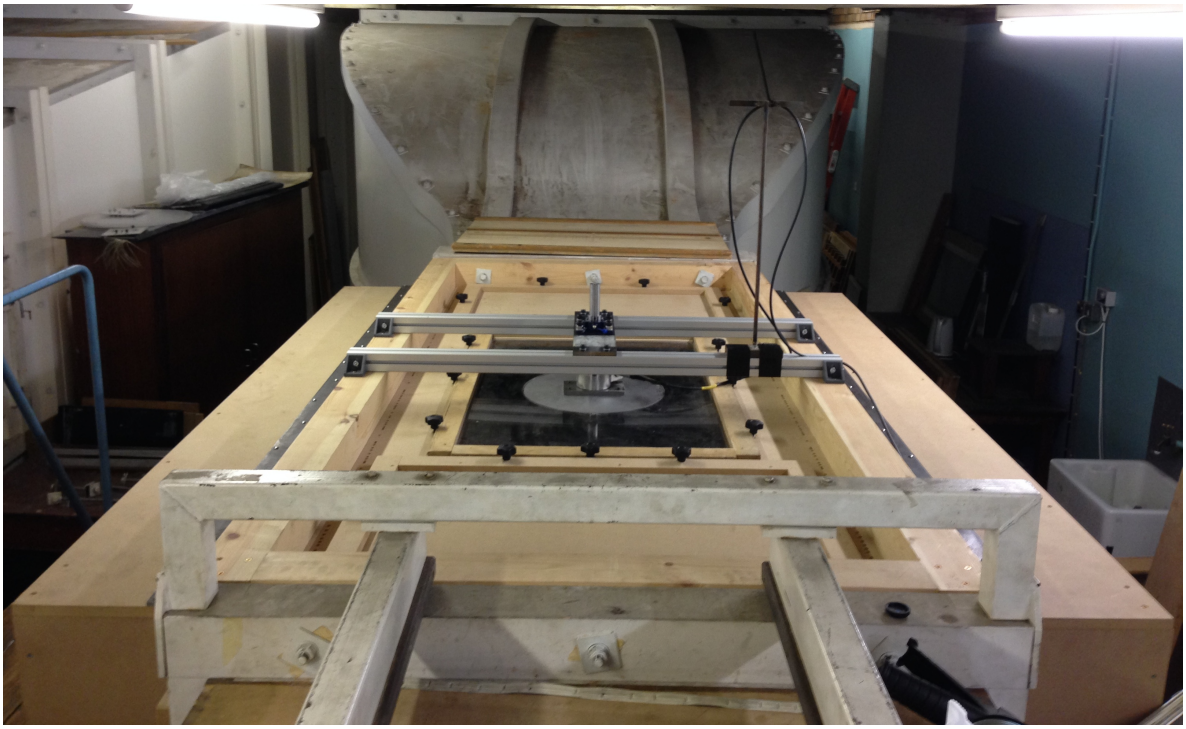


Figure 4.8: The top assembly of the apparatus, showing end plate, adapter, force transducer, bearing mount and attachments to the timber framework of the test section.

The top and bottom hub assemblies have a number of adjustable components which allow the system to be balanced to limit the forces and moments applied to the force transducers under no-flow conditions. A real-time readout of the sensors was written in National Instruments' LabVIEW package to help with the balancing process. Fine tuning was achieved by inserting very small washers between the end plates and adapter plates where necessary.

For pressure measurements, the upper force transducer and adapter plate is removed from the apparatus to allow for the pressure tapping tubes to pass out of the $c/H = 0.15$ or $c/H = 0.25$ aerofoils. The upper end plate fits directly to the axle assembly instead. The lower force transducer is replaced with a blanking unit of the same dimensions (since no force



Figure 4.9: The bottom assembly of the apparatus, with tunnel floor removed, showing end plate, adapter, force transducer, bearing mount and the cooling unit of the stepper motor.

readings are taken from the lower transducer during pressure runs, it would be in danger of unnoticed overloading). The tapping tubes are connected to a 64-channel Chell Microdaq pressure transducer.

4.3 Data acquisition and experiment control

Flow and aerofoil incidence are controlled by the PC via the outputs on a National Instruments NI USB-6229 data acquisition board. The incidence is altered using the stepper motor, with a tracking of its rotation stored at each data acquisition point. In addition incidence is also measured by an optical encoder attached to the motor shaft. The tracked incidence and encoder output are checked after each movement to ensure the motor has not slipped at any point. The output of the force transducers is digitized using a pair of NI PCI-6220 data acquisition boards, with simultaneous acquisition from both. If any of of the components of the load cell are saturated during the first 10 samples taken, raw data is saved for further analysis. An average of the readings is saved for all data points. The Chell microdaq pressure transducer connects to the PC via an Ethernet cable, with data acquisition handled in 32-bit

Matlab using a Transmission Control Protocol/Internet Protocol object.

The process is fully automated for a given set of incidences, the PC control system running from a MathWorks Matlab script. It rotates the aerofoil to the prescribed incidences in turn and at each it checks the tunnel dynamic pressure, adjusting if necessary using a proportional-integral-derivative (PID) controller, then records this along with temperature, absolute pressure, incidence according to both motor and encoder and forces and torques from the transducers or pressures from the Microdaq transducer.

4.4 Tunnel speed measurement and calibration

Dynamic pressure difference across the tunnel contraction is measured using a Furness Controls FCO510 micromanometer, feeding into a PC via a serial port. The PC provides an output voltage to the tunnel's motor controller. Speed is controlled via a two-stage calibration. First, the desired velocity at the model is converted to an appropriate "contraction velocity" based on contraction dynamic pressure difference, using a calibration between the contraction static pressure tappings and a pitot-static tube mounted at the tunnel midspan in place of a model. This converted velocity is input to a PID controller to get the tunnel to the correct speed. The PID uses a second calibration between "contraction velocity" and tunnel motor controller input voltage.

Additionally, during surface pressure measurements, a pitot-static tube is mounted in the tunnel between the contraction and the aerofoil under test. This is connected to the pressure transducer used to measure the pressure tappings. Differences between speed measurements taken using the contraction tappings and micromanometer and those from the pitot-static and pressure transducer were monitored during experiments, with no significant differences noted.

4.4.1 Tunnel contraction to centreline pitot-static

This calibration was completed at least once per session of experiments, as little variation was noted in it within sessions (see Section 4.7) and it is time consuming to complete, requiring removal of test aerofoils. A pitot-static tube is mounted in the test aerofoil's place. The tunnel motor control voltage is set to a predetermined range of values in turn. At each, the tunnel

velocity is allowed to settle before the dynamic pressures are taken from the centreline pitot-static and the contraction, using two identical Furness Controls micromanometers (having been earlier calibrated to each other using two neighbouring centreline pitot-statics). The pitot-static readings are converted into velocities, while the contraction readings are converted into a pseudo-velocity, referred to here as the "contraction velocity". In order to obtain a true velocity from the contraction, the contraction ratio plus any residual correction factor would need to be applied to raw measurements. Instead, a calibration formula is calculated directly between the centreline and "contraction" velocities.

Variations between this calibration were as high as 3% between sessions, due to seasonal weather variations and soiling of the tunnel interior, see Section 4.7.

4.4.2 "Contraction velocity" to tunnel controller voltage input

This second calibration was completed with a test aerofoil in place. Again, the tunnel motor control voltage is set to a predetermined range of values in turn and after a period of settling, the "contraction velocity" is measured. The calibration was completed at 10° intervals between 0° and 90° as the changes in blockage with incidence affect the relationship between control voltage and tunnel velocity. The calibration must be completed for each experiment type (i.e. parings of aerofoils and tunnel configuration), though where blockage is low, the same calibration could be used for a range of experiments. For example, for the $c/H = 0.1$ aerofoil, one calibration was used for all tolerant tunnel configurations.

The PID is fed the desired real velocity and the incidence at which the reading is being taken by the main experiment control Matlab script, along with both speed calibrations. The real velocity is converted to a "contraction velocity" using the tunnel contraction to centreline pitot-static calibration. The PID controller code then selects the correct "contraction velocity" to tunnel controller voltage input calibration to use by reference to the incidence. Incidence is rounded down to its nearest multiple of 10. The calibration for the incidence given is used in the PID, with tunnel voltage adjusted until the desired "contraction velocity" is achieved.

"Contraction velocity" to tunnel controller voltage input calibrations did not need to be particularly accurate, and did not require repeating. As long as the tunnel contraction to centreline pitot-static calibration is accurate, the PID controller is able to set the tunnel speed to within any experimental error (see Section 4.7) of the desired velocity.

4.5 Experimental methods

4.5.1 Angles of attack

The angles of attack tested are given in Table 4.2. Beyond 25°, the incidences tested were the same across all sessions, but the coverage of attached flow incidences was improved over the course of the study. June 2014 - Dec 2015 sessions covered the force transducer OAR calibration of the tunnel (presented later in this chapter). Feb 2015(a) covered the pressure readings (presented here and in Ch. 5) and the force transducer experiments in the solid-walled tunnel of Ch. 5. Finally, Feb 2015(b) incidences were used for the force transducer tolerant tunnel experiments of Ch. 5. Asymmetrical aerofoils were tested at Feb 2015(b) incidences, positive and negative.

Session	Incidences tested (degrees)
June 2014	-2, 0, 2, 4, 6, 8, 9, 10, 11, 12, 13, 14, 15, 17.5, 20
Sept 2014, Dec 2015, Feb 2015(a)	-2, 0, 2, 4, 6, 8, 9, 10, 11, 12, 13, 14, 15, 16, 17, 18, 19, 20, 21, 22, 23, 24
Feb 2015(b)	-4, -3, -2, -1, 0, 1, 2, 3, 4, 5, 6, 7, 8, 9, 10, 11, 12, 13, 14, 15, 16, 17, 18, 19, 20, 21, 22, 23, 24
All sessions	every 5° from 25 to 160, then: 162.5, 165, 166, 167, 168, 169, 170, 171, 172, 174, 176, 178, 180, 182, 184

Table 4.2: Incidence ranges tested in different sessions of experimentation.

For symmetrical aerofoils, zero incidence is set roughly by the operator by lining up markers on the aerofoil end plates and tunnel walls. The data acquisition software then finds an accurate zero by running the tunnel and rotating the aerofoil through a narrow sweep of incidences, taking normal force data every 0.5°. The incidence at which zero normal force occurs is found using linear interpolation. This incidence finding run is conducted at a Reynolds number of 150 000 to ensure a linear lift vs. incidence curve near to $\alpha = 0°$ for the linear interpolation. The tunnel is switched off, the aerofoil rotated to that incidence, with all records of incidence in computer memory overwritten with zero and the counter on the optical

incidence encoder reset.

For asymmetrical aerofoils, automated zeroing is not possible as zero lift and zero incidence are not coincident. Instead, the chord line of the aerofoil was marked on the aerofoil endplates and lined up with the centreline of the tunnel manually.

4.5.2 Settling times, sampling times and frequencies

Analyses of data acquired continuously from immediately after an adjustment to aerofoil incidence, at the maximum possible sampling frequencies, were used to decide on suitable settling times, sampling times and sampling frequencies. Frequencies higher than the highest frequencies of the main vibrations induced in the rig were selected. Sampling times were selected to ensure numerous periods of the lowest frequencies of data fluctuations were captured, with settling times set to ensure any ramping to final measurement values were excluded from samples.

For the force and moment transducers, a sampling rate of 1000 Hz was used throughout, while for the pressure transducer 100 Hz was used. Both are far higher than any of the main frequencies in either data stream and were chosen instead with regards to the maximum sampling rate of the pressure transducer and limits imposed on data size by the PC and software used to control the experiment. For the sampling times used for each aerofoil size and Reynolds number, see Table 4.3. Since flows are slower for larger aerofoils the times tend to be longer, as the vibrations induced in the rig tended to have longer periods in lower speed flows. Times are also longer at incidences near to normal to flow, since readings are more unsteady here, with larger vibrations of longer periods induced in these conditions. When forces were being measured, the rig required some flexibility to prevent saturation of the transducers. When surface pressures were being taken, the force transducers were removed and the rig could be held stiffer, resulting in much lower levels of vibration and so shorter sample times.

Settling times were 5 s for force and 10 s for surface pressure experiments, plus the time required to run the tunnel velocity PID controller (variable, but a minimum of 5 s). Settling times were reasonably short as the maximum difference between neighbouring incidences in any test was 5°, meaning little movement in readings between them.

		Force measurements		Pressure measurements
Aerofoil c/H	Re	$45° \leq \lvert\alpha\rvert \leq 135°$	Other α	All α
0.1	60 000	120 s	60 s	
	150 000	60 s	30 s	
	250 000	60 s	30 s	
0.15	60 000	120 s	60 s	40 s
	150 000	90 s	30 s	20 s
	250 000	60 s	30 s	20 s
0.2	60 000	120 s	60 s	
	150 000	120 s	30 s	
	250 000	60 s	30 s	
0.25	60 000	120 s	120 s	60 s
	150 000	120 s	60 s	30 s
	250 000	90 s	60 s	30 s
0.3	60 000	120 s	120 s	
	150 000	120 s	60 s	
	250 000	120 s	60 s	

Table 4.3: Sampling times for force and pressure experiments.

4.5.3 Data processing

Since the transducers rotate with the aerofoil, forces normal and tangential to the aerofoil chord are measured, as is moment about the half chord. These are post-processed into lift, drag and moment about the quarter chord.

Drag is further processed by subtracting the tare drag force associated with the end plates, obtained by measuring the forces on them when the tunnel is run without an aerofoil present. Measurements were made at flow velocities of approximately 3, 9, 15, 21 and 42 m/s (roughly correlating to flow speeds used for the Reynolds number and aerofoil size pairings used in this study). With an aerofoil in place, tare drag for a reading was calculated by interpolating from these results, using the measured flow velocity for the reading.

For lightly loaded aerofoils, the tare force is likely to be overestimated at high incidences, where the separated flow of the aerofoil reduces the velocity over a large portion of the end plates, reducing the friction drag on them. When aerofoils are loaded highly enough to induce

bending in them, the upstream edges of the endplates encroach into the flow slightly, so the tare drag is likely to be underestimated. Tare drag is an insignificant proportion of total drag post-stall, with these under- or overestimates representing an even smaller proportion of the total, so no adjustment has been made for them.

Non-dimensional forces are calculated by dividing by the measured dynamic pressure from the micromanometer mounted across the contraction and the aerofoil planform area. Surface pressures are measured by comparison to the ambient static pressure. They are non-dimensionalised using dynamic pressure measured from a tunnel-mounted pitot-static.

4.5.4 Force and pressure transducer zeroing

An offset was taken at the start and end of each experiment using the force transducers. The start offset is taken after a period of settling following the setting of zero incidence. The loads placed on the sensors by the rig itself change with incidence and are not insignificant even with the system balanced as finely as it could be. As such, each offset consists of a separate zero reading at 10° intervals across the range of incidences tested in the experiment.

The differences between the start and end offsets are not insignificant at low Reynolds numbers (see Section 4.7). These are time-apportioned across the experiment to give a time-specific local offset for each reading taken. An incidence-specific sensor zero is then interpolated from the local offset using the incidence at which the reading was taken.

For the asymmetrical aerofoils, balancing the system for accurate readings over a full 360° incidence sweep proved impossible at low Reynolds numbers due primarily to offset creep. The longer time the experiments took and the greater range of zero-flow loads on the sensors both had a negative impact on the performance of the offsetting methods. Incidences were instead tested over shorter runs and blended in post-processing, see Ch 5.

For pressure readings, the Chell microdaq was zeroed at the beginning of each experiment. Some preliminary testing zeroed it before each reading but no significant improvement in accuracy was noted and experiments took considerably longer, requiring the flow of the tunnel to be shut off for each zeroing.

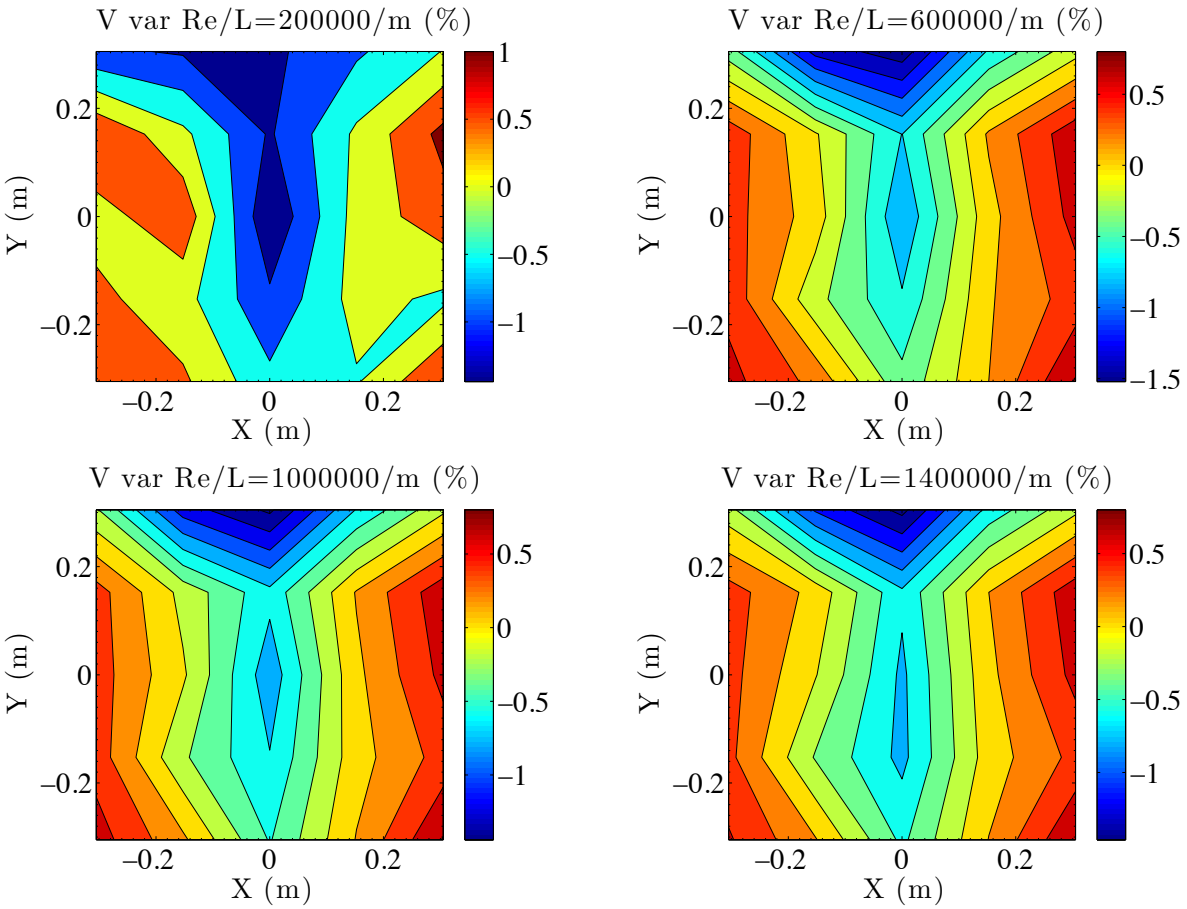


Figure 4.10: Flow velocity variation from mean stream-wise velocity across the test section, for the solid walled tunnel.

4.6 Cross-flow uniformity of the new 3' × 3' test section

Cross-sectional flow uniformity has been measured for the tunnel with solid walls in place (Fig. 4.10) and with double-slatted walls with an OAR of 0.71 (Fig. 4.11). Measurements were conducted using a pitot-static tube mounted at various points across the tunnel test section, at a range of flow velocities, presented here non-dimensionalised as Re/L. No significant variations in flow patterns with increasing velocity were noted at $Re/L > 1.4 \times 10^6$. For the smallest aerofoil used in the study, with $c/H = 0.1$, Reynolds numbers are approximately equal to $(Re/L)/10$. The plots in Figs 4.10 and 4.11 show the percentage variation from the mean flow velocity. Note that the plots extend to ±0.305 m in the x and y directions because this was the limit of measurements (the tunnel itself extends to ±0.458 m, having a 0.915 m × 0.915 m cross-section).

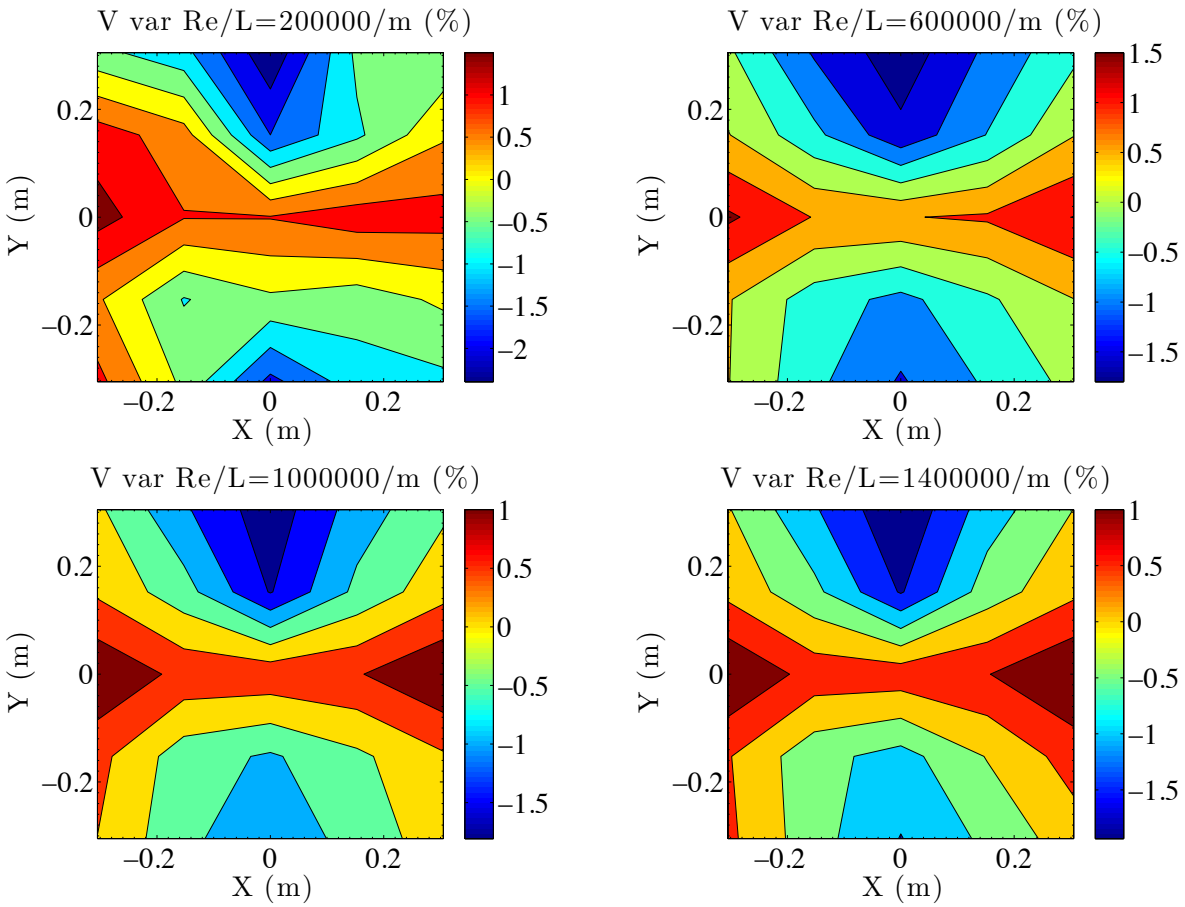


Figure 4.11: Flow velocity variation from mean stream-wise velocity across the test section, for the tolerant tunnel, DS-71 configuration.

In both tunnels, flow uniformity is near-independent of the velocity, other than at the lowest speed, where the uniformity drops off. Ideally, velocities should be within 0.25% of the mean flow in the "working range" of the jet [44], here the region around the line $x = 0$, as this is where the aerofoil is mounted. Both tunnel configurations compare poorly to this limit, but the new tolerant test section is not significantly worse that the original, solid-walled tunnel.

Note that measurements for both configurations will have been affected by the rig used to hold a pitot-static tube to take the flow uniformity readings. The rig consisted of three 10 mm diameter steel rods stretching the full width of the tunnel, two mounted vertically at approximately $x = 0$ and $x = -0.1$ m on the uniformity plots and the third mounted horizontally at the height at which readings were being taken.

4.7 Errors, accuracy and repeatability

The accuracy of readings taken with the apparatus is limited by a number of factors. The impact of these on results have been measured, with an overall error estimate calculated and presented in Fig. 4.12, along with a measured maximum error. The analysis is presented for drag and moment for the $c/H = 0.1$ NACA 0015. Estimated lift error is near identical to drag, with slightly lower measured errors. The measured error is the maximum variation of raw experimental data from averages (results for each of the Reynolds numbers at which this aerofoil was tested are the averages of at least four separate runs of the experiment). Angles around the stall at approximately 10° and 170° and where the trailing edge is pointing upstream (at incidences near 180°) have been omitted from the measured error calculation, as variations between runs are not necessarily the result of experimental error here.

Force transducers have been factory-calibrated within the last two years where they were rated with a 95% confidence level to within 1% for force measurements and 1.5% for torque measurements. Recent checks performed on them found no significant deterioration in this performance. They have a resolution of 0.0125 N for forces and 7.5×10^{-4} Nm for moments, the resolution plots in Fig. 4.12 are non-dimensionalisations of these figures based on typical dynamic pressures for the Reynolds numbers tested and the planform area of the $c/H = 0.1$ aerofoil.

Offsets are taken for the transducers at the start and end of each run of the experiment, with differences between the two time-apportioned across the experiment to give local offsets for each reading. The maximum offset difference is the maximum creep between the two offsets taken for each Reynolds number, non-dimensionalised in the same way as the resolutions.

A Reynolds number independent error results from the tunnel flow velocity measurement used to non-dimensionalise the forces measured by the transducers. The velocity is calculated from the pressure drop across the tunnel contraction ahead of the test section, using the two-stage calibration described in Section 4.4. Measurements are subject to errors resulting from variations in atmospheric conditions and the boundary layer of the tunnel. A new calibration between a tunnel centreline pitot-static tube, mounted at the model mounting point, and the contraction was conducted before each bloc of experiments (each lasting around three weeks, with four blocs conducted between June 2014 and February 2015). There are variations of over

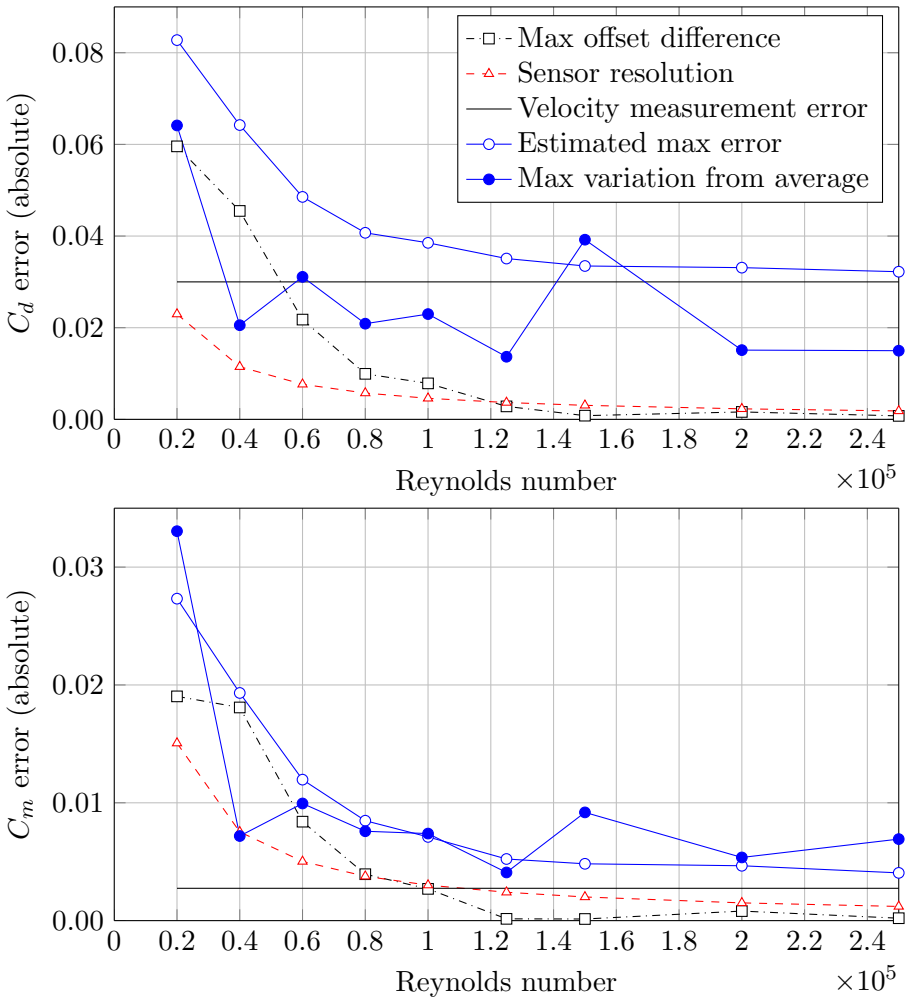


Figure 4.12: Estimated and actual maximum errors for C_d (top) and C_m (bottom) vs Re.

3% between these calibrations, resulting from seasonal weather variations and soiling to the tunnel interior surfaces (from flow visualisation seeding aerosols used by other tunnel users). For the last bloc of experiments a calibration was conducted at the beginning and end of the bloc, with maximum differences of approximately 1% noted between the two. Given the lack of significant variation in weather or tunnel surface cleanliness, this is taken as a fair estimate of the velocity measurement error. The resulting maximum experimental error to drag and moment coefficient is around 0.03 and 0.003 respectively, once the velocity measurement is squared for the non-dimensionalisation.

Total experimental error is estimated using the formula:

$$\frac{1}{2}(\text{offset error}) + \text{resolution error} + \text{velocity error} = \text{total error} \tag{4.1}$$

with the offset error being halved as a conservative estimate of the maximum impact on any one reading, given the time-apportionment of the offset difference across an experiment. Estimated errors show a strong correlation to the maximum variation from averages, see Fig. 4.12, suggesting the main sources of error in the experiment have been accounted for. There are other experimental errors resulting from, for example, vibrations in the system but these are smaller than those analysed here and have been ignored in the estimation.

Maximum absolute errors are presented in Fig. 4.12, which usually occur at maximum lift, drag or moment. The percentage errors here are taken as a fair approximation of maximum percentage errors for all readings, see Table 4.4, other than those where measurements are low, i.e. for drag or moment where flow is attached.

Reynolds number		
$c/H = 0.1$	$c/H = 0.2$	Error (%)
20 000	40 000	4.40
40 000	80 000	3.40
60 000	125 000	2.60
80 000	150 000	2.15
100 000	200 000	2.05
125 000	250 000	1.85
150 000	300 000	1.80
200 000		1.75
250 000		1.70

Table 4.4: Estimated maximum percentage error for force and moment readings.

To demonstrate the strong repeatability of experiments, Fig. 4.13 shows the average results from the tolerant tunnel for the $c/H = 0.1$ NACA aerofoil at $Re = 150\,000$, as presented later in Figs 5.3 - 5.6. Plotted alongside are the raw results of the five separate experimental runs used in the calculation of the averages.

Tolerant tunnel results for the $c/H = 0.1$ NACA 0015, used to prepare Fig. 4.12, benefit from the improvements to methodologies described later in Section 5.2.1. The accuracies

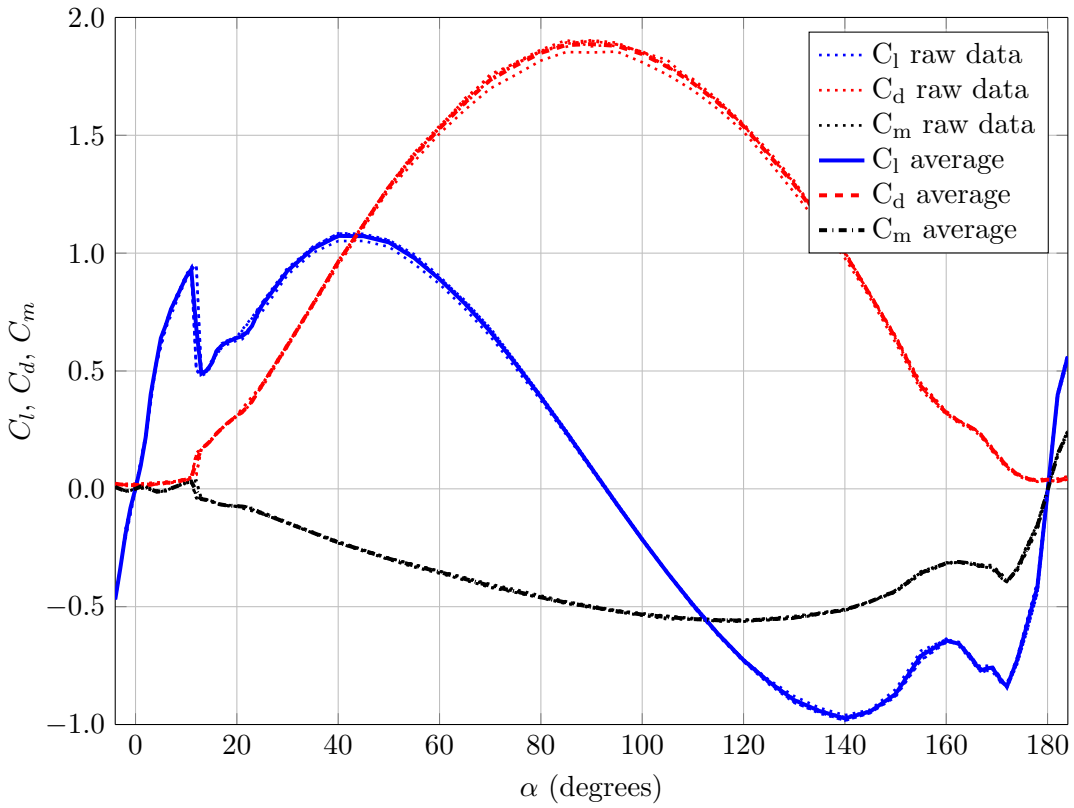


Figure 4.13: C_l, C_d and C_m vs α for the NACA 0015 from the tolerant tunnel at $Re = 150\,000$, raw runs and averages.

of the tolerant tunnel OAR calibration experiments (Section 4.8) and solid-walled tunnel experiments on the $c/H = 0.1$ NACA 0015 (Section 5.3) will be lower due to insufficient settling times, though this is only significant at lower Reynolds numbers, as described in Section 5.2.1.

For the $c/H = 0.2$ aerofoils presented in Ch. 5, velocity measurement errors will be identical to those in Fig. 4.12. The transducer errors, being absolute, will shift to the right on the plots as the larger aerofoils require a flow velocity half that of a $c/H = 0.1$ aerofoil for the same Reynolds number. The planform area is twice that of the $c/H = 0.1$ aerofoil, so measured forces are around half that of the smaller aerofoil, since $F = C_F \frac{1}{2}\rho U^2 A$. The transducer accuracies for $Re = 40\,000$ for $c/H = 0.2$ aerofoils are therefore roughly equal to those for $Re = 20\,000$ for $c/H = 0.1$ aerofoils, those for $Re = 80\,000$ roughly equal to those for $Re = 40\,000$ and so on, see Table 4.4. Accuracies for aerofoils of other sizes used in the tunnel OAR calibration are similarly affected.

For pressure readings, the only measurable error is that due to the velocity measurement. The Chell microdaq is factory rated to an accuracy of 0.05% of full scale. Comparisons were made between the microdaq and the Furness Controls micromanometer (itself factory rated to 0.025% of full scale) used for measurement of the pressure differential across the contraction, using two neighbouring pitot-statics near to the tunnel centreline, with one attached to each. Differences between the measured velocities were low, less than 0.8% (and less that 0.46% for velocities greater than 4 m/s). Though this gives increased confidence in the output of both devices, without a suitable reference flow to compare them against, no further comment can be made on the accuracy of either. Note that errors due to the micromanometer are incorporated in the velocity measurement error.

4.8 Tolerant tunnel OAR calibrations

The tunnel OAR has been calibrated using force and surface pressure measurements at Reynolds numbers of 60 000, 150 000 and 250 000. Calibrations were completed initially for forces at $Re = 150\,000$, for the double slatted wall tunnel at OARs of 0.5, 0.55, 0.59, 0.63, 0.67, 0.71 and 0.75 (denoted DS-50, DS-55 etc.) and for the single slatted wall tunnel at 0.71, 0.79, 0.83, 0.88 (SS-71, SS-79 etc.). The single slatted wall tunnel was abandoned as being unsuitable for post-stall aerofoil testing early on. Promising configurations of the double-slatted tunnel, namely the DS-67, DS-71 and DS-75 were selected, with force calibrations at $Re = 60\,000$ and 250 000, and surface pressure calibrations at all three Reynolds numbers, focussing on these three configurations.

The methods used to calibrate the tolerant tunnel by Parkinson and his students Hameury [54] and Williams [12] are described and critiqued in Section 4.8.1. The methods of the current study are then presented in turn. In Section 4.8.2, comparisons of plots of lift, drag and moment coefficients against incidence for the five NACA 0015 aerofoils are made. All aerofoils are shown on the same axes, with a plot produced for each tunnel configuration, at each Reynolds number tested. Surface pressures against normalised chord are presented for the tapped aerofoils, again on the same axes for each tunnel configuration and Reynolds number, in Section 4.8.3.

Some use is made of Hameury's methods: those used for his flat plates can sensibly

be applied to stalled aerofoils, though they are only suitable for analysis of results for a single angle of incidence at a time. Plots of C_d against OAR for the aerofoils at 90°, and suction surface C_p against OAR, are compared to Hameury's plots for his flat plate models in Section 4.8.4.

New methods designed to judge the performance of the tunnel at multiple incidences, based on consistency of results across the range of aerofoil sizes, are presented in Section 4.8.5 for force measurements and Section 4.8.6 for surface pressure measurements.

4.8.1 Parkinson's calibration techniques

The original single-slatted wall configuration of Parkinson's tunnel was designed for testing aerofoils with attached flows. Parkinson's student Williams calibrated the tunnel OAR by comparing the lift curve slopes for aerofoils with different c/H ratios at each OAR tested [12]. The OAR giving the most consistent lift curve slopes across the model sizes was judged to be the most effective at reducing blockage. Note that in free air, lift curve slope would be independent of model size should all other conditions remain the same. Testing used NACA 0015 aerofoils with c/H of 0.17, 0.34, 0.51 and 0.67, and Clarke-Y aerofoils with c/H of 0.25, 0.39, 0.53 and 0.66.

As mentioned in Section 3.3, Hameury calibrated the double-slatted wall configuration by testing different sized flat plates, plus circular cylinders and circular cylinders with splitter plates [54]. The flat plates had c/H ratios of 0.083, 0.194 and 0.333, while both cylinder types had d/H ratios of 0.083, 0.138, 0.25 and 0.333. As with the single-slatted wall tunnel, the best OAR was selected based on that which gave the most consistent results for the different sized models.

Drag coefficients, Strouhal numbers and representative pressure readings of like models were compared at each OAR. For the flat plates, the suction surface C_p was compared, while for the cylinders C_p at a selection of angular positions were used. Full pressure distributions for the models were also compared at each OAR.

Two other variables, a "blockage correction factor" and a standard deviation associated with the calculation of this factor, were also compared. These are calculated using the linear regression method of Flay et al. [82], used for comparing model car pressure distributions obtained in different slotted-walled wind tunnel configurations with an equivalent reference

pressure distribution obtained in a low-blockage, solid-walled facility. The blockage correction factor is that by which results from the tunnel are divided to give agreement to a reference-test pressure distribution. The standard deviation is a measure of residual errors in the corrected pressure distribution.

In this study, testing covers incidences where flow is attached, and where flow is separated. In both regimes, a range of incidences are tested. It was found that neither Williams's nor Hameury's methods were ideal for calibration, since they focus on only attached or separated flow respectively. The c/H range used here, 0.1 - 0.3, is shorter than that of Williams's (0.17 - 0.67). Trends in lift curve slope are less consistent and harder to draw conclusions from over this shorter range, as is evidenced in results for Williams's smaller aerofoils [12]. For these reasons, results using it are not presented here.

The regression analysis of Flay et al. was not used as there are no suitable low-blockage reference datasets available to use in calculations. Flay et al. worked with three-dimensional car models, for which very low tunnel blockage is more easily achieved than for two-dimensional aerofoils, due to the smaller blockage ratios that can be practically obtained. The calculations of Section 2.2.3 and Appendix C show that a $c/H < 4.5\%$ is required to limit blockage corrections to 5% of the readings taken. This would need a prohibitively small aerofoil and is still far from a suitable reference dataset. Instead, a new measure based on standard deviation from a mean, rather than a reference, has been developed to assess how consistent results for a range of model sizes are using a given tunnel configuration for testing, see Section 4.8.5 .

4.8.2 Force measurements for the five NACA 0015 aerofoils with various tolerant tunnel OARs and solid tunnel walls

Force measurements have been conducted using a wide range of tunnel configurations, initially at a Reynolds number of 150 000. SS-71, SS-79, SS-83 and SS-88 configurations were used. Though OARs are higher than the 0.6-0.7 identified by Williams as optimal for testing of aerofoils at moderate incidences [12], it was thought that these would be necessary to accommodate the larger blockage of stalled aerofoils. DS-50, DS-55, DS-59, DS-63, DS-67, DS-71 and DS-75 were selected based on promising configurations from Hameury's original development work on the tunnel [54] (see Figs 4.21 and 4.22 for his results) and the preliminary experiments described in Ch. 3.

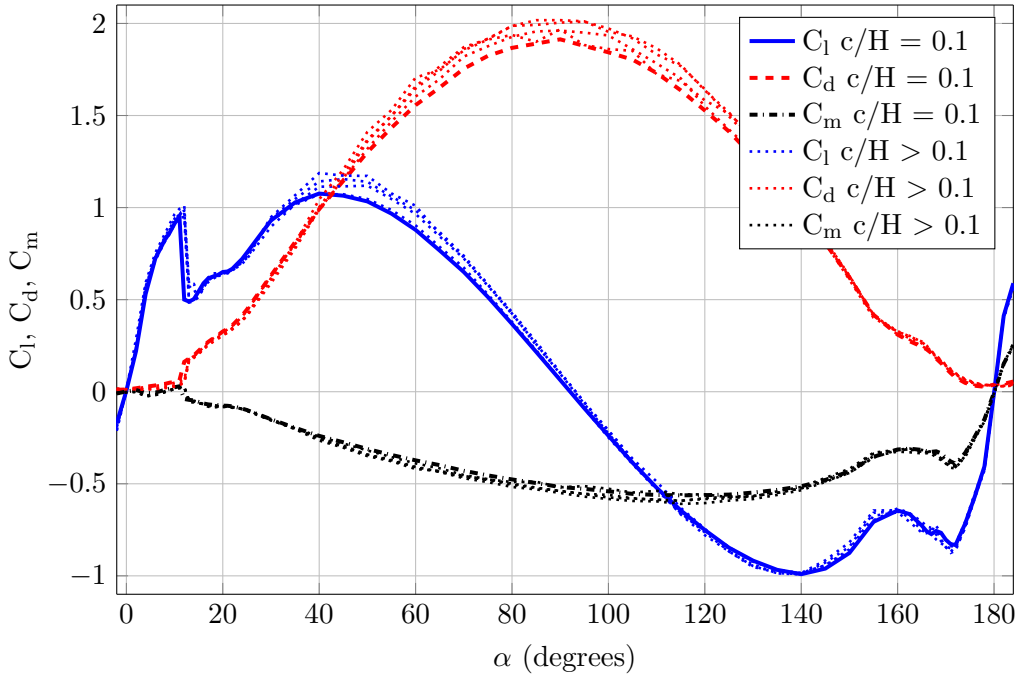


Figure 4.14: C_l, C_d and C_m vs α for $c/H = 0.1$, 0.15, 0.2, 0.25 and 0.3 NACA 0015 aerofoils taken in the tolerant tunnel, DS-67 configuration at $Re = 150\,000$.

Following this, analysis of the results identified three tolerant tunnel configurations, the DS-67, DS-71 and DS-75, as particularly strong performers in terms of their abilities to give consistent data for the five different sized aerofoils. Force measurements were extended to Reynolds numbers of 60 000 and 250 000, but using only the promising tolerant tunnels and the solid-walled tunnel. Results are presented here for the DS-67, DS-71 and DS-75 tunnels (see Figs 4.14 - 4.16) and the solid-walled tunnel, both as raw data (Fig. 4.17) and after the application of blockage corrections (Fig. 4.18). The other configurations tested at $Re = 150\,000$ and results taken at other Reynolds numbers are presented in Appendix D, see Figs D.1 - D.19. Results for the $c/H = 0.1$ aerofoil represents the nearest thing to a low blockage benchmark. As such, plots for it are thicker and of different line styles than those of the other aerofoils. c/H ratios larger than 0.1 are plotted with the same line styles and thickness.

For $Re = 150\,000$, 12 tunnel configurations were tested with each of the five aerofoils, giving 60 experiments at this Reynolds number. For $Re = 60\,000$ or 250 000, 4 tunnel types were used giving 20 experiments at each. This gives a grand total of 80 experiments for the force transducer OAR calibrations. For initial assessment of the OARs, at least one run was

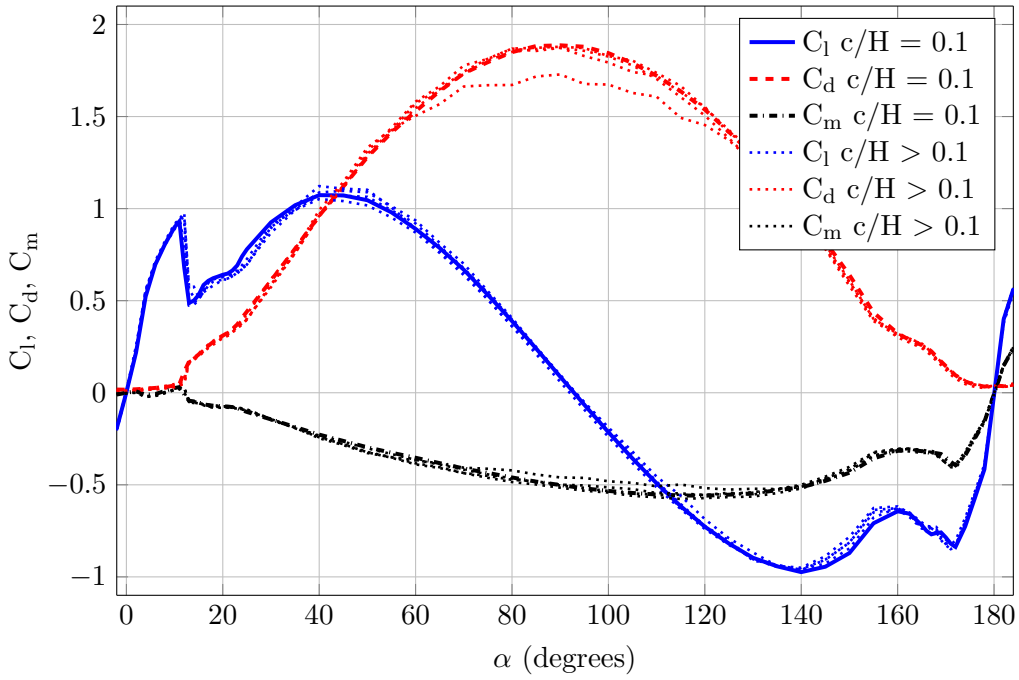


Figure 4.15: C_l, C_d and C_m vs α for c/H = 0.1, 0.15, 0.2, 0.25 and 0.3 NACA 0015 aerofoils taken in the tolerant tunnel, DS-71 configuration at $Re = 150\,000$.

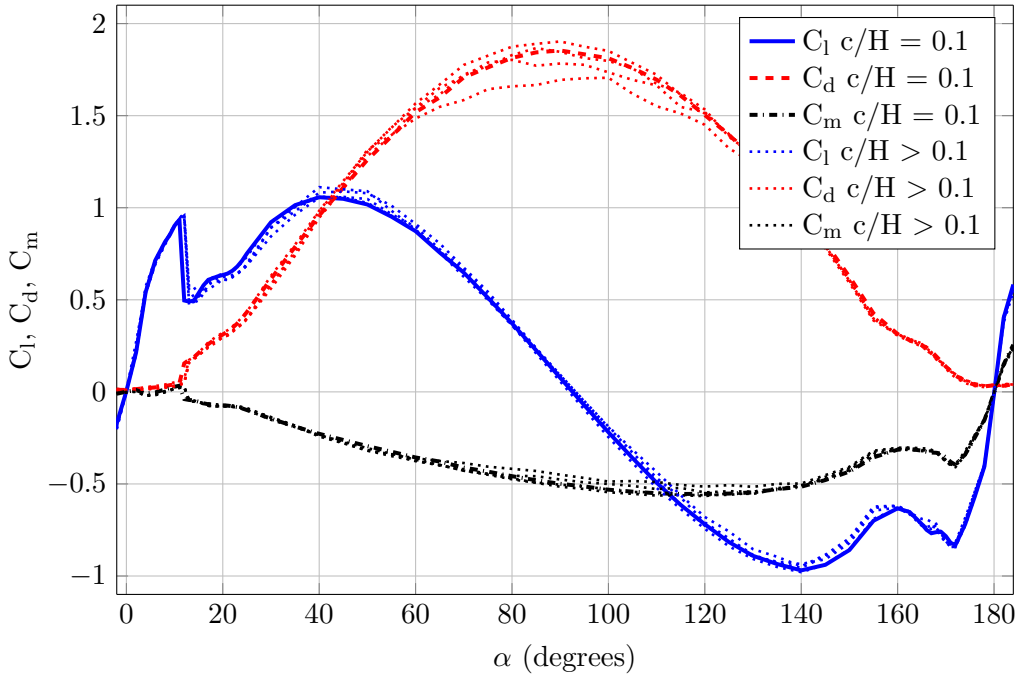


Figure 4.16: C_l, C_d and C_m vs α for c/H = 0.1, 0.15, 0.2, 0.25 and 0.3 NACA 0015 aerofoils taken in the tolerant tunnel, DS-75 configuration at $Re = 150\,000$.

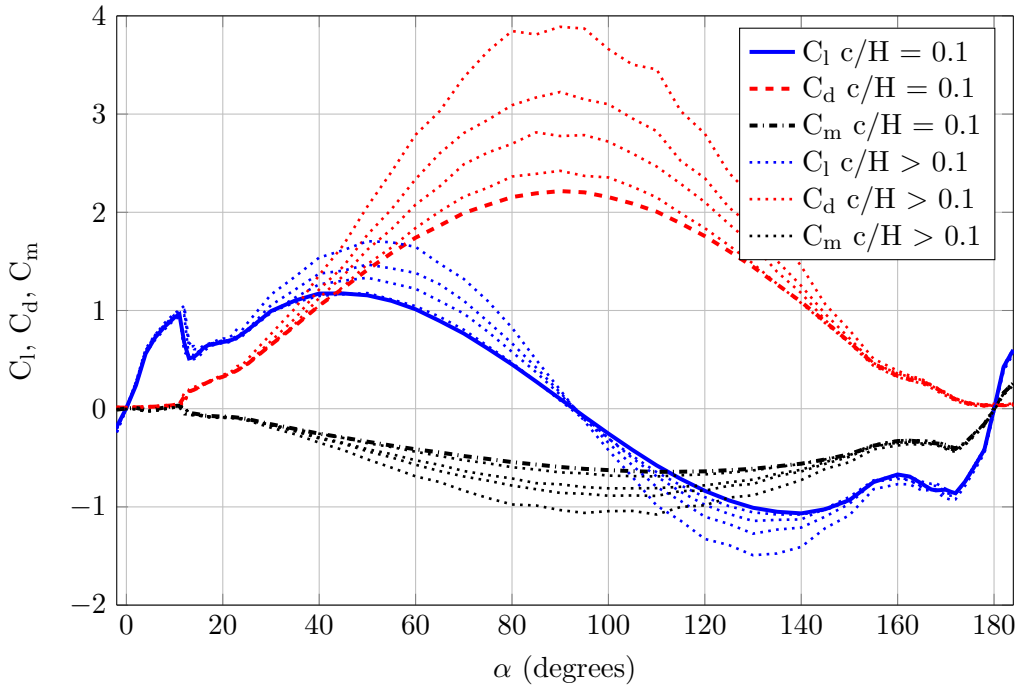


Figure 4.17: C_l, C_d and C_m vs α for $c/H = 0.1$, 0.15, 0.2, 0.25 and 0.3 NACA 0015 aerofoils taken in the solid walled tunnel at $Re = 150\,000$.

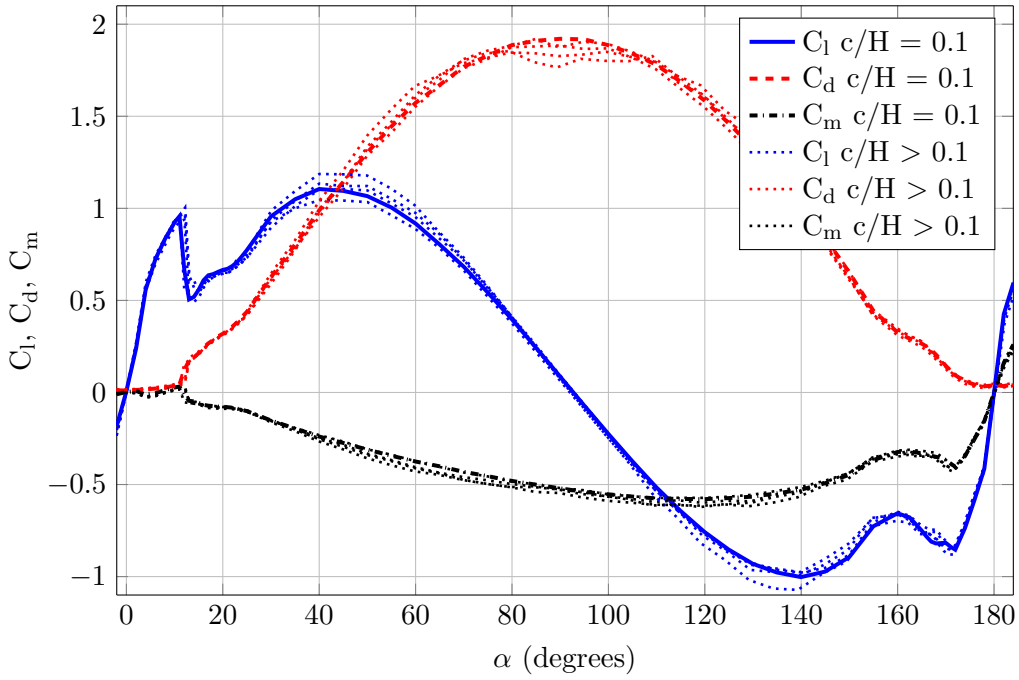


Figure 4.18: C_l, C_d and C_m vs α for $c/H = 0.1$, 0.15, 0.2, 0.25 and 0.3 NACA 0015 aerofoils taken in the solid walled tunnel at $Re = 150\,000$, ESDU corrections.

conducted for each of the experiments, with force, tunnel flow and atmospheric data recorded at incidences between $-2°$ and $184°$ at the intervals in Table 4.2 for June, September and December sessions. Once the promising tunnel configurations were selected, further runs were conducted to ensure all experiments in the DS-67, DS-71, DS-75 and solid tunnels had been run at least twice, unless otherwise specified below. The values shown in the plots presented here are averages of all the runs for that particular experiment.

The following experiments had only one run conducted: the $c/H = 0.15$ and 0.3 aerofoils at $Re = 60\,000$, the $c/H = 0.15$ aerofoil at $Re = 150\,000$ and the $c/H = 0.15$, 0.2 and 0.3 aerofoils at $Re = 250\,000$, all in the DS-67 tunnel. This was due to time constraints on wind tunnel time. By the final few sessions of experiments, Figs 4.29 - 4.31 had been compiled, showing that the choice between the DS-67, DS-71 and DS-75 tunnels was somewhat arbitrary. It was therefore decided to focus efforts on the experiments detailed in Ch. 5 rather than to repeat these runs. In any case, results from the tunnel demonstrate strong repeatability, see Section 4.7 for an analysis of this for the $c/H = 0.1$ aerofoil at $Re = 150\,000$ in the DS-71 tunnel.

For the $c/H = 0.1$ aerofoil at $Re = 250\,000$ in the DS-67 tunnel, saturation of the force transducers occurred at incidences of $50°$, $55°$, $135°$ and $140°$ on all experiment runs, in spite of adjustments being made to the rig between runs to attempt to avoid this. Runs for the $c/H = 0.1$ aerofoil at $Re = 250\,000$ required the fastest flows in the tunnel and induced large forces on the transducers. Time constraints prevented further refinement of the rig to obtain reliable data at these incidences. Instead, results for those angles for the $c/H = 0.1$ aerofoil have been omitted from the DS-67 plot in Fig. D.12.

4.8.3 Surface pressures for the two tapped NACA 0015 aerofoils with various tolerant tunnel OARs and solid tunnel walls

Surface pressure measurements at all three Reynolds numbers were conducted in the DS-67, DS-71 and DS-75 tolerant tunnel configurations, as well as the solid walled tunnel. The $c/H = 0.15$ and $c/H = 0.25$ aerofoils are equipped with surface pressure taps, mostly located at the mid-span, with some at each quarter span to check for two-dimensionality of results. Other than in the immediate vicinity of stall (approximately $2°$ of incidence immediately after the stall angle), very little difference was noted between tappings on the three span-wise

locations at equal chord-wise locations. Therefore, no quarter-span results are presented here.

The larger aerofoil has more tappings as it was not practically possible to fit as many in the $c/H = 0.15$, and some tappings failed to survive the manufacture process, see Section 4.2.3. As a stand-alone experiment, the smaller aerofoil contains insufficient tappings for good reproduction of surface pressure distributions. However, the tappings are sufficient for the purposes of this study, where comparisons are made between the results for the two aerofoils to judge tunnel performance.

Unless otherwise specified below, two runs were taken for each of the experiments conducted: the two aerofoils, three Reynolds numbers and four tunnel configurations giving a total of 24 experiments. In each run, surface pressures and tunnel flow and atmospheric information was collected at the incidences from Table 4.2, for the February (a) session experiments. Each pair of runs was then processed to give the final data set by averaging results for each pressure tapping across the two runs.

There were two exceptions to this. Three runs were taken for the $Re = 60\,000$ experiment in the DS-71 tunnel for the $c/H = 0.25$ aerofoil. Differences beyond those expected due to experimental error (see Section 4.7), around 5-6% at post-stall lift and drag peaks, were found between the first two runs. A third run was conducted using longer sampling times (see Table 4.3 for normal sampling times used). The surface pressures of this third run lay between the results of the first two runs. The final data set was based on an average of all three runs.

Two runs were conducted for the $c/H = 0.15$ aerofoil in the DS-71 configuration at $Re = 60\,000$, $150\,000$ and $250\,000$, but the first runs at all three Reynolds numbers were taken with a flawed zero incidence finder code (see Section 4.5.1) that set the zero at a slightly positive angle of 0.35°. This error was not spotted until post-processing of data after the dismantling of the rig. The single runs taken with correctly set incidences were used for the final data sets.

Results are presented in Figs 4.19 and 4.20 for the DS-67, DS-71, DS-75 and solid-walled tunnels for $Re = 150\,000$ experiments. Equivalent results for the DS-67 and DS-75, and for all configurations at $Re = 60\,000$ and $250\,000$ are included in Appendix D, see Figs D.21 - D.30. The figures show pressure coefficient plotted against normalised chord-wise location, at $\alpha = 0°$, 10° (8° for $Re = 60\,000$), 45° and 90°.

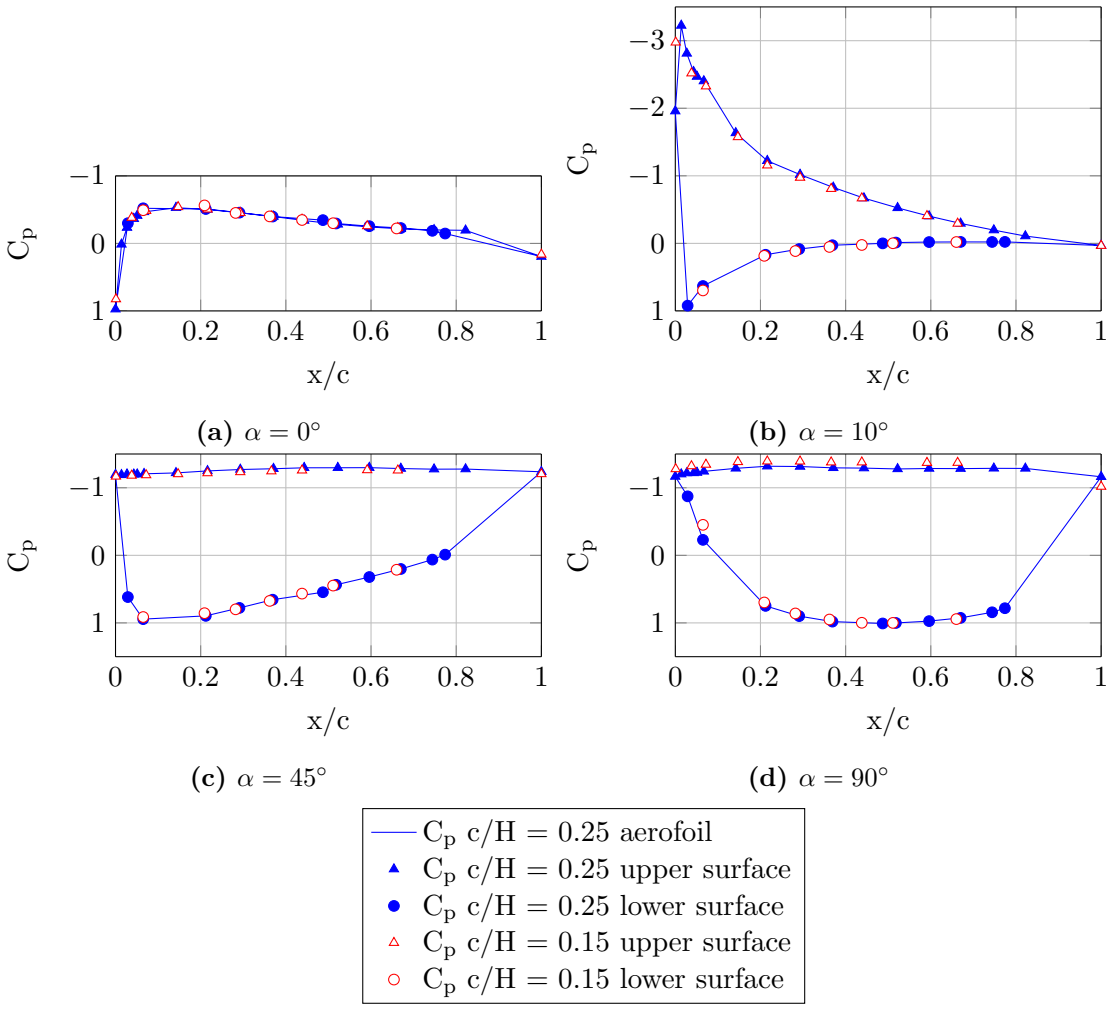


Figure 4.19: C_p plotted against normalised chord-wise position for the $c/H = 0.15$ and $c/H = 0.25$ NACA 0015 aerofoils at $Re = 150\,000$ in the DS-71 tolerant tunnel.

All of the tolerant tunnels perform similarly well, with excellent agreement of pressure distributions for the two aerofoils. For attached flow ($\alpha = 0°$ and 10°, or 8° for $Re = 60\,000$), the results are also similar for the solid-walled tunnel, with small differences notable for $\alpha = 8°$ or 10°. Post-stall (at $\alpha = 45°$ and 90°) the differences between the tolerant configurations and the solid-walled tunnel are much larger.

These differences are primarily on the suction surface of the aerofoil. The pressure surface, at normalised chord-wise positions of 0.2 - 0.8, is almost entirely insensitive to blockage. Regardless of aerofoil size or tunnel type, pressure surface pressure coefficients are near-equal. The suction surface results display a proportionality with OAR, see Section 4.8.4 for an analysis of the relationship at $\alpha = 90°$ in the tolerant and solid-walled tunnels.

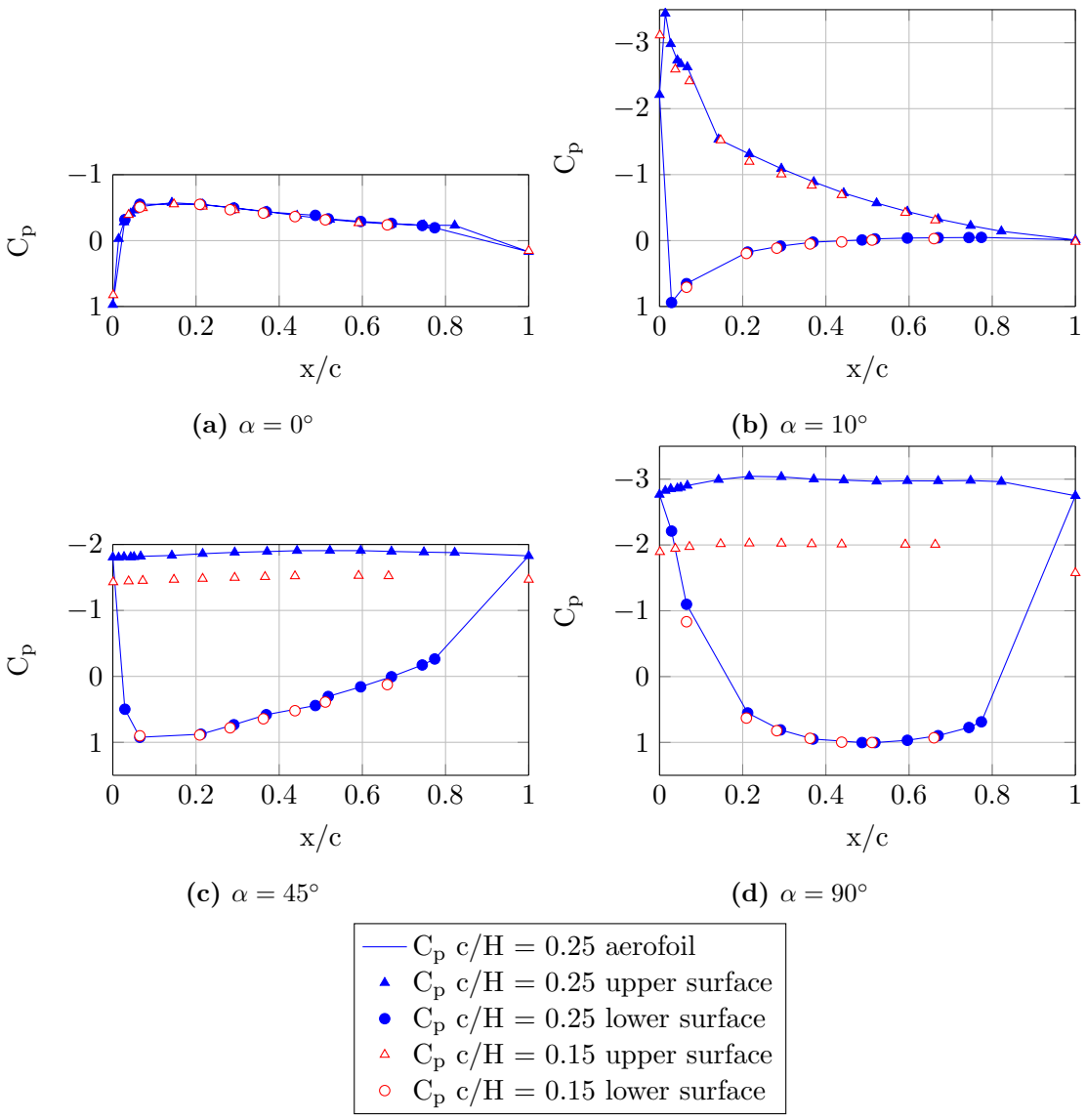


Figure 4.20: C_p plotted against normalised chord-wise position for the $c/H = 0.15$ and $c/H = 0.25$ NACA 0015 aerofoils at $Re = 150\,000$ in the solid walled tunnel.

Section 4.8.6 assesses the relationship between OAR and a new measure developed for pressure distribution similarity between the $c/H = 0.15$ and 0.25 aerofoils. Fig. 4.32 shows $c/H = 0.15$ pressure distributions for the DS-67, DS-71 and DS-75 tunnels on the same axes, highlighting how insensitive to OAR variations results are in this range of OARs.

Note that the ESDU corrections used in this study provide no means of correcting surface pressures affected by blockage [10]. Maskell's method (Section 2.1.6) does allow for this [47], but the collapse of the two aerofoils' pressure distributions is not as good as that provided by

the tolerant tunnel and is not analysed further here.

4.8.4 Hameury's methods: C_d and C_p measurements at $\alpha = 90°$

Fig. 4.21 shows C_d at 90° against OAR for the various double-slatted wall tunnel configurations tested at $Re = 150\,000$. It contains corrected results for the solid-walled tunnel plotted at OAR = 0.3. The corrected results are shown with unfilled shapes at data points. Also included are Hameury's results for flat plates [54] taken at $Re = 100\,000$. It can be seen that the DS-67, DS-71 and DS-75 configurations are the best for $Re = 150\,000$. For the DS-71 tunnel, results are particularly promising for aerofoils with c/H of 0.1 to 0.25, differences between them being within the range attributable to experimental error (1.8% at Re = 150 000, see Section 4.7). Notably, the DS-71 is better than the corrected solid tunnel.

Similar analyses were conducted at $Re = 60\,000$ and $Re = 250\,000$ for the limited range of configurations tested at these Reynolds numbers (the solid-walled, DS-67, DS-71 and DS-75 tunnels). The DS-71 and DS-75 both perform well for $c/H < 0.3$, better than the solid corrected tunnel, at $Re = 250\,000$. For $Re = 60\,000$ the best tunnel is less obvious. The C_d values for the five aerofoils are similarly spread for all the tolerant tunnel configurations and the corrected solid tunnel, suggesting they all reduce the impact of blockage on drag equally effectively.

Fig. 4.22 replicates Hameury's work on flat plates by using the results for the tapped aerofoils at 90°. The "Suction surface C_p" is based on an average of the C_p of the tappings from approximately 20% of chord to 80% of chord on that surface. Refer to Figs 4.19 and 4.20 and Figs D.21 - D.30 for the pressure distributions at 90° from which these plots were calculated. Hameury's results [54] for the suction surface pressures of his flat plates are also included, taken at $Re = 100\,000$.

For $Re = 150\,000$ the DS-75 tunnel gives the most consistent results for the two tapped aerofoils. The DS-75 was also best for $Re = 60\,000$ while for $Re = 250\,000$ the DS-71 was better. For all Reynolds numbers, the average suction surface C_p is in the range -1.2 to -1.5, similar to Hameury's flat plates with $c/H < 0.33$. In all tunnel configurations, differences between the suction surface C_p remain larger than the experimental error associated with the pressure measurements (approximately 1%).

The best OARs for C_d and C_p consistency are higher than the 0.63 selected by Hameury.

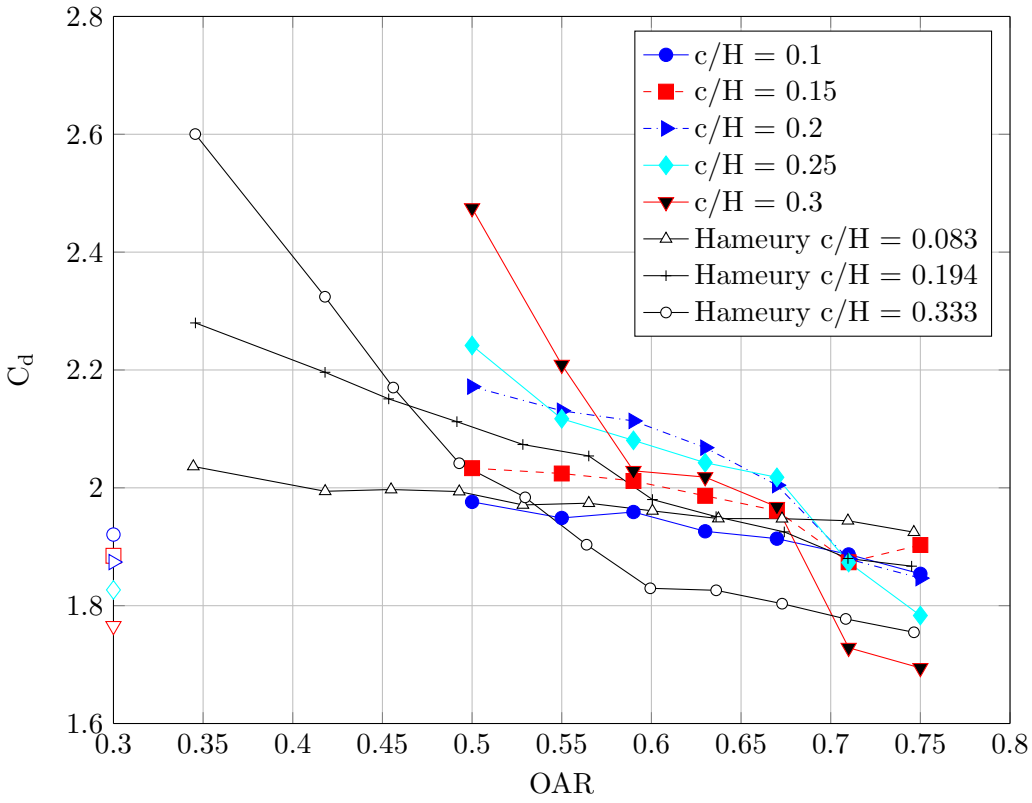


Figure 4.21: Variation of C_d at 90° as a function of OAR for five NACA 0015 aerofoils, $Re = 150\,000$, double slatted wall tunnel configurations (corrected solid-walled results are also shown, with unfilled markers, at OAR = 0.3), alongside Hameury's results for normal flat plates [54].

Differences between Hameury's results and those of the current study are likely due to the differences between the experiments. Flat plates have larger wakes than aerofoils at 90°, and Hameury's tunnel has an L/H of 2.67, while Imperial's is 2.38.

Through use of side wall (i.e. the walls without plenum chambers) pressure readings and by varying model position along the tunnel, Hameury found that test section length can be a limiting factor on tunnel performance for large c/H [54]. This is due to pressure recovery not being fully achieved at the end of the test section. It is likely that tunnel length also impacts on normal operation of the tunnel with smaller models, as other researchers have found.

A Parkinson-style tunnel was developed for boundary layer experiments at the UK's Building Research Establishment, with slatted side walls and ceiling. During development of the tunnel, it was found that their L/H of 1.02 was insufficiently small. Numerical modelling

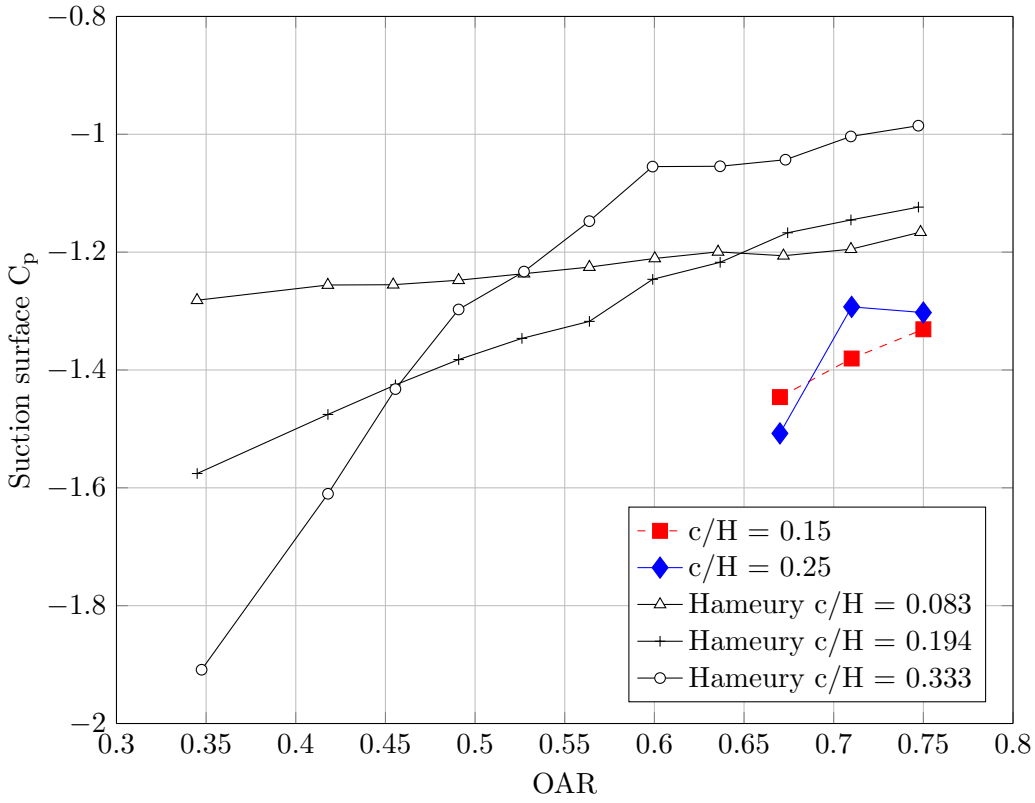


Figure 4.22: Variation of suction surface C_p at $\alpha = 90°$ as a function of OAR for the two pressure tapped NACA 0015 aerofoils, $Re = 150\,000$, double slatted wall tunnel configurations, alongside Hameury's results for normal flat plates [54].

suggested a value of around 3 was optimal [76].

A Parkinson single slatted wall tunnel test section was built for a 2.4 m × 2 m tunnel at the University of Sydney. During the calibration of the tunnel for a 25% blockage half cylinder mounted to the wall opposite the plenum chamber, the L/H ratio was varied. A value of 2.50 was found to be optimal for blockage reduction, but values longer than this as well as shorter were found to sub-optimal [83]. The longer plenums resulted in flow entering the plenum chamber upstream and independent of the model. The cause of this behaviour was unexplained, though it was thought to result from negative wake pressure downstream of the model drawing flow out of the plenum there. It was suggested that the impact of longer tolerant tunnels on results can be compensated for by using lower OARs [83].

Based on the University of Sydney tunnel calibration, it seems likely that the cause of the

larger optimal OAR of the current study is a conversely compensatory effect for the lower L/H of the tunnel compared with that of the UBC tunnel. Given the quality of data obtained from the Imperial College tolerant test section, it does not seem that the shorter plenums have limited the effectiveness of the tunnel.

4.8.5 Standard deviation of forces and moments

In lieu of a suitable low blockage reference to use in a regression analysis, a standard deviation from the mean of results for the five NACA 0015 aerofoils in a given tunnel configuration, at a given Reynolds number, has instead been used. This is calculated at each incidence at which readings were taken. The results are summed over a desired range of incidences, with the best performing tunnel having the lowest sum of standard deviations, $\sum \mathrm{SD}$, since it provides the most consistent force and moment results across the range of aerofoil sizes. As previously mentioned, in free air, forces and moments generated by an aerofoil are independent of the aerofoil's size, should Reynolds number remain constant. Therefore, the tunnel providing the most consistency across the five models gives the best approximation of free air conditions.

The same calculations were also completed using the results for the smallest aerofoil ($c/H = 0.1$) in place of the mean of the five aerofoils. This methodology is closer to those of Flay et al [82], as used by Hameury [54]: the smallest aerofoil is the least affected by blockage and the nearest thing to a low-blockage benchmark. As a comparative measure of the performance of tunnel configurations, little difference was found between the results for standard deviation from the mean and deviation from the $c/H = 0.1$ aerofoil. Results are presented here for standard deviation as it is a more commonly understood measure.

The $\sum \mathrm{SD}$ methodology requires the compiling of results of numerous individual experiments, all subject to errors as described in Section 4.7, to give single data points. If a worst-case scenario is assumed for errors in the underlying experiments, where the lower two quartiles of readings are subject to the maximum under-measurement error possible, and the upper two are subject to the maximum over-measurement, the resulting absolute error in the standard deviation is never larger than that of the readings. The summations will lead to accumulation of errors, though It is likely that they will be subject to some netting off of over and under errors in the standard deviations, reducing the overall impact. Given the low value of the standard deviations, estimation of maximum percentage errors for $\sum \mathrm{SD}$ has not been

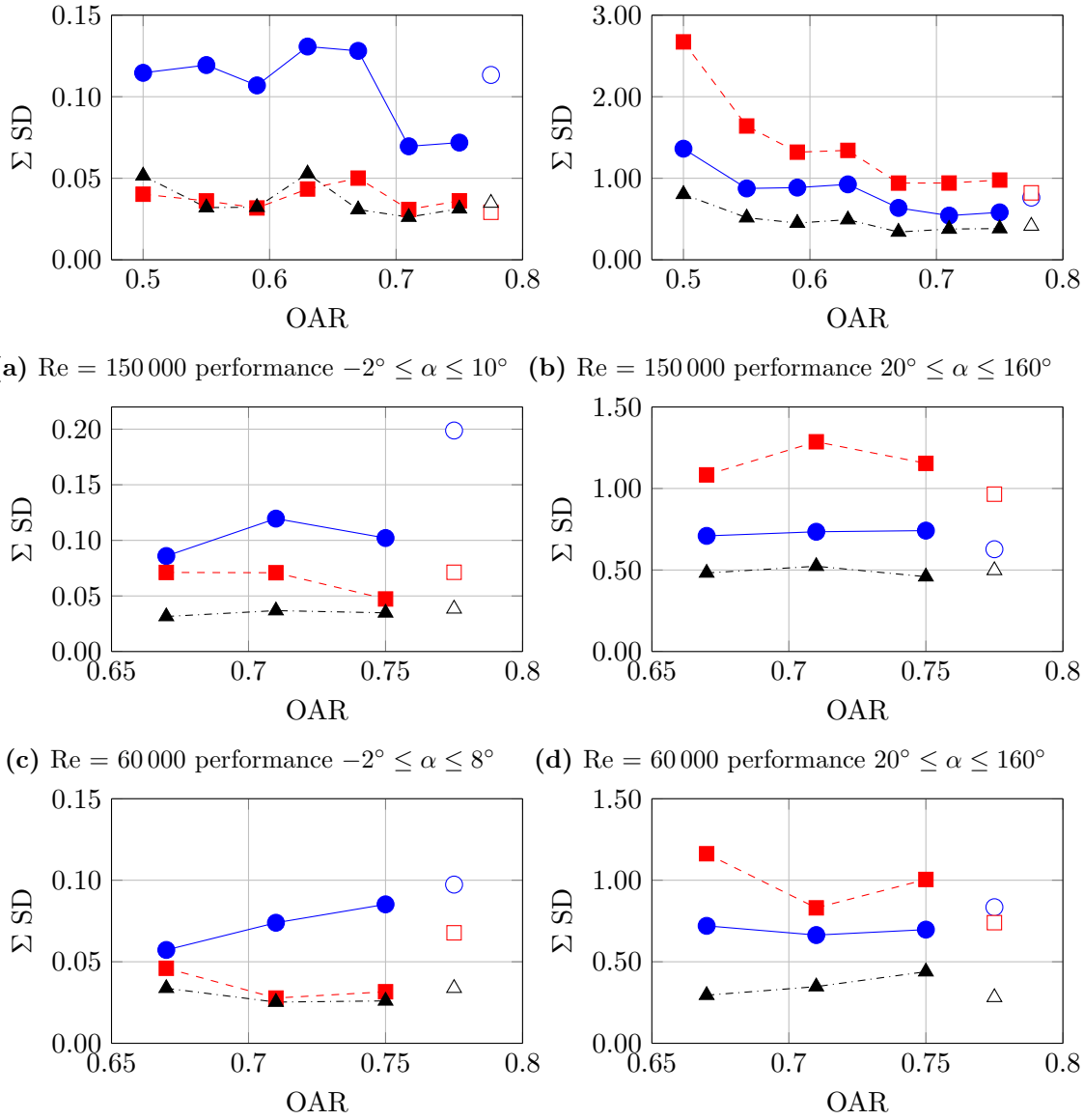
attempted. Care should be taken when drawing conclusions on tunnel performance based on the $\sum$SD analysis alone because of the potential for error accumulation. Here, the assessment is augmented with an analysis of the raw experimental outputs (Sections 4.8.2 and 4.8.3) and Hameury's tunnel calibration methods (Section 4.8.4).

For attached flow calibrations, $\sum$SD has been calculated for incidences of $-2°$ - $8°$ for 60 000 and $-2°$ - $10°$ for 150 000 and 250 000. For post-stall performance, $\sum$SD has been calculated for $20°$ - $160°$ for all Reynolds numbers. The incidences around stall have been avoided entirely as differences between the results for the aerofoils cannot necessarily be attributed to blockage here. Note that due to the problems with transducer saturation for the $c/H = 0.1$ aerofoil at $Re = 250\,000$ in the DS-67 tunnel, $\sum$SD calculations for this experiment ignore the problem incidences of $50°$, $55°$, $135°$ and $140°$, giving the DS-67 a slight unfair advantage over the other tunnels. The incidences tested changed over the course of the research, see Section 4.5.1. For the purposes of $\sum$SD calculations, only those angles tested during all runs (see Table 4.2) were considered.

Plots of the attached and separated $\sum$SD against OAR are presented in Fig. 4.23 for the double slatted wall tolerant tunnel and Fig. 4.24 for the single slatted wall tolerant tunnel. Corrected results for the solid walled tunnel are included in the figures, shown plotted at an OAR 0.775 or 0.925, and with unfilled point markers.

For attached flows at $Re = 150\,000$ (Fig. 4.23a), the DS-71 is the best of the tolerant tunnel configurations, as it has the lowest $\sum$SD for lift, drag and moment. The corrected solid walled tunnel is marginally better for drag, but worse for lift and moment. The differences in performance between the DS-67, DS-71, DS-75 and solid tunnels for drag and moment are unlikely to be significant once potential errors are considered. The single slatted wall tunnels, designed for use with attached flows, all produce results comparable to the corrected solid tunnel here (Fig. 4.24a), but perform considerably worse for lift than does the DS-71.

For detached flows (Fig. 4.23b), the DS-71 is again best for lift, while the DS-67 is better for moment. Note how insensitive to OAR the $\sum$SD measure is for all three coefficients in the range 0.67 to 0.75, with differences between the tunnels again likely to be insignificant when the potential impact of errors is considered. The tolerant tunnels perform better than the solid walled tunnel for lift and moment, but are worse for drag. Performance of the single slatted tunnels (Fig. 4.24b) are considerably worse than the doubly slatted for all three

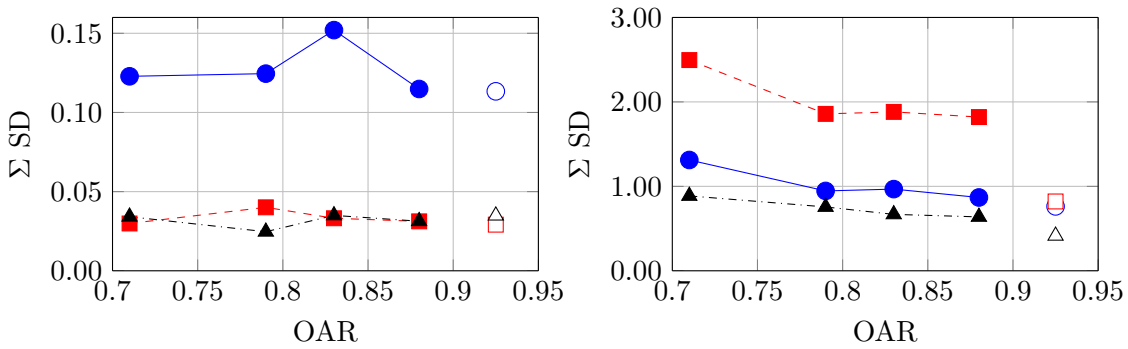


(a) Re = 150 000 performance $-2° \leq \alpha \leq 10°$ **(b)** Re = 150 000 performance $20° \leq \alpha \leq 160°$

(c) Re = 60 000 performance $-2° \leq \alpha \leq 8°$ **(d)** Re = 60 000 performance $20° \leq \alpha \leq 160°$

(e) Re = 250 000 performance $-2° \leq \alpha \leq 10°$ **(f)** Re = 250 000 performance $20° \leq \alpha \leq 160°$

Figure 4.23: Summations of standard deviations for C_l, C_d and C_m for all NACA 0015 aerofoils, plotted against OAR for double slatted wall tunnel configurations. Note that while corrected solid-walled data has an OAR of 0, it is shown plotted at OAR = 0.775.



(a) Re = 150 000 performance $-2° \leq \alpha \leq 10°$ **(b)** Re = 150 000 performance $20° \leq \alpha \leq 160°$

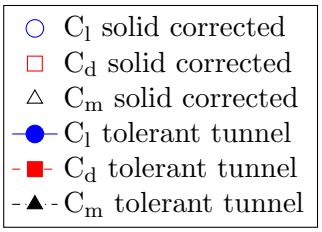


Figure 4.24: Summations of standard deviations for C_l, C_d and C_m for all NACA 0015 aerofoils, plotted against OAR for single slatted wall tunnel configurations. Note that while corrected solid-walled data has an OAR of 0, it is shown plotted at OAR = 0.925.

coefficients. Table 4.5 summarises the performance of the tunnels for C_l, C_d and C_m across the two incidence ranges for the three Reynolds numbers tested. Columns indicate the best performing tolerant tunnel and the best tunnel overall. There is also a column comparing the performance of the DS-71 and corrected solid walled tunnels.

Mostly, the tolerant tunnel out-performs the corrected solid walled tunnel data, though the solid walled tunnel performs better for drag in separated flows for all three Reynolds numbers. Trends in post-stall moment are similar to those for drag since, as described in Section 4.5.3, the force transducers measure moment about the half chord. This is processed into moment about the quarter chord by subtracting the moment of the normal force multiplied by $\frac{1}{4}c$, thus giving moment readings dependent on force measurements.

Attached flow drag and moment results are not significantly different for the DS-67, DS-71, DS-75 and corrected solid walled tunnels. Values for both are very low when flow is attached compared to other forces, regardless of aerofoil size, so $\sum$SD is also low.

Referring to Figs 4.14 - 4.18 and D.9 - D.19, it can be seen that neither the tolerant tunnel nor blockage corrections deal with blockage of the $c/H = 0.3$ aerofoil particularly well. This

Re	Force coefficient	Alpha range	Best tolerant config.	Best tunnel overall	$\sum$SD DS-71 < $\sum$SD solid corrected
150 000	Lift	−2° - 10°	DS-71	DS-71	✓
		20° - 160°	DS-71	DS-71	✓
	Drag	−2° - 10°	DS-71	Solid	✗
		20° - 160°	DS-67	Solid	✗
	Moment	−2° - 10°	DS-71	DS-71	✓
		20° - 160°	DS-67	DS-67	✓
60 000	Lift	−2° - 8°	DS-67	DS-67	✓
		20° - 160°	DS-67	Solid	✗
	Drag	−2° - 8°	DS-75	DS-75	✓
		20° - 160°	DS-67	Solid	✗
	Moment	−2° - 8°	DS-67	DS-67	✓
		20° - 160°	DS-75	DS-75	✗
250 000	Lift	−2° - 10°	DS-67	DS-67	✓
		20° - 160°	DS-71	DS-71	✓
	Drag	−2° - 10°	DS-71	DS-71	✓
		20° - 160°	DS-71	Solid	✗
	Moment	−2° - 10°	DS-71	DS-71	✓
		20° - 160°	DS-67	Solid	✗

Table 4.5: Summary of tunnel configuration performance based on standard deviation summations for all NACA 0015 aerofoils

is particularly noticeable for drag. For the solid walled tunnels, the $c/H = 0.3$ aerofoil has the highest peaks in the raw data plots (Figs 4.17, D.15 and D.18 for $Re = 150\,000$, 60 000 and 250 000 respectively). Drag can be seen to be over-corrected, with the $c/H = 0.3$ aerofoil having the lowest drag between incidences of 70° and 110°, the peak at 90° inverted to a trough, in Figures 4.18, D.16 and D.19.

The tolerant tunnel also struggles to cope with the blockage of the largest aerofoil at incidences near to 90°. For example, for the $Re = 150\,000$ runs, the $c/H = 0.3$ aerofoil

exhibits the lowest drag at incidences of 60° - 120° in the DS-71 and DS-75 tunnels, see Figs 4.15 and 4.16 resepectively. The DS-75 tunnel can also be seen to similarly over-correct for the $c/H = 0.25$ aerofoil at incidences of 80° - 110°. These over-corrections are significant even after the consideration of maximum possible errors. Similar trends can be seen in the results at $Re = 60\,000$ and $250\,000$ in Figs D.10, D.11, D.13 and D.14. Note that at less extreme incidences, for $Re = 150\,000$ and $250\,000$, the tolerant tunnel provides better results for the $c/H = 0.3$ aerofoil than the corrected solid walled tunnel. In the tolerant tunnels, drag is consistent with that of the smaller aerofoils, while the corrections under-correct drag at incidences of $< 60°$ and $> 120°$.

As mentioned in Section 2.1.9, ESDU state that use has been made of their corrections with c/H ratios of up to 0.35 [10], but it is doubtful this applies to incidences much beyond stall, given the corrections are intended for use with minimal separation. It is therefore not surprising that the results for the largest aerofoil are sub-optimal at incidences around 90°.

The causes of the tolerant tunnel's limitations are also understood. Hameury examined the flow pattern in the plenum chambers of the tunnel using a combination of smoke flow visualisation, tuft flow visualisation and plenum floor pressure tappings. He concluded that the flow fell into two general modes, depending on the extent to which the tunnel was blocked [54] and the tunnel OAR.

Under normal tunnel operating conditions, the plenum flow shows a single elongated re-circulation with a centre downstream of the streamwise centre of the tunnel. A shear layer exists within the plenum chamber, between this recirculation and the flow moving through the tunnel. There is entrainment along the shear layer, and the layer stretches the full length of the plenum, hitting the downstream end wall of the chamber. This is characterised as open cavity flow [84].

Under the other mode of operation, the recirculation is not present. Instead, there are two separation bubbles in the plenum chamber, one attached to the upstream wall and another on the downstream wall. Between these, the shear layer layer impacts on the plenum floor. See Fig. 4.25 for this flow pattern. This is characterised as shallow, closed cavity flow [84].

Hameury [54] observed the normal operating conditions for all the circular cylinder models tested (with d/H of 0.083, 0.138, 0.25 and 0.333) and the two smallest flat plates normal to the flow ($c/H = 0.083$ and 0.194). For the largest flat plate with $c/H = 0.333$, and for tests

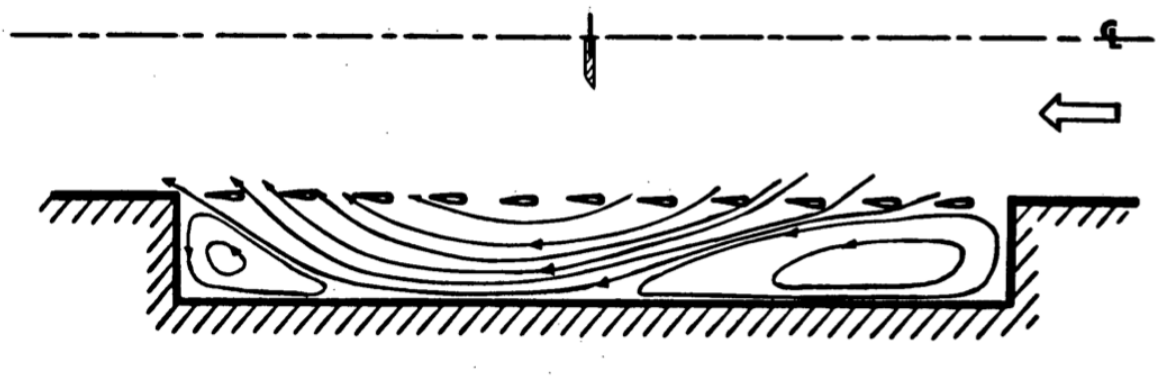
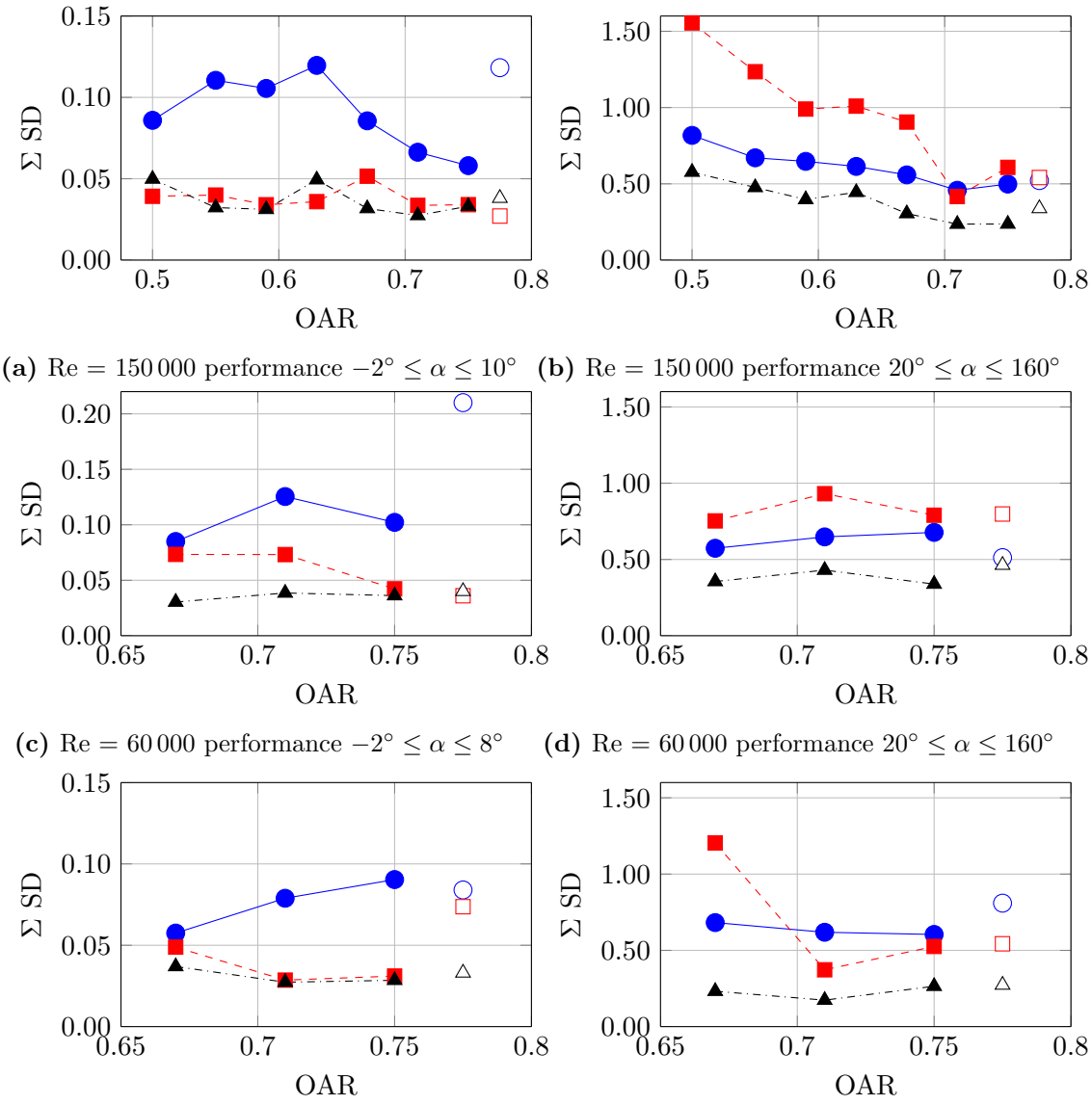


Figure 4.25: Flow pattern in tolerant tunnel plenum chamber under extreme blockage [54].

conducted without any slat aerofoils in place (i.e. with an OAR of 1) for other models, the alternate mode was observed. In the case of the large flat plate, the model blockage pushed the free shear layer between the tunnel flow and the plenum recirculation outwards to such an extent that it hit the plenum floor. For the high open area case, there were no slats present to prevent the break-up of the free shear layer and again it hit the plenum floor. Additionally, the flow deflections caused by the large flat plate were extreme enough to give angles of attack large enough to stall upstream slat aerofoils, further degrading the quality of flow in the plenums.

At incidences of 60° - 120°, the DS-71 and DS-75 tunnels are unable to accommodate the $c/H = 0.3$ aerofoil due to the plenum free shear layer hitting the plenum floor. For the DS-75 tunnel, the OAR is so low that the shear layer also hits the floor for the $c/H = 0.25$ aerofoil, at incidences of 80° - 110°. These effects manifest as the flattened drag peaks discussed above. In lower OAR tunnels, there is less evidently flattened drag peaks for the larger aerofoils, but all aerofoils suffer from a larger number of slats preventing sufficient movement of the free shear layer into the plenum chamber and manifesting in the higher drag peaks associated with conventional blockage effects in solid-walled tunnels.

In order to better judge the performance of the tolerant tunnel and ESDU blockage corrections within sensible blockage limits, the analysis of standard deviation of forces and moments has been repeated for aerofoils with $c/H < 0.3$, see Fig. 4.26. The best performing tolerant tunnel, best tunnel overall, and the comparative performance of the conventional solid walled tunnel and DS-71 tolerant tunnel for $c/H < 0.3$ are summarised in Table 4.6.



(a) Re = 150 000 performance $-2° \leq \alpha \leq 10°$ **(b)** Re = 150 000 performance $20° \leq \alpha \leq 160°$

(c) Re = 60 000 performance $-2° \leq \alpha \leq 8°$ **(d)** Re = 60 000 performance $20° \leq \alpha \leq 160°$

(e) Re = 250 000 performance $-2° \leq \alpha \leq 10°$ **(f)** Re = 250 000 performance $20° \leq \alpha \leq 160°$

Figure 4.26: Summations of standard deviations for C_l, C_d and C_m for NACA 0015 aerofoils with $c/H < 0.3$, plotted against OAR for double slatted wall tunnel configurations. Note that while corrected solid-walled data has an OAR of 0, it is shown plotted at OAR = 0.775.

Re	Force coefficient	Alpha range	Best tolerant config.	Best tunnel overall	$\sum$SD DS-71 < $\sum$SD solid corrected
150 000	Lift	$-2°$ - $10°$	DS-75	DS-75	✓
		$20°$ - $160°$	DS-71	DS-71	✓
	Drag	$-2°$ - $10°$	DS-71	Solid	✗
		$20°$ - $160°$	DS-71	DS-71	✓
	Moment	$-2°$ - $10°$	DS-71	DS-71	✓
		$20°$ - $160°$	DS-71	DS-71	✓
60 000	Lift	$-2°$ - $8°$	DS-67	DS-67	✓
		$20°$ - $160°$	DS-67	Solid	✗
	Drag	$-2°$ - $8°$	DS-75	Solid	✗
		$20°$ - $160°$	DS-67	DS-67	✗
	Moment	$-2°$ - $8°$	DS-67	DS-67	✓
		$20°$ - $160°$	DS-75	DS-75	✓
250 000	Lift	$-2°$ - $10°$	DS-67	DS-67	✓
		$20°$ - $160°$	DS-75	DS-75	✓
	Drag	$-2°$ - $10°$	DS-71	DS-71	✓
		$20°$ - $160°$	DS-71	DS-71	✓
	Moment	$-2°$ - $10°$	DS-71	DS-71	✓
		$20°$ - $160°$	DS-71	DS-71	✓

Table 4.6: Summary of tunnel configuration performance based on standard deviation summations for NACA 0015 aerofoils with $c/H < 0.3$

The superior performance of the tolerant tunnel is clearer in these new analyses. The DS-71 tunnel now gives the best detached flow drag and moment at $Re = 150\,000$ and $250\,000$, rather than the solid walled tunnel as was the case when considering all five aerofoils.

The solid walled tunnel remains superior for three Reynolds number/flow type pairings. Attached flow drag is better in the solid walled tunnel at $Re = 60\,000$ and $150\,000$, as is detached flow lift at $Re = 60\,000$. For a fourth pairing, detached flow drag at $Re = 60\,000$, while the DS-67 is the best tunnel overall, the solid walled tunnel out-performs the DS-71. For

the attached flow cases, as previously mentioned, $\sum$SD of drag is low for all the tunnels and no one tunnel significantly outperforms the others; considering all three forces and moments together it is clear that the DS-67, DS-71 and DS-75 tunnels outperform the solid walled tunnel at all three Reynolds numbers tested.

For the detached flows at $Re = 60\,000$, see Fig. 4.26d, performance of all four tunnels is relatively poor compared to that at higher Reynolds numbers. Referring back to Figs D.16, D.9, D.10 and D.11 confirms this, with none of the tunnels displaying the impressive data collapses seen in higher speed flows, see for example the DS-71 tunnel at $Re = 150\,000$ in Fig. 4.15.

4.8.6 Surface pressure distribution similarity

As with the force balance data, Hameury's pressure analysis techniques can only take tunnel OAR assessments so far. In order to judge the pressure collapse across a range of incidences, and considering both suction and pressure surfaces of the aerofoil, the following method has been developed.

Since the $c/H = 0.15$ aerofoil has fewer pressure tappings, these were used as a starting point. An equivalent C_p value at the appropriate chord-wise location on the $c/H = 0.25$ aerofoil was interpolated for each using the pressure distributions of the larger aerofoil. Absolute differences between the interpolated $c/H = 0.25$ equivalent C_p and the actual $c/H = 0.15$ C_p were calculated and summed across the $c/H = 0.15$ tappings at each incidence. The results were then summed across the representative attached flow and detached flow incidence ranges of $-2°$ - $10°$ ($-2°$ - $8°$ for $Re = 60\,000$) and $20°$ - $160°$. The maximum possible error in any of these summations is the same as that of any of the underlying pressure readings (approximately 1%, see Section 4.7). There are no commonly used corrections for pressure distributions, so no analysis of the corrected solid walled tunnel data is included.

The DS-71 tunnel performs best for attached flow at $Re = 150\,000$ and $250\,000$, and for detached flow at $Re = 250\,000$, while the DS-75 is best for attached flow for $Re = 60\,000$ and for detached flow for $Re = 60\,000$ and $150\,000$. As with the force balance data, results are similar for the three tolerant configurations, suggesting tunnel performance is relatively insensitive to OAR within the range of OARs selected for testing.

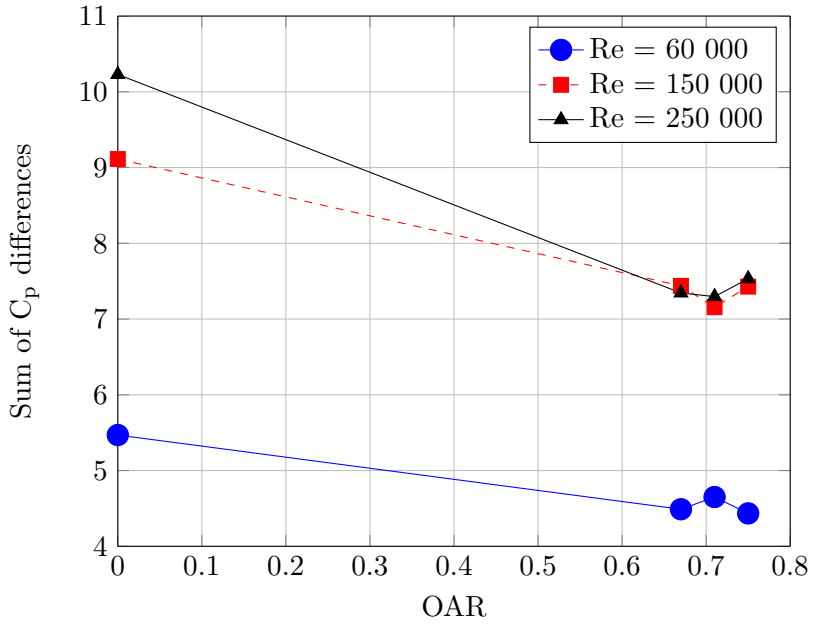


Figure 4.27: Variation of sums of difference in C_p for $-2° \leq \alpha \leq 8°$ ($Re = 60\,000$) and $-2°$ - $10°$ ($Re = 150\,000$, $250\,000$), as a function of OAR for the two pressure tapped NACA 0015 aerofoils, double slatted wall tunnel configurations.

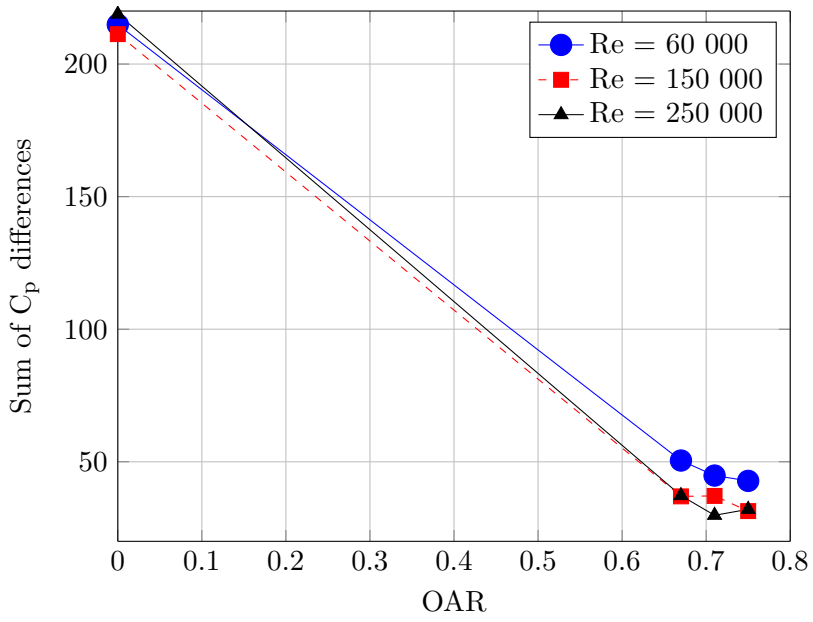


Figure 4.28: Variation of sums of difference in C_p for $20° \leq \alpha \leq 160°$, as a function of OAR for the two pressure tapped NACA 0015 aerofoils, double slatted wall tunnel configurations.

4.9 Discussion on OAR calibrations

The analyses of tolerant tunnel configurations presented in this chapter point to the double slatted configuration, with OAR of 0.67-0.75, providing the best reduction of blockage effects across a range of model sizes and Reynolds numbers. Notably, it outperforms conventional solid-walled tunnels and blockage corrections at all but $Re = 60\,000$, where neither the tolerant tunnel nor conventional methods perform particularly well.

Table 4.6 summarises the performance for aerofoils with $c/H < 0.3$ based on the standard deviation of forces and moments method described in Section 4.8.5. Analysis is split between attached and detached flow, for lift, drag and moment and $Re = 60\,000$, $150\,000$ and $250\,000$, giving 18 experiment types over which to judge the tunnels. The DS-71 is judged to be the best tunnel for eight of these, the DS-67 for four, and the DS-75 for three, with the conventional solid-walled tunnel taking the remaining three.

For surface pressure performance, using the methods of Section 4.8.6, and again splitting the judgement between attached and detached flow for $Re = 60\,000$, $150\,000$ and $250\,000$, there are six experiment types. The DS-71 tunnel is best for three of them, with the DS-75 better for the other three.

Based on all of the assessments described in Section 4.8, the DS-71 seems to be the best performer overall, and since it neighbours both the DS-67 and DS-75 in terms of OAR is a good compromise choice for the experiment types served better by those tunnels. Additionally, most of the analyses have suggested little influence of OAR within the narrowed range of 0.67-0.75. To demonstrate that this is true, specifically for low blockage experiments, Figs 4.29 - 4.31 are presented. These show lift, drag and moment coefficients against incidence for the $c/H = 0.1$ aerofoil at $Re = 60\,000$, $150\,000$ and $250\,000$. The three best performing tolerant tunnels are plotted on the same axes. Note that, as before, the $Re = 250\,000$ readings affected by transducer saturation are omitted.

For $Re = 60\,000$ there is some impact of OAR on the results. At the drag peak at $\alpha = 90°$, the spread in the results is 5.4%. At the lift peak at $\alpha = 40°$, the spread is 4.6%. Maximum experimental error from an established mean was estimated at 2.6% in Section 4.7, giving a maximum spread of 5.2% (double the maximum error), suggesting these differences between the OARs are significant for drag.

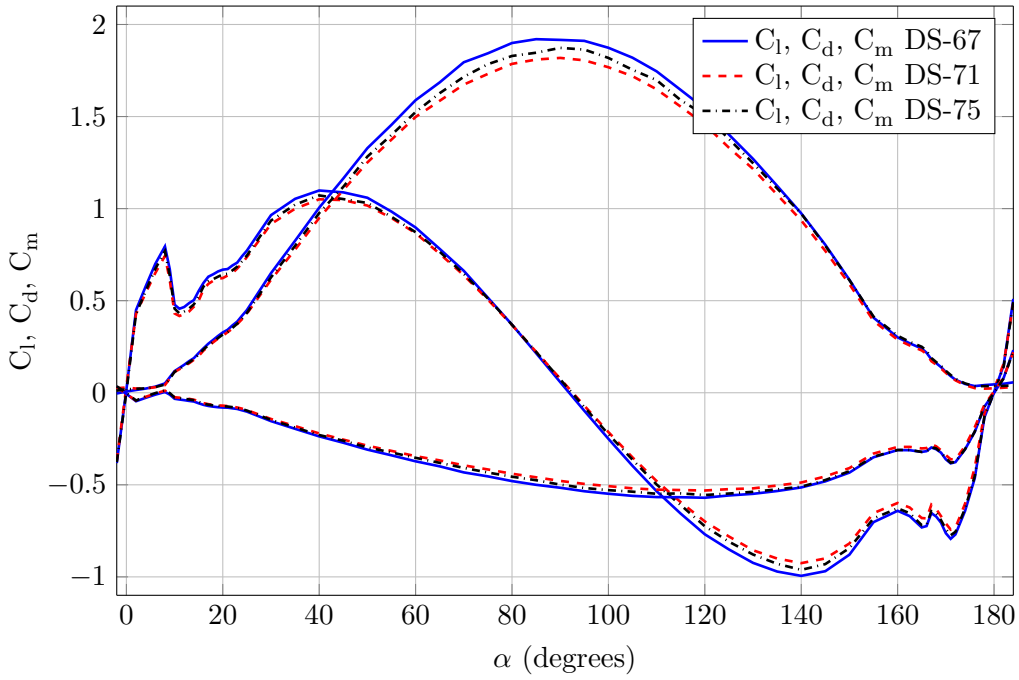


Figure 4.29: C_l, C_d and C_m vs α for the $c/H = 0.1$ NACA 0015 aerofoil taken in the tolerant tunnel, DS-67, DS-71 and DS-75 configurations, at $Re = 60\,000$.

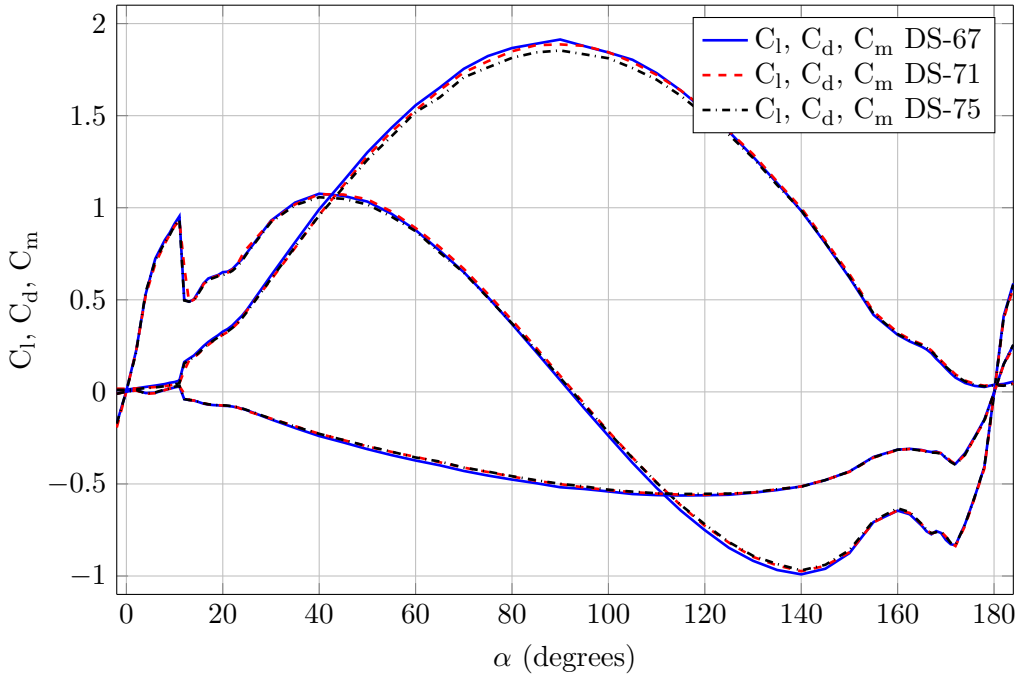


Figure 4.30: C_l, C_d and C_m vs α for the $c/H = 0.1$ NACA 0015 aerofoil taken in the tolerant tunnel, DS-67, DS-71 and DS-75 configurations, at $Re = 150\,000$.

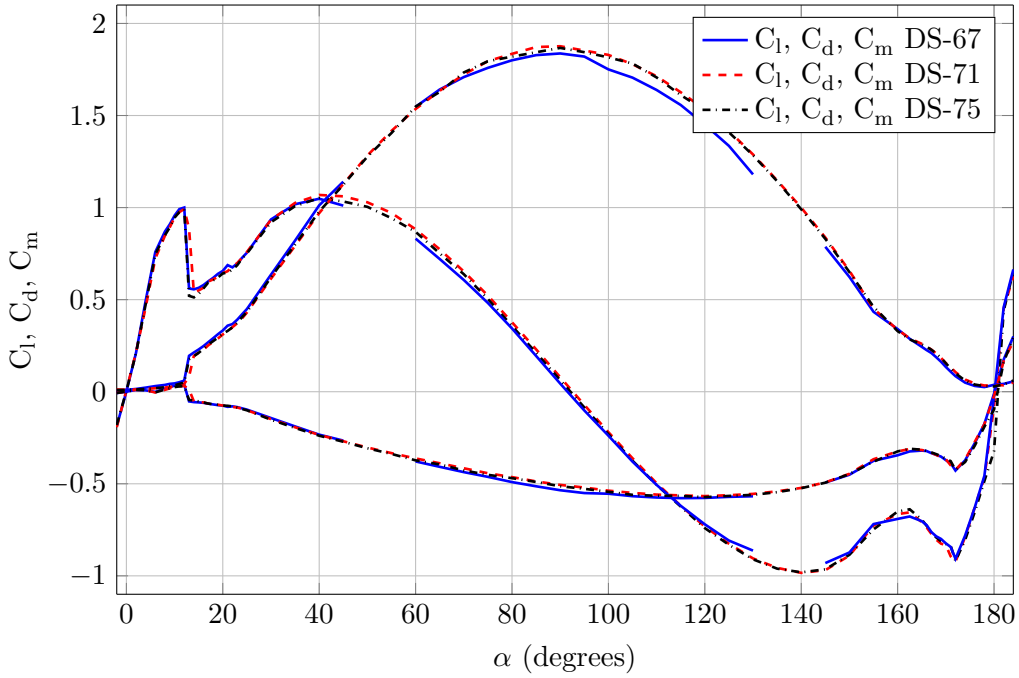
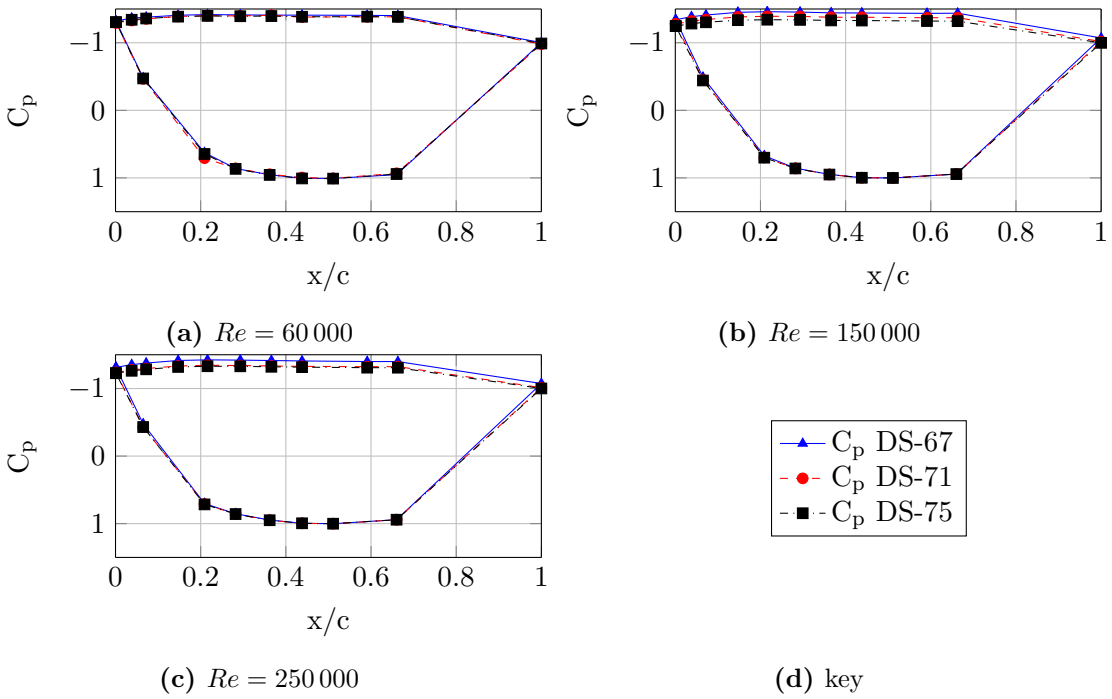


Figure 4.31: C_l, C_d and C_m vs α for the $c/H = 0.1$ NACA 0015 aerofoil taken in the tolerant tunnel, DS-67, DS-71 and DS-75 configurations, at $Re = 250\,000$.

For $Re = 150\,000$, the equivalent spreads are 3.2% for drag at 90° and 1.8% for lift at 40°, neither of these being more than double the estimated maximum error of 1.8%. Lift and drag spreads for $Re = 250\,000$ they are 2.1% and 2.0%. Again, neither are more than double the maximum error for this Reynolds number, 1.7% for 250 000.

Similar comparative plots for tunnel type were prepared for surface pressure measurements, using the $c/H = 0.15$ aerofoil. Very little difference was noted between the DS-67, DS-71 and DS-75 tunnels other than for incidences around 90°. Fig. 4.32 shows results at $Re = 60\,000$, 150 000 and 250 000 for $\alpha = 90°$. The pressure surface results are practically identical, but there are small differences in suction surface results at the higher Reynolds numbers.

These results suggest that the choice between the DS-67, DS-71 and DS-75 tunnels is somewhat arbitrary for the smaller aerofoils, and support the selection of the DS-71 for further experiments. Table 4.6 has a column summarising the performance of the configuration against the conventional solid walled tunnel. To see a more detailed comparison between results taken in the DS-71 tolerant tunnel and the conventional solid walled tunnel, across a greater range of Reynolds numbers than those used during the OAR calibration process, refer to Section 5.3.



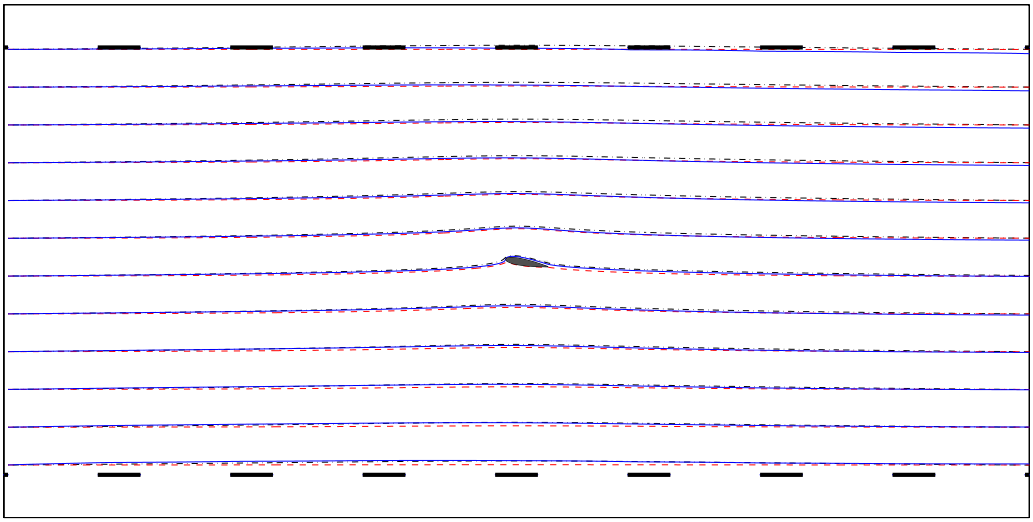
(a) $Re = 60\,000$ **(b)** $Re = 150\,000$

(c) $Re = 250\,000$ **(d)** key

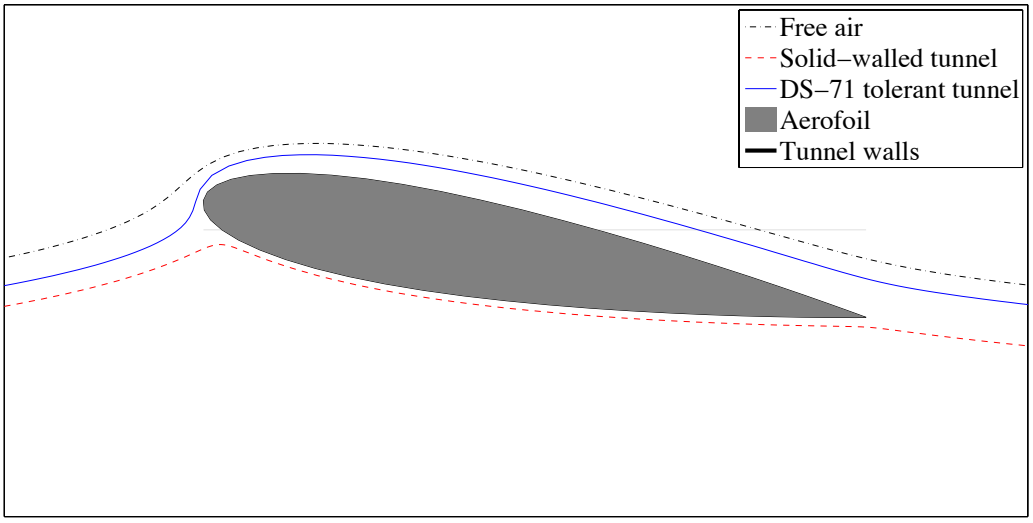
Figure 4.32: C_p plotted against normalised chord-wise position for the $c/H = 0.15$ NACA 0015 aerofoil at $\alpha = 90°$ taken tolerant tunnel, DS-67, DS-71 and DS-75 configurations.

To demonstrate how the tolerant tunnel achieves a free air approximation, simulations have been conducted using the panel method described in Section 3.2 for an aerofoil in free air, in a solid-walled tunnel and in the DS-71 tunnel. Fig. 4.33a shows streamlines around the aerofoil (starting at the same points in the flow for all three conditions) and Fig. 4.33b shows a zoomed view of the region of flow around the aerofoil. For the solid-walled and tolerant tunnels a c/H of 0.1 has been used to match the majority of experiments presented in this thesis and tunnel dimensions (L/H ratio, slat chord to H ratio) match the Imperial College 3' × 3' tolerant test section. It can be seen that the tolerant tunnel provides flow conditions closer to free air than the solid-walled tunnel: the single streamline shown in Fig. 4.33b passes above the aerofoil in free air and in the tolerant tunnel, but below the aerofoil when flow is constrained by solid tunnel walls. With streamlines close to those expected in free air, the forces and moments induced on an aerofoil under test will also be close to their equivalents in unconstrained flow.

The experimental results from the Imperial College tolerant tunnel are close to free air. At $Re = 150\,000$, for the DS-71 tunnel, there is a spread in post-stall lift coefficients of 6% (2.4% -



(a) Full tunnel.



(b) Zoomed view of region around the test aerofoil.

Figure 4.33: Modelled streamline behaviour in free air, a solid-walled tunnel and the DS-71 tolerant tunnel.

9.6% considering maximum possible errors) between the five NACA 0015s at $\alpha = 45°$, as seen in Fig. 4.15 (in free air, the peaks would be identical). Using the conventional solid walled tunnel and blockage corrections, there remains a spread in lift coefficients of 14% (10.4% - 17.6% considering errors), see Fig. 4.18. The DS-71 tunnel provides a significant improvement on conventional techniques, critically reducing the spread in lift below the 10% identified as problematic in BEM code inputs in Fig. 1.4.

Chapter 5

Force and surface pressure experiments: results, validation and analysis

The previous chapter describes experiments conducted for the purposes of calibrating the tolerant tunnel's OAR. This chapter contains results taken using the best OAR of 71%. Surface pressure distributions are given first and were taken using an identical methodology to the earlier experiments and at the same Reynolds numbers. Force transducer readings were taken with improved techniques over a wider range of Reynolds numbers. The improvements are described then the results given. Benchmark results taken in a solid walled tunnel are presented and comparisons made to those taken in the tolerant tunnel. Finally, the impact of Reynolds number, aerofoil profile camber and thickness on aerofoil performance are discussed.

5.1 Surface pressure distributions

Results are presented here for the $c/H = 0.25$ NACA 0015 from the DS-71 tolerant tunnel. The $c/H = 0.15$ aerofoil has fewer tappings so is omitted. It has been demonstrated earlier (Fig. 4.19) that results are consistent for the two aerofoils in this tunnel configuration, suggesting that the large blockage of the $c/H = 0.25$ aerofoil does not negatively impact results compared to the smaller blade.

Fig. 5.1 shows pressure distributions at incidences of 20°, 0°, 2°, 4°, 6° and 10° for the three Reynolds numbers at which pressure testing was conducted, 60 000, 150 000, and 250 000. Clearly visible, at incidences of 2° - 10°, is a laminar separation bubble on the suction surface of the aerofoil. For example, at 6°, the bubble is visible at $0.15c$ - $0.5c$ at $Re = 60\,000$, $0.15c$ - $0.35c$ at $Re = 150\,000$ and $0.15c$ - $0.3c$ at $Re = 250\,000$. At all incidences where the bubble is present, the point at which the boundary layer separates from the aerofoil is largely independent of Reynolds number. The length of the bubble decreases as Reynolds number increases, as the distance required for the separated boundary layer to transition to turbulence and reattach is reduced.

The bubble moves towards the leading edge as incidence increases and the adverse pressure gradient gets stronger, pulling the point of separation forwards. At low incidences, where separation occurs close to the trailing edge, no reattachment occurs due to the transition of the separated boundary layer occurring downstream of the end of the aerofoil. Section 1.5.5 gives some background on laminar separation bubbles and they are discussed more in the context of this study's results in Sections 5.2.3 and 5.4.

At $\alpha = 6°$ and 10°, see Fig. 5.1(e) and (f) respectively, flows show clear Reynolds number dependancy even when ignoring the laminar separation bubble, with higher negative pressure peaks at higher Re. Where flow is separated this is not the case, as shown in the results for $\alpha = 20°$ in Fig. 5.1(a). Fig. 5.2 shows pressure distributions at incidences of 30°, 50°, 90°, 150°, 170° and 180° for $Re = 150\,000$. Also included are pressure distributions from existing studies, namely those of Pope for the NACA 0015 [36], Bergeles et al. for the NACA 0012 [33] and Fage and Johansen [63] and Hameury [54] for flat plates. No attempt was made to validate the attached flow distributions to these studies as they were taken at different Reynolds numbers and other than Pope's using different profile shapes. Where flow is separated, results for the NACA 0012 and 0015 should be near-identical and flat plates will be similar other than near to the leading edge which is far less sharp in an aerofoil.

The studies all show reasonable agreement to each other. Pressure surface similarity is particularly strong, other than at $\alpha = 30°$, where the leading edge curvature still has an impact on the flow along the whole of the pressure surface, making the results profile shape-dependent. Agreement for the suction surfaces is less good, with those of Pope, the only other NACA 0015 study, consistently lower in magnitude than all the other studies. The unusually low pressures

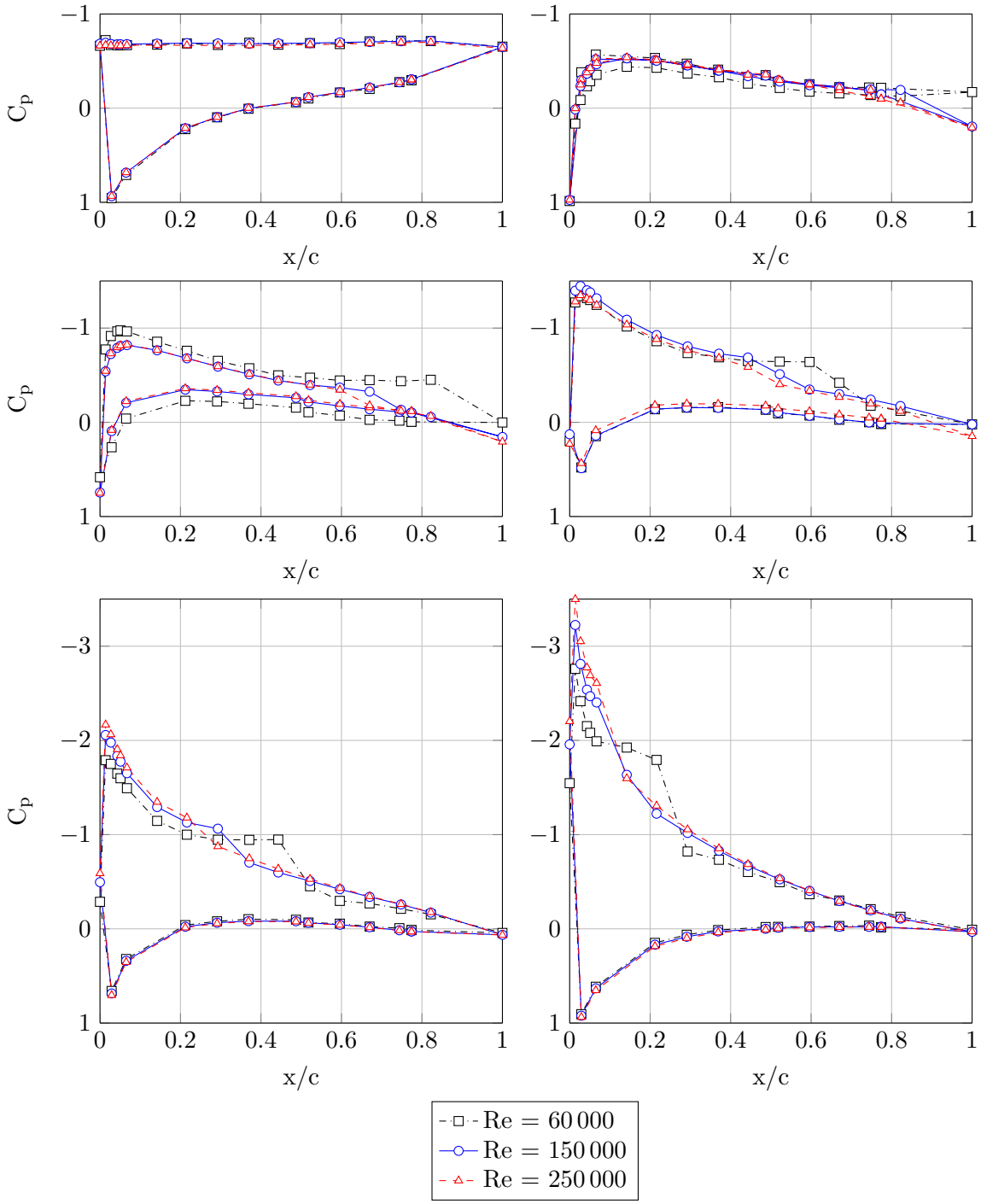


Figure 5.1: C_p plotted against normalised chord-wise position for the $c/H = 0.25$ NACA 0015 aerofoil at various Reynolds numbers at (a) 20°, (b) 0°, (c) 2°, (d) 4°, (e) 6°, (f) 10°

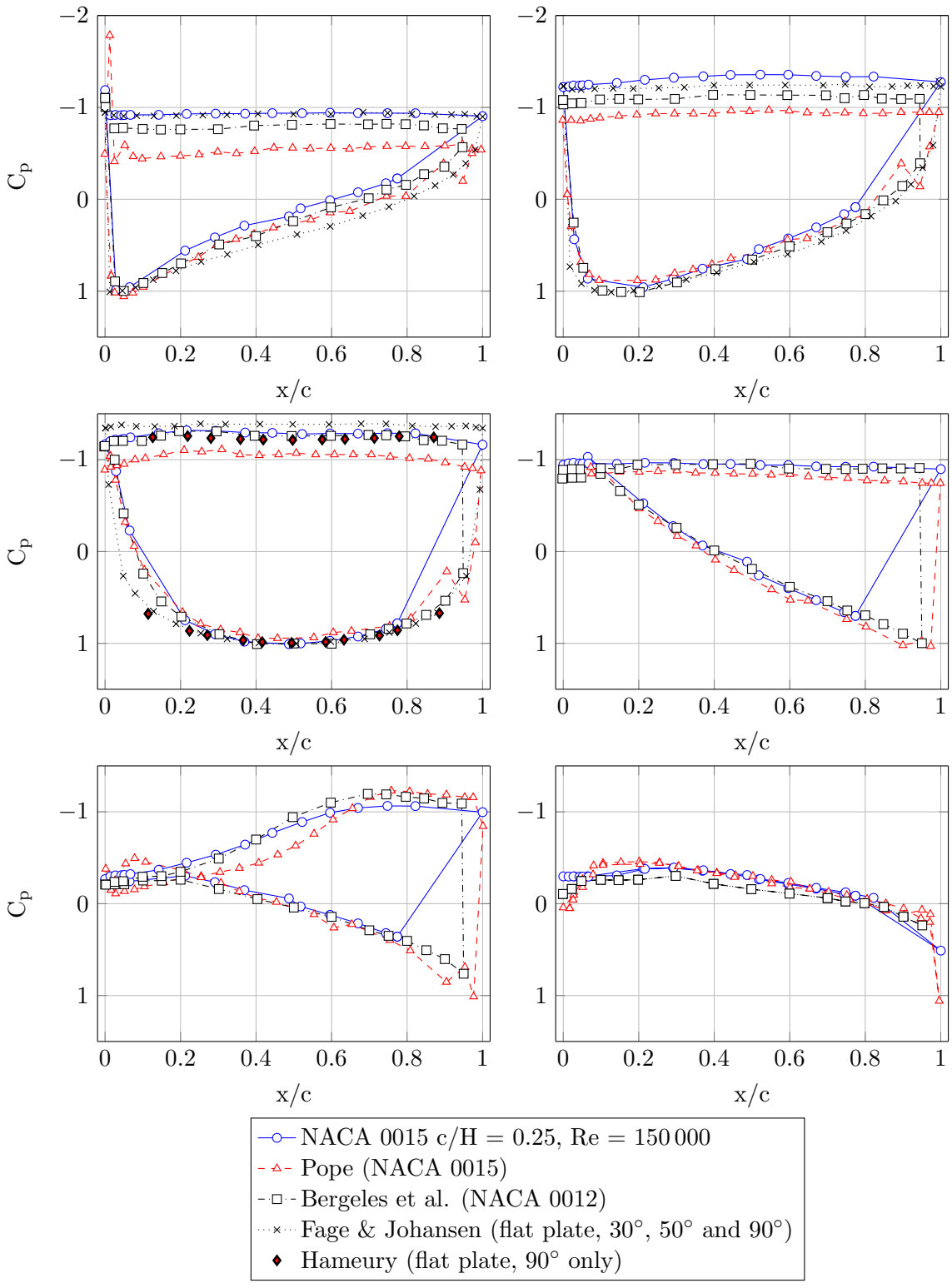


Figure 5.2: C_p plotted against normalised chord-wise position for the $c/H = 0.25$ NACA 0015 aerofoil compared to other studies at (a) 30°, (b) 50°, (c) 90°, (d) 150°, (e) 170°, (e) 180°

probably result from Pope's unusual approach to blockage reduction, using a "breather" to atmosphere and correcting only for streamline curvature. Should the "breather" allow too much flow to exit the tunnel, an over-correction for blockage will be provided resulting in low suction surface pressures but minimal changes to the pressure surface, as is the case in the tolerant tunnel with OARs higher than optimal [54]. See Appendix A.1.2 for more on Pope's methods.

The very strong agreement of this study to Hameury's flat plate at $\alpha = 90°$, taken in his original version of the tolerant tunnel, is particularly noteworthy given the identical approach to blockage reduction of the two studies.

5.2 Force transducer measurements, tolerant tunnel with OAR = 71%

The smallest NACA 0015 aerofoil ($c/H = 0.1$) was selected for testing at a wider range of Reynolds numbers. Three $c/H = 0.2$ NACA 0018 variants have also been tested at a wide range of Reynolds numbers, for use in work on Migliore's virtual camber theory [24], see Section 6.5.

Changes were made to the experimental techniques of Ch. 4 to improve the accuracy of data obtained from the apparatus, particularly at Reynolds numbers of less than 60 000. These are detailed here, with sections on new pre-offset settling times and experiment sampling times. Results for the $c/H = 0.1$ NACA 0015 are presented for $Re = 20\,000$, 40 000, 60 000, 80 000, 100 000, 125 000, 150 000, 200 000 and 250 000, and for the $c/H = 0.2$ NACA 0018 variants for $Re = 40\,000$, 60 000, 80 000, 100 000, 125 000, 150 000, 200 000 250 000 and 300 000.

5.2.1 Pre-offset settling times

Preliminary testing at Reynolds numbers below 60 000 returned some unusual results (e.g. negative drag at low incidences). It was suspected that inaccurate offsets were the cause of the negative drag readings. Per Section 4.5.1, for symmetrical aerofoils, zero incidence is set by the data acquisition software using results from a short preliminary run of the tunnel. For the tunnel OAR calibration experiments of Ch. 4, offsets were taken after a 10 s pause, following the end of the incidence zeroing tunnel run. The incidence zeroing was run at a Reynolds

number of 150 000 to ensure linearity of the lift-incidence curve near to $\alpha = 0°$. Should the settling time between the running of the zero incidence finder and the taking of the offset be insufficient, the influence of the forces measured during the incidence finding process could be captured in the offset, resulting in the negative drags measured at low Reynolds numbers. A re-analysis of settling times for the force transducers was conducted:

- Under no flow, moving between neighbouring incidences (i.e. 1° apart at low incidences, 5° apart at more extreme incidences) to test the impact of rig rotation on settling times.
- Under no flow, immediately following the running of the tunnel at $Re = 150\,000$, to test the impact of the incidence zeroing process on transducer offsets.

A standard reading was taken 10 s after the rotation/tunnel run, with a second taken 5 minutes after. The differences between the two results were processed into lift, drag and moment coefficients using the 10 s reading as a base, and typical dynamic pressures for each of the Reynolds numbers tested. No significant differences were noted between the two readings so no changes were made to earlier methods.

For the effects of the incidence zeroing process, a full set of offset readings, at 10° intervals between 0° and 180° was taken after a 10 s pause. An additional offset was taken after a five minute pause. The differences between the two results were processed into lift, drag and moment coefficients using the 10 s reading as a base, with typical dynamic pressures for each of the Reynolds numbers tested. Drag was the worst affected, with $C_d = -0.2$ between the 5 min and 10 s offsets for $Re = 20\,000$. For $Re = 60\,000$, $C_d = -0.02$, not insignificant for attached flow measurements, but for $Re = 150\,000$, $C_d = -3 \times 10^{-4}$, well within the margin of error caused by other foreseeable flaws in the experimental methods, see Section 4.7. The data taken at $Re = 60\,000$ in Ch. 4 may therefore be unreliable at low incidences, but since it is all similarly affected, remains suitable for the uses made of it for tunnel OAR calibration.

A longer five minute settling time was written into the data acquisition software between the running of the zero incidence finder and the taking of the offset, and between the taking of the offset and the main run of the experiment. A further five minute pause was added between the end of the main experiment and the taking of the second, post-experiment offset. This settling time has a large safety factor and is much longer than strictly necessary, no further settling of the transducers was noted beyond the five minute pauses.

5.2.2 Sampling times

Following the methods of Section 4.5.2, sampling times were assessed for the wider range of Reynolds numbers under test here. The times used are detailed in Table 5.1.

		Force measurements	
Aerofoil c/H	Re	$45° \leq \lvert\alpha\rvert \leq 135°$	Other α
0.1	$< 40\,000$	120 s	120 s
	40 000 - 100 000	60 s	60 s
	$> 100\,000$	60 s	30 s
0.2	$< 40\,000$	120 s	120 s
	40 000 - 100 000	120 s	60 s
	$> 100\,000$	60 s	30 s

Table 5.1: Sampling times for force and pressure experiments

5.2.3 NACA 0015

Figs 5.3 - 5.5 show results for the $c/H = 0.1$ NACA 0015 aerofoil for lift, drag and moment about the quarter chord, plotted against incidence. All figures include (a) a plot from $-4°$ to 184°, and (b) $-4°$ to 15°, focussing on the attached flow region. Fig. 5.6 shows the lift/drag polar for the aerofoil, with (a) a plot for all the results from $-4°$ to 184°, and (b) showing $-4°$ to the point at which stall occurs.

Results were taken with increasing incidence over the full incidence range, with at least four runs taken at each Reynolds number. An exception to the was $Re = 20\,000$, for which only three runs were taken due to the length of time required for the runs, and the limited accuracies achieved for this Reynolds number. Decreasing incidence results were taken for a narrower range of angles around the stall point for each Reynolds number other than 20 000 (where no stall occurred). At least three decreasing runs were conducted for each.

The results presented here are averages of all the runs for each Reynolds number. For $Re < 100\,000$, there is very little hysteresis between the increasing and decreasing results, so averages at these Reynolds numbers have been calculated taking all increasing and decreasing results together. For $Re \geq 100\,000$, results are averaged for increasing and decreasing incidence

separately, and both are shown here. For example, in Fig. 5.3(b), lift for the $Re = 250\,000$ case with slowly increasing incidence can be seen to stall at 12° - 13°, but with decreasing incidence flow does not fully reattach until 10°. Similar effects can be seen in drag and moment plots. In the polar plots, decreasing incidence runs are plotted with lighter weighted lines and smaller point markers. Note that due to the low drag scale on this plot, some small discrepancies can be seen between increasing and decreasing incidence runs outside of the incidence ranges affected by hysteresis. These are within the experimental error limits established in Section 4.7.

Drag at $Re = 20\,000$, see Fig. 5.4, is negative at incidences below 1°. This is obviously inaccurate, due to limitations when measuring forces as low as those generated by the aerofoil at such a low Reynolds number, as covered in the previous section. Other than that, attached flow results show the expected patterns, maximum lift and stall angle increase with Reynolds number, for both the increasing and decreasing incidence runs. Drag decreases with increasing Re where flow is attached. Post-stall, there is a slight positive correlation between Reynolds number and lift and drag, but the performance here is remarkably similar across all the Reynolds numbers tested. See Section 5.4 for more on Reynolds number effects. There are some unusual behaviours at Reynolds numbers of less than $100,000$ for attached flows, which are discussed alongside validation against existing studies below.

Validation

Figs 5.7 - 5.9 show results from the current study for lift, drag and moment about the quarter chord alongside selected studies for the NACA 0015 and NACA 0012. NACA 0012 results should be very similar to those of the NACA 0015 where flow is separated, since the curvature of the suction surface has limited impact on the forces induced on the aerofoil. For more detail on the referenced studies, refer to Appendix A. The post-stall results of Figs 5.7 - 5.9 represent, to the best of the author's knowledge, an exhaustive review of studies covering extensive deep stall incidences for the NACA 0012 and 0015. See Timmer [49] for a review of NACA 0012 data and Lindenberg [50] for a more comprehensive review including cambered aerofoils. Critzos et al. [34] and Sheldahl and Klimas [20] tested at a range of Reynolds numbers. Here, their lowest Re data is reproduced as it is closest to those used in the current study. Note that results for $Re = 200\,000$ from the current study are used for comparisons,

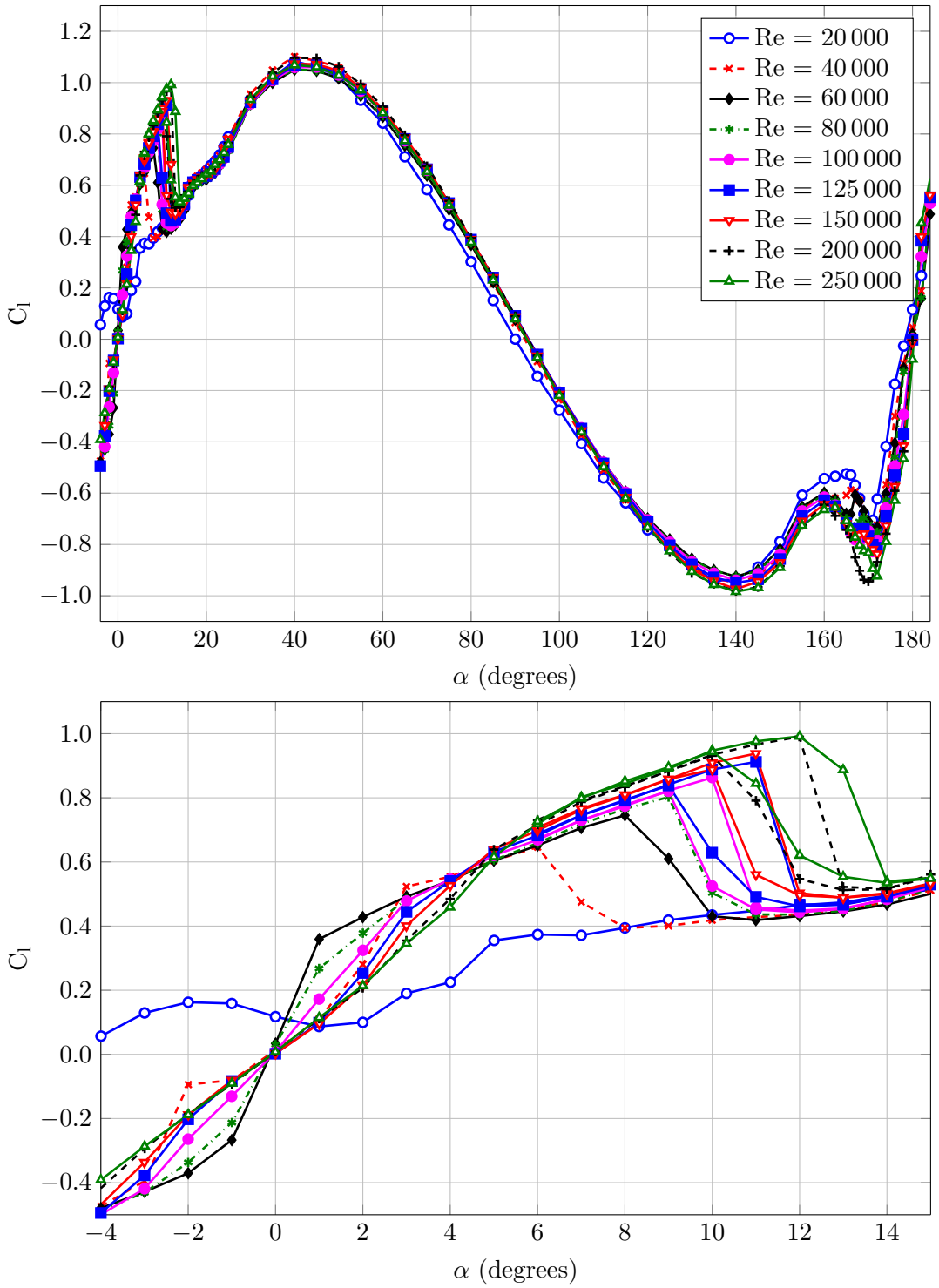


Figure 5.3: C_l vs α for the $c/H = 0.1$ NACA 0015 aerofoil taken in the tolerant tunnel, DS-71 configuration at various Re. (a) $-4° \leq \alpha \leq 184°$, (b) $-4° \leq \alpha \leq 15°$.

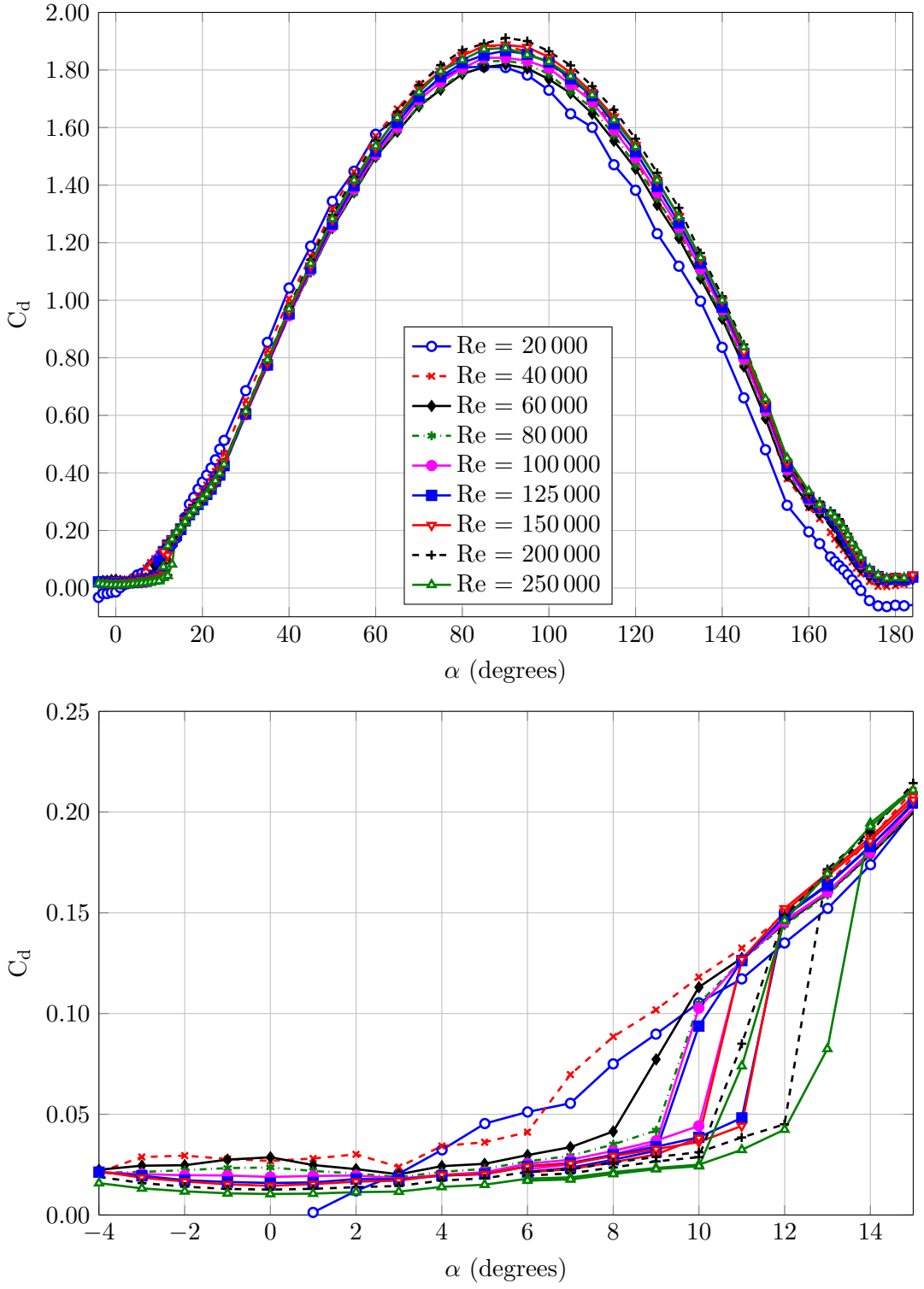


Figure 5.4: C_d vs α for the $c/H = 0.1$ NACA 0015 aerofoil taken in the tolerant tunnel, DS-71 configuration at various Re. (a) $-4° \leq \alpha \leq 184°$, (b) $-4° \leq \alpha \leq 15°$.

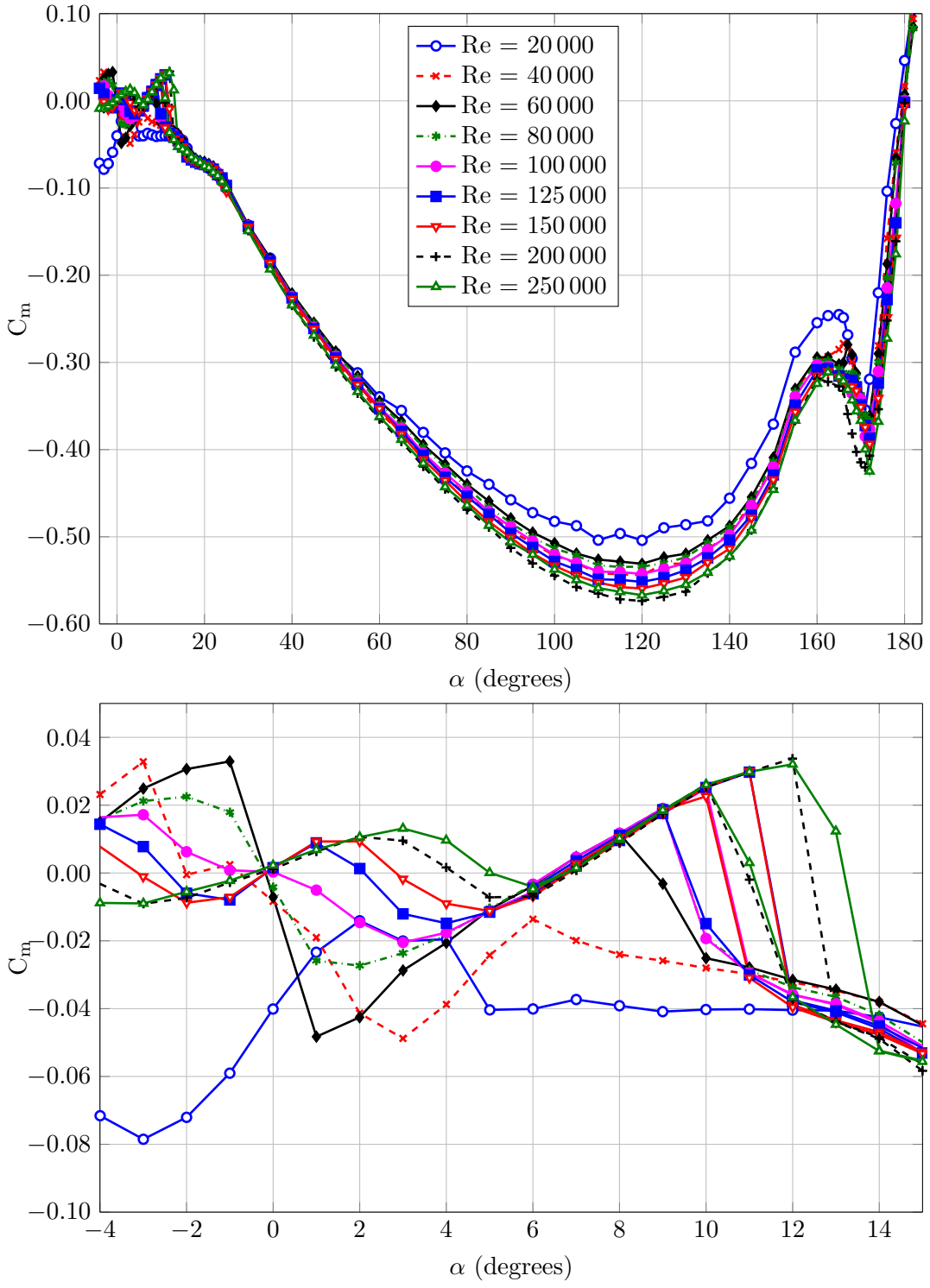


Figure 5.5: C_m vs α for the $c/H = 0.1$ NACA 0015 aerofoil taken in the tolerant tunnel, DS-71 configuration at various Re. (a) $-4° \leq \alpha \leq 184°$, (b) $-4° \leq \alpha \leq 15°$.

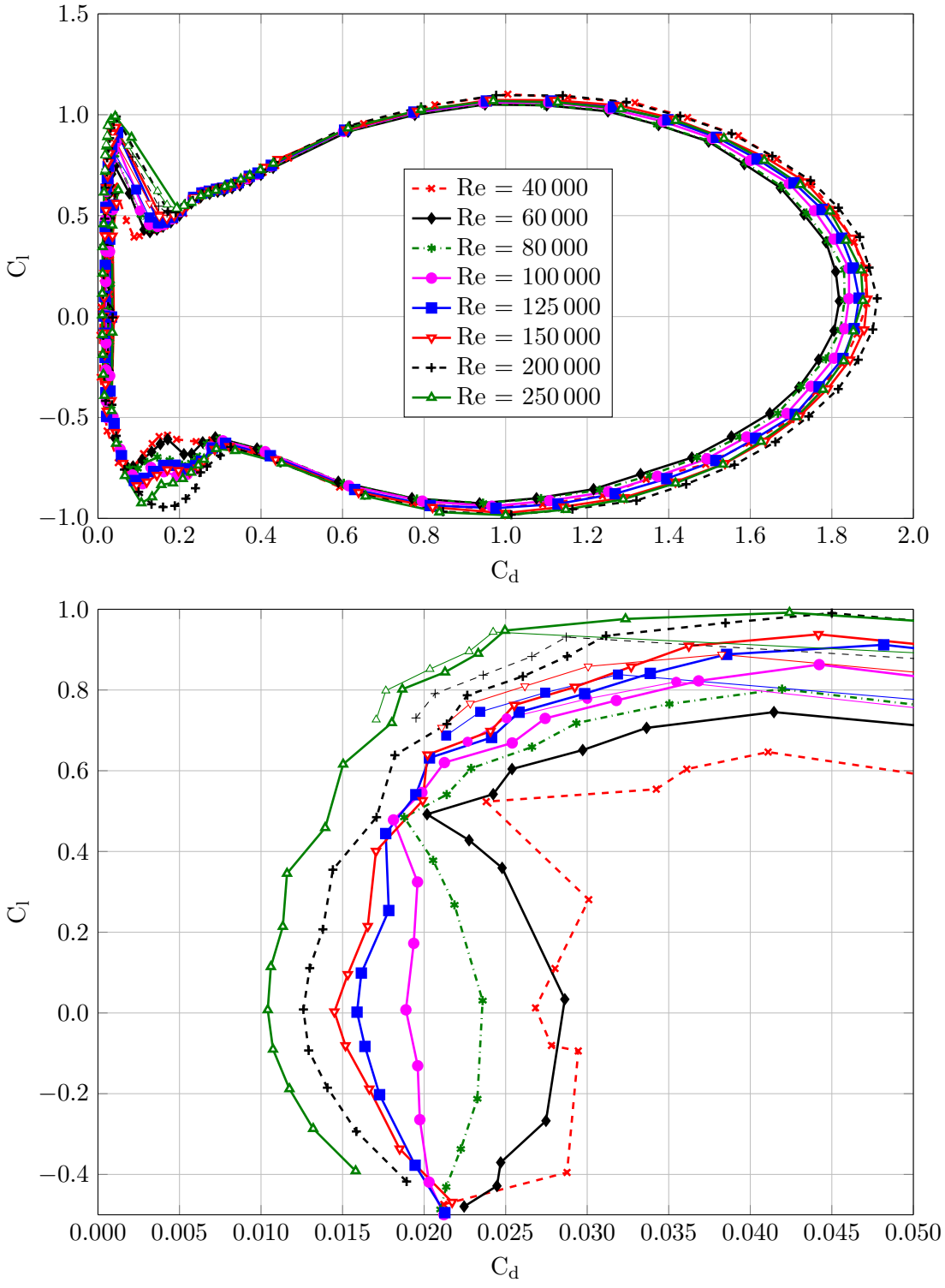


Figure 5.6: C_l vs C_d polar for the $c/H = 0.1$ NACA 0015 aerofoil taken in the tolerant tunnel, DS-71 configuration at various Re. (a) $-4° \leq \alpha \leq 184°$, (b) $-4° \leq \alpha \leq$ stall.

rather that $Re = 250\,000$. The forces induced on the $c/H = 0.1$ aerofoil at the higher Re were at the upper limits of the transducer ranges and may have been affected by sensor saturation. The $Re = 250\,000$ do not follow the trend of higher lift and drag results post-stall with higher Reynolds number, see Section 5.4.

Pope's study [36] exhibits lower post-stall peaks in spite of the far higher Reynolds number of the experiment. This is most likely the result of the unusual blockage reduction technique used, see Appendix A.1.2. See also pressure results from his study compared to others in Section 5.1, which show the atypical suction surface results of the study when flow is separated. Pope's moment data exhibits some scatter but it is much smoother than Sheldahl and Klimas's. Again, the peaks are much lower than those of the current study.

Agreement between the current study, Sheldahl and Klimas, and the NACA 0012 studies is reasonable, with good agreement to that of Sheldahl and Klimas and Bergeles et al. [33] for lift and drag, though there is a fair amount of scatter in the former reference's drag results at $70° < \alpha < 110°$. For moment, Bergeles et. al has a significantly lower trough post-stall and Sheldahl and Klimas has such extensive scatter as to be unusable post-stall. Critzos et al. [34] and Massini et al. [35] have slightly higher peaks for all relevant coefficients over most of the post-stall region (Massini et al. do not provide moment data).

All the referenced studies (excluding Pope) have low c/H of between 0.07 and 0.14 and use a variety of blockage corrections, see Ch 2 for a review of blockage corrections and Appendix A for more detail on the studies. The 10% variation between the post-stall peaks of the studies (excluding Pope) is not much larger than the variations between blockage corrections demonstrated in Fig. 2.10. Remaining differences are the result of Reynolds number and aerofoil thickness effects, as well as other inconsistencies between the experiments, and experimental error.

Figs 5.7(b) and 5.8(b) include results for the current study alongside Jacobs and Sherman [43], the only study the author could find that has tested the NACA 0015 at similar Reynolds numbers, and two NACA 0012 studies [8, 41]. Jacobs and Sherman's study has been corrected from finite wing experiments in a wind tunnel with high turbulence intensity. Stall point should be reasonably accurately rendered to within a few degrees. The characteristic kink in the lift curves of the infinite wings is not present in Jacobs and Sherman's lift curve. This is because low aspect ratio wings at low Reynolds numbers have more linear lift-incidence

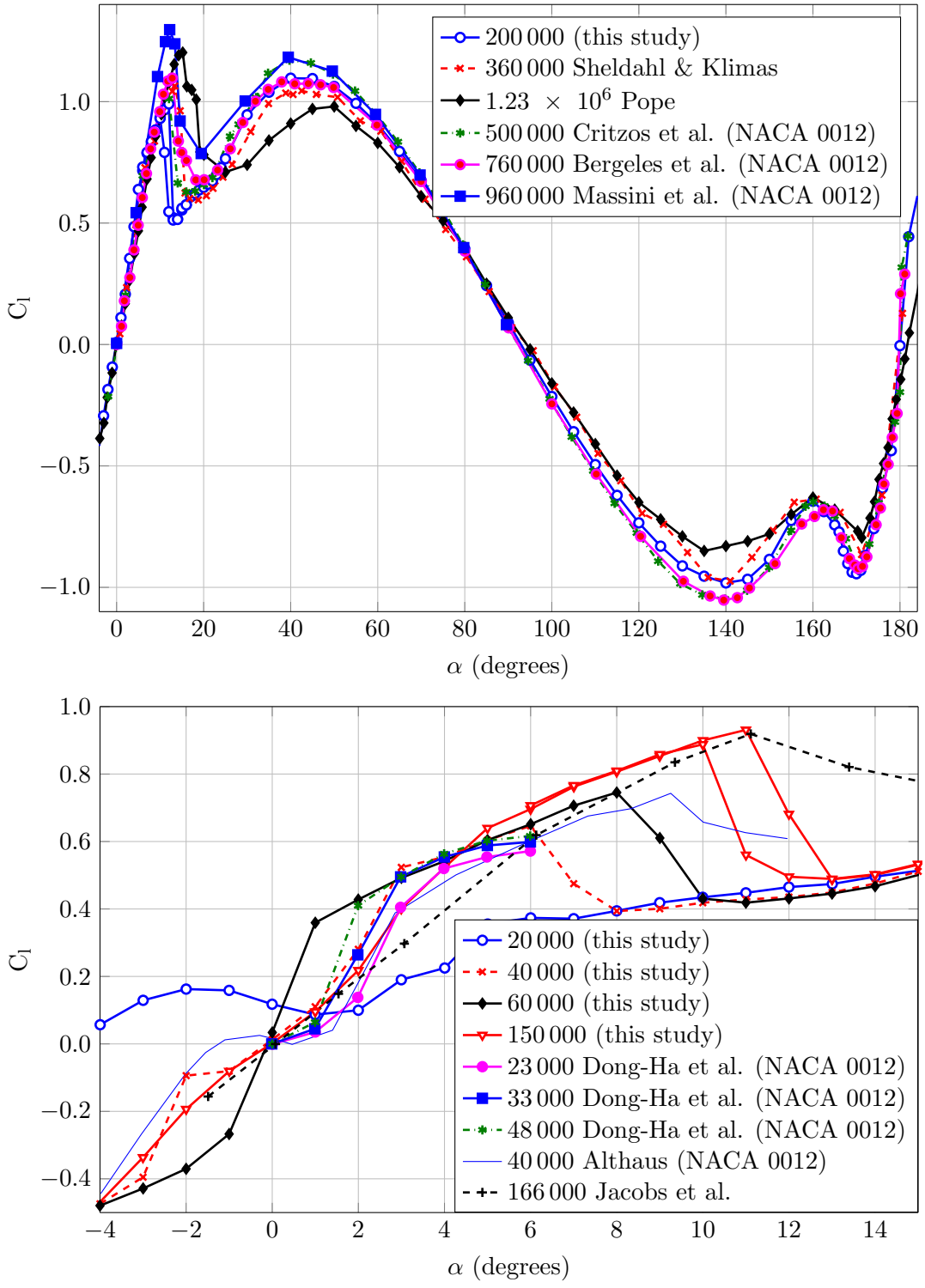


Figure 5.7: C_l vs α from various NACA 0015 and NACA 0012 studies. (a) $-4° \leq \alpha \leq 184°$, (b) $-4° \leq \alpha \leq 15°$.

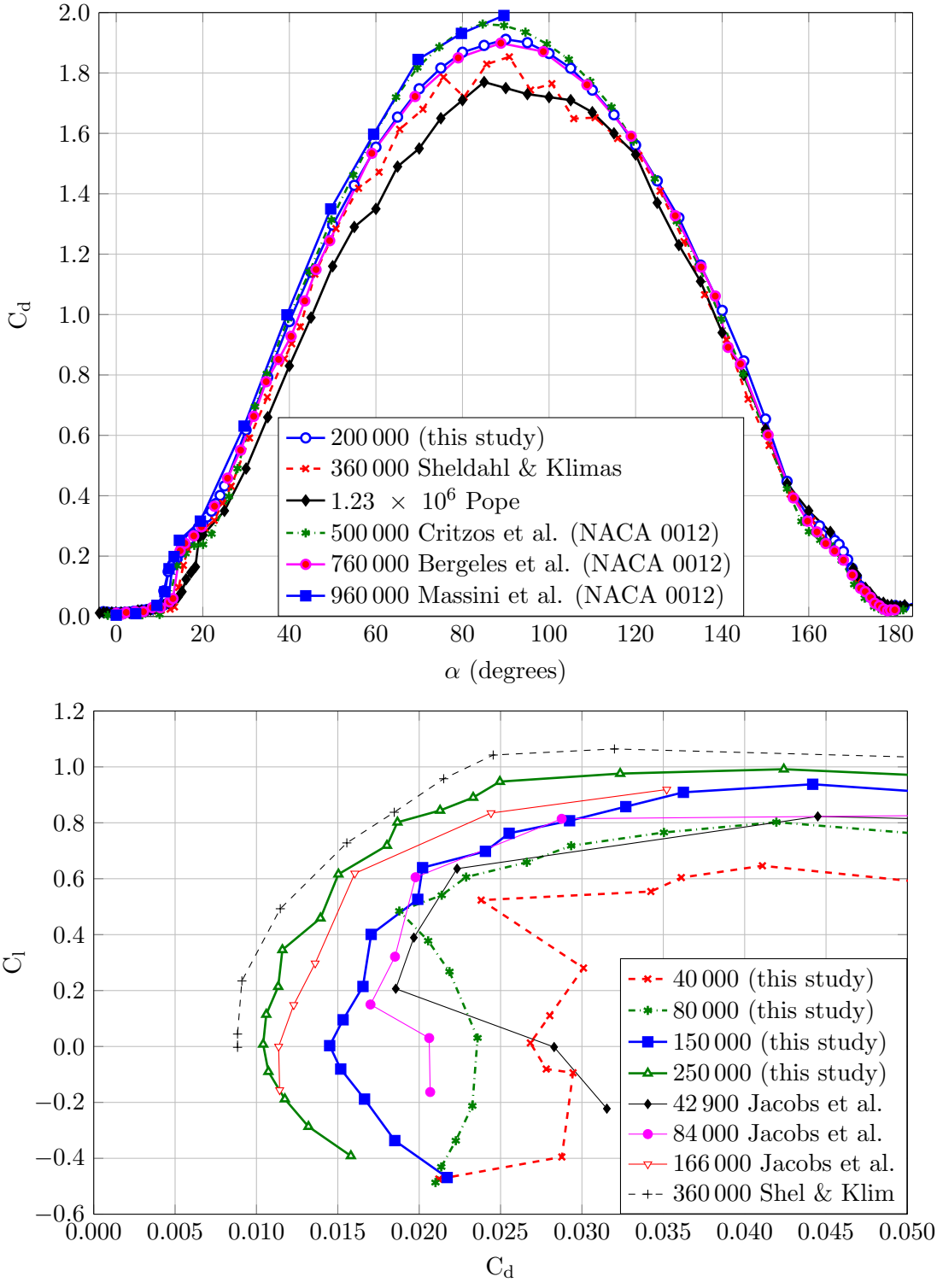


Figure 5.8: C_d vs α from various NACA 0015 and NACA 0012 studies. (a) $-4° \leq \alpha \leq 184°$, (b) $-4° \leq \alpha \leq 15°$.

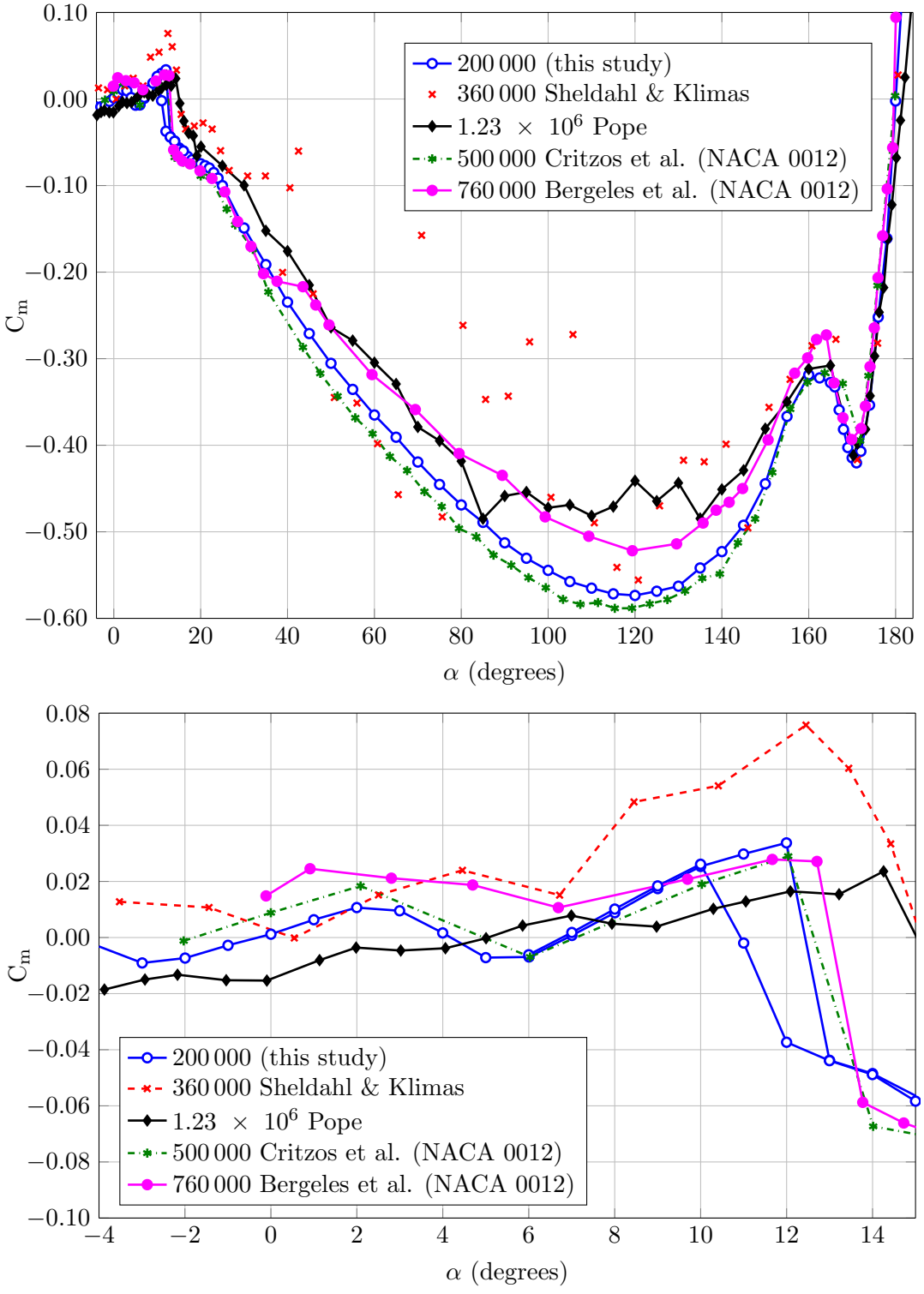


Figure 5.9: C_m vs α from various NACA 0015 and NACA 0012 studies. (a) $-4° \leq \alpha \leq 184°$, (b) $-4° \leq \alpha \leq 15°$.

curves than infinite aerofoils [85]. Stall is delayed to higher incidences for finite wings. This occurs at $\alpha = 11.34°$ with $C_{l\,\max} = 0.92$ for $Re = 166\,000$, values close to those of the current study at $Re = 150\,000$.

The laminar separation bubble that causes the kink in the lift curve has less of an impact on the performance of wings since it does not extend across the whole span. Jacobs's study exhibits a far smoother lift curve up to its stall point, close to a straight line from $\alpha = 0°$. Lifting line theory is not valid beyond stall; though Jacobs and Sherman apply additional corrections near to stall the curves still look an unrealistic approximation of two-dimensional aerofoils.

The study also provides results at $Re = 42\,900$ and $84\,000$ [43]. These show poor agreement to the equivalent Reynolds numbers of the current study. Here, at $Re = 40\,000$, stall occurs at $\alpha = 6°$ but at $\alpha = 9.5°$ for the reference. At $Re = 80\,000$, stall occurs at $\alpha = 9°$ but at $\alpha = 11.5°$ in the reference. This is partly due to the aforementioned finite wing effects and high tunnel turbulence, but in a review of just two-dimensional aerofoil studies, Selig noted significant differences between data from different studies where $Re < 100\,000$ [53]. Carmicheal found similar [28] in his low Reynolds number survey. Miley found smaller, but still significant, differences between results for the NACA 4415 taken at $Re = 1.5 \times 10^6$, a reasonably high Reynolds number [30] (Lissaman defines low Reynolds numbers as the range of 10^4 to 10^6 [86]).

Selig and Lissaman give the following reasons for the discrepancies between datasets at low Reynolds numbers:

- Flow quality: small differences in turbulence intensity have a large impact at low Re.
- Accuracy of measurements: small errors have a larger impact when variables being measured are low.
- Methods of measurement: again, small differences are accentuated when the variables being measured are low.
- Model accuracy: small variations in profiles have a far greater impact on performance at lower Re, where there is extensive laminar flow. This is particularly true if inaccuracies or roughness are extreme enough to cause premature transition of boundary layers to

turbulent states.

Note that blockage is not significantly responsible for the differences at these low incidences due to the low cross-sectional areas of aerofoils presented to the flow at low incidences.

The reviews of Selig and Carmicheal, alongside the extensive original work of Selig [81], contain a wealth of low Reynolds number data covering incidences to a few degrees beyond stall. Unfortunately they provide nothing on the NACA 0015, nor the 0012 or 0018. Comparing even similar aerofoils at low Reynolds numbers where flow is attached is of limited use, given the large impact of small differences in aerofoil shape, but NACA 0012 studies are included in Fig. 5.7(b) in lieu of any suitable NACA 0015 studies. Althaus's $Re = 40\,000$ results [8] are included as they exhibit similar unusual behaviour at incidences near to $\alpha = 0°$ as the results of the current study at $Re = 20\,000$. Lift decreases with increasing incidence in some regions, a feature not usually seen with attached flow. Both studies show positive lift at 0°, almost certainly the result of inaccuracies associated with measuring such low forces.

Laminar separation: the lift curve "bump" at low Reynolds numbers and the separation bubble at $Re > 20\,000$

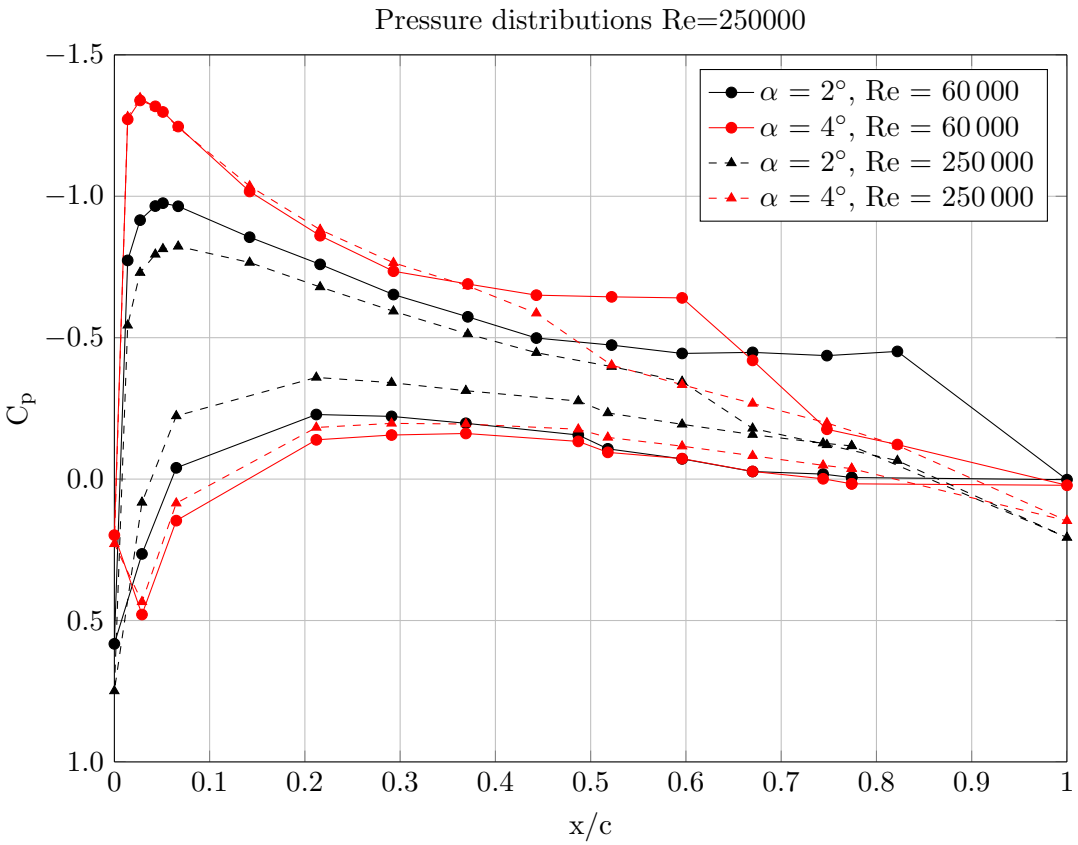
Dong-Ha's study over a limited range of incidences of 0° to 6° [41] is included as it exhibits similar extreme "bumps" in lift curves at incidences between 1° and 3°, and local drag maxima at $\alpha = 0°$, to the current study. For $Re = 40\,000$, $60\,000$ and $80\,000$, drag reduces from this local maxima to a minimum at $\alpha = 6°$, see Fig. 5.4(b) and 5.6(b). These unusual low Reynolds number polars, concave towards the C_l axis for $Re < 100\,000$, were noted by Selig for profiles that, like the NACA 0015, were not designed specifically for low Reynolds number applications [53] and are also recognised in types C and D of Carmichael's typical polar forms [28], see Fig. 1.7. Note that the polar for $Re = 40\,000$ is affected by accuracy issues and $Re = 20\,000$ is omitted entirely due to the false negative drag results. Dong-Ha et al's polars are not included on Fig. 5.8(b) for reasons of plot scaling, their drag is far higher than other results: the maximum at $\alpha = 0°$ is around 0.09, reducing to to a minimum at 6 deg of 0.06. Lift and drag were calculated from pressure readings from 24 pressure taps, so accuracy for their drag results will be limited. The figure only includes data from sources were drag is provided with sufficient accuracy (combined plots of lift and drag against incidence are poorly scaled

for drag).

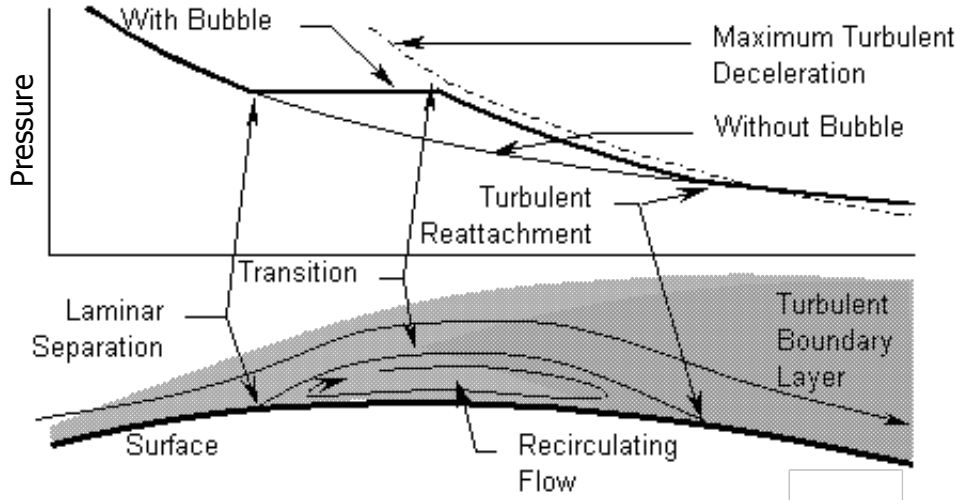
To understand the mechanisms behind this behaviour, it is useful to reexamine the pressure distributions from the previous section. Fig. 5.10a shows the pressure distributions at 2° and 4° for $Re = 60\,000$ and $Re = 250\,000$ for the $c/H = 0.25$ NACA 0015 aerofoil. All the pressure distributions show evidence of laminar separation, see Fig. 5.10b to aid with the interpretation of the distributions. The laminar separation at $\alpha = 2°$ for $Re = 60\,000$ occurs so close to the trailing edge that reattachment may not occur (note that the trailing edge pressure tap is backwards-facing, and not on the suction surface). With increasing incidence comes a stronger adverse pressure gradient on the suction surface, which pulls the point of laminar separation towards the leading edge. The separated boundary layer rapidly transitions to turbulent flow due to the greater susceptibility to do so of separated shear layers [86]. When the separation has moved far enough along the suction surface, the now turbulent boundary layer can reattach before the trailing edge (see Section 1.5.5 on laminar separation bubbles), as can be seen at $\alpha = 4°$ at $0.75c$, forming a laminar separation bubble. This leads to a reduction in drag due to an improvement in the streamlined shape of the aerofoil plus bubble. This behaviour at low incidences and low Reynolds numbers is supported by the smoke stream flow visualisations of Dong-Ha et al for the NACA 0012, see Fig. 5.11. At $\alpha = 2°$ at $Re = 23\,000$, the transition point can be seen to occur near the trailing edge, with insufficient distance on the aerofoil for flow to reattach. At $\alpha = 3°$, reattachment of the, now turbulent, boundary layer does occur. For $Re = 48\,000$, this difference in behaviour can be seen between $\alpha = 1°$ and $\alpha = 2°$.

The reason for the extreme lift "bumps" is thought to be the following. At certain incidences, for example 1° at $Re = 60\,000$, where flow separates and is unable to reattach before the trailing edge, virtual additional length is added to the aerofoil, in much the same way as a flatback aerofoil operates. See Fig. 5.11(g), where the streamlines around the aerofoil and bubble are the shape of a larger aerofoil. It's this artificial length, and the higher lift force generated with its help, that gives the "bump", coming at the expense of higher drag coefficients. At higher incidences when flow is able to reattach, the artificial length is removed from the aerofoil, the gradient of the lift/incidence curve and the drag coefficient is reducing accordingly.

At $Re = 40\,000$, the laminar separation bubble is longer than for at $60\,000$, so flow is not



(a) Pressure distributions for the $c/H = 0.25$ NACA 0015 aerofoil at $\alpha = 2°$ and $4°$, at $Re = 60\,000$ and $250\,000$.



(b) Diagram of laminar separation bubble (below) with surface pressure distribution (above) [87].

Figure 5.10: Pressure distributions and laminar separation bubbles

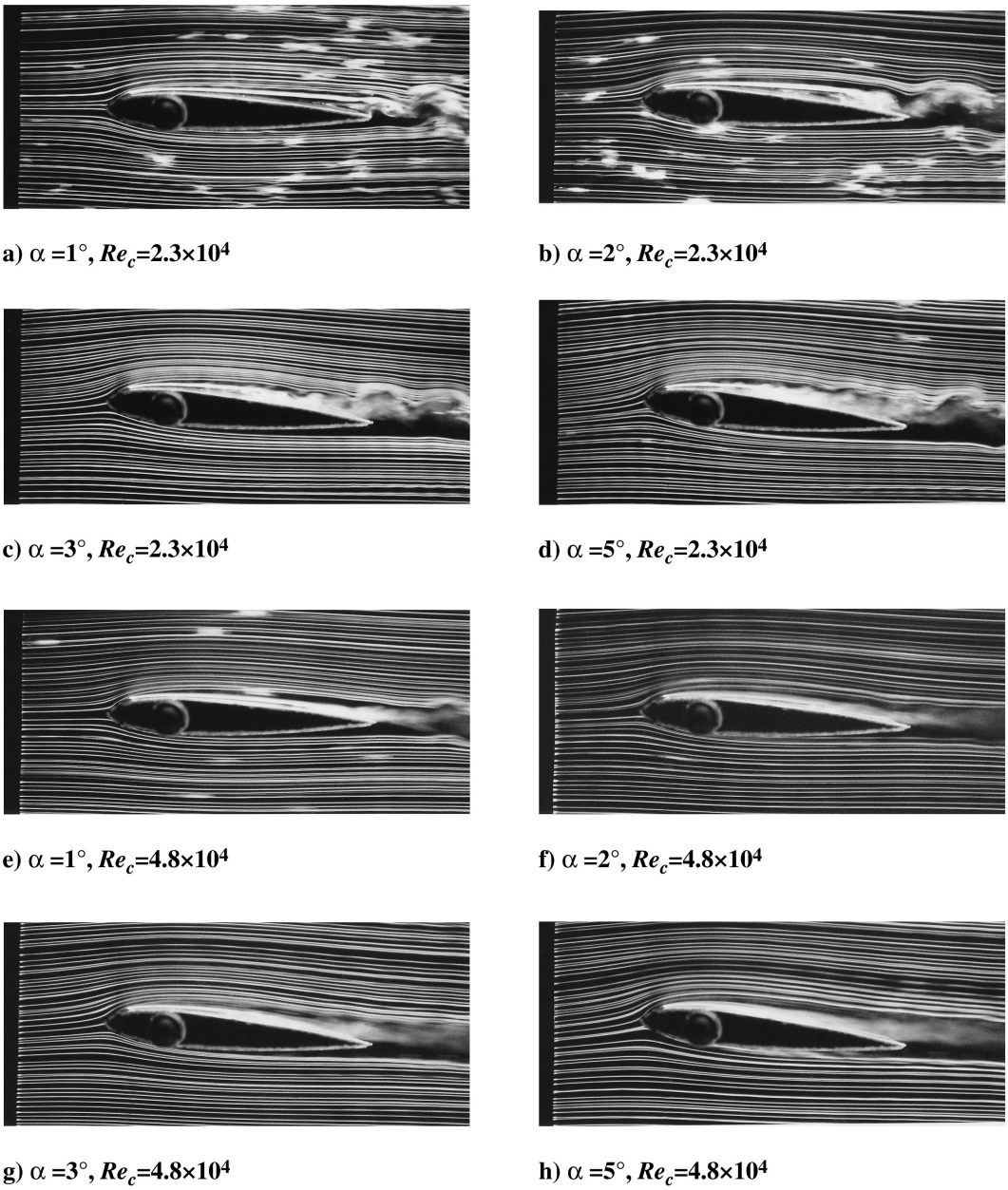


Figure 5.11: Smoke stream flow visualisation for a low incidence, low Reynolds number NACA 0012 [41].

able to reattach until a higher incidence of 3° is reached. For $Re = 20\,000$, the flow is never able to reattach. Zhou's NACA 0012 study [42] shows a similar lack of any attached flow or stall characteristic at $Re = 5\,300$, but does exhibit flow attachment and subsequent stall at $Re = 10\,500$ and $51\,000$. This Reynolds number at which flow is able to reattach is known as the critical Reynolds number [86, 28], see Section 5.4 for more on this.

Laminar separation occurs at similar locations along the suction surface at both $Re = 60\,000$ and $250\,000$, at $0.45c$ at 2° and $0.3c$ at 4°. The pressure gradients are near identical at both Reynolds numbers, but at $250\,000$ transition and reattachment occur over a much shorter length, resulting in a smaller bubble, ending at $0.67c$ at 2° and $0.52c$ at 4°. This smaller bubble has less of an impact on aerofoil performance, meaning there is far less of a "bump" in the lift incidence curve and the drag minimum occurs at $\alpha = 0°$.

All three Reynolds numbers tested with tapped aerofoils ($60\,000$, $150\,000$ and $250\,000$) have a bubble at higher incidences, towards the leading edge of the aerofoil's suction surface. This has an impact on lift curve slope, making it shallower than $2\pi\alpha$ in the region before stall in both cases. Evidence can be seen of this at all the Reynolds numbers tested.

Stall

According to Gault, at Reynolds numbers below $Re = 800\,000$, only thin aerofoil and trailing edge stall occur [26], depending on leading edge curvature. Here however, for the NACA 0015 and for the three other profiles tested, the stall is a combined thin aerofoil and leading edge stall, displaying characteristics of both.

As with thin aerofoil stall, see Section 1.5, there is a "kink" in the lift curve slope, at 3° - 6° for $Re > 100\,000$, associated with a change in laminar separation bubble behaviour. Below this incidence, the bubble moves towards the trailing edge with increasing incidence and is near to the leading edge at the "kink". As incidence continues to increase, the bubble grows larger, while the rate at which the point of separation moves forward significantly decreases, causing a decrease in the gradient of the lift curve slope (this is particularly noticeable in the 18% thick aerofoils). As with leading edge stall, at a certain incidence, the adverse pressure gradient becomes too great for the bubble to tolerate and it bursts, suddenly separating across the whole of the suction surface. Again, it is helpful to return to pressure distributions to better visualise the mechanisms behind this behaviour. Fig. 5.12 contains distributions at incidences between 6° and 13° taken at $Re = 150\,000$ for the $c/H = 0.25$ aerofoil, showing the slowing rate of movement towards the leading edge, bubble growth (particularly between 10° and 12°) and the sudden, complete separation of flow at $\alpha = 13°$.

Following Carmichael's typical lift slope forms [28], see Fig. 1.7, the aerofoil demonstrates a type D lift curve (with hystereses around stall) at all Reynolds numbers above $80\,000$. Below

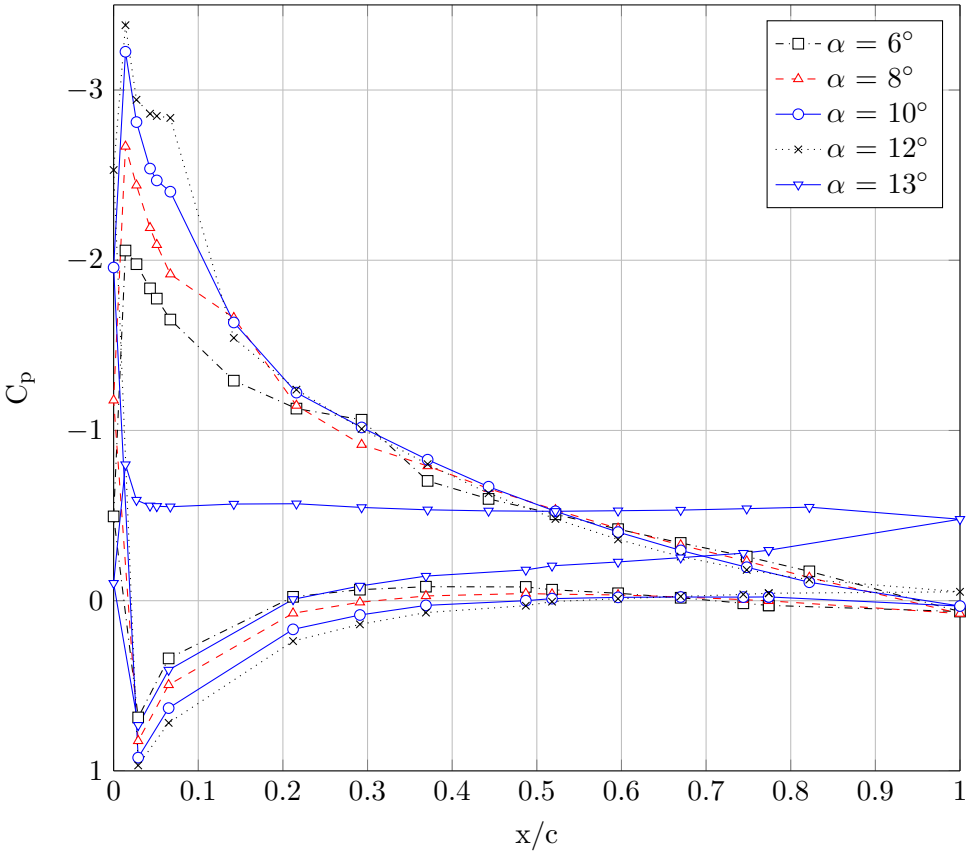


Figure 5.12: Pressure distributions at incidences around stall angle for the $c/H = 0.25$ aerofoil at $Re = 150\,000$.

this, type B, with no hysteresis and non-linear lift, is given. At $Re = 20\,000$ this regresses to type E. Polar types are type A[1] at $Re > 100\,000$ and type D below this. No polar was produced at $Re = 20\,000$ due to low accuracy of drag measurements.

The laminar separation bubbles are responsible for the hysteresis visible around stall in results for $Re > 80\,000$. Once the flow is separated and incidences are reduced below the stall angle, the flow will not reattach again until an incidence a number of degrees below the stall angle is reached, when the pressure gradient is sufficiently low enough for a bubble to reform.

5.2.4 NACA 0018

The experimental set-up and methodologies are mostly identical between the NACA 0015 and 0018, any differences are discussed below. Here, there is no $Re = 20\,000$ run, as the forces were too low to be practically measured, for the reasons given in Section 4.7.

At the upper end of the Reynolds number range, it has been possible to test up to $Re = 300\,000$ without saturating the force transducers. Tests at this Reynolds number were conducted over a limited incidence range of $-4°$ to $20°$ to limit the risk of saturation, since the variation in post-stall lift and drag is not significant at the higher end of the Reynolds number range tested. Figs 5.13 - 5.16 give plots of lift, drag and moment coefficients against incidence, and C_l vs. C_d polars, for $-4°$ - $184°$ and over a narrower range of $-4°$ - $22°$, focussing on the attached flow performance of the aerofoil.

The NACA 0018 exhibits no stall behaviour at $Re = 40\,000$, suggesting that a laminar bubble is never able to form in these flow conditions and flow never attaches to the suction surface, as for the NACA 0015 at $Re = 20\,000$, see Section 5.2.3. The critical Reynolds number at which flow can reattach is higher for the NACA 0018 than the 0015 due to the greater curvature of the aerofoil's surfaces. A greater adverse pressure gradient results on the suction surface of the NACA 0018 past the point of maximum thickness, making it harder for separated boundary layers to reattach.

Given the repeatability and accuracies achieved for the NACA 0015 aerofoil, fewer repeats were conducted on the NACA 0018. At least two were conducted for each run with increasing incidence (full incidence range) and decreasing incidence (limited to the region around stall). Results presented are the averages of these runs. Where there is no hysteresis between increasing and decreasing incidence runs (at $Re < 100\,000$), averages are taken of increasing and decreasing runs together.

Figs 5.17 - 5.19 show selected results from this study alongside those of Du et al. [37, 68] and Timmer [38], agreement to the latter reference being very good. Stall and reattachment angles are different, but not by more than $1°$ for either the $Re = 150\,000$ or $300\,000$ cases. These differences could be the result of inconsistencies in aerofoil surface finishes or the turbulence levels between the studies, or the approaches taken to minimise the impact of wind tunnel blockage (Timmer uses a solid-walled tunnel and the blockage corrections of AGARD [45] and Hackett [123], see Appendix A.1.3). Attached flow drag is lower for Timmer for the $Re = 150\,000$ runs, which could result from the different measurement techniques used (a wake rake for the reference).

Agreement of moment results are also reasonable. In addition to the causes of differences between lift and drag, here moment was measured about the half chord and quarter cord

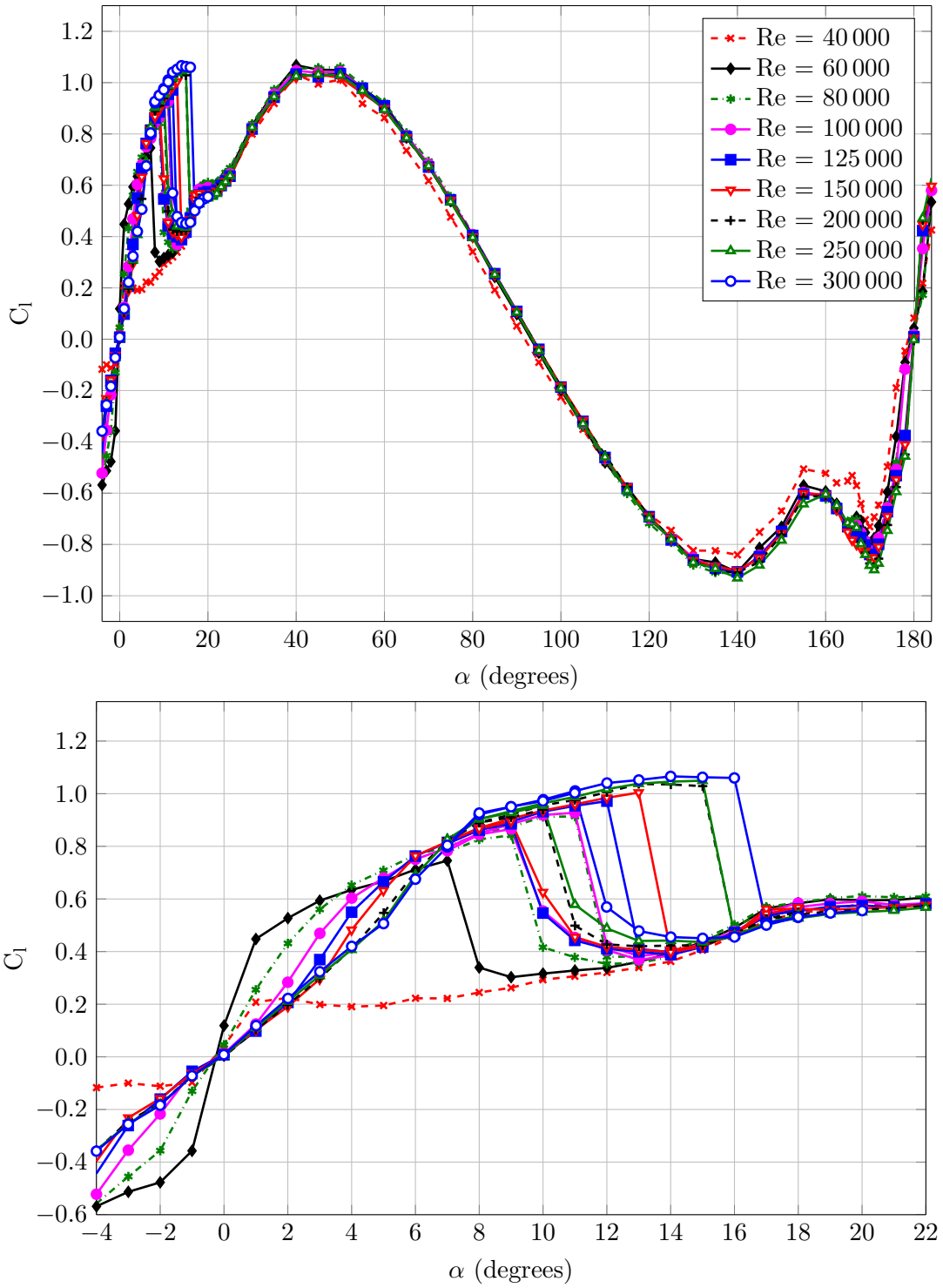


Figure 5.13: C_l vs α for the $c/H = 0.2$ NACA 0018 aerofoil taken in the tolerant tunnel, DS-71 configuration at various Re. (a) $-4° \leq \alpha \leq 184°$, (b) $-4° \leq \alpha \leq 22°$.

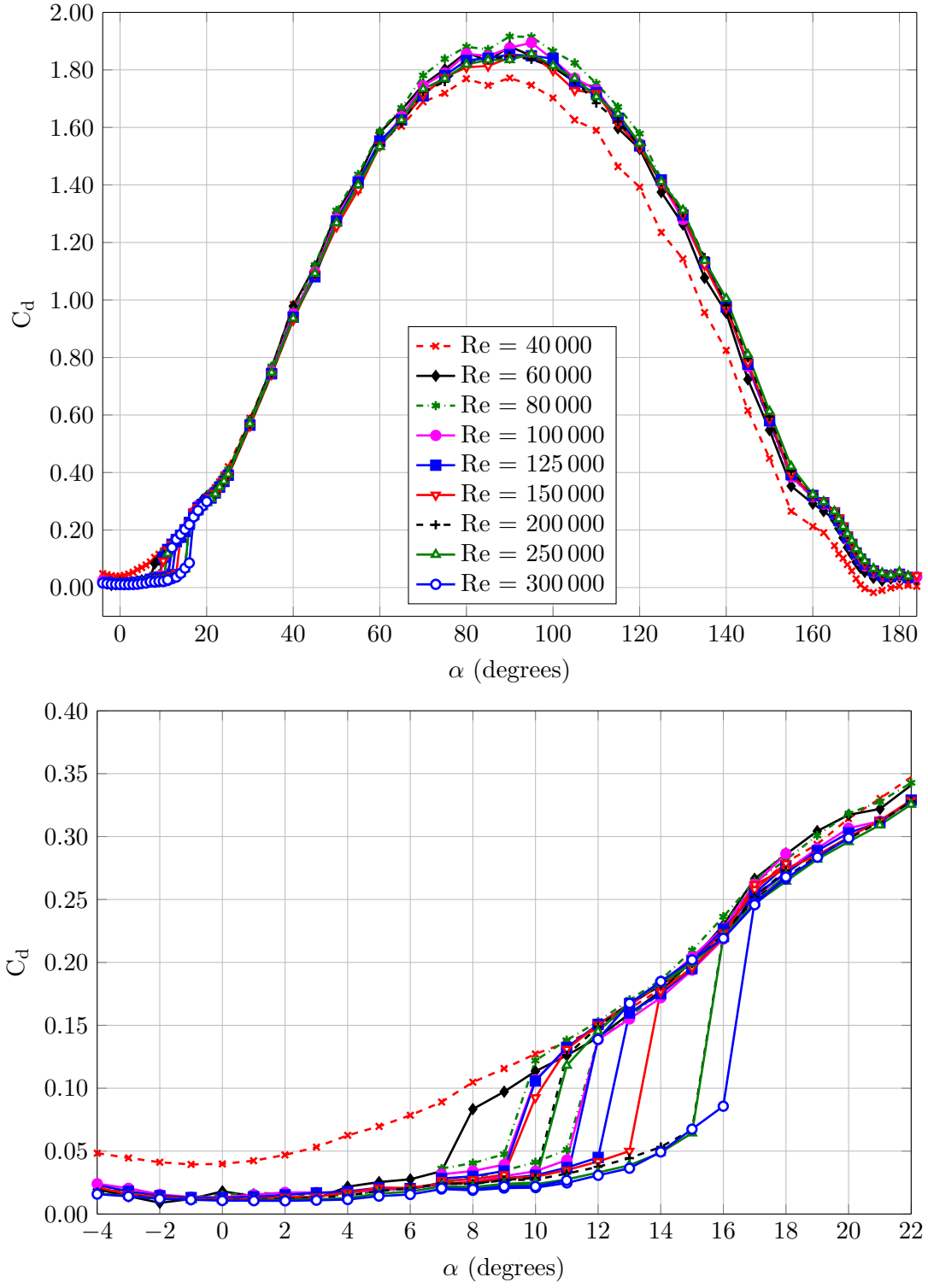


Figure 5.14: C_d vs α for the $c/H = 0.2$ NACA 0018 aerofoil taken in the tolerant tunnel, DS-71 configuration at various Re. (a) $-4° \leq \alpha \leq 184°$, (b) $-4° \leq \alpha \leq 22°$.

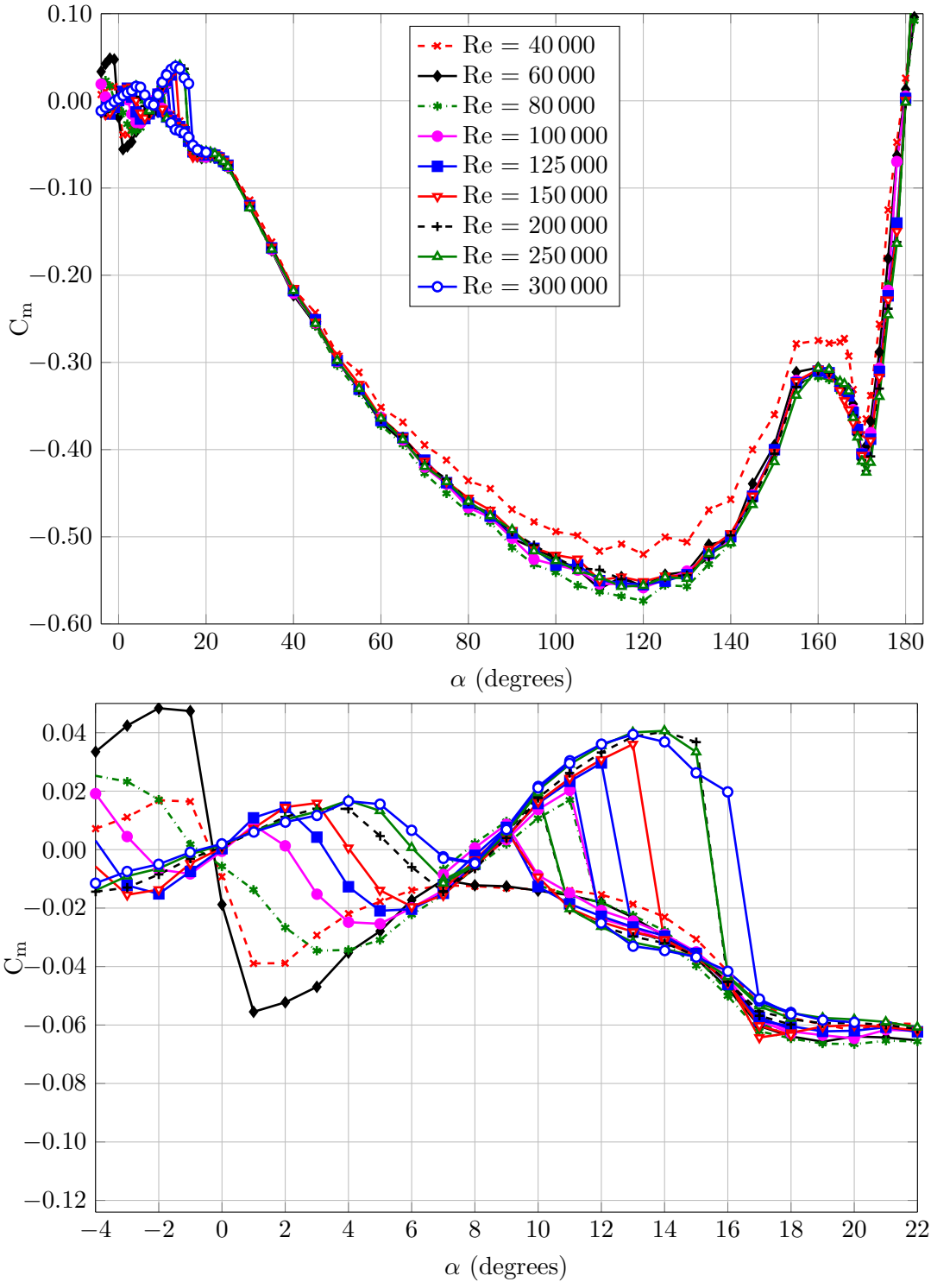


Figure 5.15: C_m vs α for the $c/H = 0.2$ NACA 0018 aerofoil taken in the tolerant tunnel, DS-71 configuration at various Re. (a) $-4° \leq \alpha \leq 184°$, (b) $-4° \leq \alpha \leq 22°$.

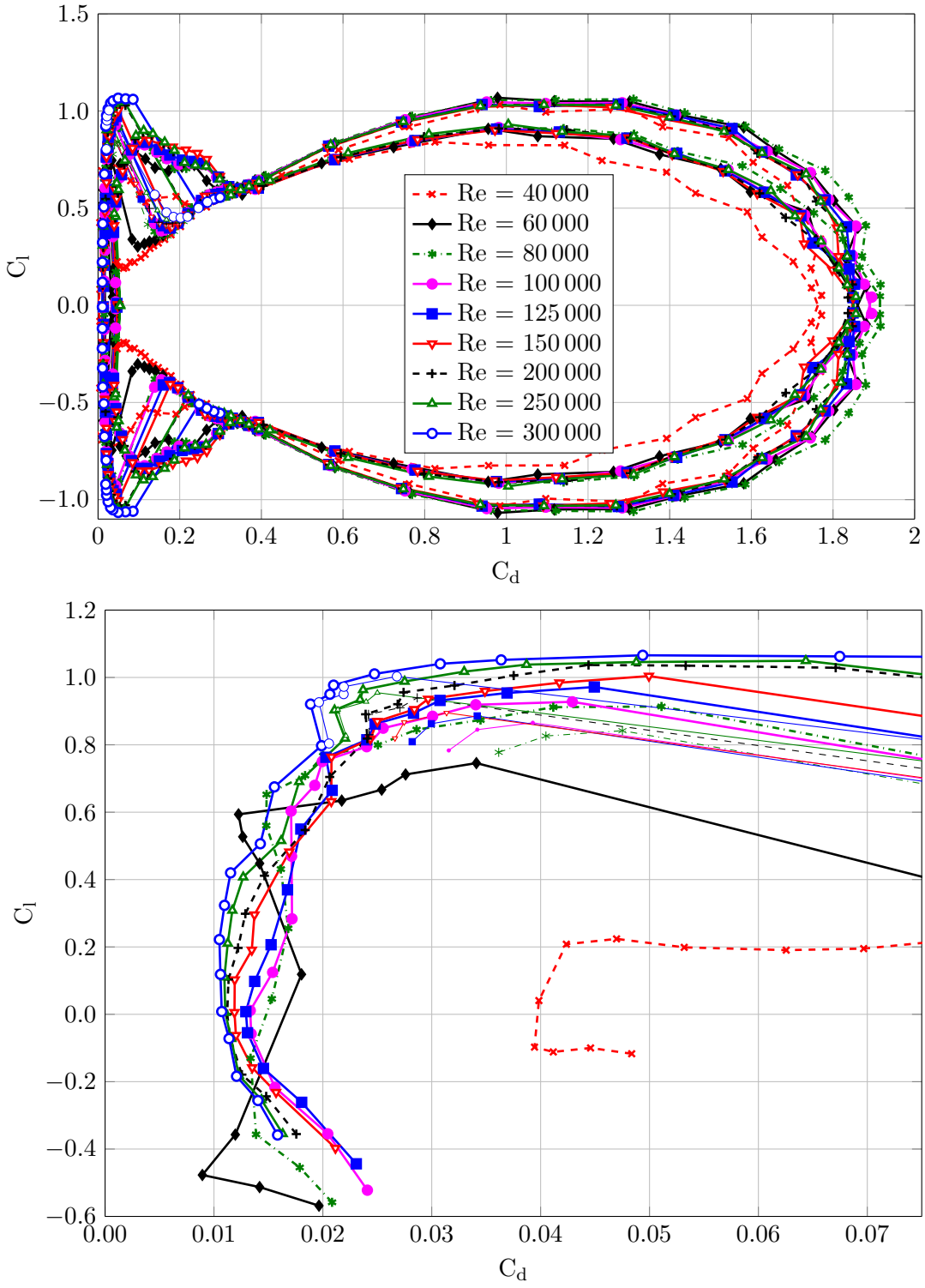


Figure 5.16: C_l vs C_d polar for the $c/H = 0.2$ NACA 0018 aerofoil taken in the tolerant tunnel, DS-71 configuration at various Re. (a) $-4° \leq \alpha \leq 184°$, (b) $-4° \leq \alpha \leq$ stall.

moment calculated from it while Timmer presumably measured directly at the quarter chord (though this is not explicitly stated).

Timmer states that the laminar bubble responsible for the bump in the lift curve slope is on the lower surface of the aerofoil. This is doubtful and not backed up by the pressure distributions for the NACA 0015 presented in Section 5.1. His analysis is based on RFoil output that also shows a bubble on the upper surface per the findings of this study. He removed the lift curve bumps with the application of forced transition at 85% of pressure surface (RFoil) and boundary layer trips at 80% of chord on both suction and pressure surfaces (experiment). It is not clear why a trip so far back along the aerofoil should result in significantly different aerofoil behaviour at the incidences where the bump occurs (at 6° - 8°, where the suction surface laminar separation bubble is upstream of 80% of chord).

Du et al. shows poor agreement to the other studies where flow is attached, with lower lifts attained. This could be partly due to the higher blockage of the experiments ($c/H = 0.28$), the $c/H = 0.3$ NACA 0015 had lower attached flow lifts than the $c/H = 0.2$ in the experiments of Ch. 4. The aforementioned general poor agreement between studies at $Re < 100\,000$ found by Selig [53] is likely responsible for some of the poor agreement observed here too, for the reasons listed in Section 5.2.3. As with Timmer, inconsistencies in aerofoil surface finishes or flow turbulence levels could also contribute to the differences.

Post-stall, agreement to Timmer's study is good, though the study only covers incidences up to 30°. The peaks of Du et al's study are higher for lift, due the higher blockage. The lower drag peaks are due to the overcorrection of the high blockage, as for the $c/H = 0.3$ NACA 0015 aerofoil in Ch. 4.

5.2.5 NACA 0018 cambered transforms

Initial testing of the cambered aerofoils returned some unusual results at low Reynolds numbers, due to the influence of a 360° offsetting process on readings in the main experiment. It proved difficult to isolate these effects, particularly at low Reynolds numbers. Instead, experiments were split into shorter runs of incidences across 60° or 90° and blended in post-processing.

For the cambered aerofoils, the testing process was again made more efficient to make better use of tunnel time. This was possible thanks to the limited variation in performance

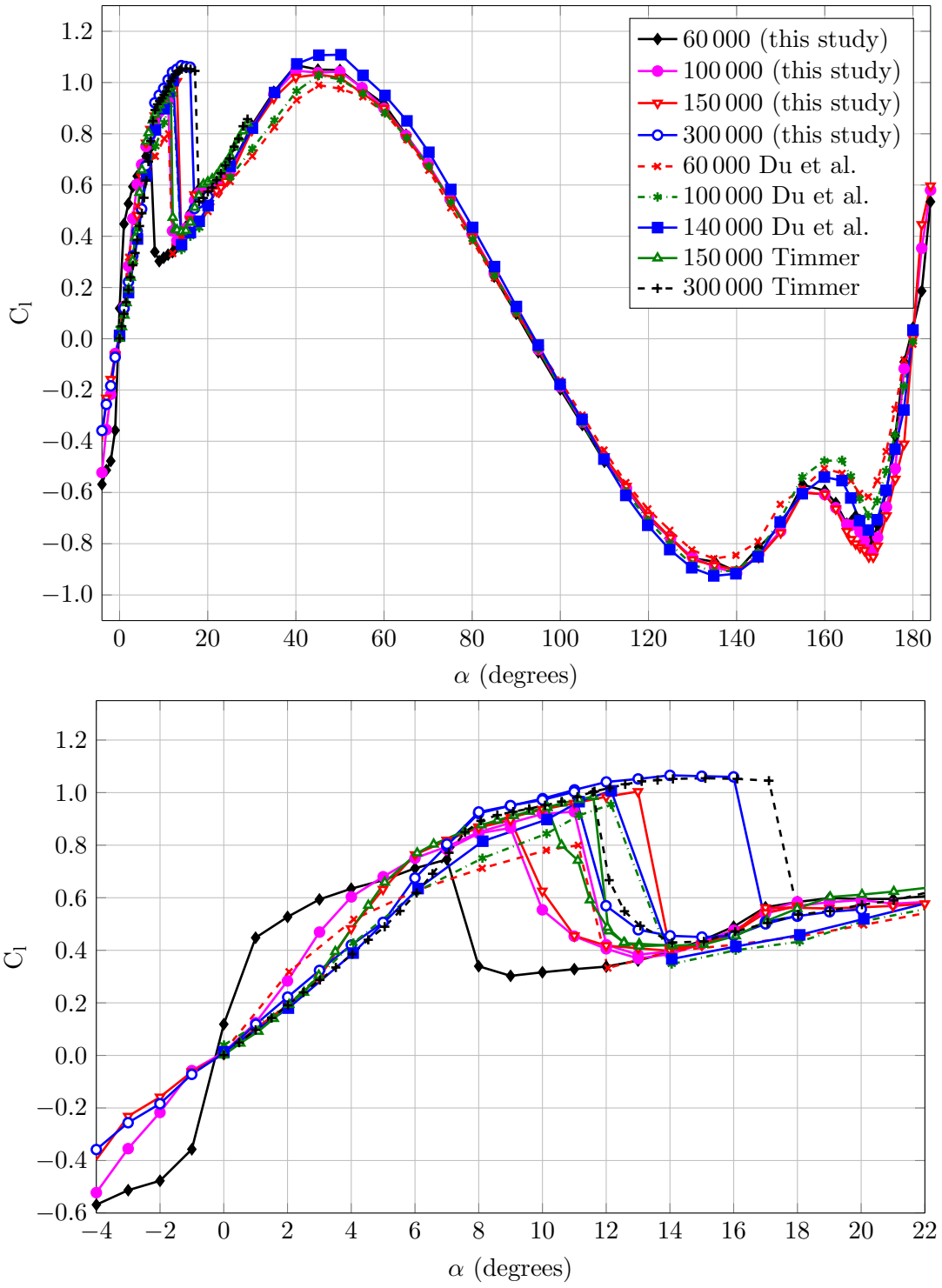


Figure 5.17: C_l vs α from various NACA 0018 studies. (a) $-4° \leq \alpha \leq 184°$, (b) $-4° \leq \alpha \leq 22°$.

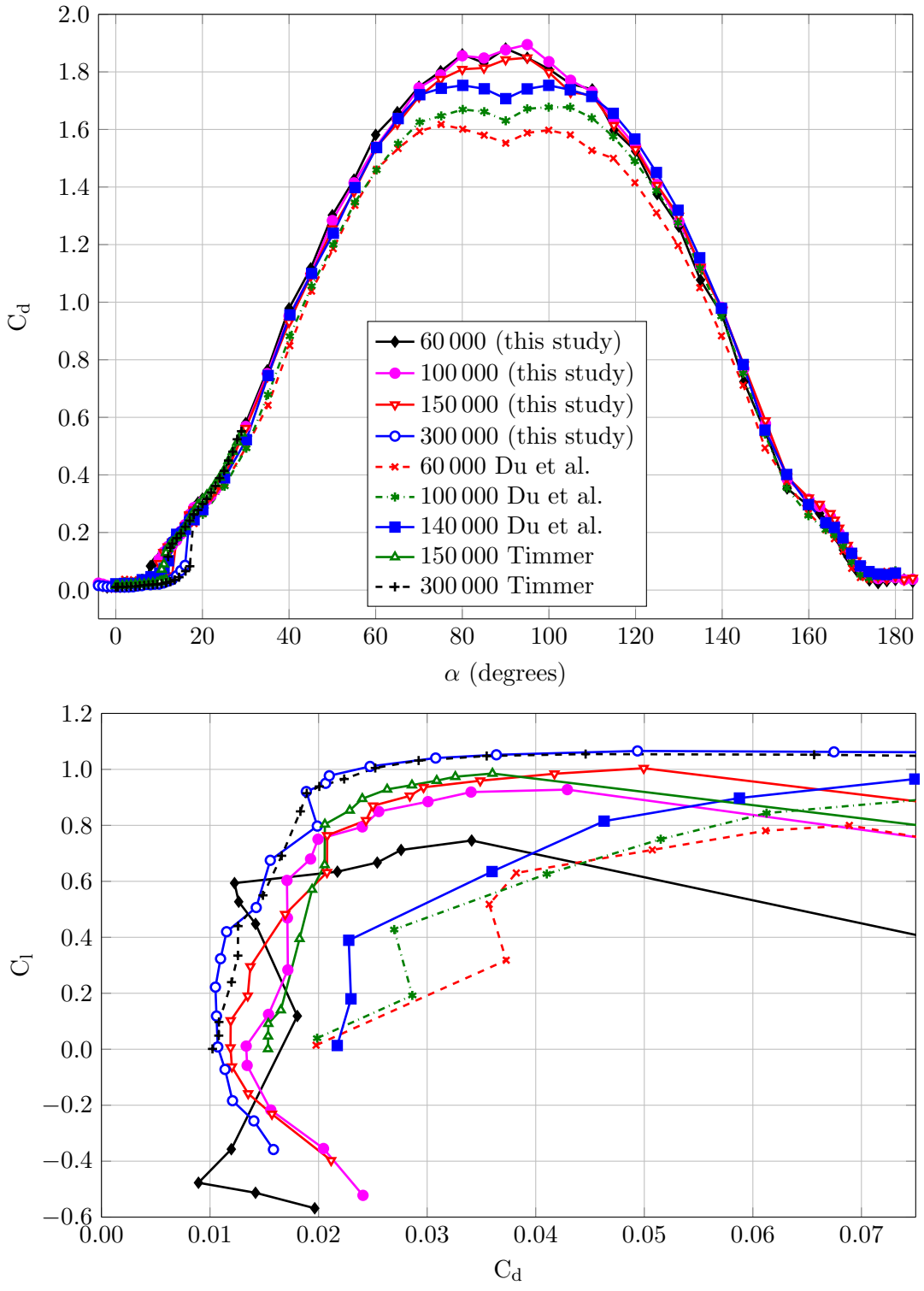


Figure 5.18: (a) C_d vs. α for incidences of $-4°$ to $184°$ and (b) C_l vs. C_d for attached flow, from various NACA 0018 studies.

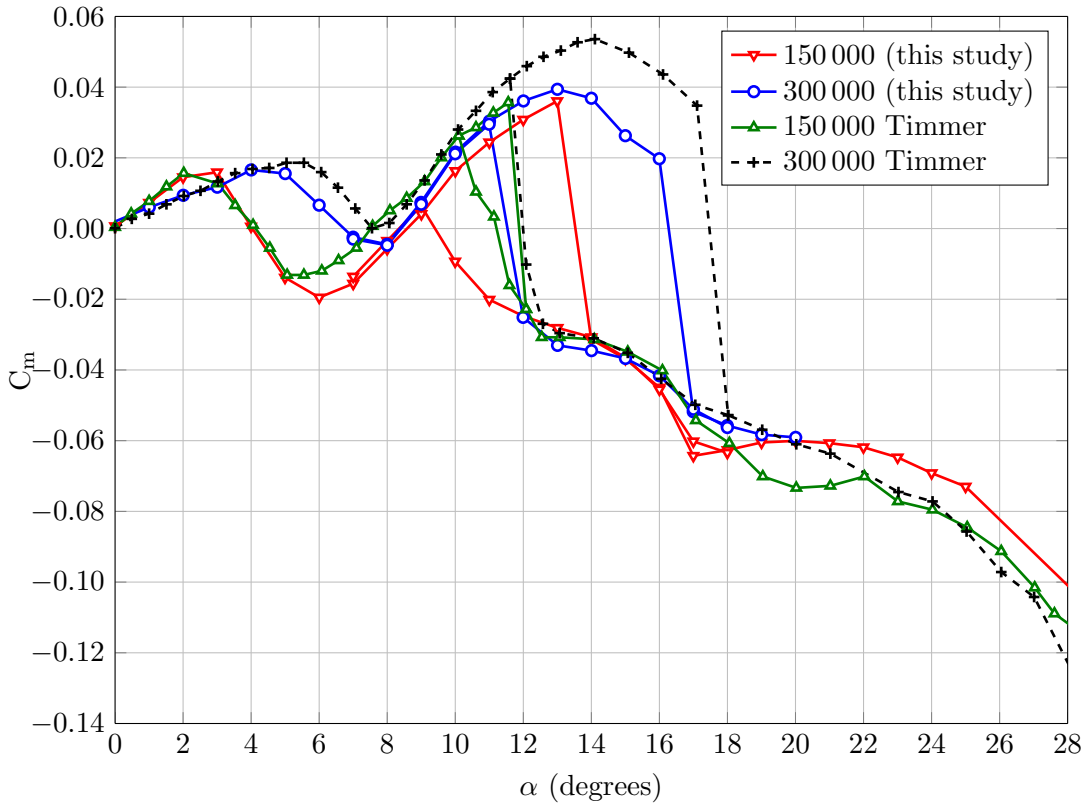


Figure 5.19: C_m vs α from various NACA 0018 studies.

at deeply stalled angles of attack, the strong repeatability of experiments, and the increased accuracy of new techniques with limited incidence ranges tested in each run. Incidences outside the ranges of $-18°$ to $22°$ (for the $c/R = 0.114$ aerofoil) or $-15°$ to $25°$ (for the $c/R = 0.25$ aerofoil) were tested at Reynolds numbers of 60 000, 80 000, 150 000 and 250 000. One run was conducted for each Reynolds number, with validation between the Reynolds numbers used to give additional confidence in the results.

The $-18°$ to $22°$ ($c/R = 0.114$ aerofoil) and $-15°$ to $25°$ ($c/R = 0.25$ aerofoil) incidence ranges were tested at least twice with increasing incidence, with at least one further run taken with decreasing incidence. This was done for all the Reynolds numbers tested (the same used for the uncambered NACA 0018: 40 000, 60 000, 80 000, 100 000, 125 000, 150 000, 200 000, 250 000 and 300 000).

Figs 5.20 - 5.23 show results for the NACA 0018 with $c/R = 0.114$, and Figs 5.20 - 5.23 for the $c/R = 0.25$ profile. Much of the analysis for the NACA 0018 is relevant for the two

cambered profiles, as they share a common c/H of 0.2. Camber increases $C_{l\,\mathrm{MAX}}$ and the stall angle at positive stall, decreasing them for negative stall. For more on camber effects, see Section 5.5.

For the $c/R = 0.25$ aerofoil, there is no stalling behaviour at $Re = 60\,000$, suggesting the critical Reynolds number at which flow can reattach is higher for this profile compared to the NACA 0018 and 0015. This is again due to the greater curvature of the aerofoil's suction surface giving a greater adverse pressure gradient, making it harder for separated boundary layers to reattach.

A unique feature of the $c/R = 0.25$ compared with all the other profiles tested is the unusual hysteresis experienced at $Re = 80\,000$, at incidences away from the stall angle. This can be seen between $\alpha = 5°$ and $\alpha = 6°$ for increasing incidence, and between 3° and 5° for decreasing incidence. There is a large change in lift coefficient, with drag also altering significantly.

As with the other aerofoils, laminar separation is present at low incidences and low Reynolds numbers, occurring close enough to the trailing edge that the separated flow transitions to turbulence downstream of the aerofoil and no reattachment occurs. As incidence is increased, so too is the adverse pressure gradient, pulling the separation point towards the leading edge and eventually allowing the turbulent flow to reattach, forming a bubble. Unique to this aerofoil is the hysteresis at the point at which the bubble forms where lift is boosted and drag reduced.

With decreasing incidence, it seems the bubble is able to stay attached to the trailing edge even when incidences of 5° and 4° are reached, where on the increasing incidence runs flow remained separated. This analysis is based on the data presented, along with Dong-Ha's flow visualisation results for the NACA 0012 [41], but would need to be confirmed with pressure readings and flow visualisation on this specific aerofoil for solid conclusions to be drawn.

5.3 Force transducer measurements, solid walled tunnel

Results were taken in the solid walled tunnel for the NACA 0015, and are presented in this section for the purposes of benchmarking the tolerant tunnel's performance against conventional techniques. Blockage and streamline curvature have been corrected for as discussed in

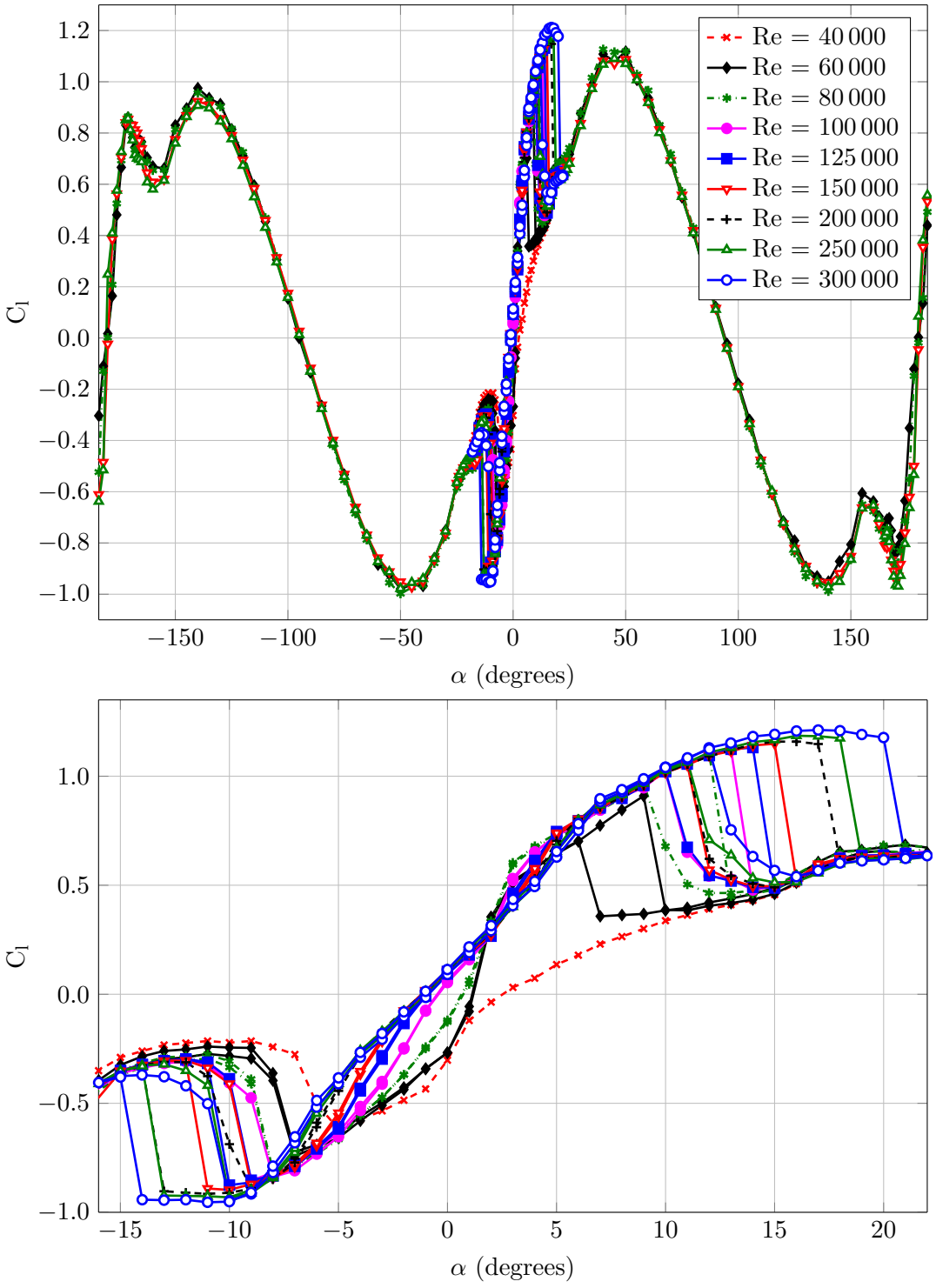


Figure 5.20: C_l vs α for the $c/H = 0.2$ transformed NACA 0018 aerofoil with $c/R = 0.114$, taken in the tolerant tunnel, DS-71 configuration at various Re. (a) $-184° \leq \alpha \leq 184°$, (b) $-16° \leq \alpha \leq 22°$.

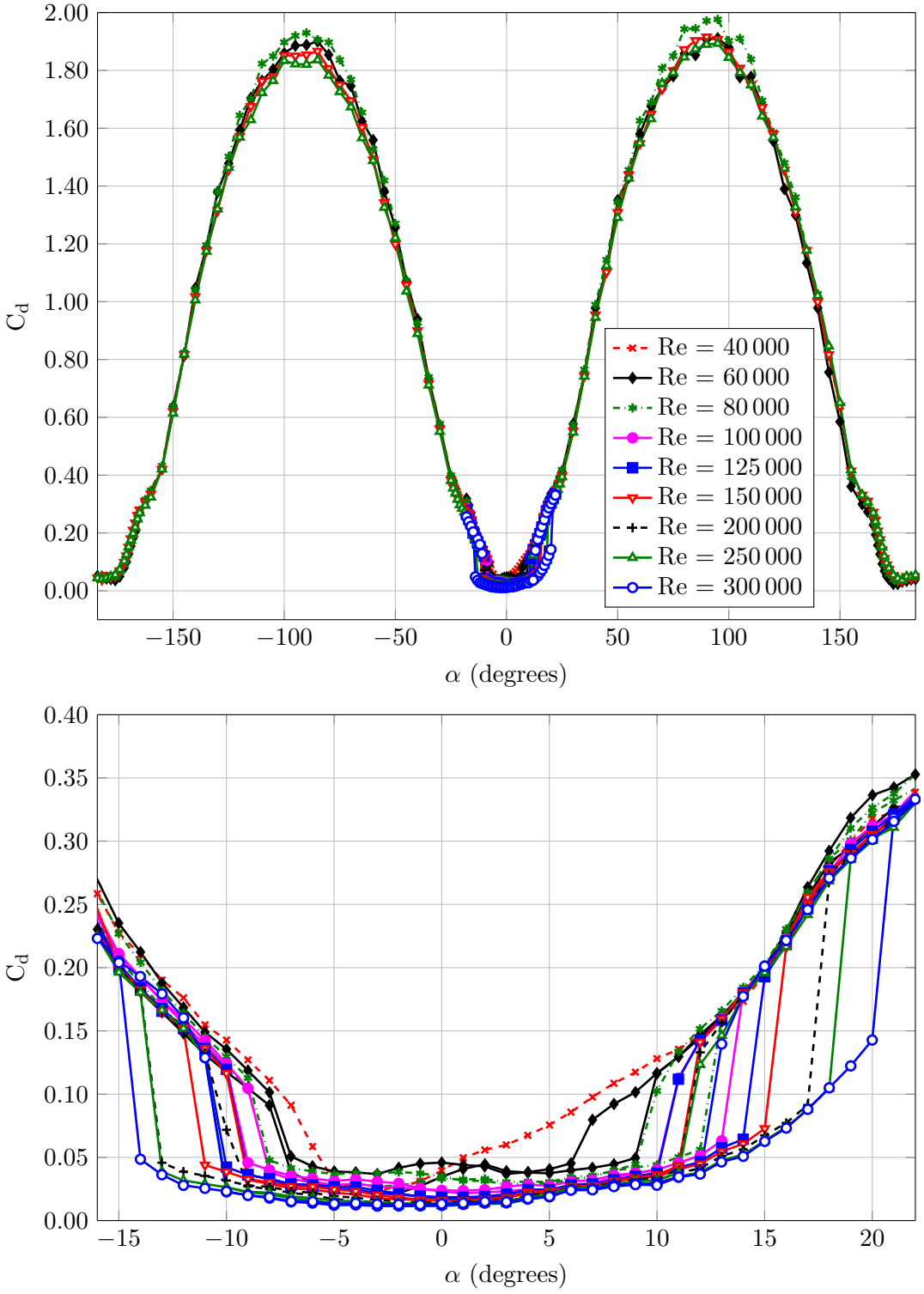


Figure 5.21: C_d vs α for the $c/H = 0.2$ transformed NACA 0018 aerofoil with $c/R = 0.114$, taken in the tolerant tunnel, DS-71 configuration at various Re. (a) $-184° \leq \alpha \leq 184°$, (b) $-16° \leq \alpha \leq 22°$.

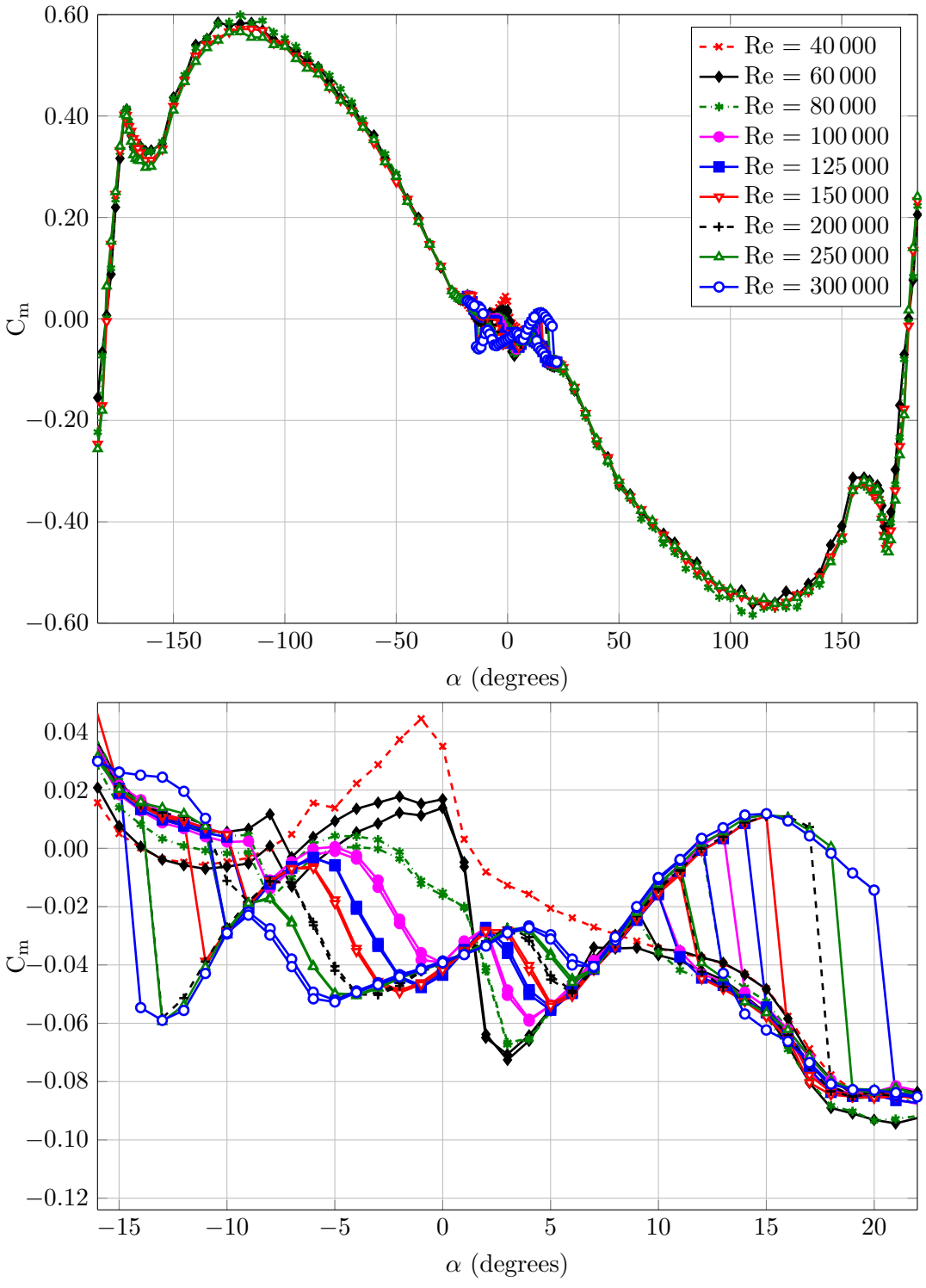


Figure 5.22: C_m vs α for the $c/H = 0.2$ transformed NACA 0018 aerofoil with $c/R = 0.114$, taken in the tolerant tunnel, DS-71 configuration at various Re. (a) $-184° \leq \alpha \leq 184°$, (b) $-16° \leq \alpha \leq 22°$.

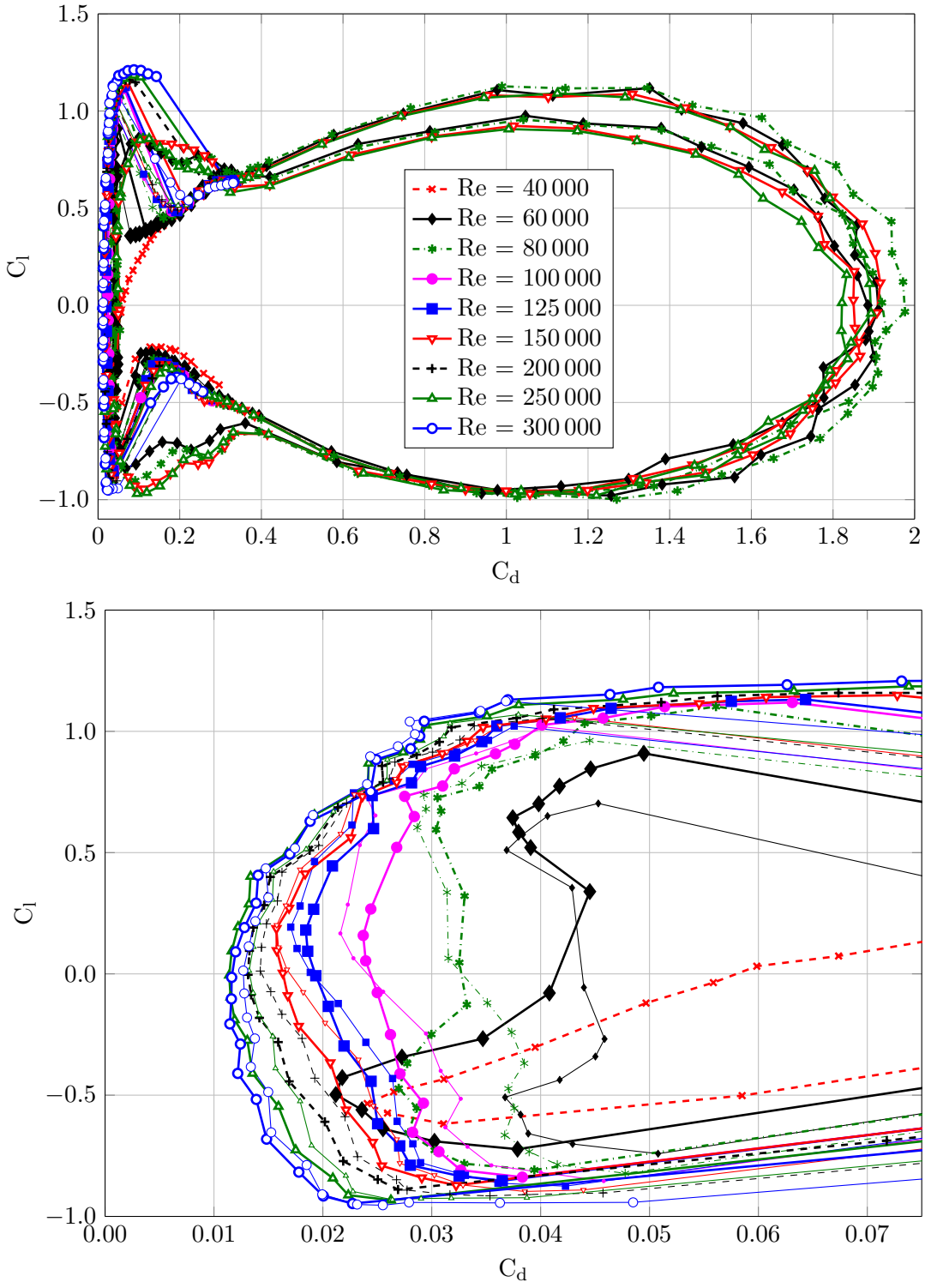


Figure 5.23: C_l vs C_d polar for the $c/H = 0.2$ transformed NACA 0018 aerofoil with $c/R = 0.114$ taken in the tolerant tunnel, DS-71 configuration at various Re. (a) $-184° \leq \alpha \leq 184°$, (b) incidences at which flow is attached.

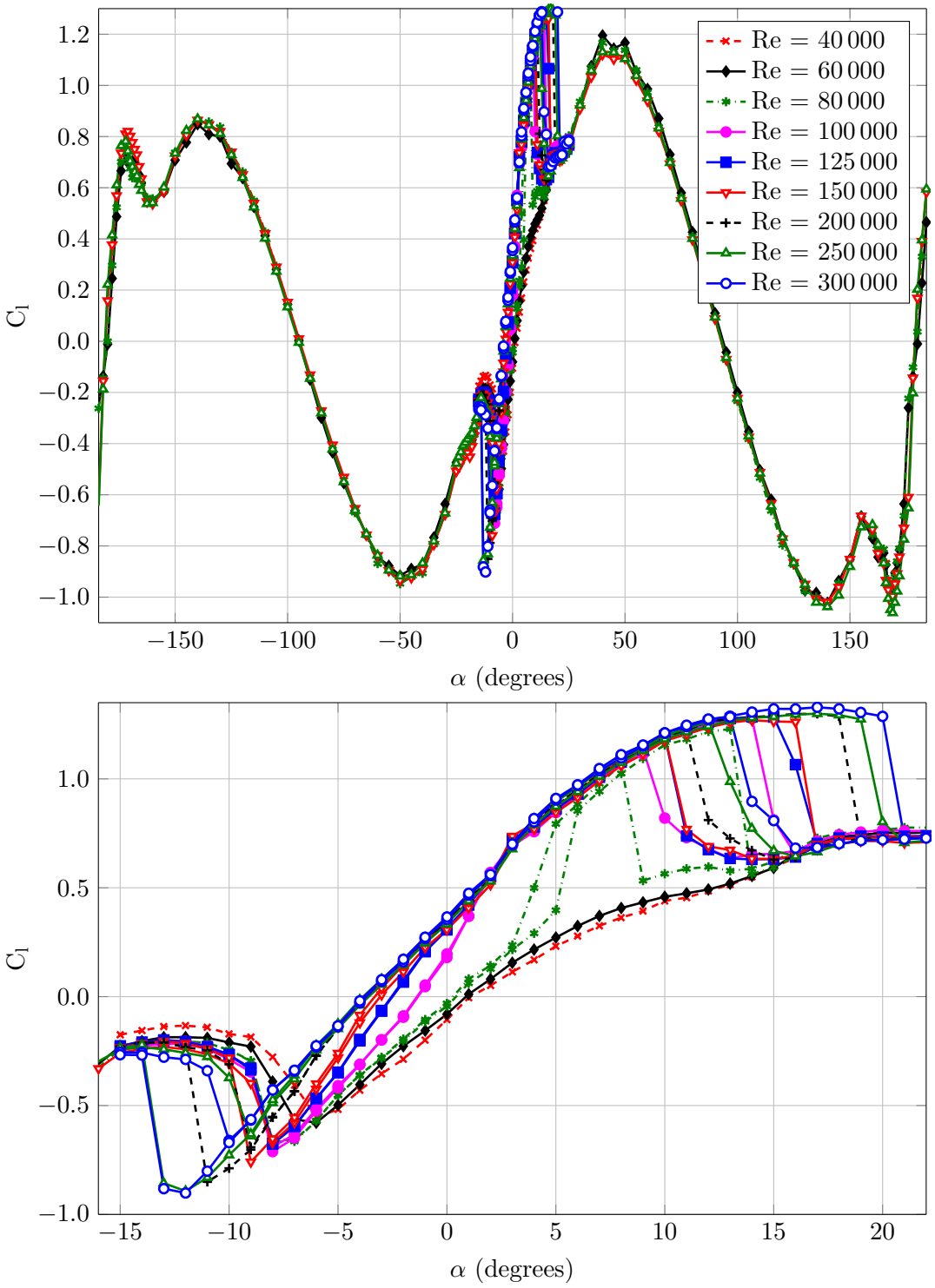


Figure 5.24: C_l vs α for the $c/H = 0.2$ transformed NACA 0018 aerofoil with $c/R = 0.25$, taken in the tolerant tunnel, DS-71 configuration at various Re. (a) $-184° \leq \alpha \leq 184°$, (b) $-16° \leq \alpha \leq 22°$.

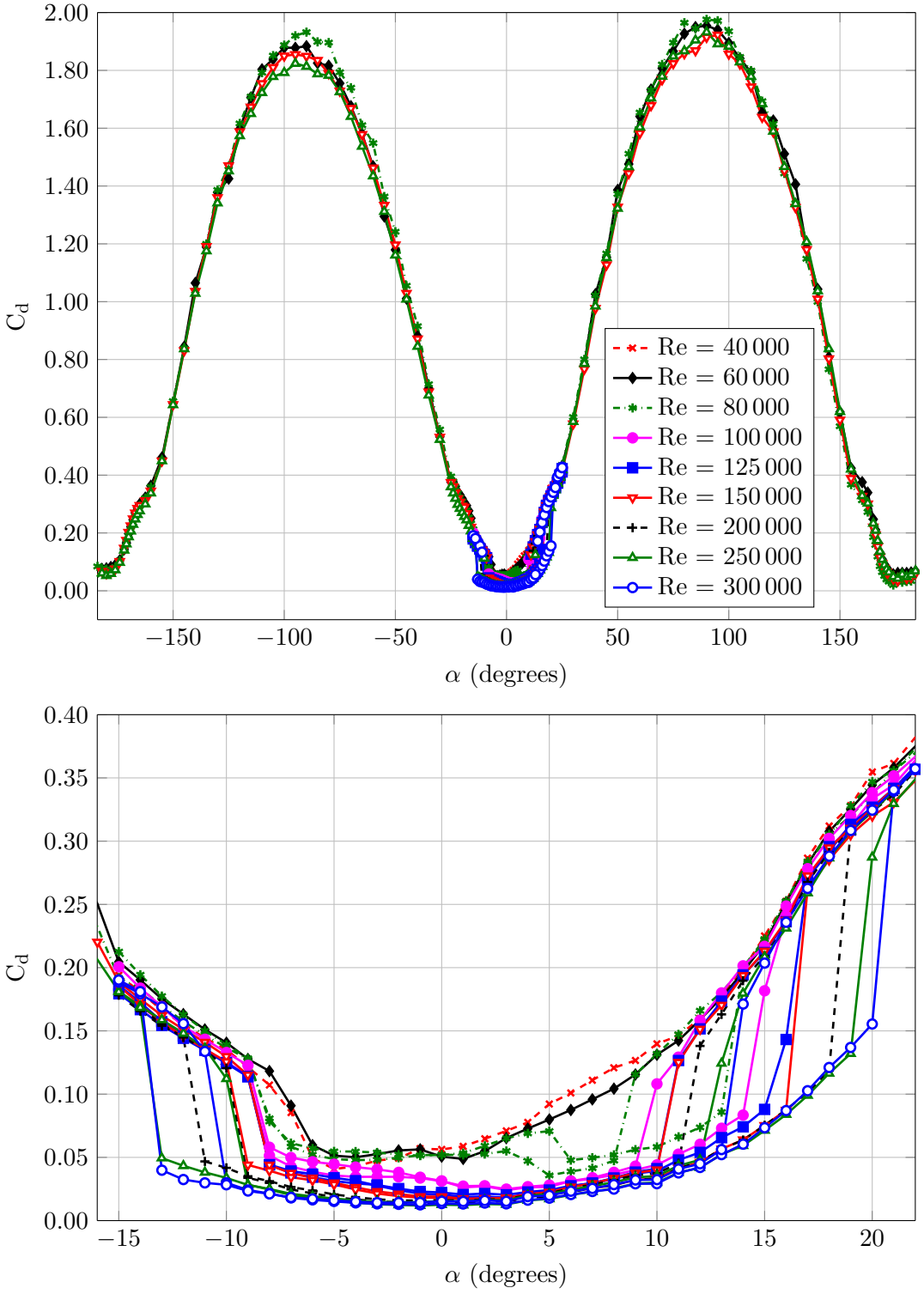


Figure 5.25: C_d vs α for the $c/H = 0.2$ transformed NACA 0018 aerofoil with $c/R = 0.25$, taken in the tolerant tunnel, DS-71 configuration at various Re. (a) $-184° \leq \alpha \leq 184°$, (b) $-16° \leq \alpha \leq 22°$.

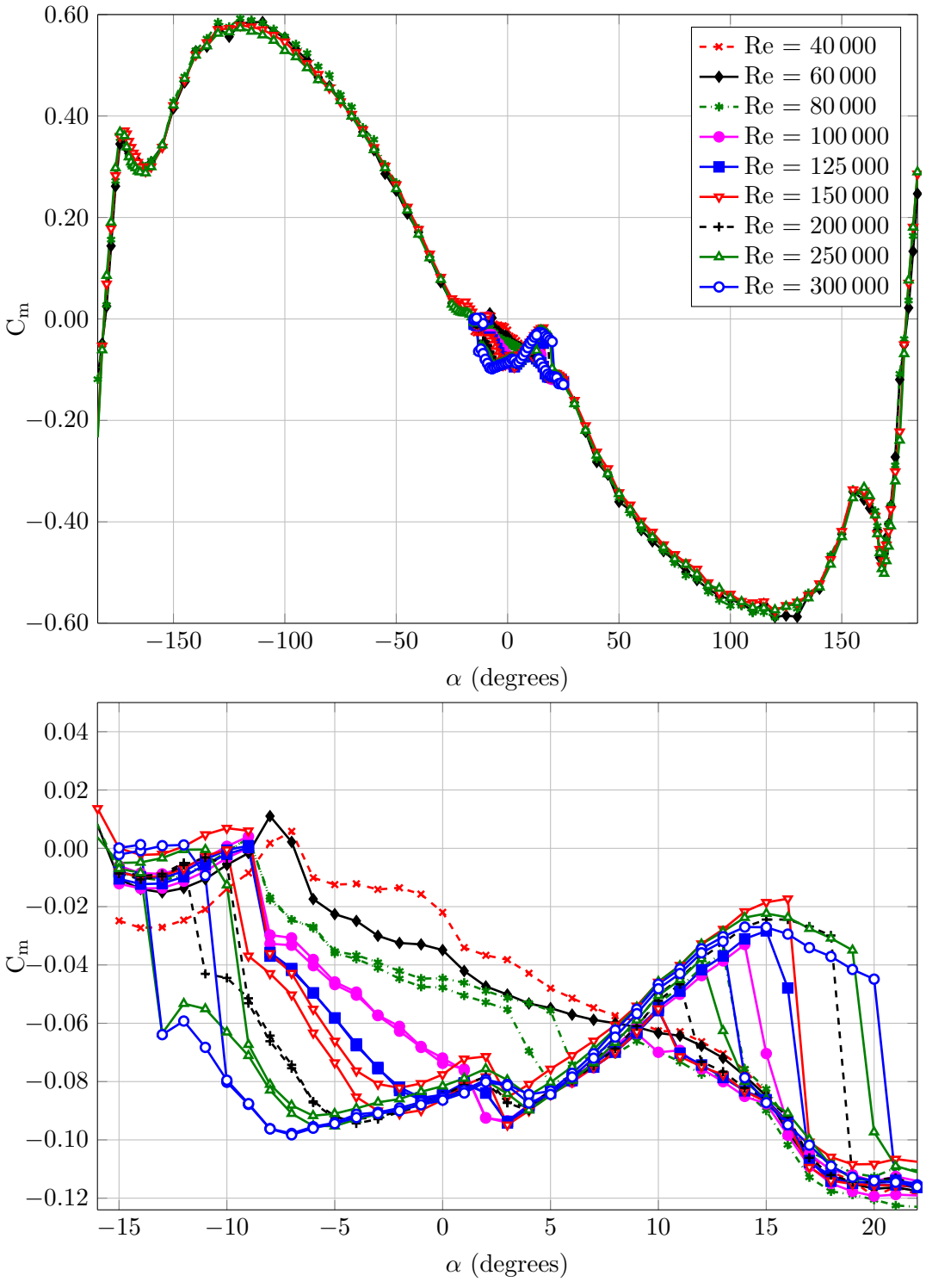


Figure 5.26: C_m vs α for the $c/H = 0.2$ transformed NACA 0018 aerofoil with $c/R = 0.25$, taken in the tolerant tunnel, DS-71 configuration at various Re. (a) $-184° \leq \alpha \leq 184°$, (b) $-16° \leq \alpha \leq 22°$.

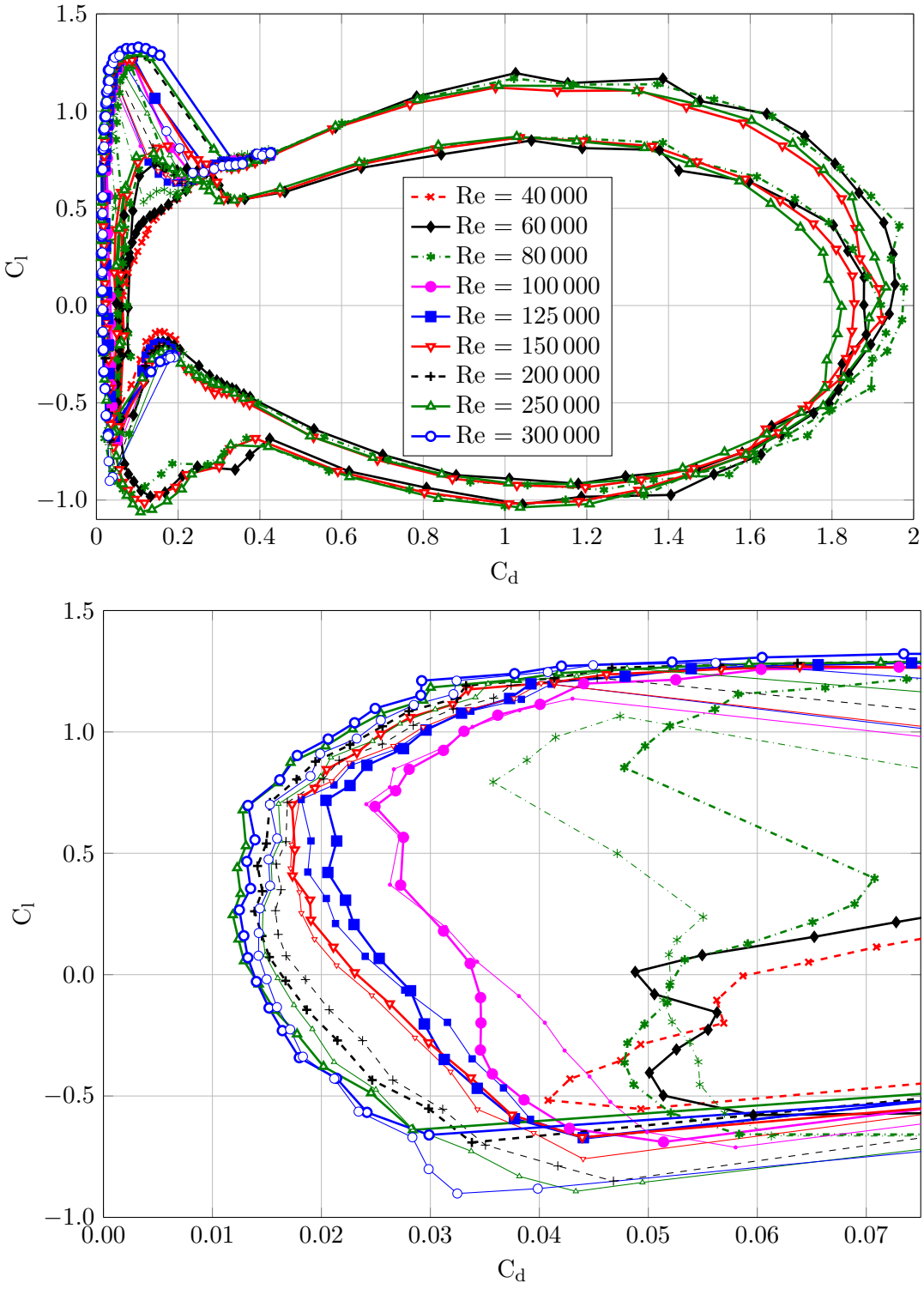


Figure 5.27: C_l vs C_d polar for the $c/H = 0.2$ transformed NACA 0018 aerofoil with $c/R = 0.25$ taken in the tolerant tunnel, DS-71 configuration at various Re. (a) $-184° \leq \alpha \leq 184°$, (b) incidences at which flow is attached.

Ch. 2. The NACA 0018 and the $c/R = 0.114$ and $c/R = 0.25$ transforms of it were also tested in the solid tunnel, but they are not presented here.

5.3.1 NACA 0015

Lift, drag and moment coefficients are shown for both increasing and decreasing incidences in Figs 5.28 - 5.30. For $Re = 20\,000$, $40\,000$ (for C_d and C_m), $60\,000$ and $80\,000$ there is very little hysteresis, so averages are calculated using increasing and decreasing incidence runs. Where there is hysteresis, separate averages are calculated for increasing and decreasing incidences.

General trends are similar between the tolerant and solid walled tunnel for the NACA 0015 with some small differences. Improvements in experimental techniques made before the tolerant tunnel data was taken are responsible for some of the differences, while others result from the approaches to blockage reduction of the tunnels. The plots in Section 5.4 are referred to here for easier comparison between the tolerant and conventional tunnel results.

Fig. 5.32a for attached flow maximum lift shows results are near identical for the two tunnels, the differences being smaller than the maximum experimental errors established in Section 4.7. Minimum drag (Fig. 5.32b) is lower for the solid tunnel, the result of improvements in techniques for the tolerant tunnel runs, particularly the longer settling times between force transducer offsetting and experimental runs.

Stall angles are near-identical to the tolerant tunnel, the only difference being the later stall of the conventional tunnel at $Re = 250\,000$, at 13° rather than 12°. Referring back to Fig. 5.3 for the lift results from the tolerant tunnel, it can be seen that the stall at $Re = 250\,000$ is less steep than other Reynolds numbers, with a still reasonably high lift at 13°. Some of the tolerant tunnel runs at $Re = 250\,000$ exhibited the NACA 0015's characteristic sharp stall at 12°, others at 13°, giving the averaged performance presented here. There are therefore minimal differences between the stall angles given in either of the tunnels.

The post-stall lift and drag results shown in Fig. 5.34 again show similar trends between the tunnels, but with lower peaks for the tolerant tunnel. This is due to the different blockage reduction techniques used. There are larger differences at low Reynolds numbers, again the result of poorer accuracy for the solid walled tunnel readings.

It was established in Ch. 4 that the tolerant tunnel is better at giving consistent results over a range of c/H ratios than the conventional tunnel. For the low blockage $c/H = 0.1$ aerofoil,

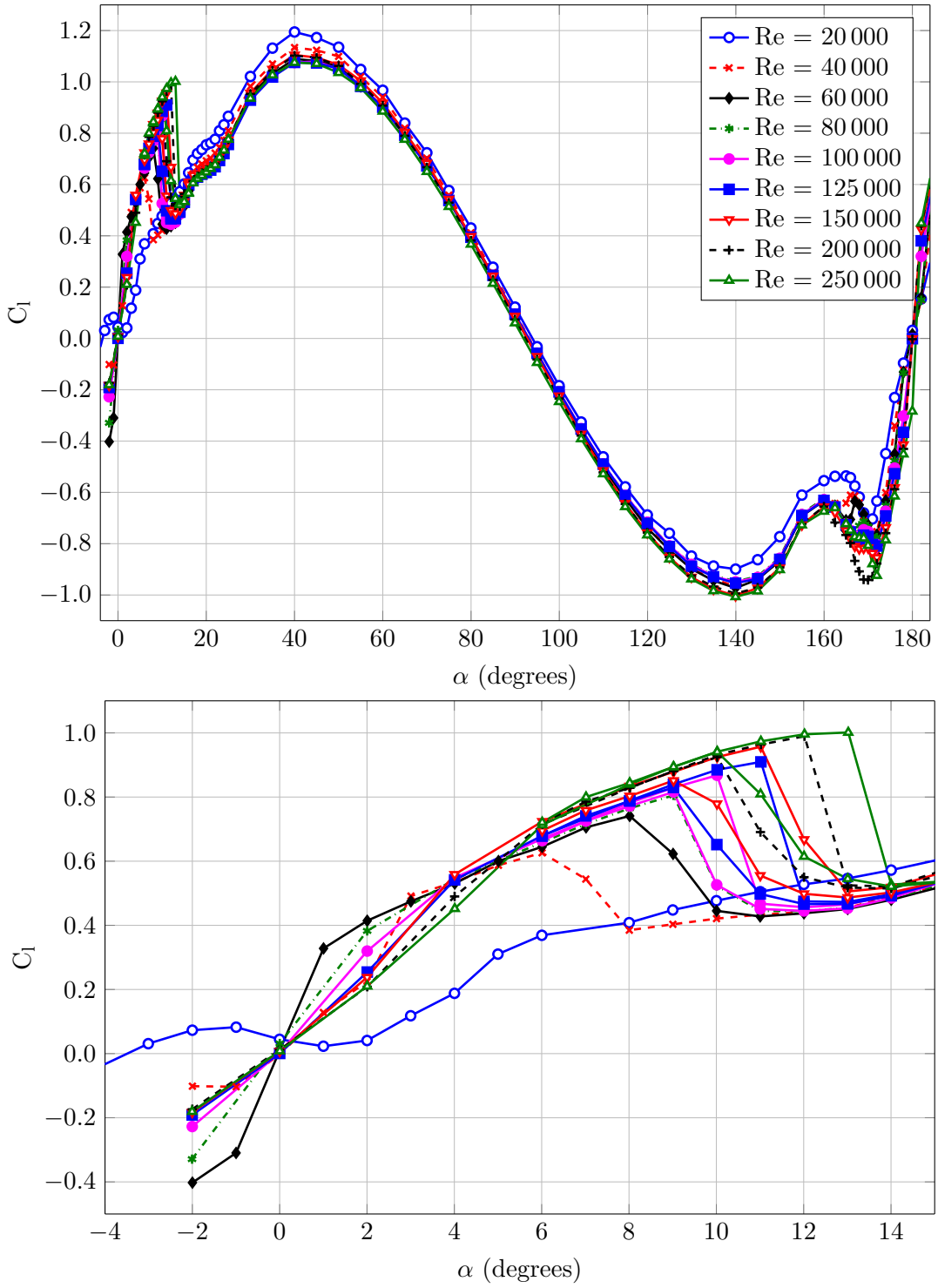


Figure 5.28: C_l vs α for the $c/H = 0.1$ NACA 0015 aerofoil taken in the solid walled tunnel, at various Re, with blockage corrections applied. (a) $-4° \leq \alpha \leq 184°$, (b) $-4° \leq \alpha \leq 15°$.

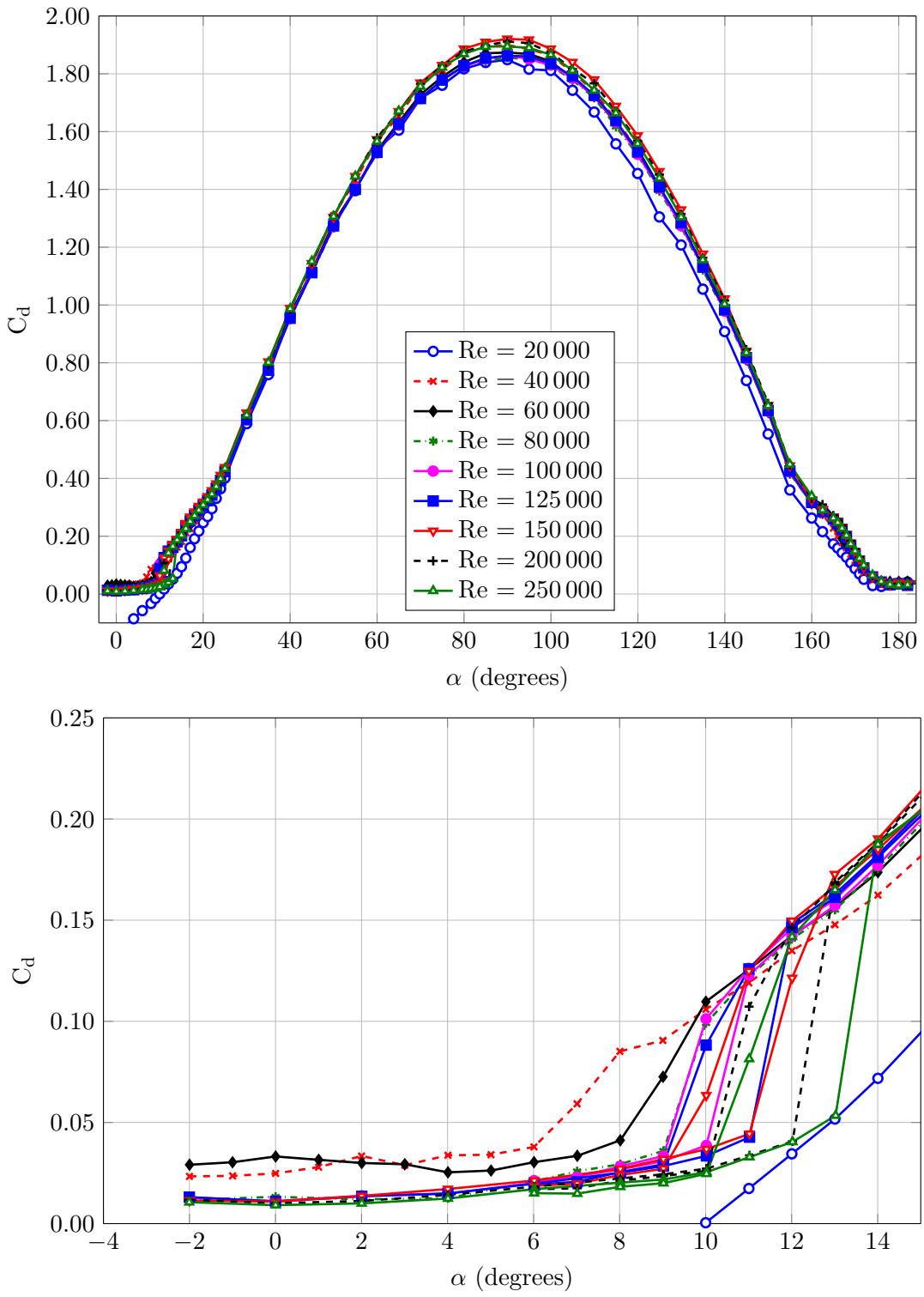


Figure 5.29: C_d vs α for the $c/H = 0.1$ NACA 0015 aerofoil taken in the solid walled tunnel, at various Re, with blockage corrections applied. (a) $-4° \leq \alpha \leq 184°$, (b) $-4° \leq \alpha \leq 15°$.

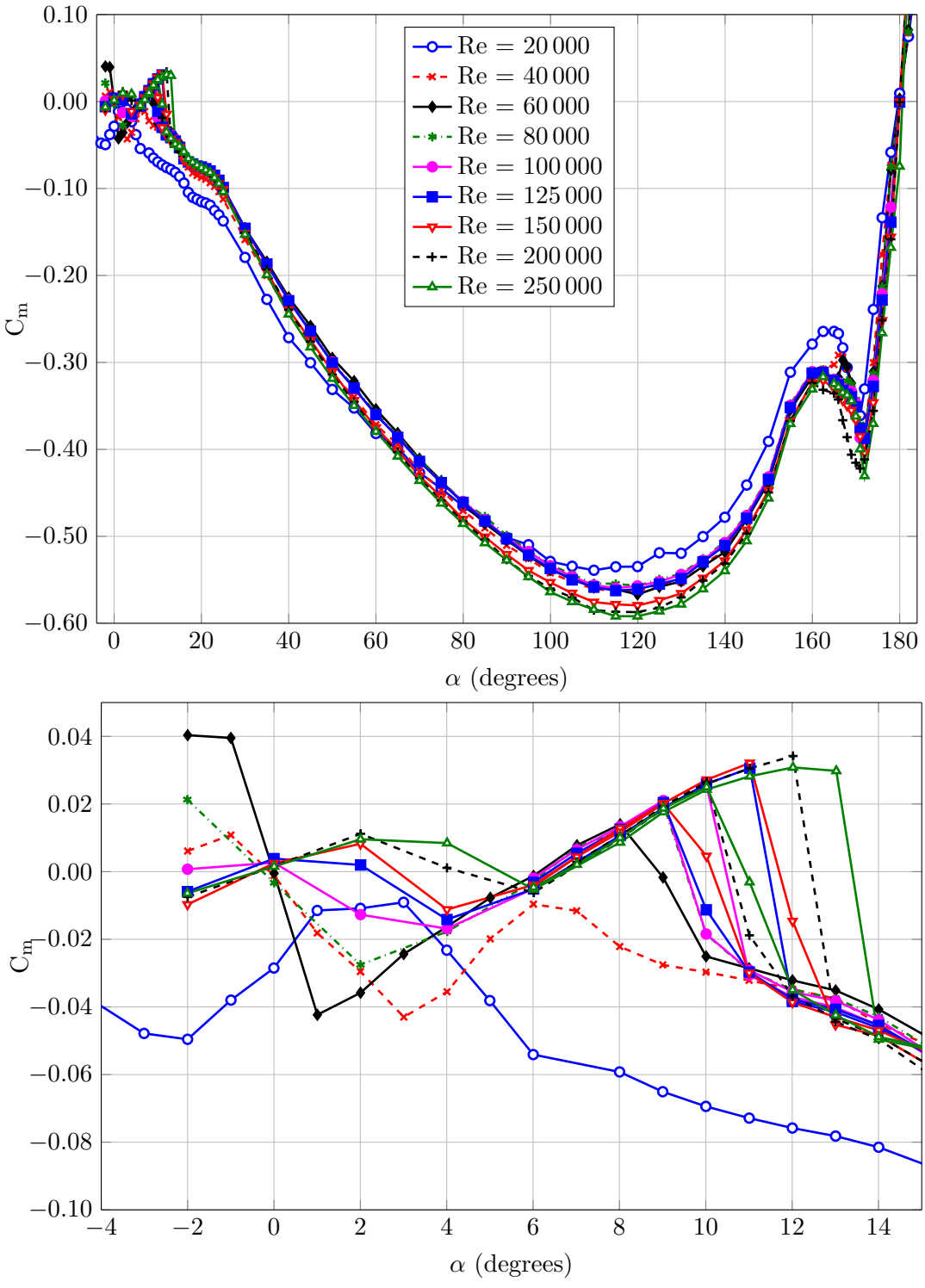


Figure 5.30: C_m vs α for the $c/H = 0.1$ NACA 0015 aerofoil taken in the solid walled tunnel, at various Re, with blockage corrections applied. (a) $-4° \leq \alpha \leq 184°$, (b) $-4° \leq \alpha \leq 15°$.

results are near-identical for the two tunnels and within, or close to, limits of established experimental error (see Section 4.7) for most readings, other than for results taken at $Re = 20\,000$ and for attached flow drag at all Reynolds numbers. These larger-than-error differences are due to the solid walled tunnel producing lower data quality data where measured forces are low, resulting from the improvements in measuring techniques made before the tolerant tunnel experiments (see Section 5.2.1). That both blockage reduction techniques produce such similar data allows confidence to be placed in the results of this study.

5.4 Reynolds number effects

The results from Figs. 5.3 - 5.30 are collated and presented here in new forms to analyse the impact of the Reynolds number of the flow on various features of the aerofoils' performance. New figures are presented for maximum C_l/C_d, maximum attached flow C_l, minimum C_d, stall angle and maximum detached flow C_l and C_d, all plotted against Reynolds number. Where applicable, error bars for tolerant tunnel experiment are included on the plots, based on the maximum errors estimated in Section 4.7. Solid-walled tunnel error bars are similar to the tolerant tunnel and have been omitted to improve the legibility of the figures. Thickness and camber effects are discussed in the following section using the same diagrams.

5.4.1 Maximum C_l/C_d

There is a general trend of higher $(C_l/C_d)_{\text{MAX}}$ with higher Reynolds number for all of the profiles tested, though this trend is reversed between $Re = 60\,000$ and $Re = 200\,000$ for the NACA 0018, see Fig. 5.31. No error bars are included on the figure as it is difficult to estimate errors for attached flow drag readings, see the following section for more on this. All three 18% thick aerofoils share a dramatic improvement in performance at a certain critical Reynolds number, 60 000 for the symmetrical profile and the $c/R = 0.114$ and 80 000 for the $c/R = 0.25$. This is the critical Reynolds number at which flow is able to reattach and form a laminar separation bubble, as discussed in Section 5.2.3.

$Re = 20\,000$ results for the NACA 0015 have been left off due to the inaccuracies of the results. Note that other low Reynolds number results ($\leq 60\,000$ for the $c/H = 0.1$ NACA 0015 and $\leq 100\,000$ for the $c/H = 0.2$ aerofoils) may also lack accuracy due to the low magnitude

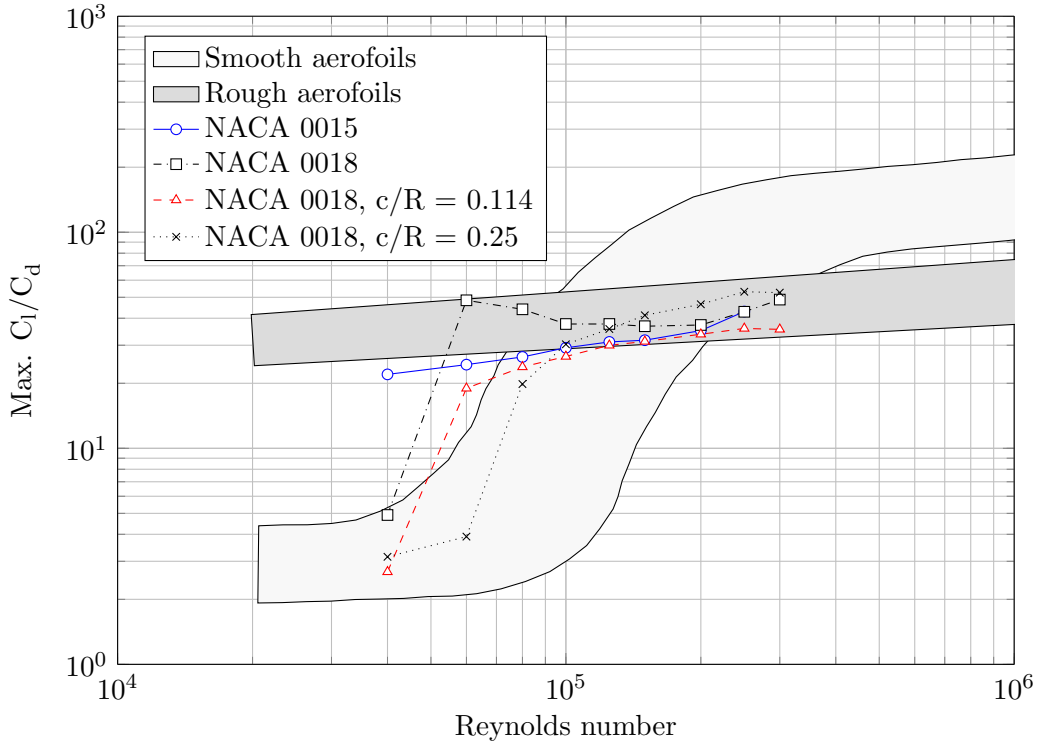


Figure 5.31: Maximum C_l/C_d vs Re for the four aerofoils tested in the tolerant tunnel, compared to trends from Lissaman's review [86].

of the drag forces being measured, see Section 4.7. Given the lack of any stall behaviour at $Re = 20\,000$ for the NACA 0015, the aerofoil would have a large drop in performance here, similar to the other profiles.

Fig. 5.31 also includes $(C_l/C_d)_{\mathrm{MAX}}$ trends for smooth and rough aerofoils, taken from Lissaman's review on low Reynolds number aerofoils [86], after [88]. The agreement to the trends for smooth aerofoils is reasonable, though the critical Reynolds numbers of all of the aerofoils, other than the $c/R = 0.25$, are lower than the range suggested in the references of 70 000 - 100 000. Carmichael notes in his review of low Reynolds number aerofoils that Re_{crit} numbers as low as 37 000 have been found [28]. The lowest of the current study, for the NACA 0015 lies somewhere between 20 000 and 40 000.

At the upper end of the Reynolds number range, the $(C_l/C_d)_{\mathrm{MAX}}$ is low for all of the profiles, agreeing more closely to the trends established for rough aerofoils, in spite of the aerofoils having low surface roughnesses (approximately 0.4 μm Ra, see Section 4.2.4). The difficulties of measuring the low magnitude, attached flow drag forces could be responsible

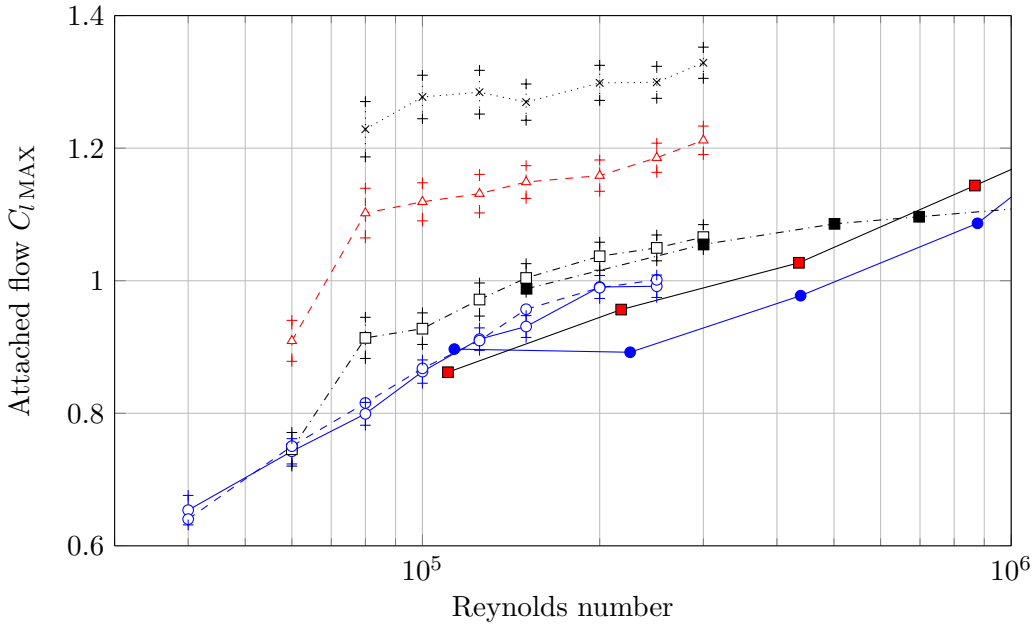
(see below).

5.4.2 Attached flow $C_{l\,\mathrm{MAX}}$ and $C_{d\,\mathrm{MIN}}$

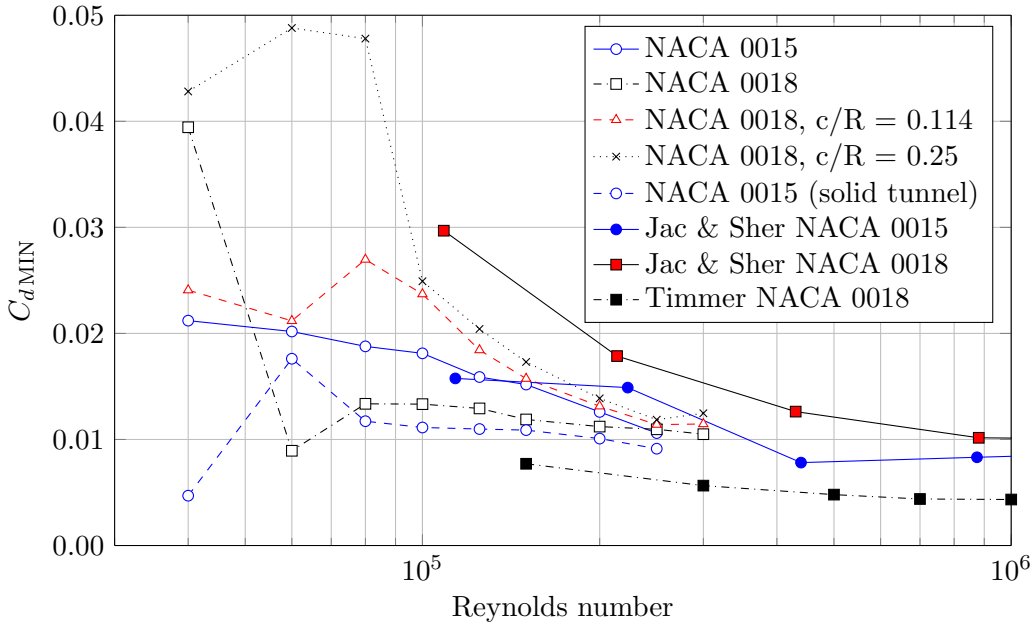
Fig. 5.32a shows the variation of attached flow maximum C_l with Reynolds number, with error bars. $C_{l\,\mathrm{MAX}}$ increases with Re across the whole range of Reynolds numbers tested for all of the aerofoil profiles. These findings are supported by the earlier studies of Timmer [38] for the NACA 0018, which shows close agreement (within experimental error of the current study) where the studies' Reynolds number ranges overlap. Jacobs and Sherman show similar trends for the NACA 0015 and 0018 [43], but there is poor agreement to the current study and to Timmer. The NACA variable density wind tunnel used for the experiments had a high level of turbulence to its flow, corrected for by applying a correction factor of 2.64 to measured Reynolds numbers to give an effective Reynolds number, shifting the plots to the right in Fig. 5.32. The aerofoil data was also obtained from corrected finite wing results. Jacobs and Sherman themselves made comparisons to other studies and noted that their corrections could be responsible for significant errors in published data [43]. See Appendix A.2.3 for more on the corrections used in Jacobs and Sherman's study.

Note that the attached flow $C_{l\,\mathrm{MAX}}$ is not always generated at the stall angle, sometimes it occurs a few degrees before. Data points are included on Fig. 5.32a only for Reynolds numbers where stall occurs, so $Re < 40\,000$ for the NACA 0015, $Re < 60\,000$ for the NACA 0018, symmetrical and $c/R = 0.114$ and $Re < 80\,000$ for the NACA 0018, $c/R = 0.25$ are omitted as there is no stall, and so no attached flow on these runs of the experiment.

Results for $C_{d\,\mathrm{MIN}}$ are included on Fig. 5.32b. Due to the low accuracy of the Re = 20 000 results for the NACA 0015, with negative drag measured, these have been omitted. Results may lack accuracy for other low Reynolds numbers due to the low magnitude of drag forces. Error bars have been omitted from this plot as maximum errors for these low force readings cannot be estimated with sufficient confidence. Again, the studies of Timmer and Jacobs and Sherman are included, with the latter showing the same Reynolds number correction-induced shift to higher Reynolds numbers as for lift. Timmer's study gives results around 0.005 lower, likely due to his use of a wake rake for drag measurements. In absolute terms drag agreement is closer than for attached flow $C_{l\,\mathrm{MAX}}$, where Timmer is 0.01 lower than the current study. All of the studies demonstrate a reduction in drag with increasing Reynolds number, as viscous



(a) Maximum attached flow C_l, with maximum error bars.



(b) Minimum C_d.

Figure 5.32: Variations with Re for the four aerofoils tested in the tolerant tunnel, compared to Timmer [38] and Jacobs and Sherman [43]

forces come to have less of an effect compared with inertial forces.

5.4.3 Stall angle

Fig. 5.33 shows stall angles (with solid data points), alongside the angles at which flow reattaches with decreasing incidence (unfilled data points), against Reynolds number. The stepper motor used to control incidence was accurate to within 0.02°, the negligible angle measurement errors resulting from it have been omitted from the figure. The increase in stall angles and flow reattachment angles with increasing Reynolds number is supported by all studies in Table 1.1 where Reynolds number is varied.

Note that Fig. 5.33 only contains data from runs where stall behaviour is discernible. All of the aerofoils tested in this study exhibit laminar separation bubbles at Reynolds numbers where there is stalling behaviour. The attached turbulent boundary layer downstream of the bubble is able to accommodate increasing pressure recoveries with increasing Reynolds number [28], thus enabling higher incidences to be reached before stall.

There is a widening of the hysteresis gap between stall and flow reattachment angles with increasing Reynolds number, with the angles being identical at $Re < 100\,000$ for the NACA 0015 and $Re < 80\,000$ for the NACA 0018. Other studies that present results with increasing incidence have shown a similar widening of the gap in this Reynolds number range [20, 38], though none have extended to Reynolds numbers below 150 000. The stability of the short laminar separation bubble that "bursts" at stall is marginal [86] and it requires a lower pressure recovery to reattach than it can tolerate before bursting. The effects of Reynolds number are more significant on the pressure recovery limit that triggers bursting of the bubble than on that at which the bubble can reform, leading to this widening.

5.4.4 Detached flow lift and drag peaks

Trends in detached flow $C_{l\,\mathrm{MAX}}$ and $C_{d\,\mathrm{MAX}}$ with Reynolds number are near-identical, see Fig. 5.34 for this study and Fig. 5.35 for aggregated results of other post-stall studies on symmetrical aerofoils that have varied Reynolds number. Note that Fig. 5.34 contains results where the aerofoils were tested post-stall, so there are limited data points for the cambered aerofoils. Drag results for the cambered aerofoils are those taken with the less curved surface

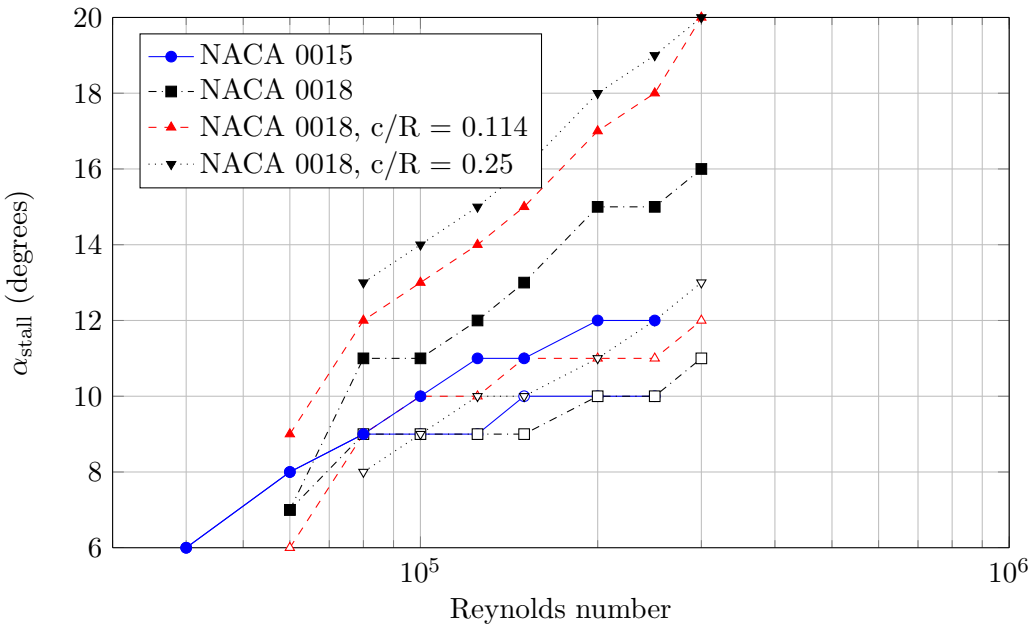


Figure 5.33: Stall angle and flow reattachment angle vs *Re* for the four aerofoils tested in the tolerant tunnel. White filled data points are for readings taken for flow reattachment (with reducing incidence).

facing upstream.

Ignoring the results at $Re = 250\,000$, which were affected by transducer saturation, and those at $Re = 20\,000$ and $40\,000$ where accuracy of readings is low, the NACA 0015 demonstrates a general trend of higher peaks with higher *Re*. This trend is significant, even when maximum experimental errors are considered. The other profiles do not demonstrate any clear trends with Reynolds number. Most of the earlier studies in Fig. 5.35 also demonstrate higher post-stall peaks with higher Reynolds numbers, and there is a similar trend across all the studies.

Ostowari and Naik conducted post-stall studies on non-symmetric aerofoils at different Reynolds numbers. They found slightly decreasing lift peaks with Reynolds number, in the range 250 000 - 1 000 000 for the NACA 4412, 4415 and 4418, with minimal impact on drag [89].

Given the limited data available, it is difficult to draw any definitive conclusions on the dependency of post-stall aerofoil performance on Reynolds number. There is clearly some dependency, but the exact nature of the relationship may also depend on aerofoil shape, rather than being a general positive correlation.The review of Ch. 2 shows that blockage likely

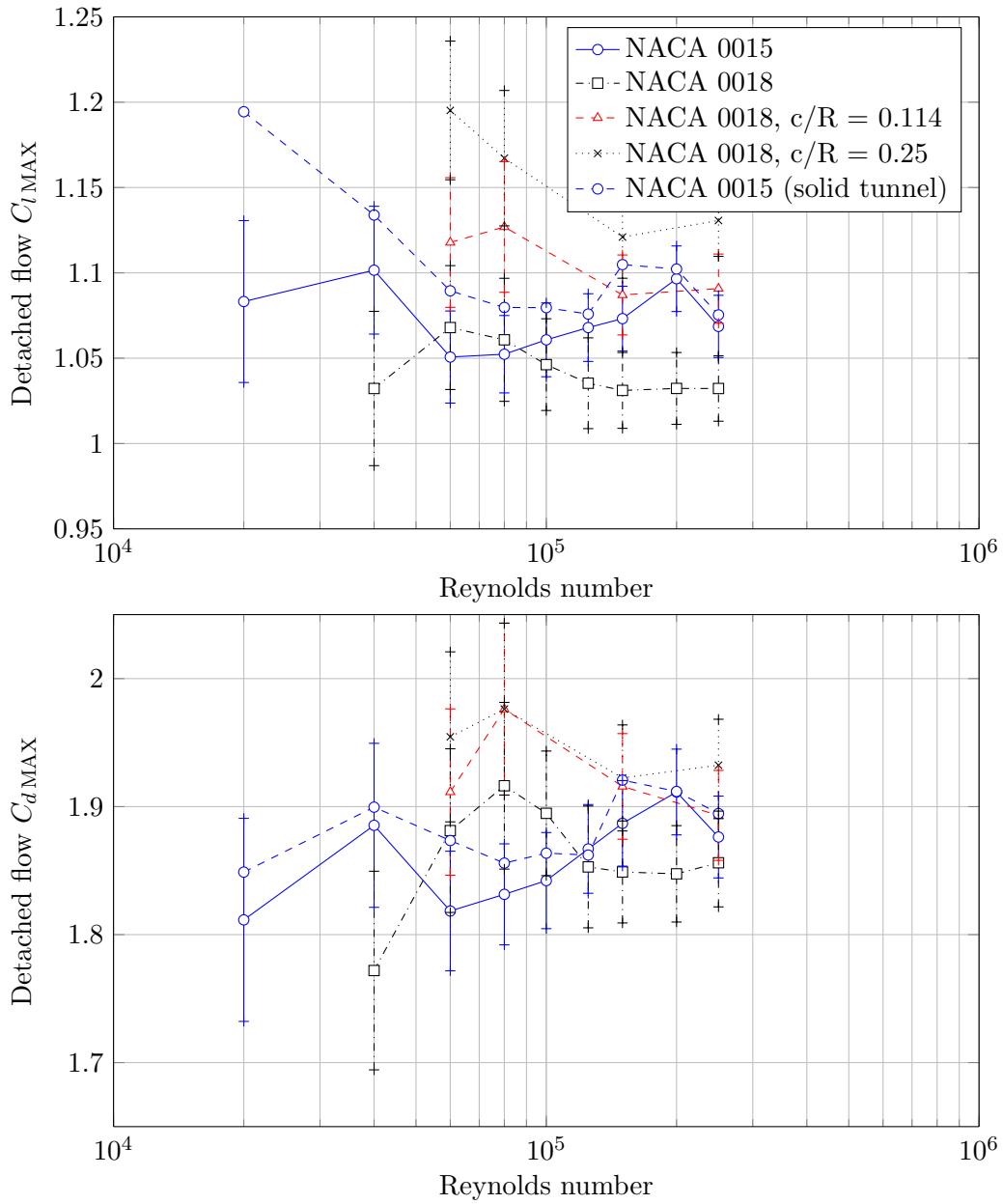


Figure 5.34: Maximum detached flow (a) C_l and (b) C_d vs Re for the four aerofoils tested in the tolerant tunnel, with maximum error bars.

has a far larger impact on experimental post-stall results than Reynolds number, hindering comparisons between datasets.

Given the small influence shown in most studies it could be a reasonable assumption that for a given profile, detached flow performance is independent of Reynolds number. Currently, this is taken to be the case in some aerofoil performance models [20, 73].

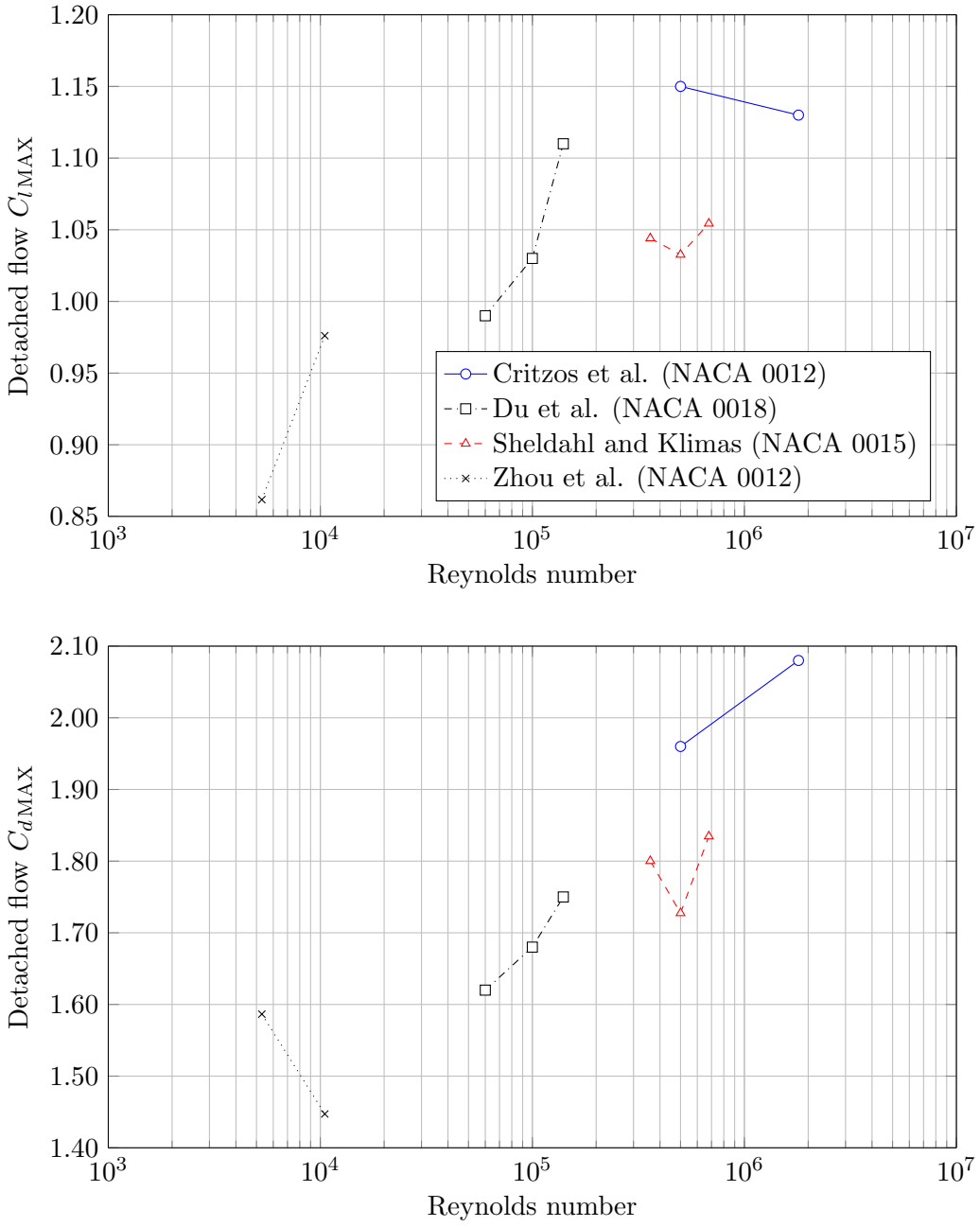


Figure 5.35: Maximum dettached flow (a) C_l and (b) C_d vs Re for the studies of Critzos et al. [34], Du et al. [37], Sheldahl and Klimas [20] and Zhou et al. [42]

5.5 Thickness and camber effects

At all but the lowest Reynolds numbers tested, thickness and camber don't have much impact on C_l/C_d. All the profiles have a Reynolds number at which they have a sudden drastic drop in performance. Thickness and camber both negatively impact on this limit, pushing it to a higher Reynolds number, see Fig. 5.31.

Higher thickness/camber gives higher attached flow lift peaks. Jacobs and Sherman demonstrated similar for thickness for the NACA 00xx (their results for the NACA 0015 and 0018 are shown on Fig. 5.32a) and 44xx families of aerofoils, and camber for the xx12 family, over the range of Reynolds numbers tested in this study [43].

Camber gives higher minimum drag in the current study, again supported by Jacobs and Sherman's findings for the xx12 family [43]. Thickness reduces minimum drag, an unusual result that could be the result of experimental error, due to the lower absolute forces on the NACA 0018 at an equivalent Reynolds number to the smaller chord NACA 0015. Jacobs and Sherman's results show the NACA 0015 to have lower drag than the 0018 [43], as shown in Fig. 5.32b.

Addition of thickness and camber increases the stall angle, and also the angle at which flow reattaches with decreasing incidence, but there is less of an impact on the latter, see Fig. 5.33. This results in a widening of the gap between the stall and flow reattachment angles with increasing thickness and camber.

Camber gives higher detached flow lift peaks, a perhaps surprising result given the expected minimal impact of profile shape where flow is fully attached. The result still stands if maximum errors are considered. The effect must be the result of either, or both, of the following:

- The pressure surface deflecting a greater mass of air downward with increasing camber. For the $c/R = 0.25$ aerofoil, the pressure surface is concave near the trailing edge, and near flat for the $c/R = 0.114$ aerofoil, so may deflect more air downward than the convex symmetrical aerofoil surface.

- The small region of suction surface near the leading edge where flow is still attached deflects more air downward (or less air upwards) with increasing camber.

Camber also increases the post-stall drag peak at $\alpha = 90°$ but this is less surprising, given the pressure surface is presented normal to the flow here. The concave surface of the $c/R = 0.25$ aerofoil is less streamlined than the symmetrical aerofoil at this incidence.

Thickness effects cannot be judged post-stall, as the different c/H ratios of the NACA 0015 and 0018 likely have a far greater impact on results than differences between their profile shapes.

Chapter 6

VAWT modelling and application of new aerofoil data to VAWT analyses

Several options are available for modelling of VAWTs, including vortex models [90] and CFD solvers for the Navier-Stokes equations [91]. The intention here is to study start-up of the turbines, where TSRs are low and a wide range of blade incidences are experienced. A blade element-momentum (BEM) method has been chosen as it can handle blades operating in separated flow without being computationally expensive, and it also allows use of the two-dimensional aerofoil data from Ch. 5 in the analysis of turbines. This chapter describes the BEM code developed by the author during this study.

The method is described, along with the models built into it to address secondary effects, namely unsteady aerodynamics, blade Reynolds number effects, blade/wake interactions, flow curvature and three-dimensional effects. Validation of the code to experiments is provided at each step. Modelling focuses on small, straight-bladed turbines as there is a body of experimental data available on them and they represent the bulk of commercially available turbines.

6.1 Blade element-momentum method

BEM methods determine turbine performance by equating: the power from aerodynamic forces on turbine aerofoils (obtained using blade element theory) and the power from forces

arising from the rate of change of fluid momentum through the turbine (obtained using momentum theory). Originally developed for horizontal axis propellers and turbines, a number of approaches have been taken to apply BEM theory to VAWTs.

Forces are calculated using momentum theory by taking the pressure losses across the turbine, modelled as an actuator disk, and applying Bernoulli's theorem. A formula for stream-wise force can be derived [92]:

$$F_T = 2\rho A_2 {V_1}^2 a(1-a) \tag{6.1}$$

where a is the axial induction factor, defined as:

$$a = \frac{V_1 - V_2}{V_1} \tag{6.2}$$

V_1 is the flow velocity at entry to the streamtube, equal to the free-stream velocity V_∞, V_2 is the velocity at the actuator and A_2 is the cross-sectional area of the actuator, see Fig. 6.1.

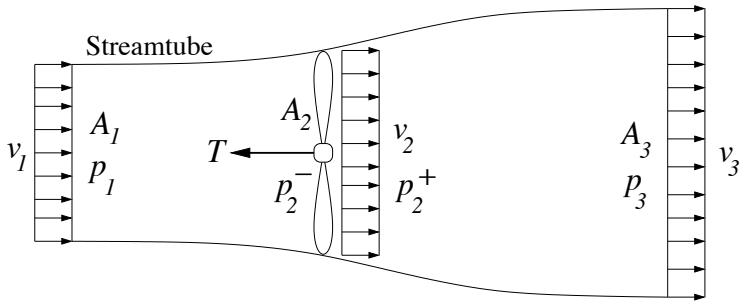


Figure 6.1: An actuator disk in a stream of velocity V_1

Blade element theory determines the forces on a blade by breaking them down into narrow strips for which local forces are calculated. Integrating theses along the length of blades gives the total force acting on the rotor. When applying the method to VAWTs, forces must also be integrated over the course of a full revolution of the turbine. This last step is needed as, unlike in HAWTs, forces are not constant at a given wind speed and rotational velocity. See Fig. 6.2 for a force and velocity diagram of a typical VAWT blade element.

In order to obtain the blade element forces, the flow velocity apparent to the blade, V_b,

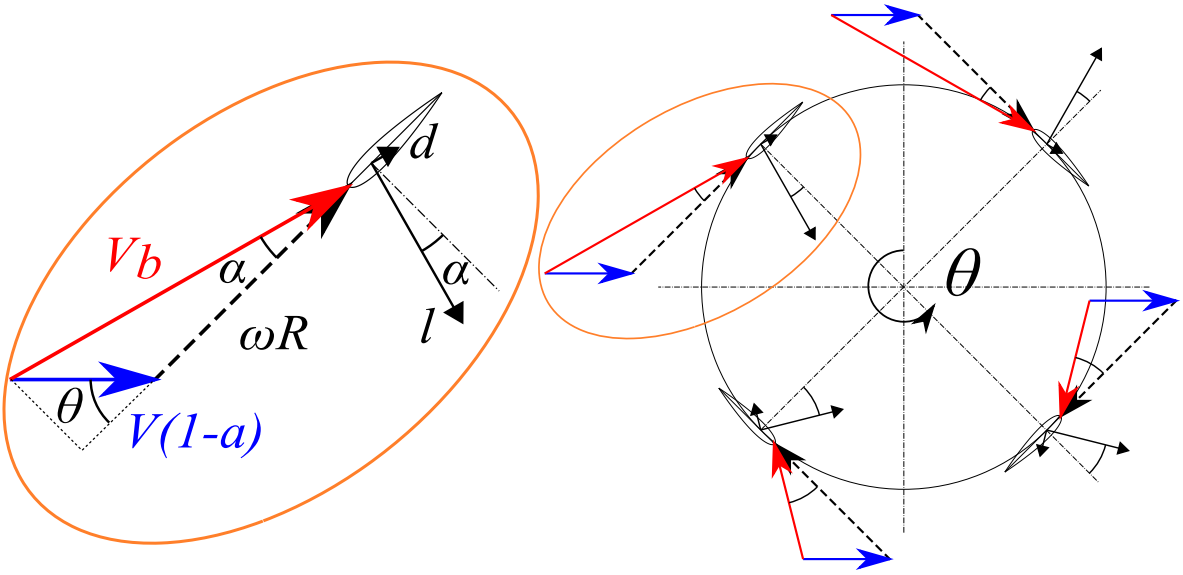


Figure 6.2: Force and velocity diagram for a VAWT blade element

and its effective incidence angle, α_b, must be calculated:

$$V_b = \sqrt{(\omega R + V_2 \cos\theta)^2 + (V_2 \sin\theta)^2} \tag{6.3}$$

$$\alpha_b = \arctan\left(\frac{V_2 \sin\theta}{\omega R + V_2 \cos\theta}\right) \tag{6.4}$$

where θ is the azimuth angle and α_b is the blade effective incidence.

Force coefficient data for aerofoil profiles are conventionally presented as lift and drag coefficients. These can be converted into tangential and normal coefficients using trigonometry:

$$C_t = C_l \sin\alpha_b - C_d \cos\alpha_b \tag{6.5a}$$

$$C_n = C_l \cos\alpha_b + C_d \sin\alpha_b \tag{6.5b}$$

The sign convention used here gives positive C_t in the direction of rotation of the turbine, and positive C_n towards the centre of rotation. The stream-wise force on a blade element can therefore be calculated as:

$$F_T = \frac{1}{2}\rho c {V_b}^2 (C_n \sin\theta - C_t \cos\theta) \tag{6.6}$$

where c is the blade chord. Note that this formula is given per unit of span.

The average force $\bar{F_T}$ of the total turbine in a streamtube can be calculated from the formula for the stream-wise force on a single blade element, by calculating the average F_T in the streamtube, considering the number of blades on the turbine and the fraction of time that they spend in the streamtube:

$$\bar{F_T} = \frac{\theta_{st}}{2\pi} N \frac{1}{2} \rho c \frac{1}{\theta_2 - \theta_1} \int_{\theta_1}^{\theta_2} {V_b}^2 \left(C_n \sin\theta - C_t \cos\theta \right) \mathrm{d}\theta \tag{6.7}$$

where N is the number of blades. θ_{st} is the angle subtended by the sector of the rotation contained within the streamtube, which divided by 2π gives the proportion of time spent in the streamtube. θ_1 and θ_2 are the azimuths of the blade at entry and exit of the streamtube.

The blade element and momentum theories are brought together by equating Eqns (6.1) and (6.7) for the stream-wise thrust force coefficient C_T:

$$\begin{aligned} 4a(1-a) = C_T &= \frac{\theta_{st}}{2\pi} \frac{Nc}{A_2} \left[\frac{1}{\theta_2 - \theta_1} \int_{\theta_1}^{\theta_2} \left(\frac{V_b}{V_1} \right)^2 \left(C_n \sin\theta - C_t \cos\theta \right) \mathrm{d}\theta \right] \\ &= \frac{\theta_{st}}{2\pi} \frac{Nc}{A_2} \; I(\theta_1, \theta_2) \end{aligned} \tag{6.8}$$

The integration-based averaging formula contained in the square brackets can be approximated as:

$$I(\theta_1, \theta_2) \approx \frac{1}{n} \sum_{i=1}^{n} \left[\left(\frac{V_{bi}}{V_1} \right)^2 \left(C_{ni} \sin\theta_i - C_{ti} \cos\theta \right) \right] \tag{6.9}$$

where

$$\theta_i = \theta_1 + \frac{\theta_2 - \theta_1}{n} \left(i - \frac{1}{2} \right) \tag{6.10}$$

and V_{bi}, C_{ni} and C_{ti} are calculated from θ_i using Eqns (6.3) - (6.5). The code described in this chapter uses this methodology.

A solution can be found to satisfy Eqns (6.3) - (6.8) by taking an iterative approach using:

$$a = \frac{C_T}{4} + a^2 \tag{6.11}$$

in the following process:

1. An initial guess of $a = 0$ is taken.

2. V_2 is calculated from Eqn. (6.2).

3. V_b and α are calculated from Eqns (6.3) and (6.4).

4. C_l and C_d are interpolated from published data for the calculated α (and blade Reynolds number based on V_b and c if using variable Re blade data) and used to calculate C_n and C_t.

5. C_T is calculated from Eqn. (6.8).

6. a new guess of a is computed from Eqn. (6.11).

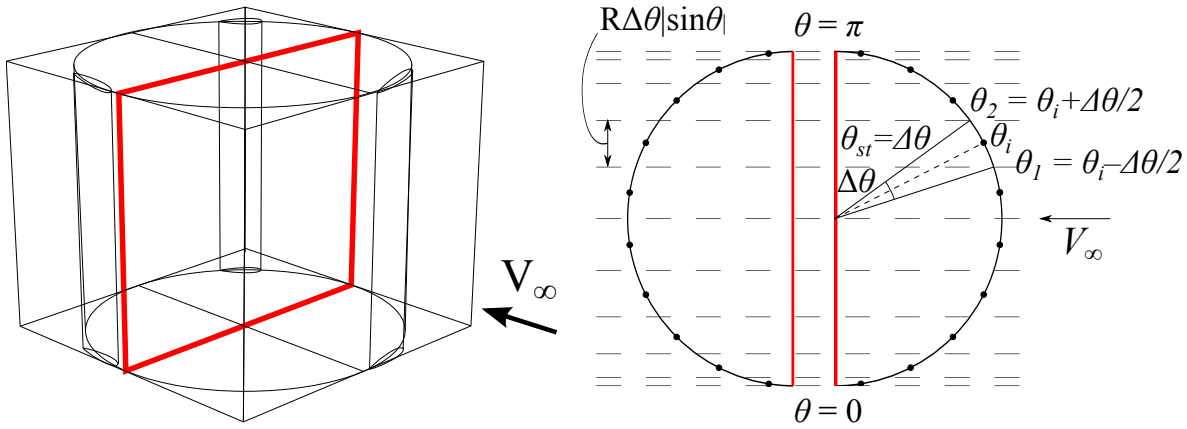
7. This process repeats from step 2, until acceptable convergence between new and old values of a is reached

With convergence complete, final blade forces are obtained, allowing turbine performance to be analysed.

6.1.1 The double-multiple streamtube model

The simplest VAWT BEM analysis, originally developed by Templin [93], models the turbine as a single actuator disk enclosed in a single streamtube. Strickland extended Templin's work to a multiple streamtube approach [94]. Discretising the flow into a number of smaller streamtubes (see Fig. 6.3b) allows the model to capture velocity variations across the turbine. The streamtubes are not of constant width, instead the sectors of rotation between streamtube edges are constant, maintaining a uniform spacing, $\Delta\theta$, between azimuth angles considered in calculations.

Paraschivoiu and Delclaux further developed Strickland's model into the double-multiple streamtube (DMS) approach [95]. Instead of a replica of the single actuator disk used for horizontal axis models, two actuators in an array are used to model the VAWT, effectively splitting the analysis of the upstream and downstream passes of the turbine blades. The exit velocity V_3 of an upstream streamtube is equal to the inlet velocity V_1 of the streamtube directly downstream from it, this "middle" equilibrium velocity is denoted V_e. As well as the assumptions made in any BEM analysis, DMS assumes that there is sufficient distance between the actuators for V_e to develop fully, a reasonable assumption for most streamtubes, other



(a) Sketch showing actuator disc location **(b)** Multiple streamtube, double actuator

Figure 6.3: VAWT streamtube and actuator arrangements, actuators shown in red

than those at θ near 0° or 180° where the upstream and downstream blade passes through the flow are close together. Given the limited regions of the rotor affected, the assumption is applied to all streamtubes regardless.

Since blades pass through each streamtube on each actuator once, $\theta_{st} = \Delta\theta$. The area A_2 can be calculated from the chosen value of $\Delta\theta$ as

$$\begin{aligned} A_2 &= R\left|\cos\left(\theta - \frac{\Delta\theta}{2}\right) - \cos\left(\theta + \frac{\Delta\theta}{2}\right)\right| \\ &= R\left|2\sin\theta\sin\frac{\Delta\theta}{2}\right| \\ &\approx R\Delta\theta\,|\sin\theta| \end{aligned} \tag{6.12}$$

If sufficiently small streamtubes are used, $I(\theta_1, \theta_2)$ can be approximated at a single θ value, giving a C_T formula of the form:

$$C_T \approx \frac{Nc}{2\pi R\,|\sin\theta|}\left(\frac{V_b}{V_1}\right)^2 (C_n\sin\theta - C_t\cos\theta) \tag{6.13}$$

Analysing turbine performance

Once convergence is achieved for all streamtubes using the iterative process described in Section 6.1, the performance of the turbines can be analysed with torque and power coefficients (C_Q and C_P respectively) calculated from the converged tangential coefficients and blade

velocities:

$$C_Q = \frac{Nc}{{V_\infty}^2 R A_{turb}} \frac{1}{2\pi} \int_0^{2\pi} R C_t {V_b}^2 \mathrm{d}\theta \tag{6.14}$$

$$\approx \frac{Nc}{{V_\infty}^2 A_{turb}} \frac{1}{n} \sum_{i=1}^{n} \left[C_{t(i)} {V_{b(i)}}^2 \right] \tag{6.15}$$

$$C_P = \lambda C_Q \tag{6.16}$$

where λ is the TSR.

6.1.2 Limitations of BEM models

BEM theory is only valid for $a < 0.5$, Eqn. (6.2) shows that at higher induction factors the flow at the end of a streamtube would be reversed, an obviously unrealistic result. To account for pressure losses, e.g. due to friction, an empirical relationship can be used to allow induction factors of up to 1, based on a fit to experimental results. Glauert first proposed extending BEM theory for $a > 0.5$ [96], the later development of Sharpe [97] is used here. The expression for the thrust coefficient, C_T, given by:

$$C_T = 4a(1-a) \tag{6.17}$$

in Eqn. (6.8) is replaced by:

$$C_T = C_{T1} - 4(\sqrt{C_{T1}} - 1)(1-a) \tag{6.18}$$

where $C_{T1} = 1.816$. The modified C_T is now used at step 6 of the iterative process described in Section 6.1 for $a_T < a < 1$, where

$$a_T = 1 - 0.5\sqrt{C_{T1}} \tag{6.19}$$

Fig. 6.4 shows the standard BEM induction factor to C_T relationship and Sharpe's empirical extension, alongside the experimental results on which it was based. Though the extension allows for a smooth reduction in streamtube exit velocities up to total blockage, the turbulent flow conditions experienced by the real turbine are complex and not well modelled. Results

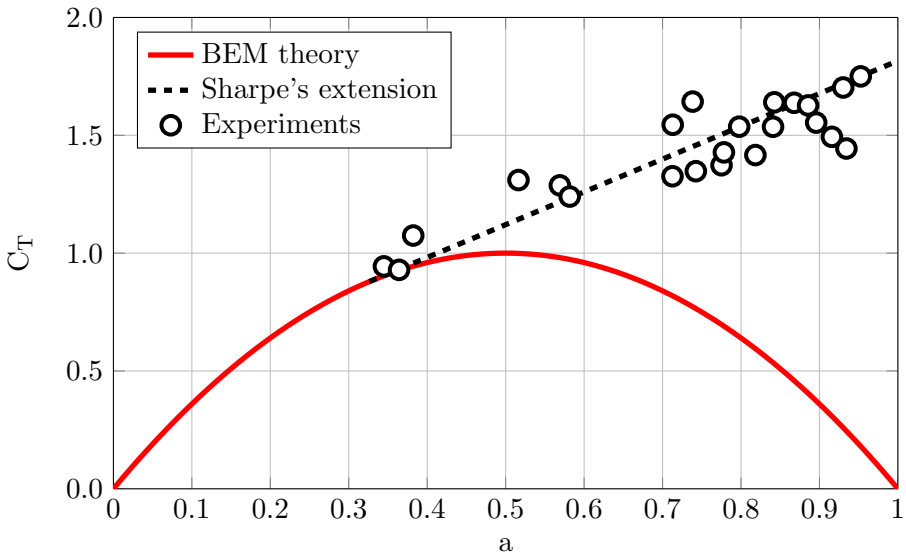


Figure 6.4: C_T vs a relationship per BEM theory and Sharpe's empirical extension [97], and experiments on which the latter is based.

where the induction factor is above a_T are therefore unlikely to be as accurate as those returned by the code where a is lower. Instances of very heavy loading beyond the limits of the extension, i.e. where $a > 1$, can be encountered. This is particularly likely to occur when modelling turbines with high solidity, and when TSRs are high [16]. If this occurs during the iterative process, but not at the final converged solution, it is tolerated. Where $a > 1$ at convergence, results from the code are not presented.

The turbulent state tends to occur at TSRs higher than that at which turbine peak power and torques are achieved, so it has a limited impact on the start-up process.

6.2 Unsteady aerodynamics

The mechanical simplicity of VAWTs does not extend to their aerodynamics. Blade apparent velocity and effective incidence are functions of wind speed, rotational velocity and the blade's azimuth angle. This makes the apparent velocity and incidence vary with time even at a constant wind speed and rotational velocity, meaning transient effects, such as unsteady aerofoil behaviour, are important contributors to VAWT performance.

The reduced frequency, k, of a system is a measure of the degree to which unsteadiness affects it and can be defined for a VAWT in terms of TSR and turbine chord-to-radius, c/R,

ratio:

$$k = \frac{1}{2}\lambda\frac{c}{R} \tag{6.20}$$

When $k = 0$, flow is steady and where $k < 0.05$ it can be considered quasi-steady and unsteady effects neglected. For $0.05 < k < 0.2$ unsteady effects are significant and beyond this the problem is considered highly unsteady, with the effects coming to dominate aerofoil behaviour [22].

For the "Durham" turbine in Table 6.1 (the turbine used to produce the data in Fig. 1.1), which has a c/R ratio of 0.21 [3], this equates to a threshold of TSR = 0.48 at which a quasi-steady analysis is no longer appropriate and TSR = 1.90 for the turbine blades to be experiencing highly unsteady flow, putting the vast majority of the start-up ramp and peak operating conditions in the unsteady realm. c/R ratios are similar to this wind tunnel model for most production VAWTs.

6.2.1 Dynamic stall

At high TSRs, rotational velocities dominate the VAWT blade velocity triangle, minimising the variation in blade relative velocity and incidence. At the low TSRs experienced during start-up, the opposite is true, with the component due to rotation comparatively small, so the VAWT blades experience a wide range of angles of attack. At TSRs of 2 or lower the effective incidence well exceeds the stall angle at points in the rotation, so dynamic stall is a key contributor to blade performance. This complex phenomenon manifests itself as large overshoots of the lift and drag forces with respect to those that would be predicted taking a quasi-steady approach, with significant hysteresis depending on whether the motion of the aerofoil is causing flow to separate or reattach [22].

Most existing dynamic studies of aerofoils are based on oscillatory pitching motion about some mean angle usually of the order of the static stall angle and provide pressure data (see [98] for a recent review of such experiments). Where more complex combined plunging and pitching motions have been studied, comparisons between pure pitching, pure plunging and combination pitch and plunge, and between combination pitch and plunge about different mean incidences is provided, showing disparities in lift hysteresis outputs for the different modes of oscillation [99].

VAWT blade motion is more complicated still, since it is analogous to a combined pitch, plunge and surge about a mean angle close to zero, with significant amplitude of variation of incidence at low TSRs, suggesting VAWT blade hysteresis will be different again to anything available in literature. In spite of this, good results have been obtained making use of a number of semi-empirical dynamic stall models for pitching motion, though mostly for higher TSRs.

The most commonly used are the Gormont model [100] (also known as the Boeing-Vertol model), first modified for use with VAWTs by Strickland et al. [90, 101], and the MIT model [102], adapted by Noll and Hamm [103] for use in HAWTs and VAWTs. Both methods allow for calculation of approximate dynamic blade forces from quasi-steady experimental data, given the rate of change blade incidence and the amplitude and mean angles of the oscillation.

Gormont's model assumes that the slope of the static C_l-α curve and the zero lift incidence α_0 remain unchanged by dynamic effects, with just the stall angle and $C_{l\ max}$ modified, the linear region of the lift curve being effectively extended beyond static stall by means of a calculated reference incidence. The MIT model delays stall to a prescribed angle of attack, at which point forces and moments delay exponentially to static values. Noll and Ham's modification uses Gormont's methods to find the prescribed dynamic stall angle.

Less common in VAWT codes is the Leishman-Beddoes [104] dynamic stall model, first applied to VAWTs by Major and Paraschivoiu [105]. It uses an indicial method where the aerofoil's behaviour is represented by separate models for distinct effects that combine to represent the complete dynamic system. Potential flow is used for the initial, quasi-steady approximation of the aerofoil performance, then empirical formulae are used to introduce unsteady nonlinear viscous effects. Finally, dynamic stall vortices are considered.

Several studies of the comparative merits of different dynamic stall models for VAWT analysis have been conducted, all of which have used DMS BEM codes to model VAWT behaviour. Paraschivoiu and Allet [31] compare the VAWT-specific models of Strickland et al. and Noll and Ham, alongside their own adaptation of Strickland, to experimental results for the Sandia 17 m VAWT [106]. Their adaptation disengages the dynamic stall model at azimuths of 105° to 225° (see Fig. 6.2 for the azimuth convention used here). For the region of the turbine power curve before peak power (of principle interest in the study of start-up),

the performance of all three models was similar. Strickland et al. performs better than Noll and Ham, but Paraschiciou and Allet's own model is slightly better still, giving very close agreement to the experiment.

Major and Paraschivoiu [105] compared their own Leishman-Beddoes approach to Strickland et al, Noll and Ham and the Sandia 17 m experiment. The indicial approach was found to perform best, but is no better than the Paraschivoiu and Allet adaptation of Strickland in the run up to peak power.

Pawsey [107] compares Strickland et al, Noll and Ham and Cardona's modification of Strickland to purely quasi-steady numerical results. Cardona disengages the model where it predicts rapidly oscillating angles of attack (possibly due to numerical instabilities of the vortex turbine model to which he applied the model) and uses an average of static and dynamic forces where incidences are much higher than static stall. The unmodified Strickland model gave unusual results at peak power, but as with the other comparative studies, the dynamic stall models all have a similar effect on the BEM code output before peak power is reached.

6.2.2 Dynamic stall model of the current study

Given the similarities of modelled turbine performance with all the reference dynamic stall models, the simplest models should be preferred, namely Strickland at al's [101, 90] VAWT-specific version of the Gormont [100] model and Noll and Hamm's [103] version of the MIT model [102]. Strickland et al. has been selected for use in this study as it is the slightly better performer of the two in the comparative studies referenced in the previous section. Strickland et al's modifications to Gormont's model comprise three elements:

- Flow is assumed to be incompressible, with all consideration of Mach numbers removed. The model was originally developed for helicopter rotors but wind turbines operate in far lower Mach regimes making this adaptation appropriate.

- Aerofoils are assumed to be thick. The original model contains an element based on thickness ratio that reduces with increasing thickness, reaching zero when $t/c = 0.1$. Since VAWT blades are almost always thicker than this, the element is removed entirely.

- The model is only applied when the angle of attack is above the static stall angle, or when the angle of attack is decreasing.

The model first requires the calculation of a reference incidence α_{ref},

$$\alpha_{ref} = \alpha_b - \gamma K_1 \sqrt{\left| \frac{c\dot{\alpha}_b}{2U} \right|} \tag{6.21}$$

based on the blade effective incidence α_b, the reduced frequency of the incidence oscillation $c\dot{\alpha}_b/2U$, where $\dot{\alpha}_b$ is the rate of change of the effective blade incidence with time, and two empirical constants, γ and K_1, given by:

$$K_1 = \begin{cases} 1 & \text{when } \dot{\alpha}_b \geq 0 \\ -0.5 & \text{when } \dot{\alpha}_b < 0 \end{cases} \tag{6.22}$$

$$\gamma = \begin{cases} 1.4 - 6(0.06 - t/c) & \text{for lift force calculations} \\ 1 - 2.5(0.06 - t/c) & \text{for drag force and moment calculations} \end{cases} \tag{6.23}$$

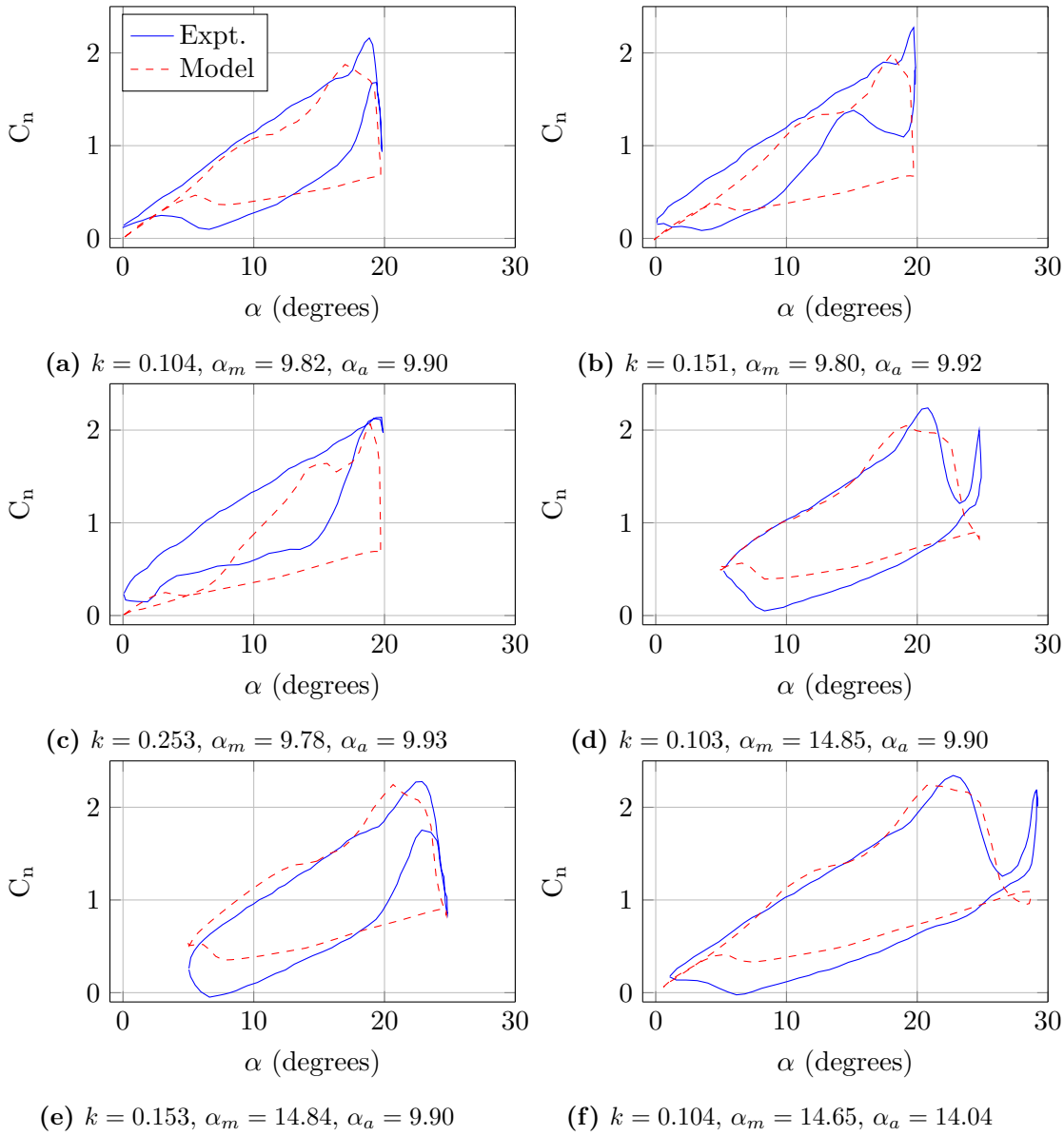
The reference angle is used to obtain lift, drag and moment from look-up tables of static experimental data, with the required forces given by

$$C_l = \left(\frac{\alpha_b}{\alpha_{ref} - \alpha_0} \right) C_l(\alpha_{ref}) \tag{6.24}$$

$$C_d = C_d(\alpha_{ref}) \tag{6.25}$$

$$C_m = C_m(\alpha_{ref}) \tag{6.26}$$

The performance of the model has been validated at an aerofoil-level against the NACA 0012 experimental results of McCroskey et al. [108]. Tests were conducted at a range of reduced frequencies, Reynolds numbers and Mach numbers. Those closest to the operating conditions of VAWTs have been selected for validation here, with $Re = 490\,000$ and $M = 0.036$. The static experimental results of Critzos et al. for the NACA 0012 at $Re = 500\,000$ and $M = 0.15$ were used for look-ups for the dynamic stall model. See Fig. 6.5 for the results of this comparison for normal force coefficient C_n. Sub-plots are labelled with the reduced frequency, mean incidence α_m and amplitude of incidence oscillation α_a of the experiment. All oscillations were sinusoidal. The model provides a reasonable approximation of the dynamic stall hysteresis loops for $k < 0.25$, particularly where incidence is increasing. There is a



(a) $k = 0.104$, $\alpha_m = 9.82$, $\alpha_a = 9.90$

(b) $k = 0.151$, $\alpha_m = 9.80$, $\alpha_a = 9.92$

(c) $k = 0.253$, $\alpha_m = 9.78$, $\alpha_a = 9.93$

(d) $k = 0.103$, $\alpha_m = 14.85$, $\alpha_a = 9.90$

(e) $k = 0.153$, $\alpha_m = 14.84$, $\alpha_a = 9.90$

(f) $k = 0.104$, $\alpha_m = 14.65$, $\alpha_a = 14.04$

Figure 6.5: Dynamic stall model C_n against α compared to McCroskey et al's test data [108] taken at $Re = 490\,000$ and $M = 0.035$.

degradation in model output quality with increasing k, results at $k \approx 0.1$ are closest to test data, those at $k \approx 0.15$ are less so. The performance at $k = 0.253$, shown in Fig. 6.5c, is not close to the experiment for increasing or decreasing incidence. For the reference turbine used in this study, a TSR of 1.9 equates to $k = 0.2$, so the majority of the start-up process occurs at $k < 0.2$, making the dynamic stall model acceptable for use in the study of start-up.

	Strickland et al. [90]	Vittecoq & Laneville [77]	Durham [2, 3]	Bianchini et al. [4, 6]	Bravo et al. [78]	Maeda et al. [79, 80]	Chua [5]
R	0.61 m	0.3 m	0.375 m	0.5 m/0.725 m	1.25 m	1 m	0.25 m
c	0.0914 m	0.061 m	0.083 m	0.2 m/0.22 m	0.4 m	0.265 m	0.07 m
N	2	2	3	2 / 3	3	2 / 4	3
s	1.15 m	0.6 m	0.6 m	0.9 m/1.45 m	3 m	1.2 m	0.5 m
c/R	0.150	0.203	0.221	0.400/0.303	0.320	0.265	0.280
Solidity	0.300	0.406	0.663	0.800/0.910	0.960	0.530/1.060	0.840
Profile (NACA)	0012	0018	0018	0015 (transformed)	0015	0021	0015

Note: all turbines have straight blades, except Bianchini's helical 3-bladed turbine

Table 6.1: Summary of turbines referenced in this paper.

In order to validate the model for use in VAWT modelling, comparisons have been made to force measurements of blades undergoing VAWT motion. Strickland et al. [90] made strain gauge measurements of blade normal and tangential forces on a VAWT with two NACA 0012 blades. For dimensions of the turbine, see Table 6.1. Experiments were conducted in a tow tank, with water as the working fluid to allow for reproduction of blade Reynolds numbers at lower absolute speeds. TSRs of 2.5, 5 and 7 were used. The blades stretch almost to the bottom of the tow tank, giving effectively two-dimensional data. Flow velocity was set so that the minimum blade Reynolds number experienced in the runs was 40 000, in order to make use of published data for the NACA 0012 in analysis (none was available at Reynolds numbers lower than this).

Vittecoq and Laneville conducted similar experiments in a wind tunnel, using a turbine with NACA 0018 blades in a wind tunnel [77]. See Table 6.1 for turbine dimensions. Experiments were three-dimensional. TSR values of 2, 2.5, 3, 3.5 and 5 were used, with detailed data presented for TSR = 2.5. Comparisons have been made between the BEM code developed during this study and the results of the these two studies at this TSR. Given the turbine dimensions, the reduced frequencies of the turbines are 0.187 for Strickland et al. and 0.254 for Vittecoq and Laneville. Figs 6.6 and 6.7 show results for the two studies for normal and

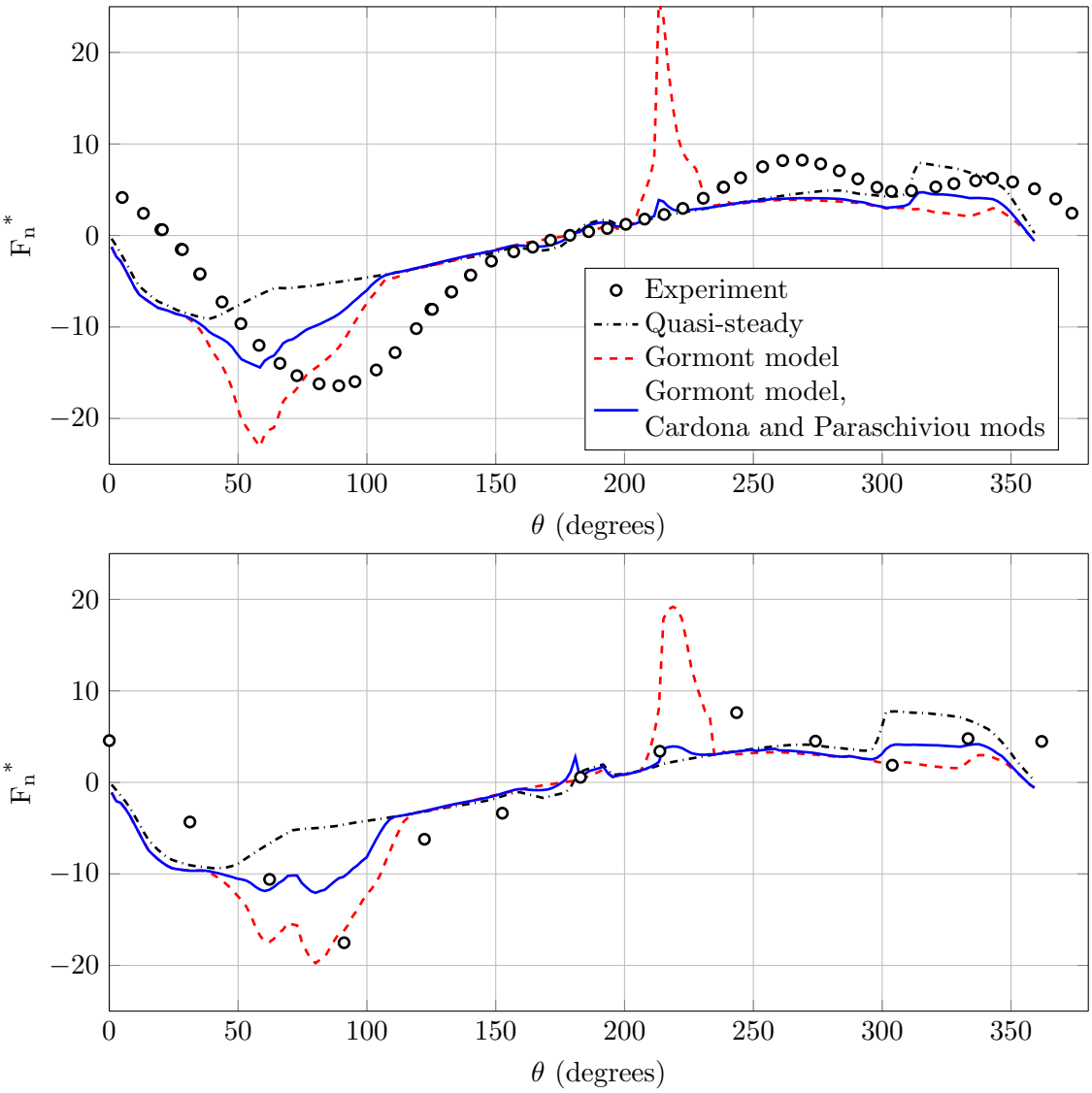


Figure 6.6: $F_n{}^*$ vs θ at TSR = 2.5, models compared to test data of (a) Strickland et al. [90] and (b) Vittecoq and Laneville [77].

tangential F^*, blade coefficients non-dimensionalised with the free stream velocity:

$$F^*_{n,\,t} = C_{n,\,t}\left(\frac{V_b}{V_\infty}\right)^2 \tag{6.27}$$

The two studies show strong agreement for $F_n{}^*$, with a large negative peak at around $\theta = 90°$ and smaller positive peaks at 250° and 250°. $F_t{}^*$ agreement is reasonable, both experiencing a peak at 70°. Vittecoq and Laneville has a negative peak at 100° that isn't

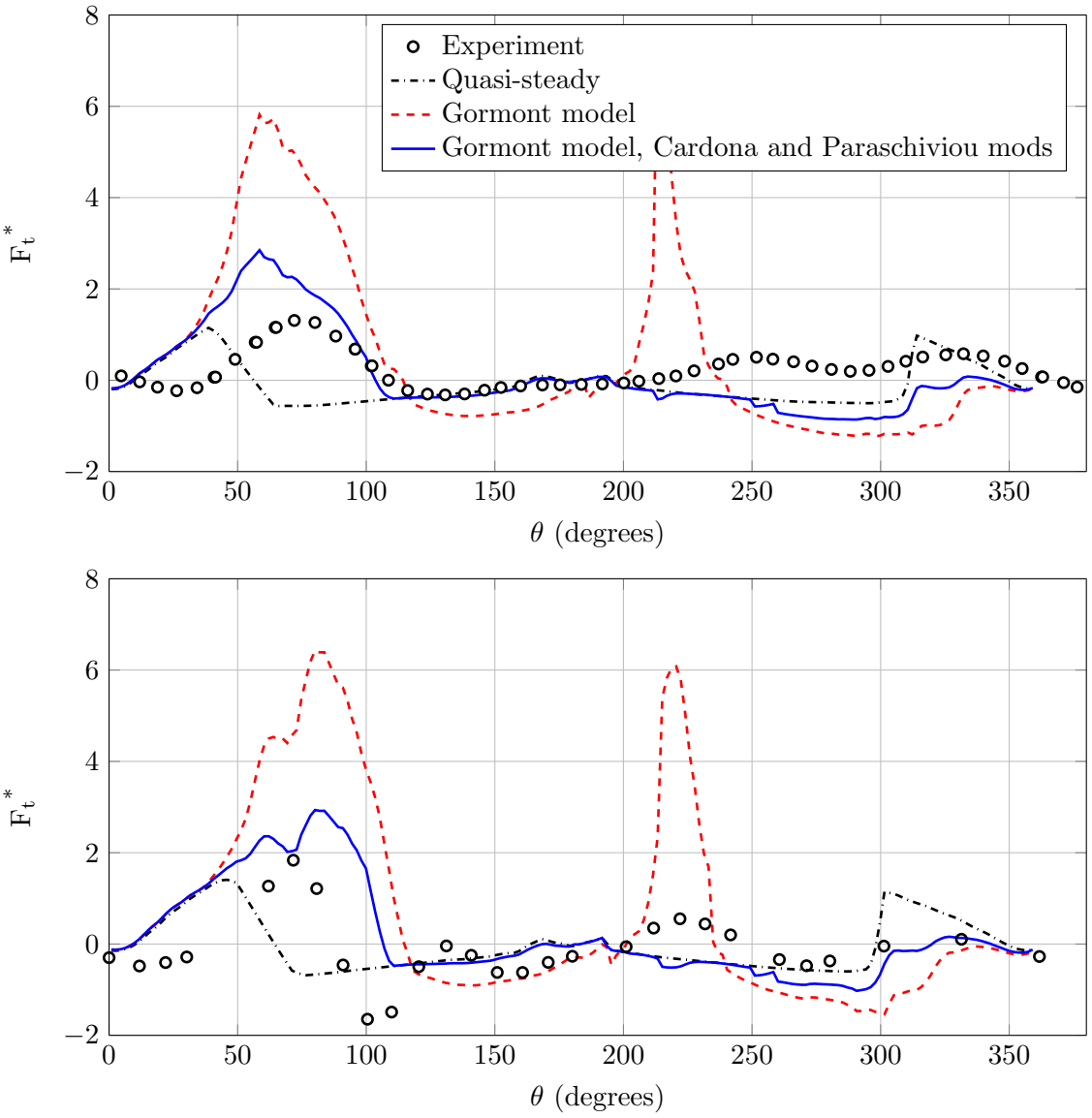


Figure 6.7: F_t^* vs θ at TSR = 2.5, models compared to test data of (a) Strickland et al. [90] and (b) Vittecoq and Laneville [77].

present in the Strickland data. Agreement is poor beyond 100°, though F_t^* is low in both cases in this region. All peaks in starred forces are of similar magnitude. Given the similar reduced frequencies and blade profiles used, the similarities are expected. The differences between F_t^* probably result from the difficulties associated with measuring a low force in a rotating experiment where noise could easily approach the order of the measured force and centrifugal forces are likely to be far higher, as well as the differences in behaviour expected between NACA 0015 and 0018 profile blades.

When simulating the studies, flow velocities have been chosen so that blade Reynolds numbers are approximately equal to the original experiments. When modelling turbines with NACA 0018 blades, experimental data for that section from Ch. 5 is used, while those for NACA 0012-bladed turbines use data for the NACA 0015. Figs 6.6 and 6.7 show simulations based on:

- A quasi-steady approach (with blade Reynolds number effects considered, see Section 6.3.)
- With dynamic stall modelled using Gormont (after Strickland et al. [101, 90]) and attached flow unsteady effects using Gormont, see Section 6.2.3.
- With dynamic stall modelled using Gormont (after Strickland et al. [101, 90]), with the aforementioned modifications of Cardona [107] and Parachiviou and Allet [31] and attached flow unsteady effects using Gormont.

The blade of the quasi-steady simulations stalls at an azimuth around 40° (note the drop in tangential forces at this point in Fig. 6.7), where the effective blade incidence is 10° to 11°, the static stall angle of for the local Re_b. In the experimental results, this stall is delayed to an azimuth of 70°, where the effective blade incidence is 17°, well beyond static stall for either the NACA 0015 or 0018 at the local Re_b, suggesting dynamic stall has a significant impact on the turbines' performance.

Strickland et al's version of the Gormont model reproduces trends in the tangential and normal forces well, other than a superfluous peak in both at $\theta = 220°$. These peaks are also present in Pawsey's simulations using this model [109]. Normal force magnitude is reasonable, though the model leads experiments by $20° - 30°$. Tangential forces are approximately in phase, but modelled output is three times larger than the experimental measurements. Pawsey's [109] and Strickland et al's own modelling [90] give similar results to the current model. Much better agreement is given at TSRs of 5 and 7 but these are of limited use to the current start-up focused study.

Cardona developed his model, which calculates results with and without dynamic stall then averages the two [107], in order to better match Strickland et al's experimental results. It gives much better performance for $F_t{}^*$, with magnitudes close to experiments. The modification

has been adopted as tangential forces are of primary importance to turbine performance and ${F_n}^*$ accuracy is not negatively impacted.

Parachiviou and Allet turn off the dynamic stall model at azimuths of 105° to 225° [31], in an effort to model the effects of blade/wake interactions in this region of the rotation, see Section 6.4 for more on this. The modification is used here as the quasi-steady models outperform the dynamic stall simulations in the identified range of azimuths.

The model combining both modifications gives better force reproduction than Strickland et al's Gormont model, but normal forces are still out of phase and the tangential forces in the downstream half of the rotor ($180° < \theta < 360°$) are not well reproduced. For a semi-empirical dynamic stall model, based on a basic aerofoil pitching motion, the agreement is acceptable.

Ideally, results at lower TSRs should be used for code validation for the purposes of a study into start-up. To the best of the author's knowledge, the only such data available is that of Maeda et al. [79, 80]. Their studies are discussed and validated against in Section 6.5, where modelling of virtual incidence and camber is built into the code.

6.2.3 Attached flow unsteady aerodynamics

In the absence of dynamic stall, unsteady effects manifest due to circulatory components (unsteady wake circulation) and non-circulatory "added mass" components resulting from fluid inertia. The original Gormont model [100] includes formulae based on Theodorsen [110] to take account of added mass and unsteady pitching effects, derived using a potential flow analysis. These are given in terms of an equivalent incidence α_{equ} and $\bar{\alpha}$, reproduced below with the original elements concerning blade coning and heaving omitted:

$$\alpha_{equ} = \alpha_b + \left[F - c\left(\frac{3}{4} - PA\right)\frac{G\omega}{V_\infty}\right] + \arctan\left\{\left[c\left(\frac{3}{4} - PA\right)F + \frac{GV_\infty}{\omega}\right]\frac{\dot{\alpha}}{V}\right\} \tag{6.28}$$

$$\bar{\alpha} = \frac{c}{4}\left[\frac{\dot{\alpha}}{V_\infty} - \left(PA - \frac{1}{2}\right)\ddot{\alpha}\frac{c}{{V_\infty}^2}\right] \tag{6.29}$$

where F is Theodorsen's lift deficiency factor, G is Theodorsen's phase lag factor, PA is the dimensionless pitch axis (the quarter chord here) and $\ddot{\alpha}$ is the second derivative of incidence with time. F and G are functions of k, shown in Fig. 6.8.

The formulae are implemented by altering the dynamic stall equations Eqns (6.24) and

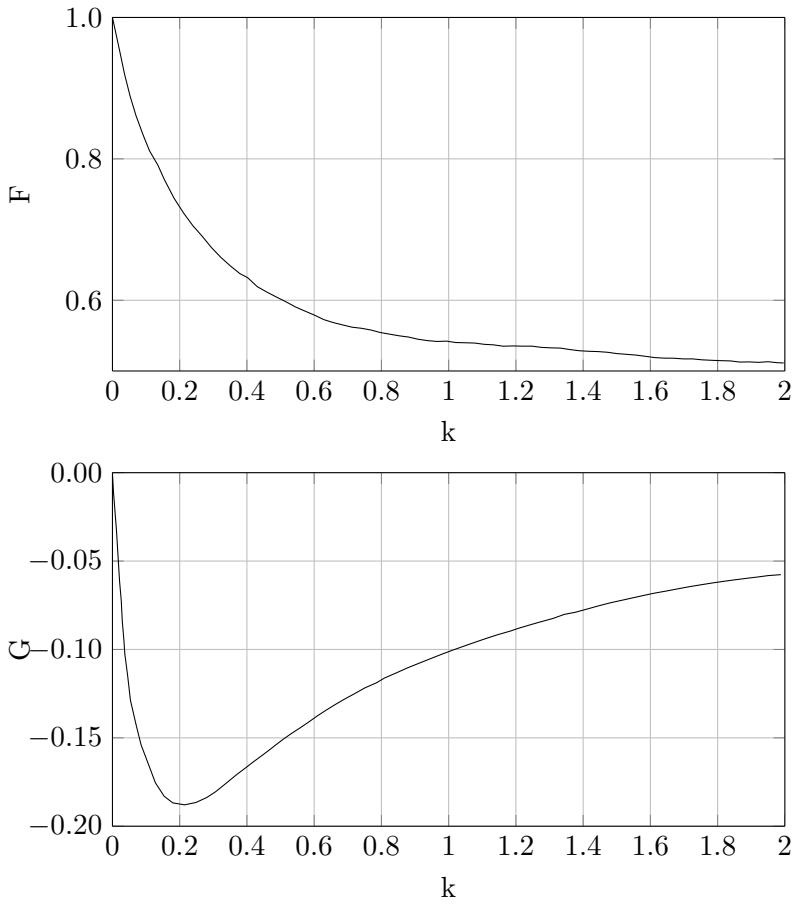


Figure 6.8: Theodorsen's F and G functions against k

(6.26) as follows (Eqn. (6.25) for drag remains unchanged):

$$C_l = \left(\frac{\alpha_{equ} + \bar{\alpha}}{\alpha_{ref} - \alpha_0}\right) C_l(\alpha_{ref}) \tag{6.30}$$

$$C_{m\ PA} = C_m(\alpha_{ref}) + \left(PA - \frac{1}{4}\right) C_d \sin\alpha_b + \left(\frac{\left[\alpha_{equ}\left(PA - \frac{1}{4}\right) + \bar{\alpha}\left(PA - \frac{3}{4}\right)\right]\cos\alpha_b}{\alpha_{ref} - \alpha_0}\right) C_l(\alpha_{ref}) - \frac{\pi}{8}\left(PA - \frac{3}{8}\right)\ddot{\alpha}\frac{c^2}{{V_\infty}^2} \tag{6.31}$$

Theodorsen's formulae are included in the BEM model of this study, with F and G implemented using an iteration from a look-up table. They have a minimal impact on the results of Figs 6.6 and 6.7. Code output is similar regardless of whether or not attached flow unsteady effects are switched on or off, but they can have more significant effects at higher k.

6.3 Blade Reynolds number effects

Due to the vertical axis of rotation, VAWT blades experience a wide range of Reynolds numbers even when the turbine is operating at a steady TSR. Blade apparent velocities are higher as the blade is moving into the wind and lower as it moves away. For example, in Sheldahl et al's experiment considered in this section, the turbine blades are experiencing Reynolds numbers of 40 000 - 110 000. The BEM code considers blade Reynolds number effects by performing a two-dimensional iteration for the lift and drag data from Chaper 5, based on incidence and Reynolds number, at step 4 of the iterative process described in Section 6.1. Data for $Re = 20\,000$ is not used due to its low accuracy. Lift and drag coefficients of zero at $Re = 0$ are included in the look-up data.

Figs 6.9 and 6.10 are presented to demonstrate the importance of proper blade Reynolds number consideration. The output of the BEM code from Figs 6.6 and 6.7 is included along with experimental results. Also plotted is the output of the code with the variable Reynolds number model turned off, with a fixed Re_b of 80 000 applied (the approximate mean Re_b of the experiments). In the regions where the variable Reynolds number is close to the mean, at $90° < \theta < 150°$ and $230° < \theta < 290°$ where the blade is travelling across the flow, there is limited impact on model output. Differences manifest at azimuths near 0° of 180° where Re_b is furthest from the mean, or where the modelled output it reliant on heavily Reynolds number-dependent attached flow quasi-steady data, at $50° < \theta < 90°$ and $290° < \theta < 340°$.

It is perhaps surprising that the peaks in $F^*_{n,t}$ in the first quadrant of the rotation are higher at the fixed Re_b, given that variable Re_b is higher than 80 000 here, and aerofoil performance generally improves with higher Reynolds number. This behaviour can be explained by examining some inputs and workings of the code, namely the dynamic stall α_{ref} (defined in Eqn. (6.21)) and the underlying quasi-static lift data for the NACA 0015 and 0018, presented in Figs 5.3 and 5.13. At $50° < \theta < 90°$, the code outputs $0° < \alpha_{ref} < 9°$. In this region of incidences, drag coefficient decreases with increasing Reynolds number as expected. Due to the effects of the laminar separation bubble (see Section 5.2.3), lift coefficient also decreases with increasing Reynolds number, explaining the higher peaks in normal and tangental forces at the lower fixed Re_b.

The variable Re_b peaks are further from the experiment for than the fixed for F^*_n but are

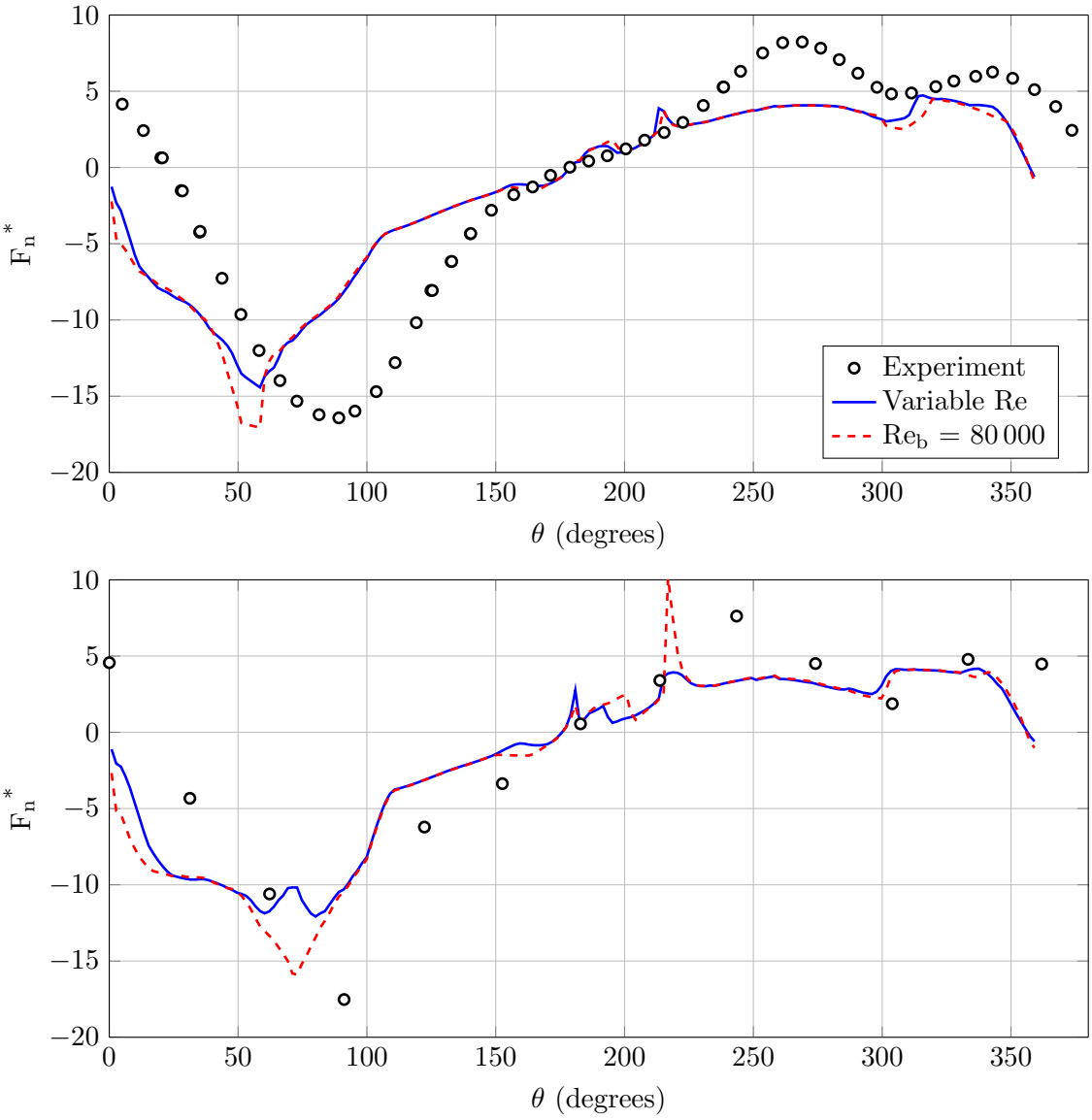


Figure 6.9: $F_n{}^*$ vs θ at TSR = 2.5, models with and without variable Re_b, compared to test data of (a) Strickland et al. [90] and (b) Vittecoq and Laneville [77].

closer for F_t^*, and the variable results are smoother at $100° < \theta < 360°$. For these reasons, variable Re_b are used in the final version of the BEM code.

6.4 Blade-wake interactions

Blade-wake interactions occur in VAWTs, with blades on the downstream half of the rotation encountering the wakes of those on the upstream half of the rotation. At certain TSRs

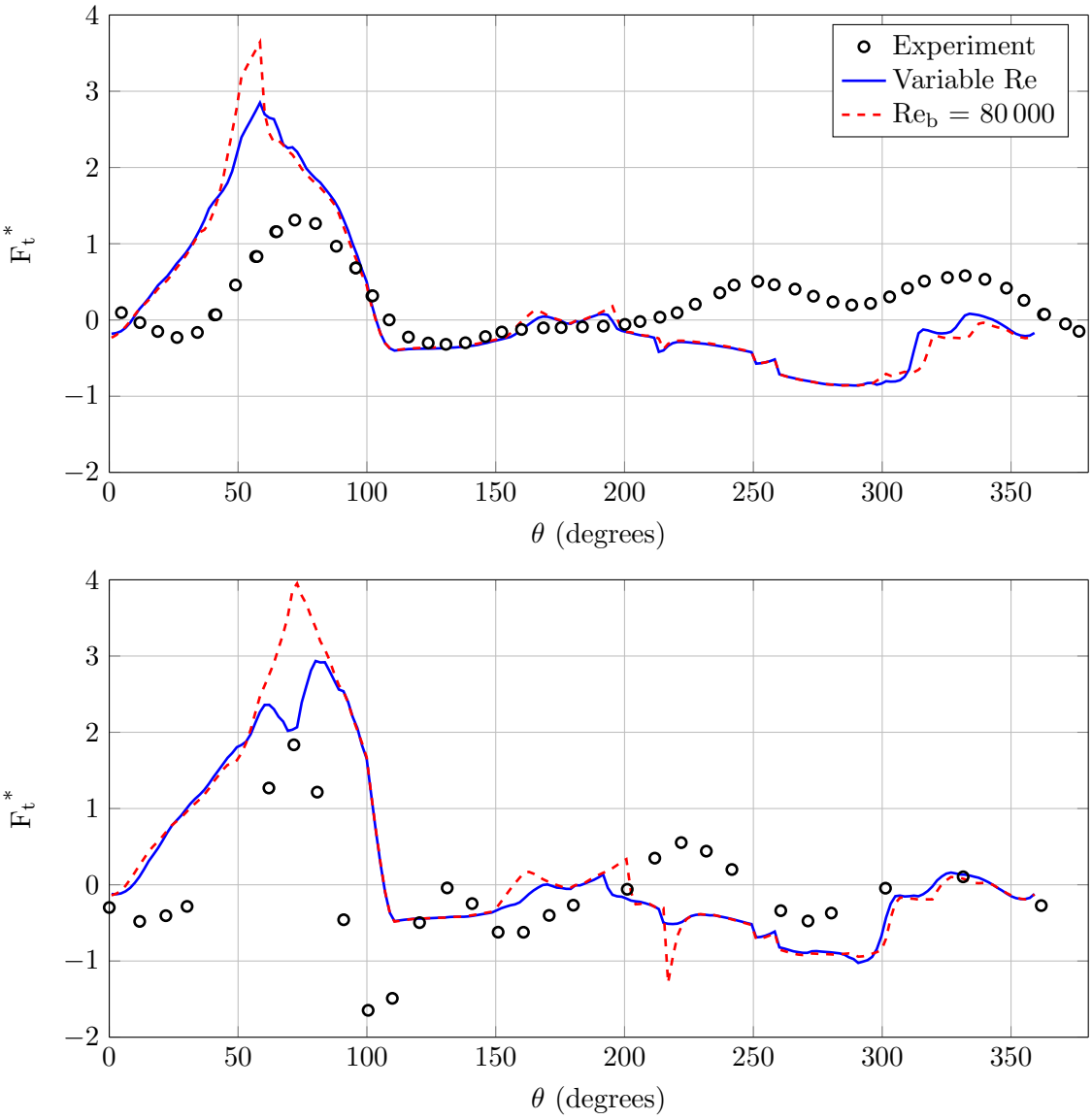


Figure 6.10: $F_t{}^*$ vs θ at TSR = 2.5, models with and without variable Re_b, compared to test data of (a) Strickland et al. [90] and (b) Vittecoq and Laneville [77].

these interactions have a more significant impact than others, the range of 0.5>TSR>1.6 sees particularly extensive blade-wake interactions [23], a region of TSRs key to start-up. Some work has been conducted on blade-wake interactions by the author, making comparisons between a code that captures their influence (a discontinuous-Galerkin solver for the Navier Stokes equations) and one that doesn't (a simplified quasi-steady version of the BEM code described in this chapter) [111]. This work suggests blade-wake interactions are prevalent at azimuths of 150° to 190° at TSR = 1.

The final version of the BEM code gives some consideration to blade-wake interactions through the use of the aforementioned Paraschivoiu and Allet [31] modification to the dynamic stall model, turning off the model at certain azimuths. The modification was developed in response to results of a dye release experiment in a water channel [112], which identified $105° < \theta < 225°$ as a turbulent region of the rotation, resulting from wakes of blades passing through lower azimuths. This turbulence delays the onset of dynamic stall, so a quasi-steady approach is used instead in the identified azimuth range. The similarities of the azimuth ranges identified by Paraschivoiu and Allet [31] and in the development of the discontinuous-Galerkin solver used in this study [23], and the better agreement to experimental blade forces in Figs 6.6 and 6.7 of the quasi-steady model in the identified range, support the adoption of the modification in the BEM code.

6.5 Migliore's virtual camber and incidence effects

Flow curvature has been demonstrated to have a large impact on small Darrieus turbine performance. These effects, caused by the curved paths that VAWT blades follow in operation, were first proposed by Migliore et al. [24]. They manifest in a virtual blade camber and incidence, giving blade performance characteristics analogous to those of a cambered blade at incidence in a rectilinear flow. Migliore never went beyond his theoretical approach to verify his proposals experimentally. Several studies have reassessed the theory numerically, including Cardoa's aformention study which yielded the dynamic stall model used in this study [107]. Recent work by Bianchini et al. has attempted to address the problem experimentally, using a turbine with NACA 0015 profiles transformed after Migliore [4, 6], see Section 4.2.2 for more on the transform applied to the blade shapes and Table 6.1 for more on Bianchini's turbine.

The NACA 0018 and the two cambered aerofoils based on it presented in Ch. 5 were tested to enable assessment of Migliore's theory. This section contains that assessment, using data obtained from the aerofoils and the author's own BEM model described in this chapter. Results are then given from a collaborative project with Bianchini's team at the University of Florence using data from the aerofoils with BEM and CFD modelling techniques developed by the Italian team.

6.5.1 Imperial BEM code results

Vittecoq and Laneville's turbine has NACA 0018 blades and $c/R = 0.203$. Following Migliore's theory for a turbine with this c/R, a blade mounted at the quarter chord will have virtual incidence of 2.908° and a maximum virtual camber of 2.53% at 50% of chord. To model the turbine with available experimental data, the appropriate incidence has been used. The NACA 0018 transform with camber applied to replicate the virtual blade in a turbine with $c/R = 0.25$ is the nearest match to the virtual camber. The aerofoil has a maximum camber of 3.11% at 50% of chord.

Fig. 6.11 shows the output of the code and experiment as presented previously, alongside results using the cambered blade at incidence. The most notable improvement is to the phase alignment of the model and experiment, with a narrowing of the gap in azimuth between modelled and experimental peaks and troughs in blade forces. Modelled F_t^* peaks are also reduced and are closer to the experimental values. At azimuths above 180° performance of the virtual aerofoil is worse than for the physically matched blade profile. For F_n^* the phase shift is the only significant impact of the virtual camber and incidence.

Maeda et al. took pressure readings from a tapped VAWT blade tested in a wind tunnel. Blade forces are calculated from the pressures, measured at 32 points around the blade. They provide tangential forces from a two-bladed turbine at TSRs of 1.38, 2.19 and 2.58 [79] and tangential and normal forces from a four-bladed turbine at TSRs of 1.01, 1.68 and 2.03 [80]. In both studies, the turbine uses NACA 0021 blades, with $c/R = 0.265$ (see Table 6.1). The virtual blade of their turbine would have a maximum camber of 3.30% at 50% of chord and an incidence 3.796°.

Accuracy of the experimental data may be limited due to the method of measurement, particularly for tangential forces, and the static stall of a NACA 0021 occurs at higher incidence and with larger $C_{l\,max}$ than the 0015 or 0018, but qualitatively it is still useful and allows assessment of the code's performance at $TSR < 2.5$. Results of the first of their two studies (the two-bladed turbine study) show poor agreement to Strickland et al. and Vittecoq and Laneville at the comparable TSR of 2.58, with F_t^* peak in the upstream half of the rotation being double that of the other studies. Their later study shows much stronger agreement to the literature and provides both normal and tangential forces. Only results of validation

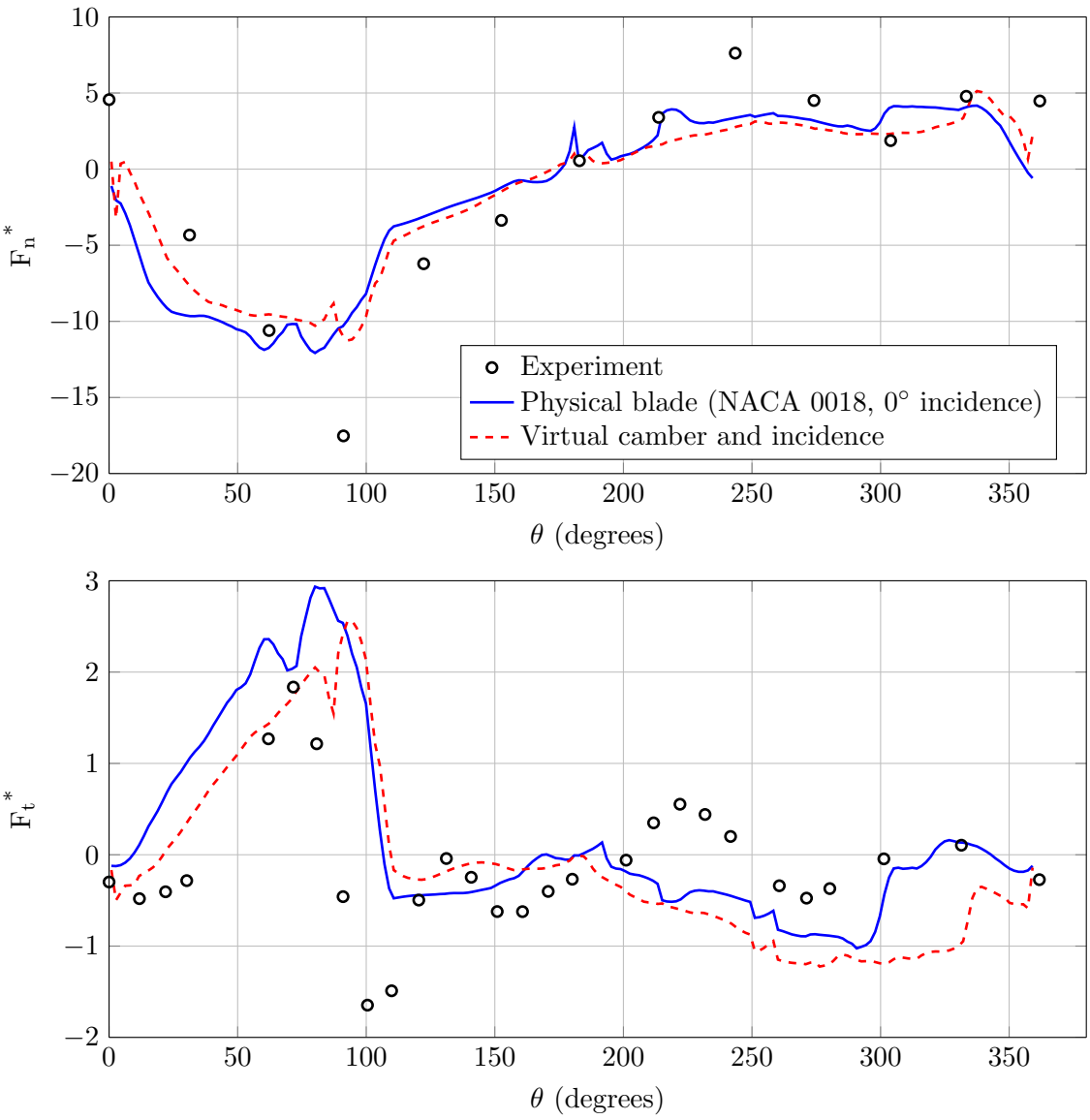


Figure 6.11: (a) $F_n{}^*$ and (b) $F_t{}^*$ vs θ at TSR = 2.5, models with and without virtual camber and incidence effects, compared to test data of Vittecoq and Laneville [77].

against the later study are presented here, in Fig. 6.12.

The blades of their VAWT are set with an incidence of 8° from the tangent to their circumference of rotation as this produced better turbine power readings. Blades have been set at an incidence of 8° in the BEM model and the $c/R = 0.25$ NACA 0018 blade is used to approximate the 0021 with virtual camber.

There is a general underestimation of forces at the peaks in the upstream half of the rotation. The code is also out of phase by around 20° of azimuth. The BEM code should

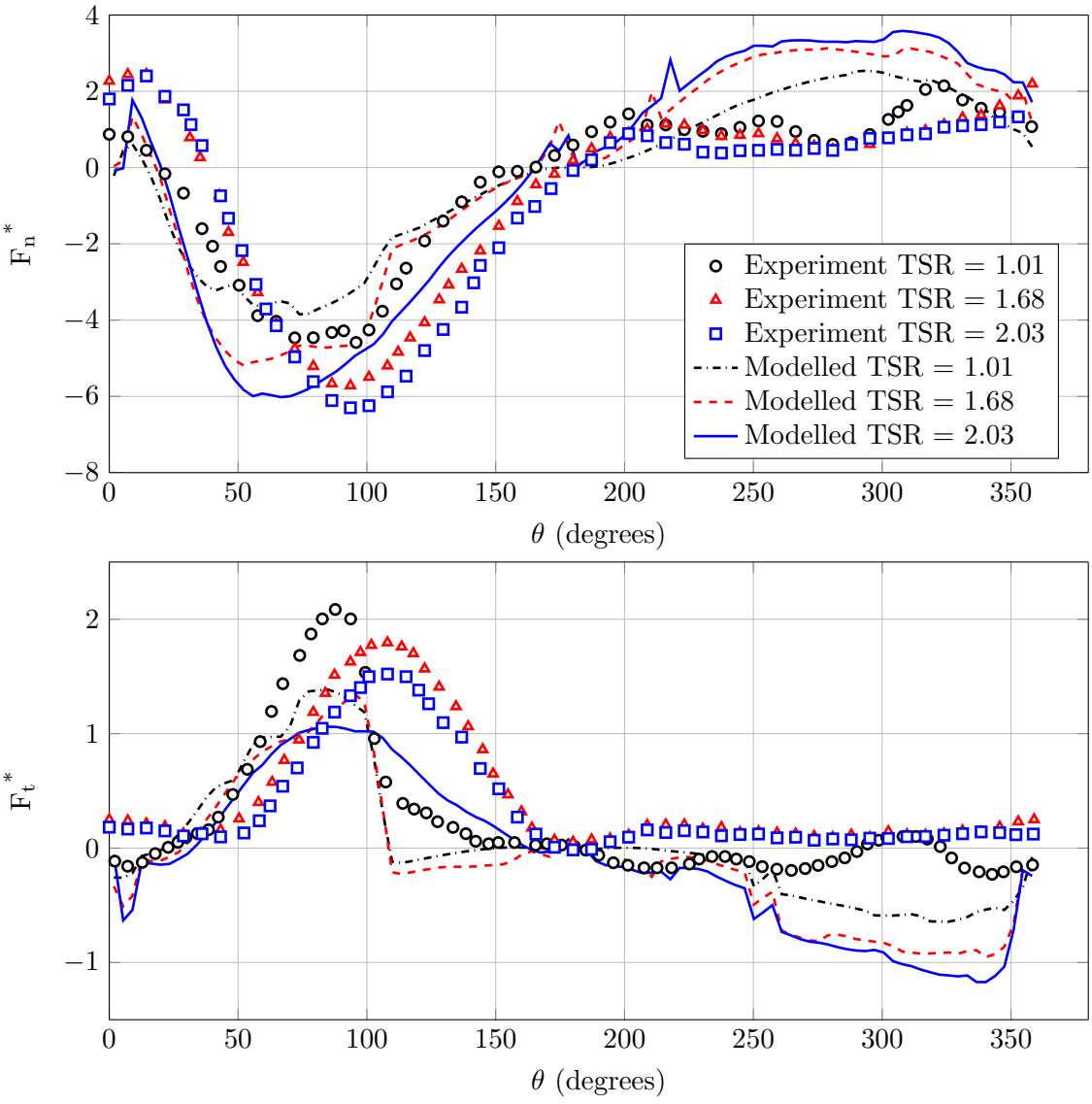


Figure 6.12: (a) $F_n{}^*$ and (b) $F_t{}^*$ vs θ at various TSRs compared to test data of Maeda et al. [80].

have been run with 11.796° of incidence (8° physical incidence plus 3.796° virtual incidence) but this induced heavy loading at TSR = 2.03 rendering the BEM output unreliable. The lack of the virtual incidence is the cause of the modelled phase lead.

Trends between the experimental results are well captured by the code, with lower F_t^* peaks and smoother stalls the higher the TSR. The lowest TSR leads the others and has a sharper, earlier stall at $\theta = 100°$. F_n^* peaks increase with increasing TSR. As with Vittecoq and Laneville in Fig. 6.11, blade performance is poorly modelled in the the second half of the

rotation. Note that Maeda et al's turbine extracts very little energy in the downstream half of the rotation due to its very high solidity of 1.06. Given that measured tangential forces are also low in the second half of the rotation for the studies of Strickland et al. and Vittecoq and Laneville, it may be best to set them equal to zero at $\theta > 180°$ in the BEM code.

6.5.2 Collaborative project with the University of Florence

The collaborating team from the University of Florence have been conducting research on Migliore et al's theory for a number of years. Initial work compared BEM output, using polars for symmetrical aerofoils and cambered aerofoils, to experimental turbine data [4, 6]. The blades use a profile based on the NACA 0015, transformed for the turbine's c/R of 0.4. The cambered aerofoil polars were taken from literature and give only an approximate representation of virtual camber effects. Later, a technique was developed to find the effective incidence of VAWT blades in CFD simulations [113]. This allowed plots of aerofoil lift and drag against incidence to be processed from the simulations. CFD results for a turbine with virtually cambered blades were compared to experimental results for a symmetrical NACA 0018 from literature.

The collaborative project takes a new approach to the problem. The transforms of the NACA 0018 presented in Ch. 5, for turbines with c/R of 0.114 or 0.25, were custom-built for the purposes of the study. The NACA 0018 was chosen as it is commonly used in VAWT research, while the c/R ratios of the transformed aerofoils were chosen for comparability to those used in Migliore's original paper of 0.114 and 0.26 [24]. The larger c/R ratio was modified slightly based on the turbines in Table 6.1 to improve the applicability of the data to analysis of their performance (The average c/R of the Vittecoq and Laneville, Durham, Bravo and Maeda turbines is 0.25). The aerofoil with c/R of 0.114 has a maximum camber of 1.42% at 50% of chord, while the c/R of 0.25 has 3.11% maximum camber at 50% of chord as before.

Based on Migliore's proposal, in the rectilinear flow of the wind tunnel experiments the transformed aerofoils should perform as the unmodified NACA 0018 would in VAWTs with similar c/R ratios and conversely the NACA 0018 tunnel results should be similar to those of the transformed aerofoils when used in VAWTs with concave surface towards the axis. For the VAWT blade force data, CFD simulations have been conducted at several TSRs using

ANSYS Fluent. Results for TSRs of 2.1 and 3.1 are reproduced here. Forces calculated have been processed into plots of lift and drag against effective incidence using the aforementioned technique [113].

The effective incidence calculation is documented in the publications arising from the collaboration [114, 115, 116] and described briefly below:

- Pressure distributions for the VAWT blades are obtained from CFD simulations and normalised so that $-1 < C_p < 1$.
- Similar normalised distributions are obtained for a range of incidences using XFOIL.
- Comparisons are made between the XFOIL pressure distributions and the Fluent output. The incidence of the most similar XFOIL distribution is taken as the effective blade incidence of the CFD.

Due to the reliance on XFOIL's panel method, the technique is limited to conditions where the effective blade incidence is below the static stall angle. Where a symmetrical blade is used in the CFD, its virtually cambered equivalent must be used in XFOIL, and vice-versa. Fig. 6.13 shows results for the comparisons, demonstrating that matching to virtual equivalent is necessary, suggesting that Migliore et al's theory is correct. The incidences calculated using the comparisons are displayed on each sub-figure. It should be noted that since the calculation works from a starting point of the CFD VAWT output, the incidences produced by it are inclusive of any virtual incidence effects. Thus, different incidences are calculated at different c/R ratios for the same aerofoil, in spite of TSR and azimuth being the same.

Fig. 6.14 contains experimental lift coefficient data from Ch. 5 for the NACA 0018 and the two transforms of it. Overlaid on the plots is the reconstructed C_l vs. incidence data extracted from the turbine CFD simulations. As with the pressure distributions, there is a clear correlation between blades and their virtual equivalents rather than between geometrically identical profiles. The agreements are equally good at both of the TSRs simulated.

Fig. 6.15 shows turbine power curves output from Fluent and from the University of Florence VARDAR BEM code. For the $c/R = 0.25$ case, once again, good agreement between the CFD and the BEM code requires pairing of blades with virtual equivalents. For the $c/R = 0.114$ case, camber appears to have little impact on either simulation, with the outputs

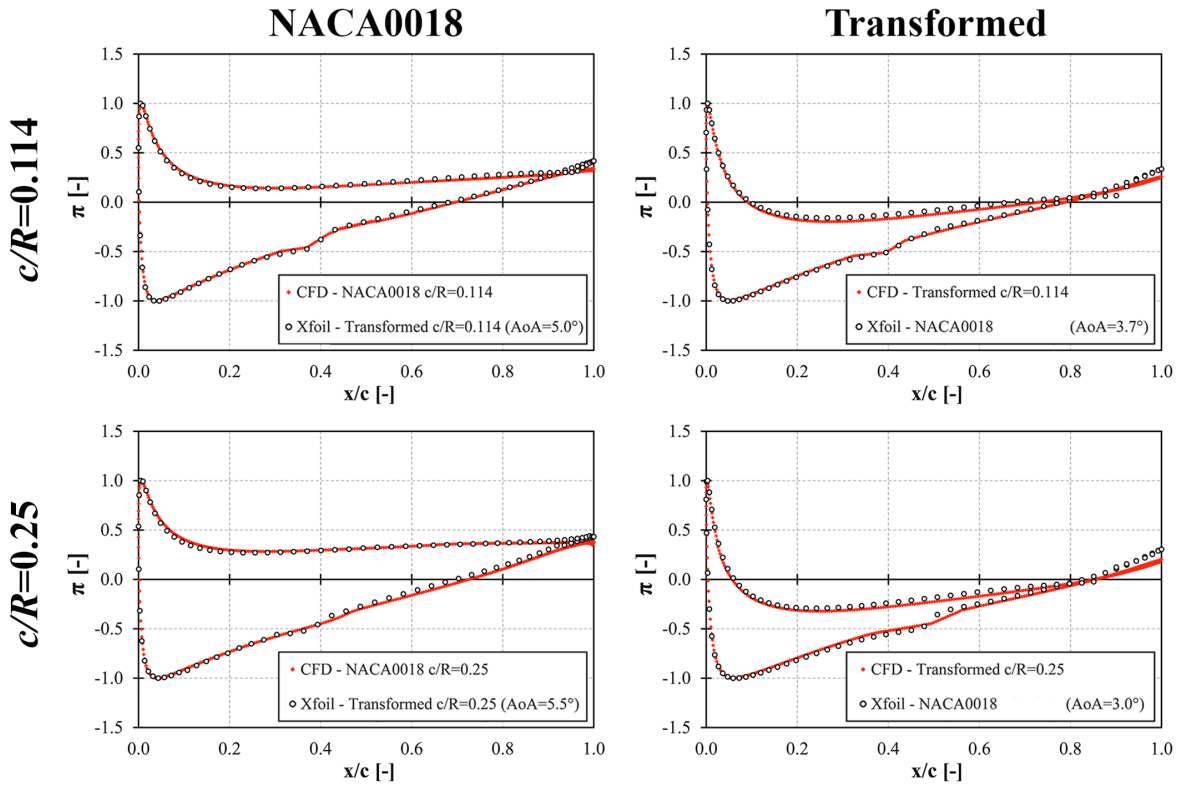


Figure 6.13: Pressure distribution comparisons between XFOIL and Fluent outputs at $\theta = 32.8°$.

nearly identical regardless of blade shape, suggesting that virtual camber is relevant where c/R is high, but is less important for lower c/R turbines.

6.6 Three-dimensional effects

The BEM code iterative process of Section 6.1 is performed as a two-dimensional simulation. The blade force against azimuth plots presented in Sections 6.5 - 6.2.1 are two-dimensional, as most of the studies used for validation are also two-dimensional. When modelling the performance of a real turbine, consideration of three-dimensional effects must be built into the code.

The laminar separation bubble that affects attached flow performance of aerofoils at low Reynolds numbers has a less significant impact on finite wings, see Section 5.2.3. No adjustments have been made for this, potentially impacting on performance at high TSRs where attached flow blade performance dominates, but having a minimal impact on the start-up

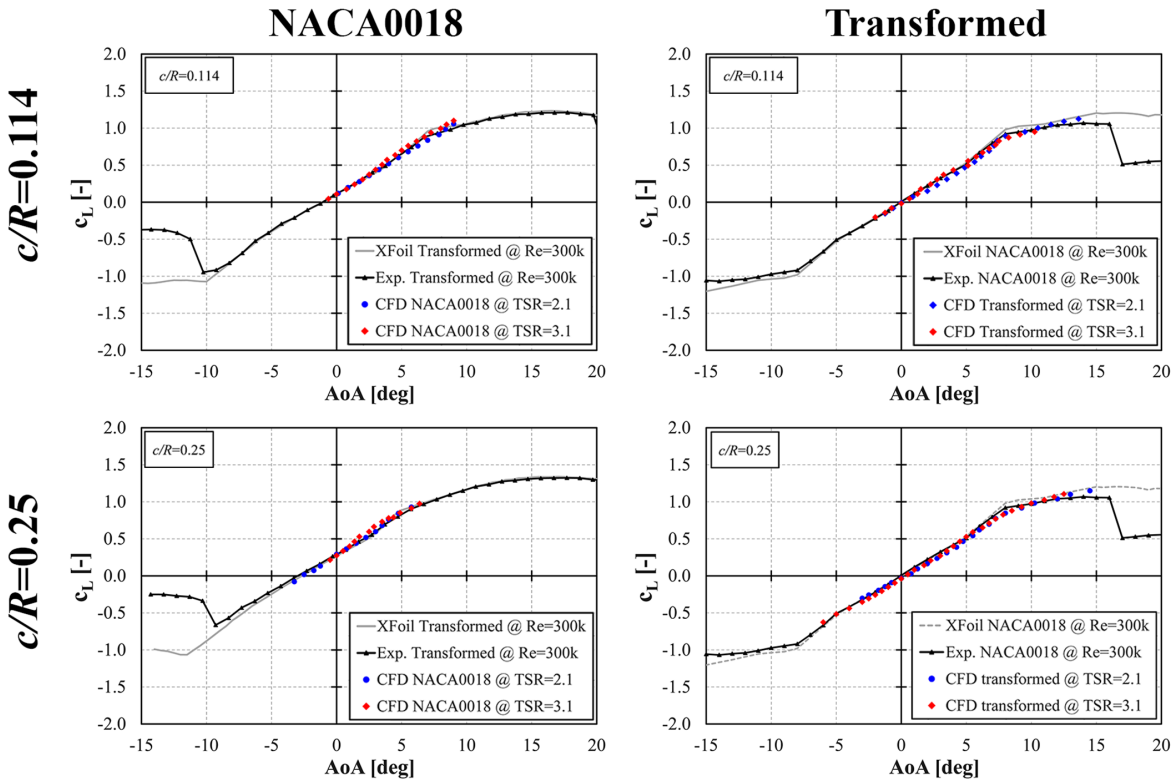


Figure 6.14: C_l vs. incidence - reconstructed results from Fluent VAWT simulations compared to aerofoil experiment: (a) $c/R = 0.114$ Trans. expt. NACA 0018 CFD (b) $c/R = 0.114$ NACA 0018 expt. trans. CFD (c) $c/R = 0.25$ Trans. expt. NACA 0018 CFD (d) $c/R = 0.25$ NACA 0018 expt. trans. CFD.

process.

6.6.1 Finite blade effects

The wing tips of finite blades induce span-wise flow along the blades, and a downwash component perpendicular to the local flow velocity. The span-wise flow can be modelled by applying a streamtube expansion model to the BEM code. The effects of the flow are only significant neat to the blade tips and have a limited impact on full blade performance. They have been neglected in the code.

Downwash has been considered using Lanchester-Prandtl lifting line theory and assuming

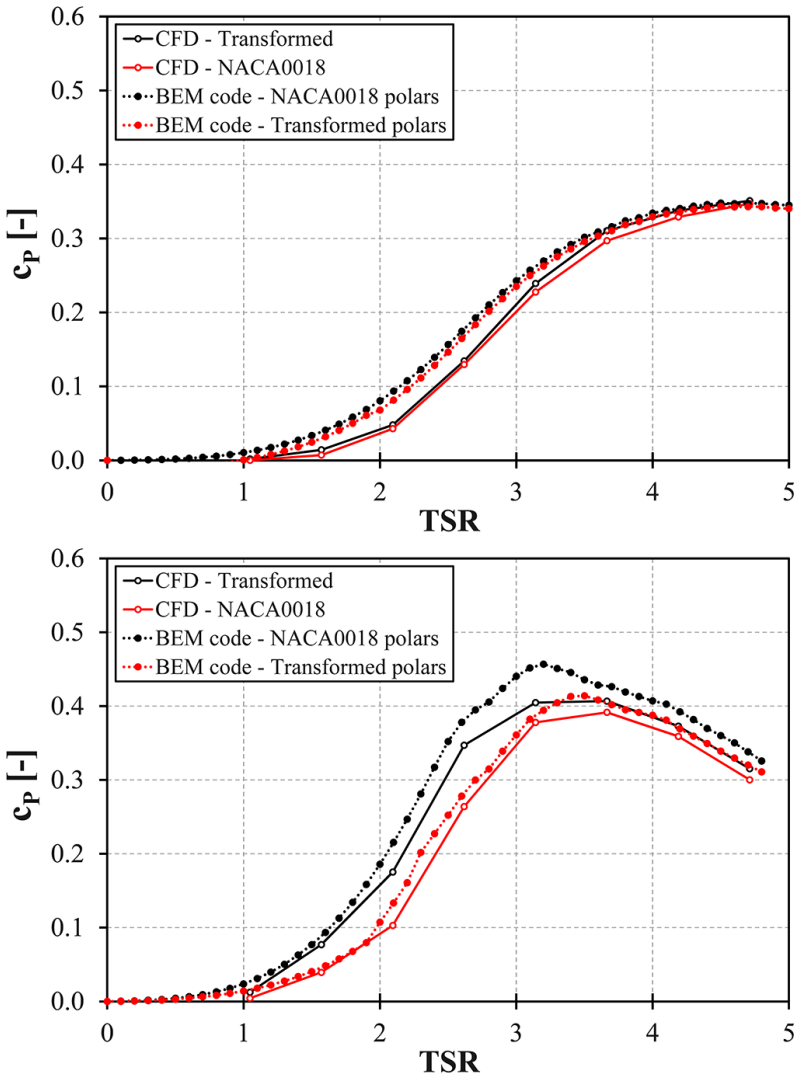


Figure 6.15: Turbine power curves from Fluent simulations and the University of Florence BEM code: (a) $c/R = 0.114$, (b) $c/R = 0.25$.

an elliptic lift distribution, adjusting blade lift and drag as follows:

$$C_{l\,3D} = C_{l\,\infty} / \left(1 + \frac{a_0}{\pi \mathcal{AR}}\right) \tag{6.32}$$

$$C_{d\,3D} = C_{d\,\infty} + \frac{{C_{l\,3D}}^2}{\pi \mathcal{AR}} \tag{6.33}$$

where a_0 is the attached flow lift curve slope, approximated as:

$$a_0 = 1.8\pi \left(1 + 0.8\frac{t}{c}\right) \tag{6.34}$$

The classical theory does not correct drag well at high incidences. At an effective incidence of 90°, $C_l = 0$ so the three-dimensional drag is equal to the two-dimensional aerofoil, a clearly unrealistic result. Viterna and Corrigan provide a formula for maximum drag coefficient at 90° [40] based on results of a number of experimental studies from Hoerner [74]:

$$C_{d\,\mathrm{MAX\ 3D}} = 1.11 + 0.18\mathit{AR} \tag{6.35}$$

Eqns (6.33) and (6.35) have combined into a new drag correction:

$$C_{d\,3\mathrm{D}} = C_{d\,\infty}\frac{C_{d\,\mathrm{MAX\ 3D}}}{C_{d\,\mathrm{MAX}\,\infty}} + \frac{{C_{l\,3\mathrm{D}}}^2}{\pi\mathit{AR}} \tag{6.36}$$

$C_{d\,\mathrm{MAX}\,\infty}$ is obtained from an iteration between blade Reynolds number and drag at 90°.

Lifting line theory also provides a correction to incidence:

$$\alpha_{3\mathrm{D}} = \alpha_{2\mathrm{D}} - \frac{C_{l\,3\mathrm{D}}}{\pi\mathit{AR}} \tag{6.37}$$

The BEM code calculates incidence during the iterative process, before application of the dynamic stall model. A retroactive correction to incidence after this is challenging to implement. For a turbine with blade aspect ratio of 12 (towards the low end for the turbines in Table 6.1), the maximum adjustment to incidence is 2°. The effects on lift and drag of a 2° difference in incidence are much smaller than that of other inconstancies in the code (for example, the use of a simple semi-empirical dynamic stall model, the lack of proper consideration of wakes), so the lifting line incidence adjustment has been omitted from the code.

6.6.2 Stall smoothing

Finite wings undergo a less sharp stall than infinite aerofoils [117]. Lifting-line corrections do not provide a shallowing of stall. This has been provided for by smoothing the stall in the underlying aerofoil data. The simple procedure used omits lift and drag data for 5° after stall, see Fig. 6.16 for a set of smoothed lift and drag coefficients. For asymmetric blades, the process is only applied to the stall at positive incidence.

The stall smoothing is also used in the two-dimensional results presented in this chapter. The sudden changes in blade behaviour resulting from aerofoil stall gives inconsistencies in

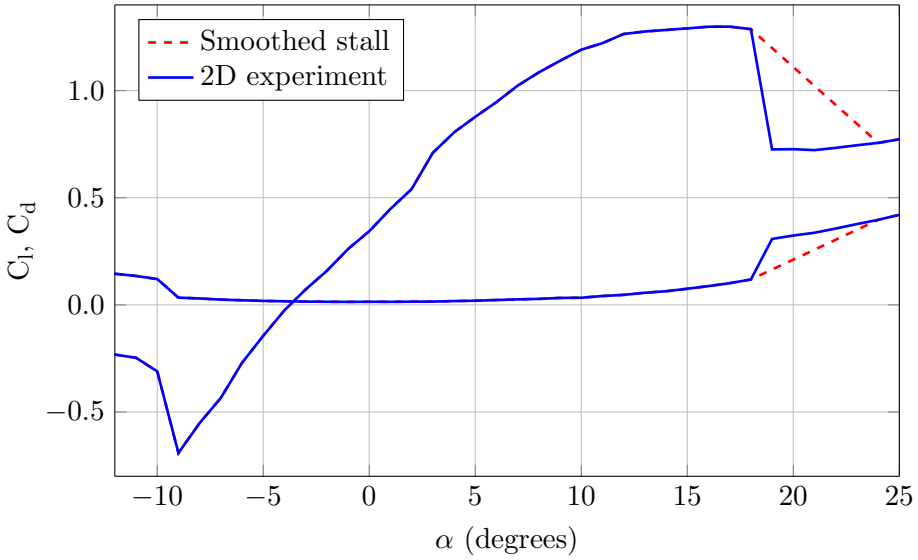


Figure 6.16: C_l and C_d vs α for the NACA 0018, $c/R = 0.25$ aerofoil at $Re = 200\,000$ with smoothed stall.

turbine performance. Where neighbouring streamtubes have very different induction factors (resulting from the sudden change in blade forces), blade incidence changes rapidly between them also. The dynamic stall model predicts very high blade forces where incidence is calculated to change at a very high rate, further exacerbating the problem. Smoothing stall removed this behaviour from the code.

6.7 Full turbine modelling

In summary, the BEM code uses a DMS approach, with smoothing of stall applied to input aerofoil coefficient data and variable blade Reynolds numbers used in the iterative process. Gormont's dynamic stall model is applied with the modifications of Strickland, Cardona and Paraschivoiu and Allet. Modifications to account for Migliore's virtual camber can be implemented by changing the input aerofoil data and setting a different fixed blade incidence.

6.7.1 Parasitic drag

The resistive torque due to the parasitic drag of turbine blade supporting struts is estimated using the method of Paraschivoiu [118]. The torque is approximated to act at the centre point of the strut, at $R/2$, with the whole strut experiencing the same relative velocity. The

velocity is approximated as the rotational velocity at the strut centre point, $\omega R/2$. Resistive torque is then given as

$$T_{res} = \frac{1}{8} C_{d\,\mathrm{strut}} \rho \omega^2 c_{\mathrm{strut}} R^4 \tag{6.38}$$

where c_{strut} is the chord of the strut and $C_{d\,strut}$ is its drag coefficient.

6.7.2 Power and torque modelling

Of the studies listed in Table 6.1, only those of Bianchini et al. [4, 6], Bravo et al. [78] and Maeda et al. [79, 80] provide plots of torque or power against TSR. Bianchini et al. provide data from a two turbines, one with two straight blades and another with three helical blades [4, 6], both using NACA 0015 profiles transformed after Migliore (see Section 6.5). Their power data is given in a non-standard form due to a non-disclosure agreement with the turbine's manufacturer, making it unusable for code validation. The very high solidity of Maeda et al's four-bladed turbine makes modelling full turbine performance with a BEM code impossible at all but very low TSRs, making it too unsuitable. Their two-bladed turbine is suitable for modelling.

Bravo's turbine has comparatively large blades for its size, giving a high c/R of 0.32 and with three blades it also has a high solidity of 0.96. These features make it a less than ideal candidate for modelling with a BEM code. The study was however the only source the author could find providing experimental C_p data from a straight-bladed VAWT with symmetrical NACA 0015 or 0018 blades. Data is also provided down to a TSR of 0.3, making it ideal for a study of start-up. Most studies give field or wind tunnel data on troposkein-shaped turbines, with C_p figures rarely provided for $TSR < 1.5$, see for example work on a variety of turbine sizes by Sandia [119, 120, 121] and the Canadian National Research Council [93].

Fig. 6.17 contains C_p against TSR from the study, taken at free stream velocities of 6, 8 and 10 m/s, alongside BEM code output. Due to the large chord of the blades on the turbine, even when simulating the 6 m/s experiment the upper Reynolds number limits of the experiments from Ch. 5 were reached at low TSRs, rendering minimal differences between the modelled output regardless of the free stream velocity.

The turbine has NACA 0015 blades. In comparing between modelled $F^*_{n,t}$ against azimuth plots for the NACA 0018, the NACA 0018 and the two transformed NACA 0018s, it was found

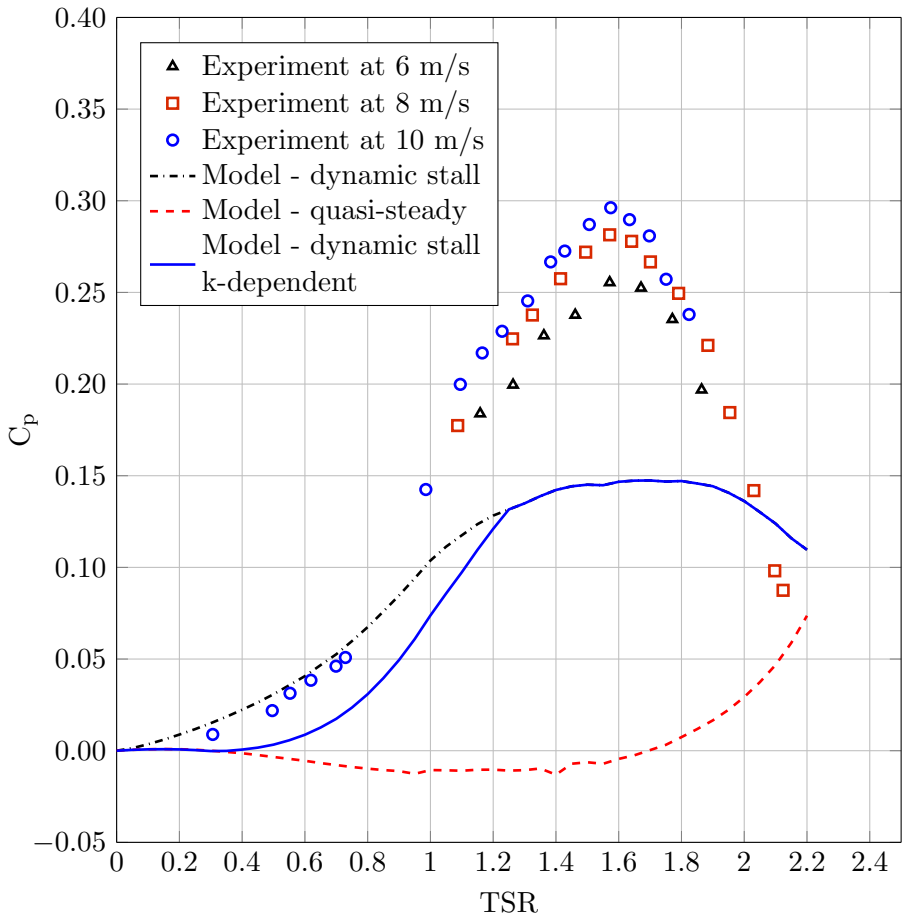


Figure 6.17: C_p vs TSR compared to the test data of Bravo et al. [78].

that differences between the NACA 0015 and the three 18% thick aerofoils were far greater than those between the thicker aerofoils. It was therefore decided to model the effects of virtual camber and incidence by applying the calculated virtual incidence of 4.58° to turbine blades, using experimental results for the uncambered NACA 0015.

Initial modelling yielded results far lower than the experiments, $C_{p\,\mathrm{MAX}} < 0.05$ at a TSR of just over one and the TSRs at the upper end of the performance envelope below two. In Section 6.5.1 the code has been shown to predict large negative torques in the upstream half of the rotation at low TSRs, when high solidity turbines produce very little torque here, negative or otherwise. Due to the high solidity of the Bravo et al. turbine it was decided to set blade forces of zero at $\theta > 180°$. The modelled results shown in Fig. 6.17 all use this methodology.

The quasi-steady output shares few similarities with the experimental output, highlighting the importance of proper consideration of dynamic effects. The output with consideration of

dynamic stall gives a much better alignment for the performance envelope and the TSRs at which $C_{p\,\mathrm{MAX}}$ occurs. Power coefficient itself is around 50% of the experiment. This is likely due in part to the underestimation of blade forces in the upstream half of rotation at low TSRs that can be seen in Fig. 6.12. A lack of experimental data at sufficiently high Reynolds numbers to model performance accurately at a TSR of 1.6 also contributes. The overestimation of tangential forces at a TSR of 2.5 seen in Figs 6.10-6.11 is reflected in the code producing higher C_p than the experiment at $\lambda > 2.05$. At TSRs above 2.2 the turbine was too heavily loaded for the BEM analysis to be applicable.

At low TSRs, the dynamic stall code overestimates the experiment and fails to predict the low torques evident in the plots of TSR with time presented in Ch. 1. Since where $k < 0.05$ a problem can be considered quasi-steady and unsteady effects neglected [22] and the quasi-steady code does produce the expected low torques and powers where k is low, a k-dependent dynamic stall code has been developed, also shown in Fig. 6.17. For $k < 0.05$ the quasi-steady results are used. For $0.05 < k < 0.2$, there is a gradual transition between quasi-steady and dynamic models and at $k > 0.02$, where the problem is considered highly unsteady only the dynamic model is applied. This gives results that qualitatively match the real performance of the turbine at all TSRs below 2.05, though results throughout are around 50% of the experiment.

Fig. 6.18 shows results for Maeda et al's two-bladed turbine, alongside the same model outputs as those provided for Bravo et al. The NACA 0021 blades with c/R of 0.265, mounted with a fixed incidence of 6°. The modelled turbine uses experimental data for the NACA 0018 blade with c/R = 0.25. Incidence is set at 9.796°, the 6° fixed incidence plus 3.796° virtual incidence calculated for the turbine. Again, the k-dependent code provides a reasonable qualitative match to the performance of the real turbine but results are around half that of the experiment. The dip in the C_p curve between TSRs of 1.5 and 2 results from the dynamic stall model. At these TSRs the blade effective incidence limits are just beyond the static stall angle. The dynamic stall model is switched on when incidence is increasing and above the static stall, or when incidence is decreasing, per Strickland's version of the Gormont model, see Section 6.2.2. This provides only a small extension to the attached flow regime as incidence is increasing, but a much larger increase in detached flow when incidence is decreasing, resulting in reduced torques [109]. It is not present in the modelling of Bravo et al. as the higher

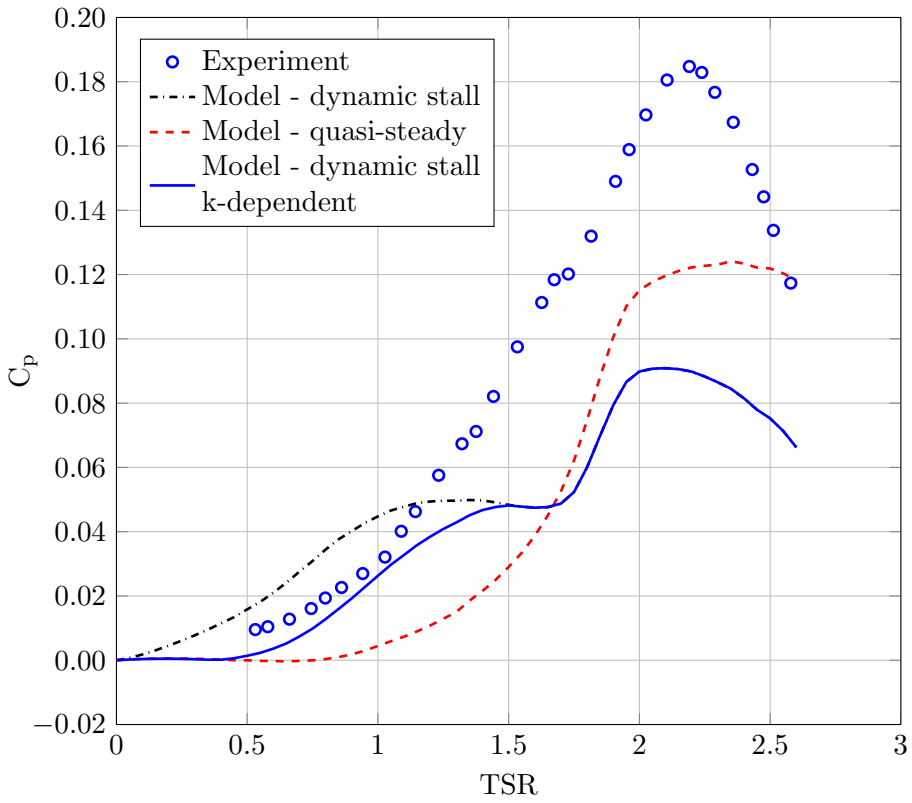


Figure 6.18: C_p vs TSR compared to the test data of Maeda et al. [79].

solidity of the turbine results in a peak C_p occurring at a TSR below the dynamic-stall model induced dip (which would occur at higher TSRs due to the lower static stall of the NACA 0015 compared the NACA 0018, $c/R = 0.25$).

6.7.3 Start-up modelling

A time-dependent extension to the BEM code has been developed to enable reproduction of plots of TSR against time. The code is run over a range of TSRs for the given flow velocity, writing a torque map to memory as it goes, a matrix of blade torques based on azimuth and TSR. The time-dependent extension works by calculating a turbine acceleration by iterating blade torques from this map based on their azimuthal position and the TSR at a given time step.

Fig. 6.19 shows modelled turbine acceleration for the Durham turbine (see Table 6.1) alongside the author's earlier experimental results using the same turbine [3]. Modelling used the techniques established in the previous section, with blade forces in the downstream half

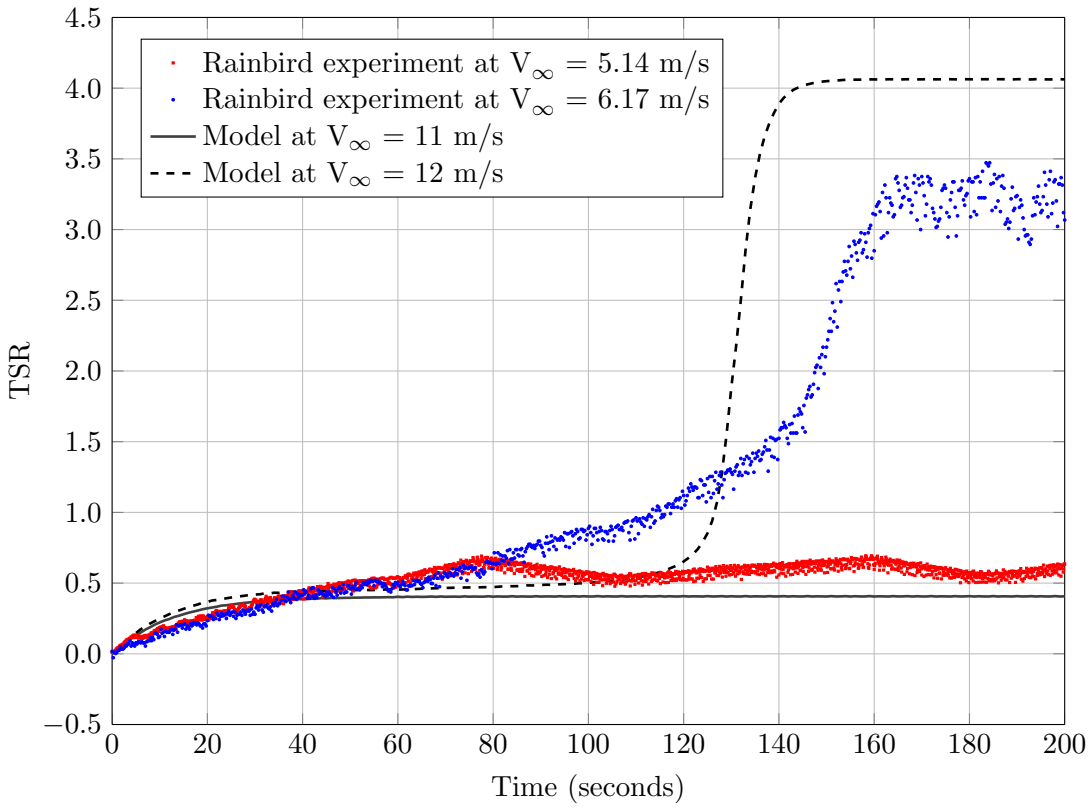


Figure 6.19: TSR development with time for the Durham turbine compared to the author's earlier experiments [3].

of the rotation set to zero, and a quasi-static approach used for $k < 0.05$. The turbine has three NACA 0018 blades and $c/R = 0.221$, approximated using the NACA 0018, $c/R = 0.25$ aerofoil data, with virtual incidence of 3.17°.

The modelled output matches the trends of the experiment well, the correlation of the lower free stream velocities is particularly good. For the higher free steam velocity, the final TSR attained is higher for the model. The overestimation of blade torques at $\lambda \gtrsim 2$ established in Section 6.5.1 pushes the final equilibrium state to a higher TSR. It takes less time for the model to accelerate the turbine to this final TSR. As well as the uncertainties of the blade modelling, the acceleration model relies on inputs of turbine rotor mass, rotor arm drag coefficients and bearing resistance. These variables have been estimated data rather than measured directly, affecting the accuracy of the solution.

Importantly, the model replicates the different accelerations patterns of the experiment dependent on wind speed and so can help in drawing conclusions as to the mechanisms

behind the behaviour. The question of whether or not a turbine will self-start is probably not dependant on dynamic effects. For the Durham turbine, divergence between the self-starting and non-self-starting acceleration paths occurs at a TSR of 0.45-0.65 (experiment) and 0.40-0.45 (modelled), equivalent to k of 0.05-0.07 (experiment) and 0.044-0.05 (modelled) where dynamic effects will be weak and the underlying quasi-steady behaviour of the blades still dominates [22]. In the model, dynamic effects are gradually introduced in the interval $0.05 < k < 0.2$ so will be minimal where the accelerations diverge. However, given the very low torque generation during the idling phase, a minimal absolute impact could be significant in relative terms.

It is also doubtful that post-stall blade performance is responsible for the divergence. Results presented in Figs 5.24-5.27 show minimal variation between the post-stall results for the NACA 0018, $c/R = 0.25$ blade. Since $\lambda < 1$ at the point of divergence, a full range of effective incidences between $-180°$ to $+180°$ are experienced by the blade over the course of a rotation. Fig. 6.20 shows maxima and minima of blade incidence for the two model runs. Comparing with Fig. 6.19, it can be seen that the turbine in the higher speed flow starts its acceleration past the long period of idling at around 100 seconds but the incidence range only starts to change after 120 seconds, and before this point incidence maxima and minima are identical for the two runs. It is therefore unlikely that self start is caused by a narrowing of the incidence range to a region where blades perform better.

It seems instead that blade Reynolds number effects are the key contributor to the the self-start process at these low TSRs. Fig. 6.21 shows mean, maximum and minimum Reynolds numbers against time for the start-up process. The y-axis is marked with the Reynolds numbers at which the NACA 0018, $c/R = 0.25$ was tested. It can be seen that turbine blades experience a mean Reynolds number of approximately 53 000 at 11 m/s and 58 000 at 12 m/s. In Fig. 5.31 it can be seen that aerofoil behaviour changes significantly at $Re = 60\,000$. At this Reynolds number and lower, there is no region of incidences where flow is attached. Attached flow brings with it higher lift and lower drag and so better blade performance.

The blade Reynolds number minima are near identical for the two runs throughout the idling phase, but the maxima are different, the lower run at around 77 000, the higher 86 000-88 000. Experimental results for the aerofoil at $Re = 80\,000$ have more extensive regions of attached flow than at 60 000. It is proposed that in flows above a certain limit, during

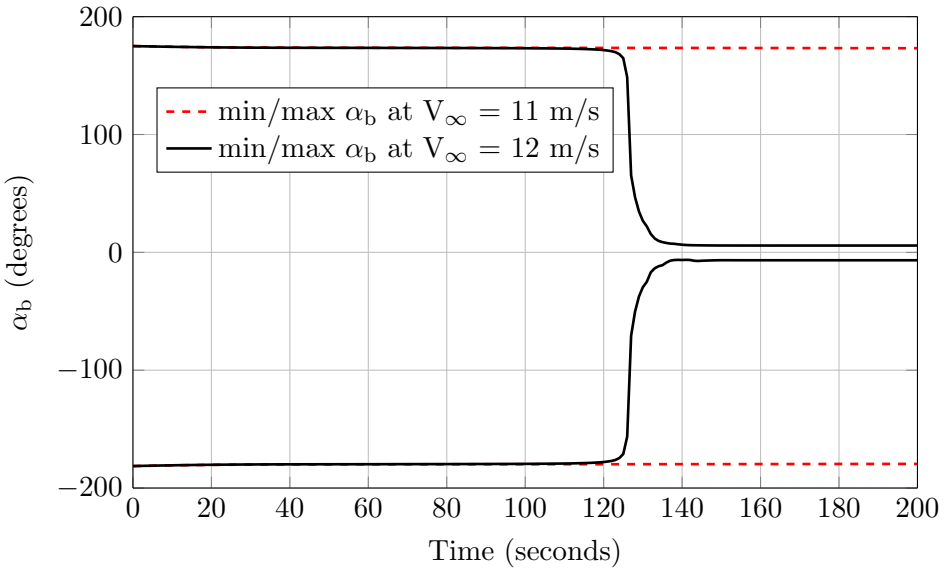


Figure 6.20: Modelled α_b development with time for the Durham turbine.

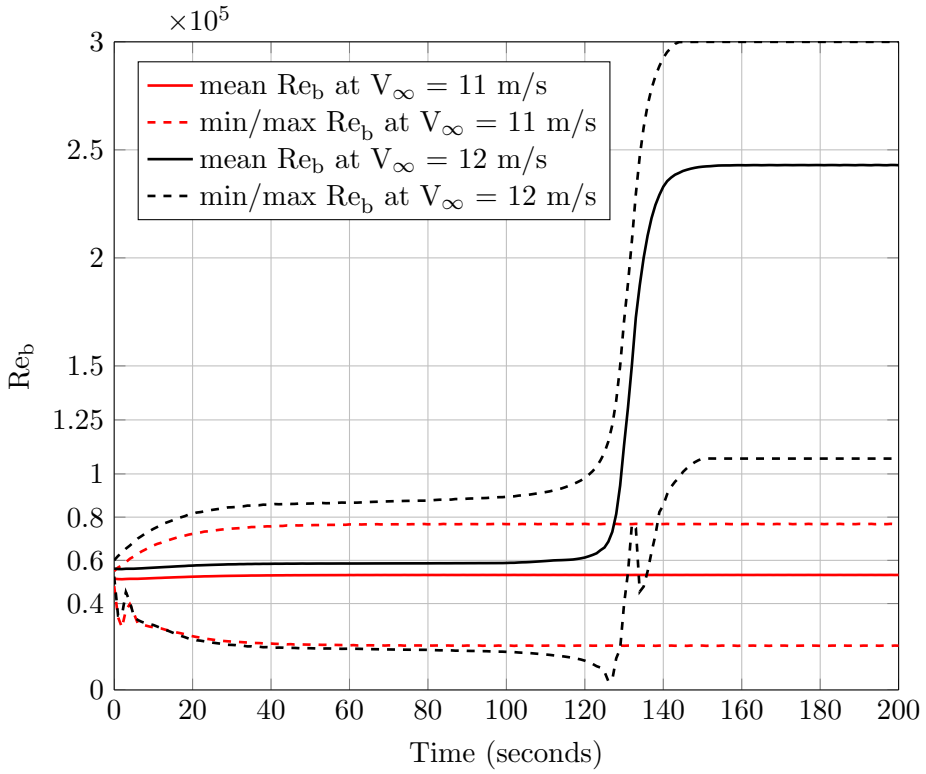


Figure 6.21: Modelled Re_b development with time for the Durham turbine.

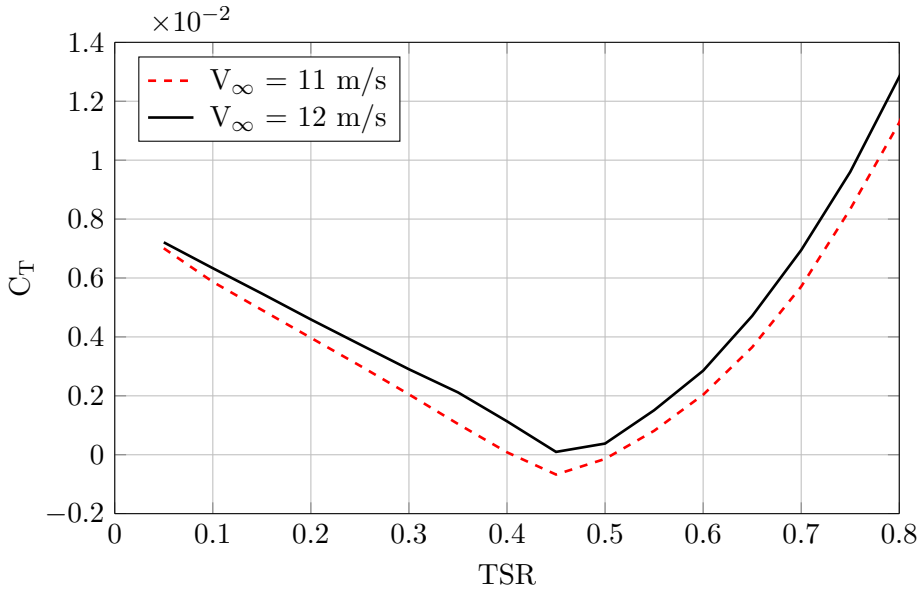


Figure 6.22: C_T vs TSR for the Durham turbine.

the idling phase, the turbine blades experience attached flow sufficient to marginally improve rotational velocity, so that on the next cycle, slightly more attached flow is experienced, producing a slow but steady acceleration. At a certain TSR, Reynolds numbers are high enough for attached flows to be extensive and the blade performance becomes good enough to accelerate the turbine rapidly to its highest equilibrium state. In flows below the limit, the blades never experience regions of attached flow sufficient to slowly accelerate the turbine through the idling phase.

At the diverging TSR of 0.45, torques are very low in either flow condition, Fig. 6.22 shows a zoomed in view of C_T against TSR in this region. For the 11 m/s flow, C_T dips below zero, so the turbine is unable to accelerate past this point, the model replicating the so-called torque "dead band" successfully [1].

The model flow velocities are double that of the experiments. The better performance at lower speeds by the real turbine could be related to inconsistencies and approximations in the model, particularly the underestimation of blade torques at $\lambda \lesssim 2$, as well as phenomena the code does not attempt to address. Roughness on the surfaces of the turbine blades, or turbulence in the real flow around the turbine would give blade performance analogous to that at higher Reynolds numbers. Finite blades are less affected by laminar separation bubbles that dictate flow attachment or lack thereof at low Reynolds numbers.

In spite of these differences between the experiment and model, the conclusions drawn from the model appear sound. Reynolds number effects being largely responsibly for different turbine acceleration patterns in different wind speeds also explains why turbines that are accelerated through the dead-band by artificial means are capable of sustaining high TSRs under their own power once their blades have attained a certain key speed [19].

Chapter 7

Research achievements

This chapter provides a summary of the research achievements of the study, along with suggestions for further work. It is broken into two sections covering the major contributions made, first on the high-quality post-stall aerofoil data produced and the new techniques used to obtain it, the second on the explanation of VAWT self-start behaviour, achieved through BEM modelling using the new aerofoil data. These are followed by an impact assessment on the findings of the research.

7.1 The provision of a highly accurate set of post-stall aerofoil data

A new, highly accurate set of post-stall data has been provided for the NACA 0015 aerofoil, tested at incidences of $0° \leq \alpha \leq 180°$. The method used to provide the new data is demonstrated to be more reliable than current best practice. Blockage reduction, identified in this study as the major source of inconstancies between post-stall studies in the literature, is better than can be achieved using conventional solid-walled wind tunnels and blockage corrections. The method itself is a contribution, with the passive, blockage-tolerant tunnel design of Parkinson used for the testing of deeply stalled aerofoils for the first time. The test section has two solid walls, between which the test aerofoil is mounted, and two slatted walls, opposite the pressure and suction surfaces of the test aerofoil (when the aerofoil is at moderate incidence).

Five different-sized NACA 0015 aerofoils, with c/H ratios of 0.1, 0.15, 0.2, 0.25 and 0.3, were tested in the blockage tolerant tunnel and a solid-walled tunnel to assess the blockage reduction of the tolerant tunnel and blockage corrections. When tested at the same Reynolds number, force, pressure and moment coefficients for the five aerofoils should ideally be identical, as they would be in free air. As such, performance of the tunnels was assessed using a regression analysis to measure the consistency of force, pressure and moment coefficient results for the five aerofoils.

Compared against ESDU blockage corrections, the tolerant tunnel is better at reducing blockage for the five aerofoils. At $Re = 150\,000$, corrected solid walled data has a spread in lift coefficients of 14% at $\alpha = 45°$. For the tolerant tunnel, this is reduced to 6%. Corrections are derived using potential flow theory so should not be applied where flows are extensively separated. The tolerant tunnel therefore represents a more reliable, and more theoretically sound approach to the study of stalled aerofoils, a significant improvement on conventional techniques.

The tolerant tunnel has an open area ratio (OAR, of open space to total wall space in its slatted walls) of 71%. This was selected by testing the five aerofoils with a selection of OAR walls and using the regression analysis to select the best performer. A review of blockage correction methods for solid walled tunnels was conducted. Selected corrections were applied to the results from the solid-walled tunnel, with the regression analysis used again to identiry the ESDU corrections as the best performers.

A review of existing aerofoil studies extending into the deep stall region of incidences has also been conducted, showing significant spread between them. Applying the selection of blockage corrections to a single dataset from the solid walled tunnel revealed significant differences between the corrected data, almost as large as the spread of data between existing studies. Taking these findings along with the typically small differences resulting from experimental errors (due to model accuracy, measurement accuracy and flow quality) or Reynolds number variation, it can be concluded that blockage and the steps taken to minimise it are the main source of inconsistencies in the literature.

A comparative study has been conducted using the smallest NACA 0015, the aerofoil least affected by blockage. The tolerant tunnel results for the aerofoil, across a Re range of 20 000 - 250 000, have been compared to results obtained from the conventional, solid walled tunnel

and processed with the ESDU blockage corrections. Differences between the two are small, within the limits of experimental error. Given blockage has been identified as the largest source of experimental inconsistencies, that two methods for reducing it give similar results supports the assertion that the results represent a highly accurate set of post-stall aerofoil data, the initial aim of this study.

With the data confirmed as a good approximation of free air results, analyses of the effects of Reynolds number and camber on results have been presented for the NACA 0015, alongside the NACA 0018 and two cambered NACA 0018 transforms. Attached flow lift peaks and stall angle increase with Re while minimum drags decrease, as expected, in the 20 000 - 300 000 range of Reynolds numbers tested. Where similar, reliable studies exist, findings of this study strongly corroborate earlier work. $(C_l/C_d)_{\mathrm{MAX}}$ show the expected drop in aerofoil performance at $Re < Re_{\mathrm{crit}}$, where Re_{crit} is the lowest Reynolds number at which a laminar separation bubble can form on the aerofoil's suction surface. Below this, there is no flow attachment and no stall. Stall, where is does exist, is a combined thin aerofoil and leading edge stall.

Detached flow lift and drag is less affected by Reynolds number. Taking this study's results alongside those of others, a positive correlation between Reynolds number and post-stall lift and drag is apparent, but conclusions on this cannot be definitive given the many other possible causes of inconsistencies between studies.

Attached flow effects of camber are as expected: if camber is added, lift peaks, stall angles and minimum drags all increase. Camber also increases post-stall lift and drag peaks, a perhaps surprising result given that many models of post-stall aerofoil performance ignore camber effects in deep stall. Camber also increases Re_{crit}, making cambered aerofoils less effective than symmetrical blades at the lower end of the Reynolds number range tested.

7.1.1 Further work

Low Reynolds number tests ($Re < 100\,000$) gave some unusual results at moderate incidence ($\alpha < 2^{\circ}$). It is proposed in this study that laminar separation near the the trailing edge, with no bubble formation, is to blame. A combined force, pressure tapping and flow visualisation study would confirm this, the findings being useful for micro UAV design, as well as the study of wind turbine start-up.

Pressure tests of this study were mostly for the purposes of tunnel OAR configuration and only conducted at Reynolds numbers of 60 000, 150 000 and 250 000. It would be useful to test at a wide range of Reynolds numbers in the DS-71 tunnel configuration. A smaller aerofoil than the $c/H = 0.25$, with more pressure tappings than the $c/H = 0.15$, would provide better quality data than that obtained in this study.

The tolerant tunnel design has been used in the past for dynamic aerofoil testing. The rig used in this study could be easily adapted for dynamic aerofoil testing by replacing the incidence controlling stepper motor with a unit capable of faster operation.

7.2 An explanation of VAWT start-up behaviour

The key achievement of the modelling side of this study is the successful reproduction of flow velocity-dependent VAWT self-start. In higher speed flows the model predicts successful self-start, at lower speeds a "dead band" of torques are encountered and self-start fails. Where start-up occurs, the acceleration follows the characteristic non-linear pattern of VAWTs, with a long idling period followed by rapid speed increases to the highest possible equilibrium state. Where start-up does not occur, the model settles at a lower equilibrium state. The "dead band" or idling period occur in a region of TSRs at which torques are low or negative of around 0.5 - 1.5, resulting from a heavy reliance on post-stall blade performance for torque generation.

The findings demonstrate that whether or not a turbine will self-start is primarily a result of blade Reynolds number effects, related to the jump in aerofoil performance at the critical Reynolds number Re_{crit} at which a laminar separation bubble is able to form on the aerofoil's suction surface. The presence of "dead bands" of negative torque is dependent on turbine dimensions and blade profiles, and flow conditions.

A BEM code based on a double actuator, multiple streamtube representation of the Darrieus VAWT was used for the start-up modelling. It includes consideration of unsteady aerodynamics (including dynamic stall), blade Reynolds number effects, blade-wake interactions, virtual camber and incidence, and finite blade effects.

The aerofoil data from the current study was used in the BEM code and is of sufficient quality to model VAWT performance with confidence. The 6% spread between the post-stall

lift peaks of the five different-sized aerofoils taken in the tolerant tunnel, mentioned in the previous section, is much lower than the spread between existing studies in spite of the c/H range of the aerofoils tested here being far wider than that of the literature. A 10% difference in post-stall lift peaks, well within the range in the literature, affected whether the BEM code predicts a successful self-start or not, suggesting simulations using data from the literature could be unreliable.

Novel work on virtual camber has been conducted, with new, cambered aerofoils fabricated such that their profiles take the virtual shape of a NACA 0018 when used in VAWTs with c/R of 0.114 and 0.25. The aerofoils have been tested as described above and the data used to model NACA 0018-bladed turbines. Agreement to turbine experiments is closer for the transformed aerofoils at incidence than for the NACA 0018 at zero incidence, particularly for higher c/R. It is therefore demonstrated that virtual camber and incidence have a real impact on turbine performance and should be considered when designing VAWTs. The impact can be approximated by applying virtual incidence and using lift and drag data for the original symmetrical blade.

The BEM code has been validated against VAWT blade force data from the literature. The code provides a reasonable representation of the upstream half of the rotation, but downstream performance is less good. The flow here is complex, with several features that the low-order BEM code does not model well. Turbulence and blade-wake interactions in particular are not adequately modelled in the code. Using high-solidity experiments as a basis, blade forces are instead approximated as zero in the downstream half of the rotation. Turbine power curves show good agreement to experiments in terms of trends, but the actual power outputs predicted by the code are low.

7.2.1 Further work

The BEM code requires further development to improve its accuracy. Blade forces in the upstream half of the rotation are underestimated at low TSR and overestimated at high TSR. In the downstream half they are not well modelled. An experimental campaign using a VAWT with instrumented blades, or access to existing turbine data not currently in the public domain, would enable improvements to be made through further validation of the code.

The dynamic stall model applied in the BEM code takes an average of static results and the

results of Gormont's simple, empirical dynamic stall model commonly used in VAWT research. It provides reasonable agreement to experimental blade forces but as the calculation suggests (averaging with static forces), the original dynamic stall model is a poor fit. The model was developed for pure pitching oscillations. A VAWT-specific dynamic stall model built around the complicated combined pitch, plunge and surge of VAWT blade motion, with effective incidences extending well beyond stall, would represent a real advance in BEM modelling of the turbines. As mentioned in the previous section, the tolerant tunnel could be used for this, but it may be better to work from a full VAWT with a blade mounted via a load cell for force measurement, or fitted with tappings for pressure measurements.

7.3 Impact and beneficiaries of the research

The key beneficiaries of the research presented in this thesis are wind turbine manufacturers, who will be able to use the aerofoil data provided for the modelling of turbines (both horizontal and vertical axis) in low wind speeds or during start-up. UAV designers and manufacturers are additional beneficiaries as they also require good quality aerofoil data at the Reynolds numbers provided here.

The applicability of the datasets is limited to smaller turbines due the Reynolds number range covered. In a windspeed of 6 m/s (the average in much of the UK), at a TSR of 1, the maximum blade size that the data could be used to model is 0.51 m, typically used in VAWTs with diameters of around 2.5 m, or a rated power of 3 kW. The majority of commercially available VAWTs are of a comparable scale.

VAWT manufacturers could also make use of the computer modelling of VAWT start-up, and the conclusions drawn from this, in the design of turbines better able to extract useful energy in low wind speeds. The key finding in this context is the linking of two previously described phenomena, namely the virtual camber imparted on VAWT blades in motion, and the Re_{crit} below which flow cannot attach to an aerofoils suction surface. Since camber increases aerofoil Re_{crit} and at $Re < Re_{\text{crit}}$ performance deteriorates significantly, turbine blades should be designed for start-up with virtual camber in mind.

Additionally, a correlation between post-stall aerofoil performance and camber has been found. Profiles with greater camber induce higher lift and drag at incidences beyond the stall

angle. This means that it should be possible to design a better blade for small and medium-scale VAWT self-start. Camber should be tailored to give appropriate post-stall performance once virtual camber is considered. There will, however, always be a region of TSRs at which torques are low. While camber has some affect on post-stall forces, it is limited, meaning that blade designs for better start-up will be limited in their effectiveness. The findings of this study will, however, help with the avoidance of "dead bands" of torque at moderate wind speeds in future VAWT designs.

Bibliography

[1] Watson, G., "The self-starting capabilities of low-solidity fixed pitch Darrieus rotors," *Wind Energy Workshop, 1st*, Vol. 1, 1979, pp. 32–39.

[2] Hill, N., Dominy, R., Ingram, G., and Dominy, J., "Darrieus turbines: the physics of self-starting," *Proceedings of the Institution of Mechanical Engineers Part A: Journal of Power and Energy*, Vol. 223, No. 1, 2009, pp. 21–29.

[3] Rainbird, J., *The aerodynamic development of a vertical axis wind turbine*, MEng Project Report, School of Engineering, University of Durham, UK, 2007.

[4] Bianchini, A., Carnevale, E., and Ferrari, L., "A model to account for the virtual camber effect in the performance prediction of an H-Darrieus VAWT using the momentum models," *Wind Engineering*, Vol. 35, No. 4, 2011, pp. 465–482.

[5] Chua, K., *Design and testing of a vertical axis wind turbine rotor*, BEng Project Report, Faculty of Mechanical Engineering, University of Technology, Malaysia, 2002.

[6] Bianchini, A., Ferrari, L., and Magnani, S., "Start-up behavior of a three-bladed H-Darrieus VAWT: experimental and numerical analysis," *Proceedings of the ASME Turbo Expo*, 2011, pp. 6–10.

[7] Worasinchai, S., Ingram, G., and Dominy, R., "The effects of improved starting capability on energy yield for small HAWTs," *ASME Turbo Expo*, 2011.

[8] Althaus, D., *Profilpolaren für den Modellflug Vol. 1*, Neckar-Verlag, 1980.

[9] Dominy, R., Lunt, P., Bickerdyke, A., and Dominy, J., "Self-starting capability of a Darrieus turbine," *Proceedings of the Institution of Mechanical Engineers, Part A: Journal of Power and Energy*, Vol. 221, No. 1, 2007, pp. 111–120.

[10] ESDU, "Lift-interference and blockage corrections for two-dimensional subsonic flow in ventilated and closed wind-tunnels," Engineering Sciences Data Unit, 76028, 1978.

[11] Parkinson, G., "The tolerant tunnel: concept and performance," *Canadian Aeronautics and Space Journal*, Vol. 36, No. 3, 1990, pp. 130–134.

[12] Williams, C., *A new slotted-wall method for producing low boundary corrections in two-dimensional airfoil testing*, Ph.D. thesis, Department of Mechanical Engineering, University of British Columbia, 1975.

[13] Parkinson, G., "A tolerant wind tunnel for industrial aerodynamics," *Journal of Wind Engineering and Industrial Aerodynamics*, Vol. 16, 1984, pp. 293–300.

[14] Kong, L., Hameury, M., and Parkinson, G., "Unsteady-flow testing in a low-correction wind tunnel," *Journal of Fluids and Structures*, Vol. 12, No. 1, 1998, pp. 33–45.

[15] Parkinson, G. and Hameury, M., "Performance of the tolerant tunnel for bluff body testing," *Journal of Wind Engineering and Industrial Aerodynamics*, Vol. 33, 1990, pp. 35–42.

[16] Borg, M., Shires, A., and Collu, M., "Offshore floating vertical axis wind turbines, dynamics modelling state of the art. Part I: Aerodynamics," *Renewable and Sustainable Energy Reviews*, Vol. 39, 2014, pp. 1214–1225.

[17] "Nenuphar Twinfloat description," http://www.nenuphar-wind.com/en/22-the-twinfloat.html, Accessed: 14th December 2015.

[18] South, P. and Rangi, R., "A wind tunnel investigation of a 14 ft. diameter vertical axis windmill," National Research Council of Canada, LTR-LA-105, 1972.

[19] South, P. and Rangi, R., "An experimental investigation of a 12 ft. diameter high speed vertical axis wind turbine," National Research Council of Canada, LTR-LA-166, 1975.

[20] Sheldahl, R. and Klimas, P., "Aerodynamic characteristics of seven symmetrical airfoil sections through 180-degree angle of attack for use in aerodynamic analysis of vertical axis wind turbines," SAND80-2114, Sandia National Laboratories, 1981.

[21] McCroskey, W., Carr, L., and McAlister, K., "Dynamic stall experiments on oscillating airfoils," *AIAA Journal*, Vol. 14, No. 1, 1975, pp. 57–63.

[22] Leishman, J., *Principles of Helicopter Aerodynamics*, Cambridge University Press, 2006.

[23] Ferrer, E., *A high order Discontinuous Galerkin-Fourier incompressible 3D Navier-Stokes solver with rotating sliding meshes for simulating cross-flow turbines*, Ph.D. thesis, Department of Engineering Science, Oxford University, 2012.

[24] Migliore, P., Wolfe, W., and Fanucci, J., "Flow curvature effects on Darrieus turbine blade aerodynamics," *Journal of Energy*, Vol. 4, No. 2, 1980, pp. 49–55.

[25] McCullough, G. and Gault, D., "Examples of three representative types of airfoil-section stall at low speed," NACA, TN 2502, 1951.

[26] Gault, D., "A correlation of low-speed, airfoil-section stalling characteristics with Reynolds number and airfoil geometry," NACA, TN 3963, 1957.

[27] ESDU, "The low-speed stalling characteristics of aerodynamically smooth aerofoils," Engineering Sciences Data Unit, 66034, 1966.

[28] Carmichael, B., *Low Reynolds number airfoil survey*, NASA, CR 165803, 1981.

[29] Khoo, H., *Separated flow past wind turbine aerofoil sections*, M.Phil. Project Report, Department of Aeronautics, Imperial College, London 1991.

[30] Miley, S., *A catalog of low Reynolds number airfoil data for wind turbine applications*, Technical Report RFP-3387 UC-60, Department of Aerospace Engineering, Texas A&M University, 1982.

[31] Paraschivoiu, I. and Allet, A., "Aerodynamic analysis of the Darrieus wind turbines including dynamic-stall effects," *Journal of Propulsion and Power*, Vol. 4, No. 5, 1988, pp. 472–477.

[32] "Urban Green Energy Visionair3 description," http://www.urbangreenenergy.com/products/visionair3, Accessed: 14th December 2015.

[33] Bergeles, G., Athanassiadis, N., and Michos, A., "Aerodynamic characteristics of NACA 0012 aircraft in relation to wind generators," *Wind Engineering*, Vol. 7, No. 4, 1983, pp. 247–262.

[34] Critzos, C., Heyson, H., and Boswinkle, R., "Aerodynamic characteristics of NACA 0012 airfoil section at angles of attack from 0 to 180 degrees," NACA, TN 3361, 1955.

[35] Massini, G., Rossi, E., and D'Angelo, S., "Wind tunnel measurements of aerodynamic coefficients of asymetrical airfoil sections for wind turbine blades extended to high angles of attack," *in Proceedings of the European Community Wind Energy Conference*, Herning, Denmark, June 1988, pp. 241–245.

[36] Pope, A., "The forces and pressures over a NACA 0015 airfoil through 180 degrees angle of attack," Technical Report E-102, Georgia Institute of Technology, 1947.

[37] Du, L., Berson, A., and Dominy, R., "NACA0018 behaviour at high angles of attack and at Reynolds numbers appropriate for small wind turbines," ECS Technical Report 2014/08, Durham University, 2014.

[38] Timmer, W., "Two-dimensional low-Reynolds number wind tunnel results for airfoil NACA 0018," *Wind engineering*, Vol. 32, No. 6, 2008, pp. 525–537.

[39] Rossetti, A. and Pavesi, G., "Comparison of different numerical approaches to the study of the H-Darrieus turbines start-up," *Renewable Energy*, Vol. 50, No. 2013, 2013, pp. 7–19.

[40] Viterna, L. and Corrigan, R., "Fixed pitch rotor performance of large horizontal axis wind turbines," *Workshop on Large Horizontal-Axis Wind Turbines*, Vol. 1, 1982, pp. 69–85.

[41] Kim, D., Chang, J., and Chung, J., "Low-Reynolds-Number Effect on Aerodynamic Characteristics of a NACA 0012 Airfoil," *Journal of Aircraft*, Vol. 48, No. 4, 2011, pp. 1212–1215.

[42] Zhou, Y., Alam, M., Yang, H., Guo, H., and Wood, D., "Fluid forces on a very low Reynolds number airfoil and their prediction," *International Journal of Heat and Fluid Flow*, Vol. 32, No. 1, 2011, pp. 329–339.

[43] Jacobs, E. and Sherman, A., "Airfoil section characteristics as affected by variations of the Reynolds number," NACA, TR 586, 1937.

[44] Rae, W., Pope, A., and Barlow, J., *Low speed wind tunnel testing*, Wiley, New York, 3rd ed., 1999.

[45] Garner, H., Rogers, E., Acum, W., and Maskell, E., "Subsonic wind tunnel wall corrections," AGARDograph 109, AGARD, 1966.

[46] Ewald (Ed.), B., "Wind tunnel wall corrections," AGARDograph 336, AGARD, 1998.

[47] Maskell, E., "A theory of the blockage effects on bluff bodies and stalled wings in a closed wind tunnel," ARC, RM 3400, 1963.

[48] Poisson-Quinton, P. and de Sievers, A., "Étude aerodynamique d'un élément de pale d'hélicoptère," *AGARD Conference Proceedings No. 22*, Göttingen, Germany, December 1967, pp. 4.1–4.35.

[49] Timmer, W., "Aerodynamic characteristics of wind turbine blade airfoils at high angles-of-attack," *in Proceedings of TORQUE 2010: The Science of Making Torque from Wind*, Crete, 2010, pp. 7178.

[50] Lindenburg, C., "Stall coefficients: aerodynamic airfoil coefficients at large angles of attack," *IEA Symposium on the Aerodynamics of Wind Turbines*, National Renewable Energy Laboratory, Colorado, USA, December 2000.

[51] Althaus, D., *Profilpolaren für den Modellflug Vol. 2*, Neckar-Verlag, 1980.

[52] Selig, M., Deters, R., and Williamson, G., "Wind tunnel testing airfoils at low Reynolds numbers," *49th AIAA Aerospace Sciences Meeting, AIAA*, Orlando, Florida, January 2011.

[53] Selig, M., Donovan, J., and Fraser, D., "Airfoils at low speeds," SoarTech Publications, 1989.

[54] Hameury, M., *Development of the tolerant wind tunnel for bluff body testing*, Ph.D. thesis, Department of Mechanical Engineering, University of British Columbia, 1987.

[55] Glauert, H., "The interference of wind channel walls on the aerodynamic characteristics of an aerofoil," ARC, RM 867, 1923.

[56] Allen, H. and Vincenti, W., "Wall interference in a two-dimensional-flow wind tunnel, with consideration of the effect of compressibility," NACA, TR 782, 1944.

[57] Lock, C., "The interference of a wind tunnel on a symmetrical body," ARC, RM 1275, 1929.

[58] Glauert, H., "Wind tunnel interference on wings, bodies and airscrews," ARC, RM 1566, 1933.

[59] Thom, A., "Blockage corrections in a closed high-speed tunnel," ARC, RM 2033, 1943.

[60] Thompson, J., "Present methods of applying blockage corrections in a closed rectangular high-speed wind tunnel," ARC, Report 11 385, 1948. (Unpublished).

[61] Batchelor, G., "Interference on wings, bodies and airscrews in a closed tunnel of octagonal section," Australian Council for Aeronautics, TR ACA-5, 1944.

[62] Pankhurst, R. and Holder, D., *Wind-tunnel technique: an account of experimental methods in low- and high-speed wind tunnels*, Pitman, London, 1952.

[63] Fage, A. and Johansen, F., "On the flow of air behind an inclined flat plate of infinite span," *Proceedings of the Royal Society of London. Series A*, Vol. 116, No. 773, 1927, pp. 170–197.

[64] Fage, A. and Johansen, F., "The structure of vortex sheets," *The London, Edinburgh, and Dublin Philosophical Magazine and Journal of Science*, Vol. 5, No. 28, 1928, pp. 417–441.

[65] Hackett, J., Wilsden, D., and Lilley, D., "Estimation of tunnel blockage from wall pressure signatures: a review and data correlation," NASA, CR-15 2241, 1979.

[66] Courchesne, J. and Laneville, A., "A comparison of correction methods used in the evaluation of drag coefficient measurements for two-dimensional rectangular cylinders," *Journal of Fluids Engineering*, Vol. 101, No. 4, 1979, pp. 506–510.

[67] Wolf, S., "Adaptive wall technology for improved wind tunnel testing techniques – a review," *Progress in Aerospace Sciences*, Vol. 31, No. 2, 1995, pp. 85–136.

[68] Du, L., Berson, A., and Dominy, R., "Aerofoil behaviour at high angles of attack and at Reynolds numbers appropriate for small wind turbines," *Proceedings of the Institution of Mechanical Engineers, Part C: Journal of Mechanical Engineering Science*, Vol. 229, No. 11, 2014, pp. 2007–2022.

[69] Broughton, C., Rainbird, W., and Kind, R., "An experimental investigation of interference effects for high blockage bluff bodies in a slotted-wall wind tunnel test section," *Journal of Wind Engineering and Industrial Aerodynamics*, Vol. 56, No. 1, 1995, pp. 23–39.

[70] Dietz, R. and Laster, M., "Wind tunnel corrections for high angle of attack models," AGARD, R-692, 1981.

[71] Malek, A., *An investigation of the theoretical and experimental aerodynamic characteristics of a low-correction wind tunnel wall configuration for airfoil testing*, Ph.D. thesis, Department of Mechanical Engineering, University of British Columbia, 1983.

[72] McCroskey, W., "A critical assessment of wind tunnel results for the NACA 0012 airfoil," NASA, TM 100019, 1987.

[73] Spera, D., "Models of lift and drag coefficients of stalled and unstalled airfoils in wind turbines and wind tunnels," NASA, CR 2008-215434, 2008.

[74] Hoerner, S., *Fluid-dynamic lift*, Hoerner Fluid Dynamics, Vancouver, 1985.

[75] Hess, J. and Smith, A., "Calculation of potential flow about arbitrary bodies," *Progress in Aerospace Sciences*, Vol. 8, 1967, pp. 1–138.

[76] Parkinson, G., Kong, L., and Cook, N., "Configuration criteria for a blockage-tolerant wind tunnel," *Journal of Wind Engineering and Industrial Aerodynamics*, Vol. 40, No. 2, 1992, pp. 215–219.

[77] Vittecoq, P. and Laneville, A., "The aerodynamic forces for a Darrieus rotor with straight blades: Wind tunnel measurements," *Journal of Wind Engineering and Industrial Aerodynamics*, Vol. 15, No. 13, 1983, pp. 381–388.

[78] Bravo, R., Tullis, S., and Ziada, S., "Performance testing of a small vertical-axis wind turbine," *Proceedings of the 21st Canadian Congress of Applied Mechanics*, 2007, pp. 470–471.

[79] Maeda, T., Kamada, Y., Murata, J., Li, Q., Kawabata, T., and Kogaki, T., "measurements of flow field and pressure distribution of straight-bladed vertical axis wind turbine," *Proceedings of the European Wind Energy Association Conference and Exhibition*, Vienna, Austria, February 2013.

[80] Li, Q., Maeda, T., Kamada, Y., Murata, J., Kawabata, T., and Furukawa, K., "Analysis of aerodynamic load on straight-bladed vertical axis wind turbine," *Journal of Thermal Science*, Vol. 23, No. 4, 2014, pp. 315–324.

[81] Selig, M., Lyon, C., Giguere, P., Ninham, C., and Guglielmo, J., *Summary of low-speed airfoil data, Vols. 1-5*, SoarTech Publications, 1995-2012.

[82] Flay, R., Elfstrom, G., and Clark, P., "Slotted-wall test section for automotive aerodynamic tests at yaw," SAE, Technical Paper 830302, 1983.

[83] Glanville, M. and Kwok, K., "Further investigation of the blockage-tolerant wind tunnel technique," *Journal of Wind Engineering and Industrial Aerodynamics*, Vol. 69–71, 1997, pp. 987–995.

[84] Sinha, S., Gupta, A., and Oberai, M., "Laminar separating flow over backsteps and cavities. II-Cavities," *AIAA Journal*, Vol. 20, No. 3, 1982, pp. 370–375.

[85] Bastedo Jr, W. and Mueller, T., "Performance of finite wings at low Reynolds numbers," *Proceedings of the Conference on Low Reynolds Number Airfoil Aerodynamics*, 1985, pp. 195–205.

[86] Lissaman, P., "Low-Reynolds-number airfoils," *Annual Review of Fluid Mechanics*, Vol. 15, No. 1, 1983, pp. 223–239.

[87] "Aerodynamics of teardrop wingmasts," http://www.tspeer.com/Wingmasts/teardropPaper.htm, Accessed: 2nd April 2016.

[88] McMasters, J. and Henderson, M., "Low-speed single-element airfoil synthesis," *The Sci. and Technol. of Low Speed and Motorless Flight Pt. 1*, NASA, 1979, pp. 1–31.

[89] Ostowari, C. and Naik, D., "Post-stall wind tunnel data for NACA 44XX series airfoil sections," SERI/US Department of Energy, STR-2559, 1985.

[90] Strickland, J., Smith, T., and Sun, K., "Vortex model of the Darrieus turbine: an analytical and experimental study. Final report," SAND81-7017, Sandia National Laboratories, 1981.

[91] Scheurich, F. and Brown, R., "Vertical-axis wind turbines in oblique flow: sensitivity to rotor geometry," *EWEA Annual event (formerly known as EWEC)*, 2011.

[92] Glauert, H., *The elements of aerofoil and airscrew theory*, Cambridge University Press, 1983.

[93] Templin, R., "Aerodynamic performance theory for the NRC vertical-axis wind turbine," National Research Council Canada, LTR-LA-160, 1974.

[94] Strickland, J., "Darrieus turbine: a performance prediction model using multiple streamtubes," SAND75-0431, Sandia National Laboratories, 1975.

[95] Paraschivoiu, I. and Delclaux, F., "Double multiple streamtube model with recent improvements (for predicting aerodynamic loads and performance of Darrieus vertical axis wind turbines)," *Journal of Energy*, Vol. 7, No. 3, 1983, pp. 250–255.

[96] Glauert, H., "The analysis of experimental results in the windmill brake and vortex ring states of an airscrew," ARC, TR 1026, 1926.

[97] Sharpe, D., "Wind turbine aerodynamics," In: Freris, L.L., *Wind energy conversion systems*, Prentice Hall London, 1990.

[98] Corke, T. and Thomas, F., "Dynamic stall in pitching airfoils: aerodynamic damping and compressibility effects," *Annual Review of Fluid Mechanics*, Vol. 47, No. 1, 2015, pp. 479–505.

[99] Rival, D. and Tropea, C., "Characteristics of pitching and plunging airfoils under dynamic-stall conditions," *Journal of Aircraft*, Vol. 47, No. 1, 2010, pp. 80–86.

[100] Gormont, R., "A mathematical model of unsteady aerodynamics and radial flow for application to helicopter rotors," USAAMRDL, TR 72-67, 1973.

[101] Strickland, J., Webster, B., and Nguyen, T., "A vortex model of the Darrieus turbine: an analytical and experimental study," *Journal of Fluids Engineering*, Vol. 101, 1979, pp. 500–505.

[102] Johnson, W., "The response and airloading of helicopter rotor blades due to dynamic stall," MIT Aeroelastic and Structures Research Laboratory, TR 130-1, 1970.

[103] Noll, R. and Ham, N., "Dynamic stall of small wind systems," Aerospace Systems, Inc., Burlington, MA, USA, RFP-3523, 1983.

[104] Leishman, J. and Beddoes, T., "A semi-empirical model for dynamic stall," *Journal of the American Helicopter Society*, Vol. 34, No. 3, 1989, pp. 3–17.

[105] Major, S. and Paraschivoiu, I., "Indicial method calculating dynamic stall on a vertical axis wind turbine," *Journal of Propulsion and Power*, Vol. 8, No. 4, 1992, pp. 909–911.

[106] Worstell, M., "Aerodynamic performance of the 17-metre-diameter Darrieus wind turbine," SAND78-1737, Sandia National Laboratories, 1979.

[107] Cardona, J., "Flow curvature and dynamic stall simulated with an aerodynamic free-vortex model for VAWT," *Wind Engineering*, Vol. 8, 1984, pp. 135–143.

[108] McAlister, K., Pucci, S., McCroskey, W., and Carr, L., "An experimental study of dynamic stall on advanced airfoil sections, Volume 2: pressure and force data," NASA, TM 84245,1982.

[109] Pawsey, N., *Development and evaluation of passive variable-pitch vertical axis wind turbines*, Ph.D. thesis, University of New South Wales, 2002.

[110] Theodorsen, T., "General theory of aerodynamic instability and the mechanism of flutter," NACA TR 496, 1935.

[111] Rainbird, J., Peiro, J., and Graham, J., "Vertical-axis wind turbine start-up modelled with a high-order numerical solver," In: Montlaur, A. and Ferrer, E. *CFD for wind and tidal offshore turbines*, Springer, 2015.

[112] Fraunie, P., Beguier, C., Paraschivoiu, I., and Brochier, G., "Water channel experiments of dynamic stall on darrieus wind turbine blades," *Journal of Propulsion and Power*, Vol. 2, 1986, pp. 445–449.

[113] Balduzzi, F., Bianchini, A., Maleci, R., Ferrara, G., and Ferrari, L., "Blade design criteria to compensate the flow curvature effects in H-Darrieus wind turbines," *Journal of Turbomachinery*, Vol. 137, No. 1, 2014, pp. 011006–011006.

[114] Bianchini, A., Balduzzi, F., Rainbird, J., Peiro, J., Graham, J. M., Ferrara, G., and Ferrari, L., " An experimental and numerical assessment of airfoil polars for use in Darrieus wind turbines. Part 1 - flow curvature effects," *Journal of Engineering for Gas Turbines and Power*, Vol. 138, No. 3, 2016, pp. 032602–1:032602–10.

[115] Bianchini, A., Balduzzi, F., Rainbird, J., Peiro, J., Graham, J., Ferrara, G., and Ferrari, L., "An experimental and numerical assessment of airfoil polars for use in Darrieus wind turbines. Part II - post-stall data extrapolation methods," *Journal of Engineering for Gas Turbines and Power*, Vol. 138, No. 3, 2016, pp. 032603–1:032603–10.

[116] Rainbird, J., Bianchini, A., Balduzzi, F., Peiro, J., Graham, J., Ferrara, G., and Ferrari, L., "On the influence of virtual camber effect on airfoil polars for use in simulations of Darrieus wind turbines," *Energy Conversion and Management*, Vol. 106, 2015, pp. 373–384.

[117] Ostowari, C. and Naik, D., "Post stall studies of untwisted varying aspect ratio blades with an naca 4415 airfoil section – Part I," *Wind Engineering*, Vol. 8, No. 3, 1984, pp. 176–194.

[118] Paraschivoiu, I., *Wind turbine design: with emphasis on Darrieus concept*, Presses Internationales Polytechnique, 2002.

[119] Sheldahl, R. and Blackwell, B., "Wind tunnel performance data for the Darrieus wind turbine with NACA 0012 blades," SAND76-0130, Sandia National Laboratories, 1977.

[120] Sheldahl, R. and Blackwell, B., "Free-air performance tests of a 5-metre-diameter Darrieus turbine," SAND77-1063, Sandia National Laboratories, 1977.

[121] Worstell, M., "Aerodynamic performance of the 17-m-diameter Darrieus wind turbine in the three-bladed configuration: an addendum," SAND79-1753, Sandia National Laboratories, 1982.

[122] Abbott, I., Von Doenhoff, A., and Stivers Jr, L., "Summary of airfoil data," NACA, TR 824,1945.

[123] Hackett, J., "Tunnel-induced gradients and their effect on drag," *AIAA Journal*, Vol. 34, No. 12, 1996, pp. 2575–2581.

[124] Fuglsang, P., Antoniou, I., Sørensen, N., and Aagaard Madsen, H., "Validation of a wind tunnel testing facility for blade surface pressure measurements," Technical Report Risø-R-981(EN), Risø National Laboratory, 1998.

[125] Kim, D.H., Yang, J.H., Chang, J.W. and Chung, J., "Boundary layer and near-wake measurements of NACA 0012 airfoil at low Reynolds numbers," *47th AIAA Aerospace Sciences Meeting*, Orlando, Florida, January 2009.

[126] Jacobs, E. and Abbott, I., "The NACA variable-density wind tunnel," NACA, TR 416, 1932.

Appendices

Appendix A

Aerofoil studies referenced in the thesis

A.1 Aerofoil experiments covering a wide range of incidences

A.1.1 The NACA 0012

Sheldahl and Klimas [20]

Tests were conducted on 0.15 m chord NACA 0009, 0012 and 0015 aerofoils, along with a modified 0012, at effective Reynolds numbers of 360 000, 500 000 and 700 000. The authors go on to synthesise results for a range of Reynolds numbers from 10 000 to 10 000 000 and for additional sections (the NACA 0018, 0021 and 0025) from their experimental results using computational methods. Some higher Reynolds number testing at 860 000 and 1 760 000 used a larger NACA 0012, with chord of 0.38 m, for $\alpha < 30°$.

Experiments were conducted in a 2.13 m $\times$ 3.05 m test section fitted with splitters to give a 0.91 m $\times$ 2.13 m section for two-dimensional aerofoil testing, with flow conditions measured in this isolated section. Aerofoils span the whole of the 0.91 m width of the splitter section and are mounted between two endplates that sit flush with the splitter plates. Lift, drag and moment were measured using a force balance, with drag also obtained using a wake survey for low angles of attack. Rae et al's corrections [44] were used, including buoyancy. No mention is made of the reinstatement of terms of ${\epsilon_B}^2$ to the corrections used (see Section 2.1.5) so

presumably they were used per the reference. Reynolds number was also corrected for wind tunnel turbulence, the actual Reynolds numbers of the tests based on measured flow velocity and atmospheric conditions were 260 000, 390 000 and 620 000, with correction factors of 1.38, 1.29 and 1.13 applied respectively to obtain the effective Reynolds numbers, again using Rae et al.'s turbulence correction (see Section 2.1.8). Post-stall results exhibit very little dependency on Reynolds number, hence the inclusion of only data taken at $Re = 360\,000$ in Fig. 1.8 of this thesis.

This study is highly influential in VAWT research, frequently used when modelling turbine performance. The synthesised results over a wide range of Reynolds numbers are however very unrealistic around stall, as noted by other researchers [109]. Only the original experimental results are used in this study.

Critzos et al. [34]

Critzos et al. provide data from two different tunnels, the Langley low-turbulence pressure tunnel (LTPT) and the Langley 300mph 7 ft × 10 ft tunnel (7 × 10). These will be covered separately. Unusually, they provide their raw data for both tunnels, alongside corrected data.

The LTPT tunnel has a 2.29 m × 0.91 m test section. Tests were conducted at $Re = 1\,800\,000$ with $M = 0.15$, and $Re = 500\,000$ with $M = 0.12$. The model had a chord of 0.15 m and spanned the 0.91 m width of the tunnel, mounted between small end-plates mounted flush with the tunnel walls. It was supported at one end by a universal joint that restricted movement but not rotation, and at the other by a force balance, which therefore measured 50% of lift and drag forces and 100% of moment. The aerofoil profile is "thought", according to the paper, to be accurate to within 0.076 mm. Corrected data is provided using two methodologies, that of Allen and Vincenti [56], (on which Rae et al's are based) and that of Abbott et al. [122], which is identical but for its handling of wake blockage, for which a boundary measurement method is used. Results reproduced in Fig. 1.8 of this thesis use Abbot et al. which are around 2.5% higher than Allen and Vincenti in the post-stall region of incidences.

Little information is given on the 7 × 10 tunnel experiments. The tunnel has a 2.13 m × 3.05 m test section and tests were conducted at $Re = 1.36 \times 10^6$ with $M = 0.2$. A 0.305 m chord aerofoil was used which spanned the 2.13 m width of the tunnel. Corrections used are

those of Allen and Vincenti [56]. No wind tunnel turbulence corrections to Reynolds numbers are mentioned for either tunnel.

Bergeles et al. [33]

Tests were conducted in a 1.4 m × 1.8 m tunnel with splitter plates installed to give a 0.34 m × 1.4 m two-dimensional test section. The model had a 0.2 m chord and ended 1.5 mm short of the splitter plates at each end. It had a profile accurate to within 0.08 mm and was mounted to a six-component force balance. It was tapped for pressure readings at 16 points on one of its surfaces. Lift and drag are provided from the balance and an integration of the pressure readings. At incidences below 5°, a wake survey is used for drag rather than the balance. Balance readings are rated to an accuracy of 3%-8%, and the wake survey to 5%.

For the balance and wake survey measurements, blockage corrections use the "classic approach" covered in ESDU [10], AGARD [45], Rae et al. [44] and Pankhurst and Holder [62], all of which are referenced, in the region of incidences before stall (there is very little difference between the corrections at low incidence). Post-stall, Maskell's blockage correction [47] is used. For the pressure measurements AGARD corrections are used. The Reynolds number is corrected with a wind tunnel turbulence factor of 1.195 after Rae et al. (see Section 2.1.8).

Massini et al. [35]

A 3 m diameter circular cross-section tunnel was used, fitted with splitters to give an approximate 0.8 m x 3 m two-dimensional test section. The aerofoil model has a 0.4 m chord and spans the 0.8 m width of the test section, fitted between two endplates that sit flush with the splitters. The aerofoil has 67 pressure tappings, with a further 16 in each endplate, 34 in the splitters, and one tap each on the floor and ceiling of the test section. Force measurements were taken using a six-component force balance.

The conference paper presents preliminary findings from a larger study (though no subsequent publications could be found) and does not state whether the lift and drag data it gives was collected using the tappings or the balance. Presumably the balance was used. Raw data is given alongside corrections using Rae et al. [44] and Maskell [47]. Reynolds numbers are adjusted with a turbulence factor of 1.3 (see Section 2.1.8), giving corrected $Re = 950\,000$.

Zhou et al. [42]

Tests were conducted over a range of incidences from 0° to 90° for Reynolds numbers of 5 300 and 10 500, and over 0° to 40° for a Reynolds numbers of 51 000. A 0.3 m × 0.6 m water tunnel was used, with a 0.1 m chord, 0.27 m span model, fitted between two 0.25 m × 0.25 m square end plates.

A high sensitivity 3-component load cell was used for lift and drag force measurements, fitted with a "torque resisting system" that prevents any torques being transmitted to the load cell but provides no resistance to force transfer. Drag is also estimated using a momentum conservation method calculated from cross-stream velocity distributions with good agreement between this and the load cell measurements. Blockage was corrected "at high incidence" using Maskell [47]. No other corrections were applied. The turbulence intensity of the flow is measured at 0.4-0.5%, though no corrections are made for this. Using Rae et al.'s correction this would require a turbulence factor of 1.3 - 1.4 (see Section 2.1.8).

The results taken at $Re = 5\,300$ exhibit no attached flow lift peak or stall, while those at 10 500 do, suggesting that the Re_{crit} of the aerofoil tested, below which a laminar separation bubble cannot form, lies somewhere between these values.

A.1.2 The NACA 0015

Sheldahl and Klimas [20]

See Section A.1.1.

Pope [36]

A 2.74 m diameter circular tunnel was fitted with two-dimensional inserts to give a tunnel of approximate dimensions 0.76 m × 2.74 m. Testing was conducted at $Re = 1.23 \times 10^6$ (corrected for tunnel turbulence with a factor of 1.2). The model used has a chord of 0.46 m, tapped for pressure readings at 50 locations. Surface accuracy was measured with feeler gauges and found to be accurate to 0.13 mm. The model is mounted between end plates that sit flush with the tunnel inserts and spans the 0.76 m width of the tunnel. Data is presented for lift and drag obtained with the tappings and with a force balance, with post-stall lift and drag peaks approximately 10% higher using the force balance.

Lift interference is corrected for, though corrections to incidence were neglected as they were found to be small before stall. An additional study was conducted on models with chords of 0.15 m, 0.30 m and 0.46 m with little difference found between results post-stall. It was concluded that a "breather" downstream of the model fortuitously yields a blockage tolerance to the wind tunnel, so rendering solid and wake blockage corrections unnecessary, with none made.

A.1.3 The NACA 0018

Timmer [38]

Readings were taken for incidences of 0° to 30° in a 1.8 m × 1.25 m rectangular cross-section tunnel. A 0.25 m chord model spanned nearly the whole of the 1.8 m width, the gap at both ends of the aerofoil is smaller than 0.5 mm. Forces and moments were measured with a six-component mechanical balance. Drag was also measured using a wake rake. Balance drag measurements were corrected for the influence of the small gaps between the edges of the aerofoils and the tunnel walls.

Readings were taken at Reynolds numbers of 150 000, 300 000, 500 000, 700 000 and 10^6. The turbulence intensity of the tunnel was measured at 0.02% at 10 m/s to 0.07% at 70 m/s, corresponding to Reynolds numbers of 150 000 and 10^6 respectively, judged to be sufficiently low to not require corrections to the Reynolds numbers.

Data was taken for increasing and decreasing incidences around stall, with significant hysteresis found at all Reynolds numbers. AGARD corrections [45] were applied up to the incidence at which leading edge flow separation occurs. Beyond this, Maskell's method, as modified by Hackett [123], has been used.

Runs were completed with free transition and with a 0.48 mm thick zigzag tape located just before 80% of chord on both the upper and lower surfaces. This removed a "kink" in the lift curve that Timmer states is caused but the influence of a laminar separation bubble on the pressure surface of the aerofoil, at around 90% of chord. The zigzag tape has no effect on the hysteresis around stall, so doesn't suppress the suction surface laminar separation bubble at angles near to the stall.

Du et al. [37, 68]

A 0.46 m × 0.46 m wind tunnel was used, with a conventional solid walled test section and an open jet with side walls but no floor and ceiling. The aerofoil has 44 pressure tappings, a 0.13 m chord and spans the full width of the tunnel. Reynolds numbers of 60 000, 100 000 and 140 000 were used, surface pressures were measured using a scanivalve and processing into lift and drag data via the methods of Fuglsang et al. [124]. AGARD corrections are applied [46, 45], but raw data is also provided. The specific corrections used from the AGARD publications used are not stated. Since the c/H is large at 0.28, the choice of correction regime has a significant impact on results, so here the raw data has been used and reprocessed with the ESDU blockage corrections used in the current study.

A.2 Low-Reynolds number aerofoil experiments

A.2.1 Althaus [8, 51] (various aerofoils)

Note that these references are in German. Automated translation software was used to obtain the following information. The wind tunnel has a 0.37 m × 0.6 m cross section. Aerofoil models have chords of 0.2 m and span the 0.37 m width of the tunnel, mounted between two end plates that sit flush with the tunnel walls. Experiments are conducted for incidences below 20°, at Reynolds numbers of 40 000 - 200 000. The NACA 0009, 0012 and 0033 aerofoils are tested, among many other profiles.

Lift is measured with a load cell, drag using a wake rake. The corrections of Abbott et al. [122] (as used by Critzos et al, see above) are applied to the data. Turbulence intensity of the tunnel was measured at 0.08% using a hot wire. No corrections were made to Reynolds number for this.

A.2.2 Dong-Ha et al. [41] (NACA 0012)

Testing was conducted over a narrow range of incidences (below 6°) at Reynolds numbers of 2.3×10^4, 3.3×10^4 and 4.8×10^4. A 0.18 m chord, 0.5 m span aerofoil was used in a 0.5 m × 0.5 m wind tunnel. The aerofoil has 24 pressure tappings from which measurements were taken, with lift and drag calculated from the pressure distributions. Boundary layer

flow visualisations were also conducted, using a smoke-wire method. No blockage corrections are mentioned in the reference, nor in an earlier reference describing experimental techniques [125]. Presumably, given the low incidences tested, they were deemed unnecessary.

A.2.3 Jacobs and Sherman [43] (various aerofoils)

Testing was conducted in the NACA variable density wind tunnel, with pressures of 0.25, 0.5, 1, 2, 4, 8, 15 and 20 atmospheres used to obtain effective Reynolds numbers of 40 000 - 310 000. The test section has a 1.524 m diameter circular cross-section.

Aerofoils have 127 mm chords and 762 mm spans and are finite, mounted on partly-shielded supporting struts. Forces and moments are measured using a balance connected to the struts. Drag and moment results at effective $Re < 800\,000$ are considered unreliable due to the sensitivity of the measuring equipment used. The main concern with the data presented is, however, stated to be the interpretative methods used, particularly those for Reynolds number and aspect ratio corrections.

Corrections to infinite aspect ratio use classical lifting-line theory for downwash and induced drag, with the addition of appropriate factors to consider wall interference at the same time, following methods established earlier for the same facility [126]. They are then corrected for the influence of the rectangular wing tips using empirical corrections derived from experiments on elliptical and rectangular planform wings. The corrections are assessed as providing good sectional data for $C_l < 1$, but as stall is approached the suitability of the corrections diminishes. A final empirical correction (a 4% increase in $C_{l\,\mathrm{MAX}}$) is applied to improve performance around stall. The correction was derived from experiments on wings with a variety of aspect and taper ratios. It is presented with the caveat that 4% is of the order of measurement error of these experiments. Support interference is not corrected, with an acknowledgement that this could cease to be negligible at low Reynolds numbers.

Effective Reynolds numbers have been corrected with a turbulence factor of 2.64, suggesting the variable density tunnel has a very high turbulence intensity of around 2%. At some low Reynolds numbers only lift measurements are presented due to the low quality of drag and moment readings.

As the original authors note, data from this study is somewhat unreliable. Specific reference is made to new tests on the NACA 0012 in a lower turbulence facility that show lower

drag than Jacobs and Sherman's results, even after application of all their corrections. The study is referenced here in the absence of any better alternatives.

Appendix B

Method of images

The method of images is a mathematical technique used in potential flow theory to impose boundary conditions on the domain under study. The domain is extended by duplicating it in a mirror image, reflected along a line of symmetry. By considering the mirror image alongside the original domain, boundary conditions are imposed along the line of symmetry.

B.1 Lift interference

The potential of a vortex of strength Γ located at x,z on the origin of the coordinate system is:

$$\Phi(x,z) = -\frac{\Gamma}{2\pi}\arctan\left(\frac{z}{x}\right) \tag{B.1}$$

and the velocity components are

$$u = \frac{\Gamma}{2\pi}\left(\frac{z}{x^2+z^2}\right) \tag{B.2a}$$

$$w = -\frac{\Gamma}{2\pi}\left(\frac{x}{x^2+z^2}\right) \tag{B.2b}$$

The test aerofoil is modelled as a flat plate with chord c mounted at the quarter chord at the origin and represented by a point vortex at the quarter chord point. The walls of the tunnel, separated by height H, are represented as an infinite system of images of it. Opposite pairs of images will induce no stream-wise velocity at the test aerofoil half chord as they

cancel each other out. Conversely, the upwash induced by each pair is additive. For the first pair, at the test aerofoil half chord:

$$w = -\frac{\Gamma}{\pi}\left(\frac{c/4}{H^2 + (c/4)^2}\right) \tag{B.3}$$

If $\Gamma = \frac{1}{2}C_l U_u c$

$$w = -\frac{C_l U_u}{8\pi}\left(\frac{c^2}{H^2 + (c/4)^2}\right) \tag{B.4}$$

assuming $c/4 << H$

$$\Delta\alpha = -\arctan\left(\frac{w}{U_u}\right) \approx -\frac{w}{U_u} = \frac{C_l}{8\pi}\left(\frac{c}{H}\right)^2 \tag{B.5}$$

The next pair of vortices is twice as far away, so will be 1/4 as effective and act in the opposite direction. The next pair beyond that is three times away so will be 1/9 as effective and act in the same direction and so on. The influence of the infinite system can therefore be calculated as:

$$\begin{aligned}
\Delta\alpha &= \frac{C_l}{8\pi}\left(\frac{c}{H}\right)^2 \sum_{i=1}^{\infty} \frac{-1^{(i+1)}}{i^2} \\
&= \frac{C_l}{8\pi}\left(\frac{c}{H}\right)^2 \left(1 - \frac{1}{4} + \frac{1}{9} - \frac{1}{16} + \ldots\right) \\
&= \frac{C_l}{8\pi}\left(\frac{c}{H}\right)^2 \left(\frac{\pi^2}{12}\right) \\
&= \frac{\pi}{96}\left(\frac{c}{H}\right)^2 C_l
\end{aligned} \tag{B.6}$$

B.2 Solid blockage

The potential of a source-sink doublet of strength μ located at x,z on the origin of the coordinate system is:

$$\Phi(x, z) = -\frac{\mu}{2\pi}\left(\frac{x}{x^2 + z^2}\right) \tag{B.7}$$

and the velocity components are

$$u = \frac{\mu}{2\pi}\left(\frac{x^2 - z^2}{(x^2 + z^2)^2}\right) \tag{B.8a}$$

$$w = \frac{\mu}{2\pi}\left(\frac{2xz}{(x^2 + z^2)^2}\right) \tag{B.8b}$$

The test aerofoil is modelled as a cylinder with radius a mounted at its centre at the origin and represented as a point doublet, and the tunnel walls, separated by height H, are represented as an infinite system of images of it. Opposite pairs of images will induce no upwash at the cylinder centre as they cancel each other out. The effect of the pairings on stream-wise velocity is additive. For the first pair, at the cylinder centre:

$$u = \frac{\mu}{\pi}\left(\frac{1}{H^2}\right) \tag{B.9}$$

if $\mu = 2\pi a^2 U_u$, where a is the cylinder radius

$$\begin{aligned} u &= 2\frac{a^2 U_u}{H^2} \\ \epsilon_{sb} = \frac{u}{U_u} &= 2\frac{a^2}{H^2} \end{aligned} \tag{B.10}$$

The next pair of vortices is twice as far away, so will be 1/4 as effective. The next pair beyond that are three times away so will be 1/9 as effective and so on. The influence of the infinite system can therefore be calculated as:

$$\begin{aligned} \epsilon_{sb} &= 2\frac{a^2}{H^2}\sum_{i=1}^{\infty}\frac{1}{i^2} \\ &= 2\frac{a^2}{H^2}\left(1 + \frac{1}{4} + \frac{1}{9} + \frac{1}{16} + \dots\right) \\ &= 2\frac{a^2}{H^2}\frac{\pi^2}{6} \\ &= \frac{\pi^2}{3}\left(\frac{a}{H}\right)^2 \end{aligned} \tag{B.11}$$

B.3 Wake blockage

The potential of a source of strength m located at x,z on the origin of the coordinate system is:

$$\Phi(x,z) = \frac{m}{2\pi} \ln \sqrt{x^2 + z^2} \tag{B.12}$$

and the velocity components are

$$u = \frac{m}{2\pi} \left(\frac{x}{x^2 + z^2} \right) \tag{B.13a}$$

$$w = \frac{m}{2\pi} \left(\frac{z}{x^2 + z^2} \right) \tag{B.13b}$$

The wake of the test aerofoil is modelled as a point source at the origin, with a corresponding system of sinks far enough downstream to be ignored in this analysis. The walls of the tunnel, separated by height H, are represented as an infinite system of images of the sources and sinks. The influence of the system at the midspan of the tunnel far upstream of the model is calculated. At this point, opposite pairs of images will induce no upwash as they cancel each other out but they will induce a stream-wise velocity. For the n^{th} pair of source images, at a distance x upstream:

$$u = \frac{m}{\pi} \left(\frac{x}{x^2 + (nH)^2} \right) \tag{B.14}$$

taking $m = \frac{1}{2} C_{du} U_u c$ and summing for the infinite system of sources:

$$u = \frac{1}{2\pi} C_{du} U_u c \sum_{i=1}^{\infty} \left(\frac{x}{x^2 + (nH)^2} \right) \tag{B.15}$$

Evaluating the sum to infinity:

$$\begin{aligned} \epsilon_{wb} = \frac{u}{U_u} &= \frac{1}{2\pi} C_{du} \frac{c}{H} \sum_{i=1}^{\infty} \left(\frac{x/H}{(x/H)^2 + n^2} \right) \\ &= \frac{1}{2\pi} C_{du} \frac{c}{H} \left[\frac{\pi (x/H) \coth(\pi x/H) - 1}{2x/H} \right] \end{aligned} \tag{B.16}$$

and if x is far upstream:

$$\lim_{x\to\infty} \epsilon_{wb} = \frac{1}{4} C_{du} \frac{c}{H} \tag{B.17}$$

Appendix C

Derivation of a formula for calculating the required c/H ratio for blockage corrections to be less than 5%

First, an inequality is established:

$$\frac{C_{du} - C_{d\,FA}}{C_{du}} < 0.05 \tag{C.1}$$

From Eqns (2.20) and (2.18):

$$\frac{C_{du} - \dfrac{C_{du}(1-\epsilon_{sb})}{(1+\epsilon_B)^2}}{C_{du}} < 0.05 \tag{C.2}$$

$$\implies 0.95(1+\epsilon_B)^2 < 1 - \epsilon_{sb}$$

Using Eqn. (2.17) and expanding $(1+\epsilon_B)^2$ gives:

$$(1+\epsilon_B)^2 = 1 + 2\epsilon_{sb} + 2\epsilon_{wb} + {\epsilon_{sb}}^2 + 2\epsilon_{sb}\epsilon_{wb} + {\epsilon_{wb}}^2 \tag{C.3}$$

Substituting (C.3) in (C.2) and rearranging:

$$2.9\epsilon_{sb} + 1.9\epsilon_{wb} + 0.95{\epsilon_{sb}}^2 + 1.9\epsilon_{sb}\epsilon_{wb} + 0.95{\epsilon_{wb}}^2 < 0.05 \tag{C.4}$$

Eqn. (2.13) gives ϵ_{wb} in terms of c/H; manipulation of Eqn. (2.11) gives ϵ_{sb} similarly:

$$\epsilon_{sb} = \zeta \left(\frac{c}{H}\right)^2 \tag{C.5}$$

where:

$$\zeta = \frac{\pi k_{aero}\tau}{6}(1 + 1.2\tau)\left(1 + \frac{1.1}{\tau}\alpha^2\right) \tag{C.6}$$

$\tau = t/c$ and k_{aero} is a constant for a given profile such that $A_{aero} = k_{aero}\tau c^2$. $k_{aero} = 0.68$ for the NACA 0012 and 0.65 for the NACA 0015.

Substituting Eqns (2.13) and (C.5) into (C.4) and rearranging gives a quartic inequality in c/H:

$$0.95\zeta^2\left(\frac{c}{H}\right)^4 + 1.9K_{wb}C_{du}\zeta\left(\frac{c}{H}\right)^3 + (2.9\zeta + 0.95{K_{wb}}^2{C_{du}}^2)\left(\frac{c}{H}\right)^2 + 1.9K_{wb}C_{du}\left(\frac{c}{H}\right) < 0.05 \tag{C.7}$$

Appendix D

Additional plots

D.1 Force measurements for the five NACA 0015 aerofoils with various tolerant tunnel OARs at $Re = 150\,000$

D.1.1 Single slatted wall

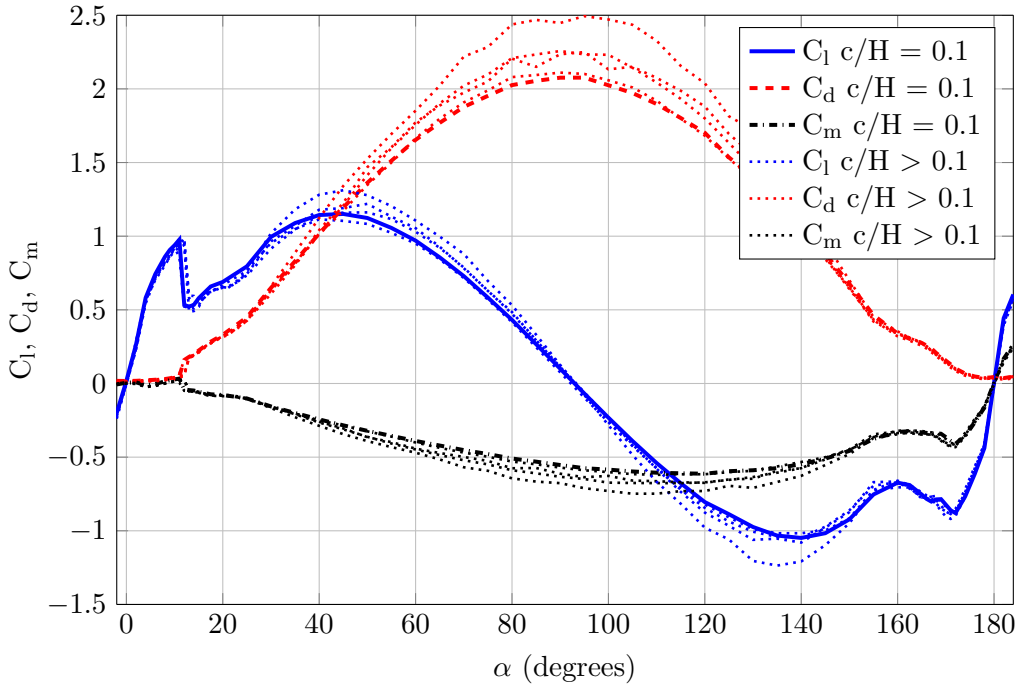


Figure D.1: C_l, C_d and C_m vs α for $c/H = 0.1$, 0.15, 0.2, 0.25 and 0.3 NACA 0015 aerofoils taken in the tolerant tunnel, SS-71 configuration at $Re = 150\,000$.

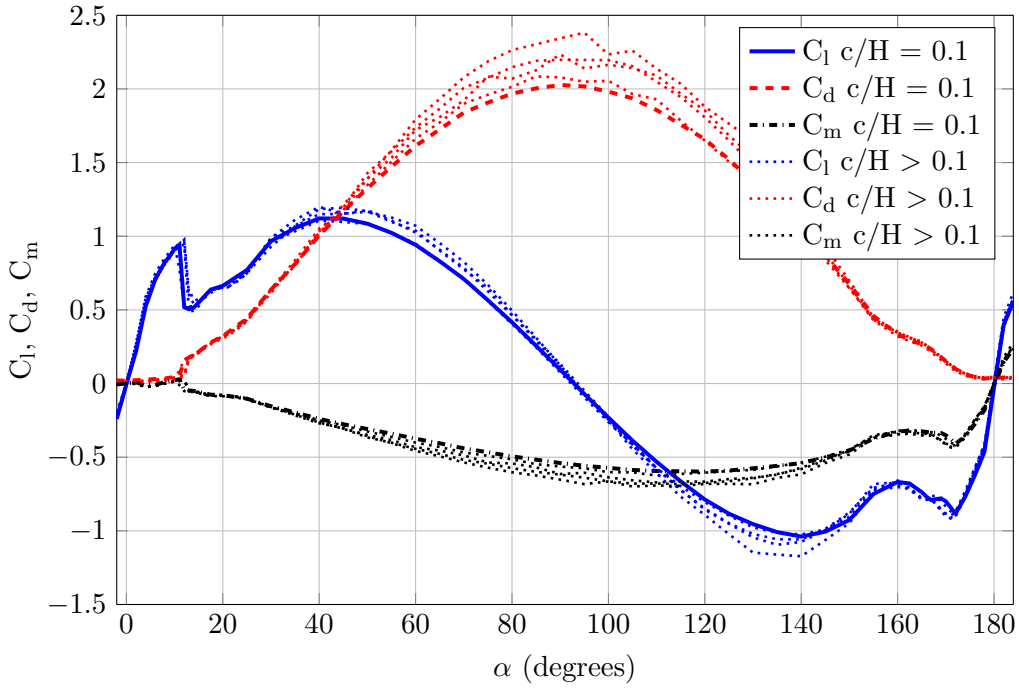


Figure D.2: C_l, C_d and C_m vs α for $c/H = 0.1$, 0.15, 0.2, 0.25 and 0.3 NACA 0015 aerofoils taken in the tolerant tunnel, SS-79 configuration at $Re = 150\,000$.

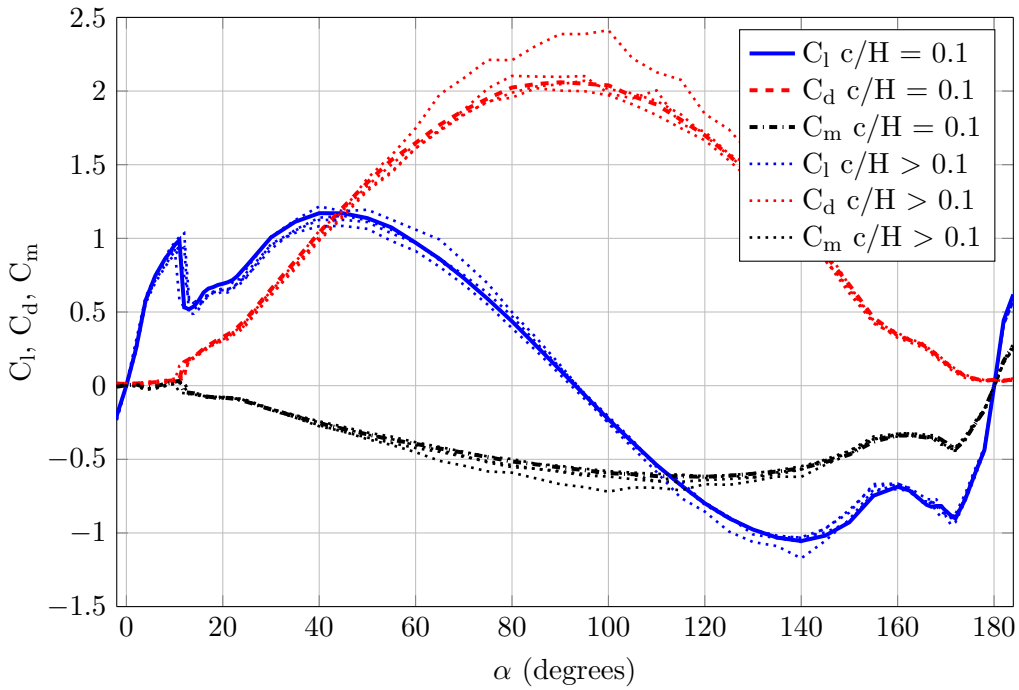


Figure D.3: C_l, C_d and C_m vs α for $c/H = 0.1$, 0.15, 0.2, 0.25 and 0.3 NACA 0015 aerofoils taken in the tolerant tunnel, SS-83 configuration at $Re = 150\,000$.

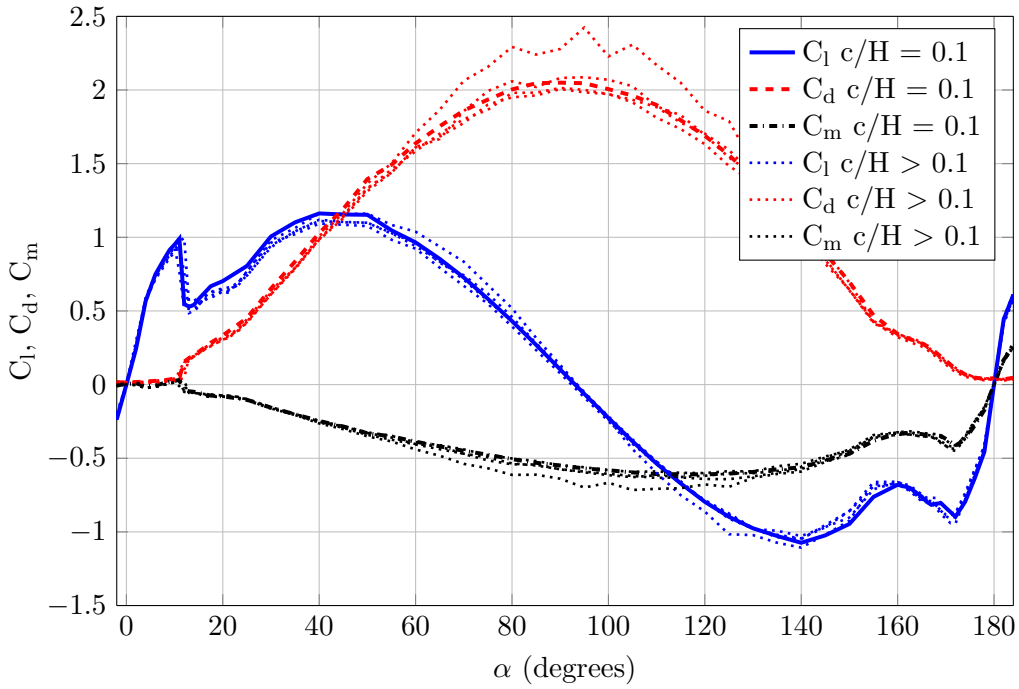


Figure D.4: C_l, C_d and C_m vs α for $c/H = 0.1$, 0.15, 0.2, 0.25 and 0.3 NACA 0015 aerofoils taken in the tolerant tunnel, SS-88 configuration at $Re = 150\,000$.

D.1.2 Double slatted walls

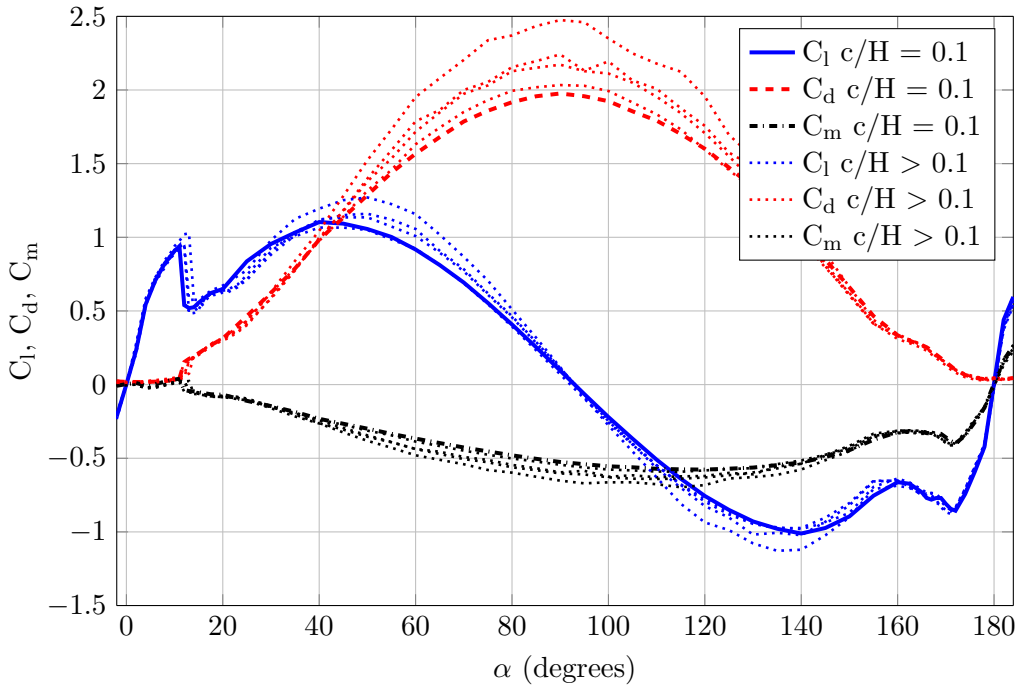


Figure D.5: C_l, C_d and C_m vs α for $c/H = 0.1$, 0.15, 0.2, 0.25 and 0.3 NACA 0015 aerofoils taken in the tolerant tunnel, DS-50 configuration at $Re = 150\,000$.

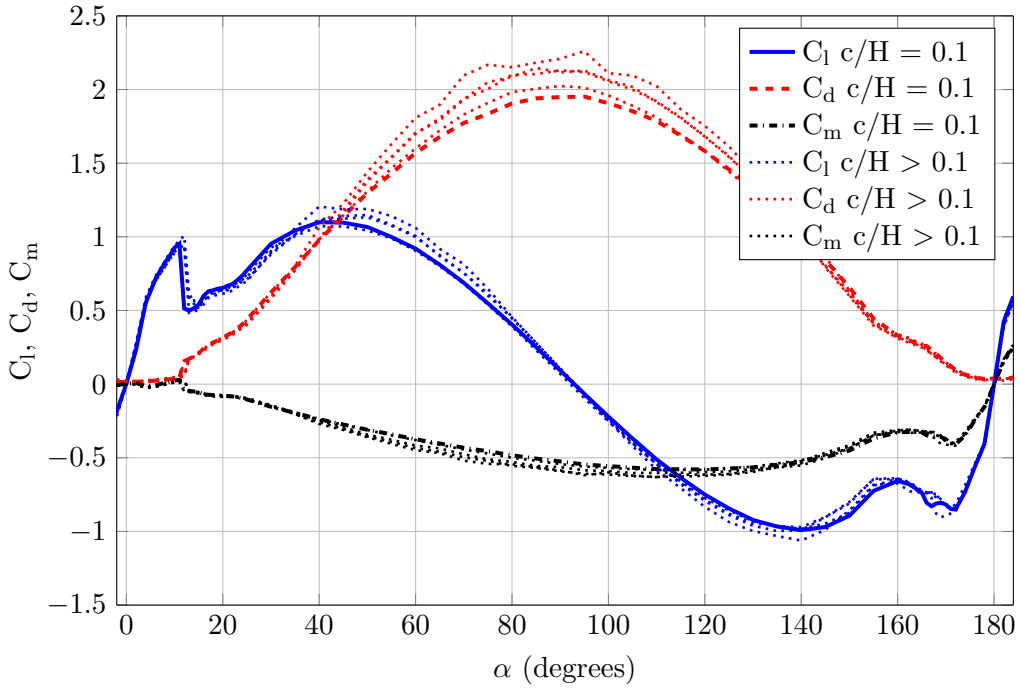


Figure D.6: C_l, C_d and C_m vs α for $c/H = 0.1$, 0.15, 0.2, 0.25 and 0.3 NACA 0015 aerofoils taken in the tolerant tunnel, DS-55 configuration at $Re = 150\,000$.

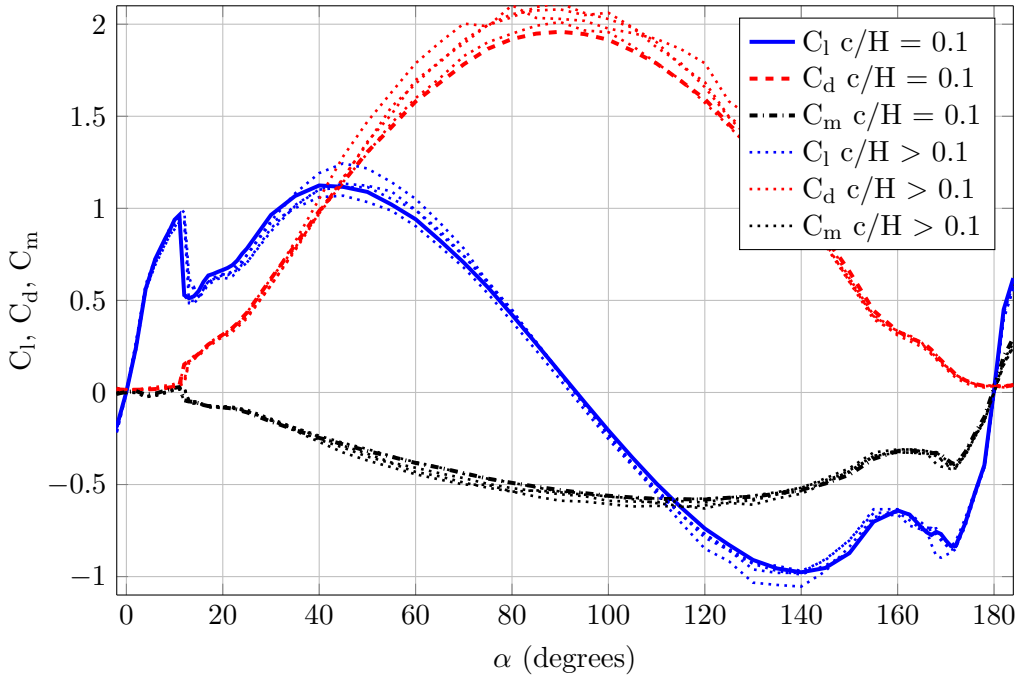


Figure D.7: C_l, C_d and C_m vs α for $c/H = 0.1$, 0.15, 0.2, 0.25 and 0.3 NACA 0015 aerofoils taken in the tolerant tunnel, DS-59 configuration at $Re = 150\,000$.

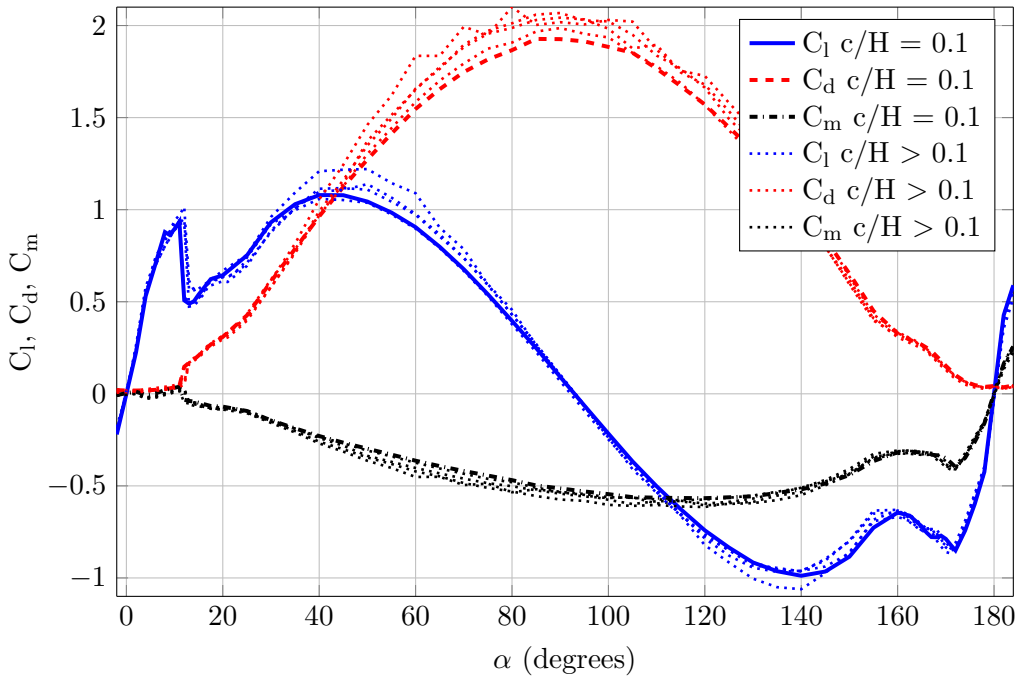


Figure D.8: C_l, C_d and C_m vs α for $c/H = 0.1$, 0.15, 0.2, 0.25 and 0.3 NACA 0015 aerofoils taken in the tolerant tunnel, DS-63 configuration at $Re = 150\,000$.

D.2 Force measurements for the five NACA 0015 aerofoils with various tolerant tunnel OARs at $Re = 60\,000$

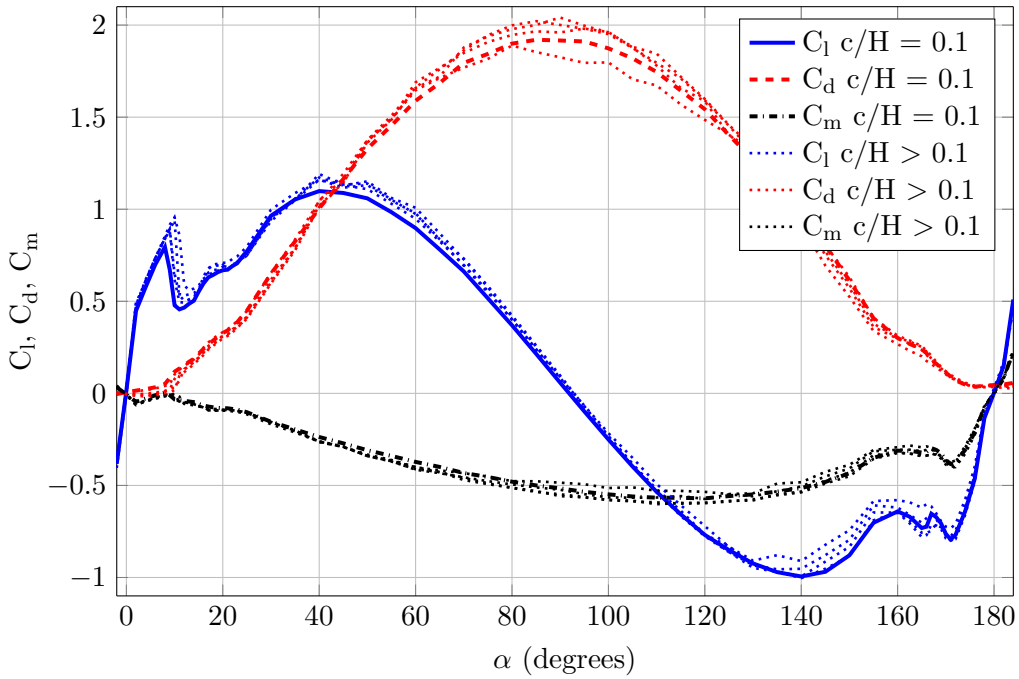


Figure D.9: C_l, C_d and C_m vs α for $c/H = 0.1$, 0.15, 0.2, 0.25 and 0.3 NACA 0015 aerofoils taken in the tolerant tunnel, DS-67 configuration at $Re = 60\,000$.

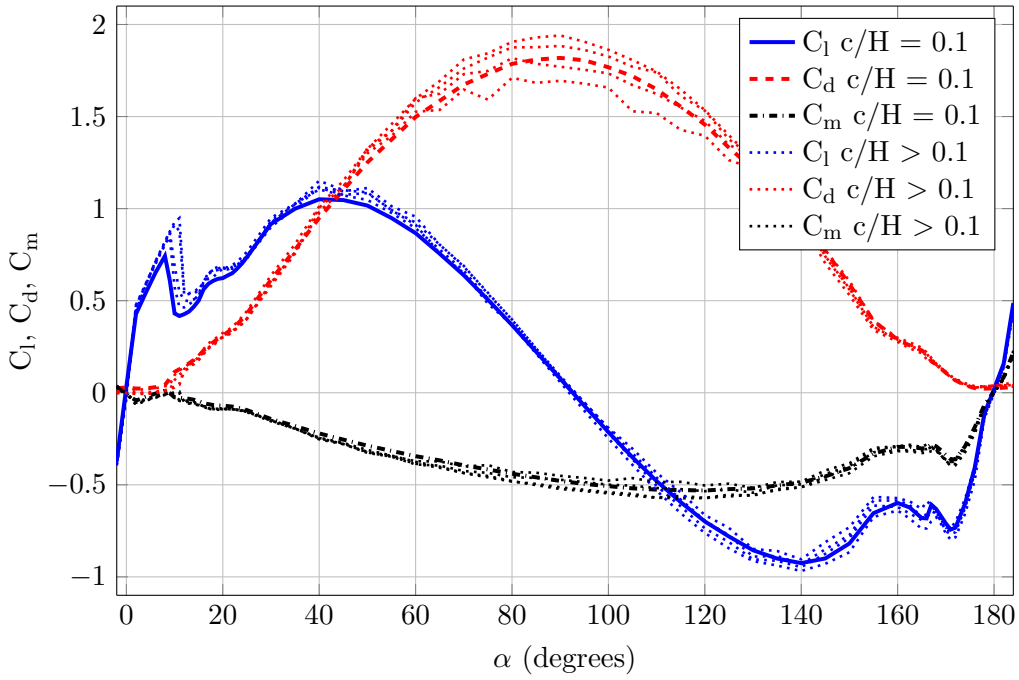


Figure D.10: C_l, C_d and C_m vs α for c/H = 0.1, 0.15, 0.2, 0.25 and 0.3 NACA 0015 aerofoils taken in the tolerant tunnel, DS-71 configuration at Re = 60 000.

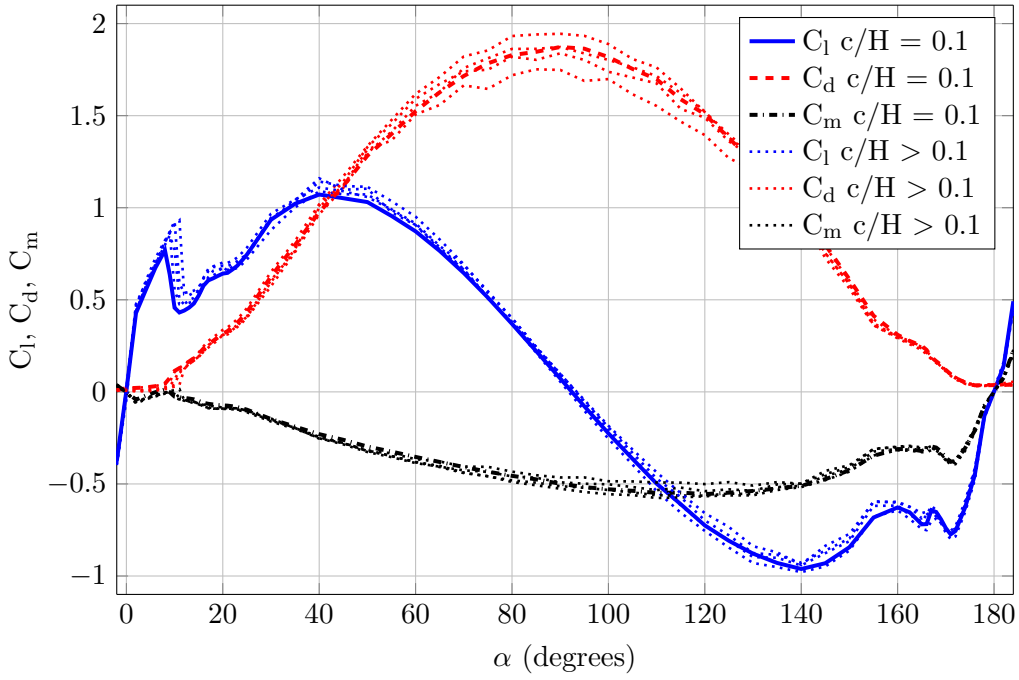


Figure D.11: C_l, C_d and C_m vs α for c/H = 0.1, 0.15, 0.2, 0.25 and 0.3 NACA 0015 aerofoils taken in the tolerant tunnel, DS-75 configuration at Re = 60 000.

D.3 Force measurements for the five NACA 0015 aerofoils with various tolerant tunnel OARs at $Re = 250\,000$

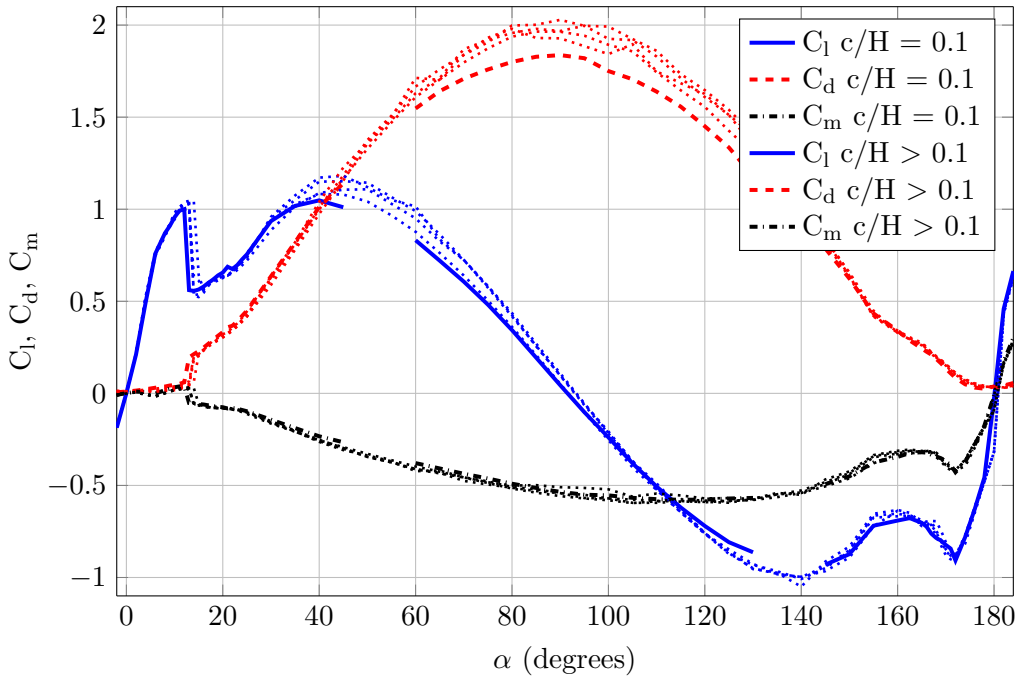


Figure D.12: C_l, C_d and C_m vs α for $c/H = 0.1$, 0.15, 0.2, 0.25 and 0.3 NACA 0015 aerofoils taken in the tolerant tunnel, DS-67 configuration at $Re = 250\,000$.

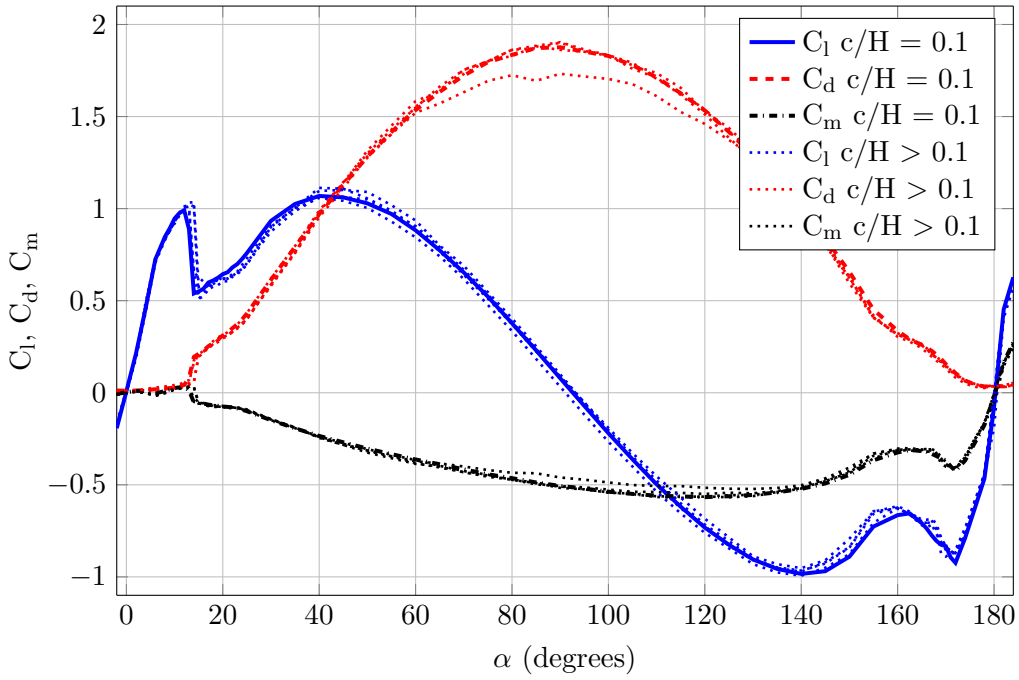


Figure D.13: C_l, C_d and C_m vs α for $c/H = 0.1$, 0.15, 0.2, 0.25 and 0.3 NACA 0015 aerofoils taken in the tolerant tunnel, DS-71 configuration at $Re = 250\,000$.

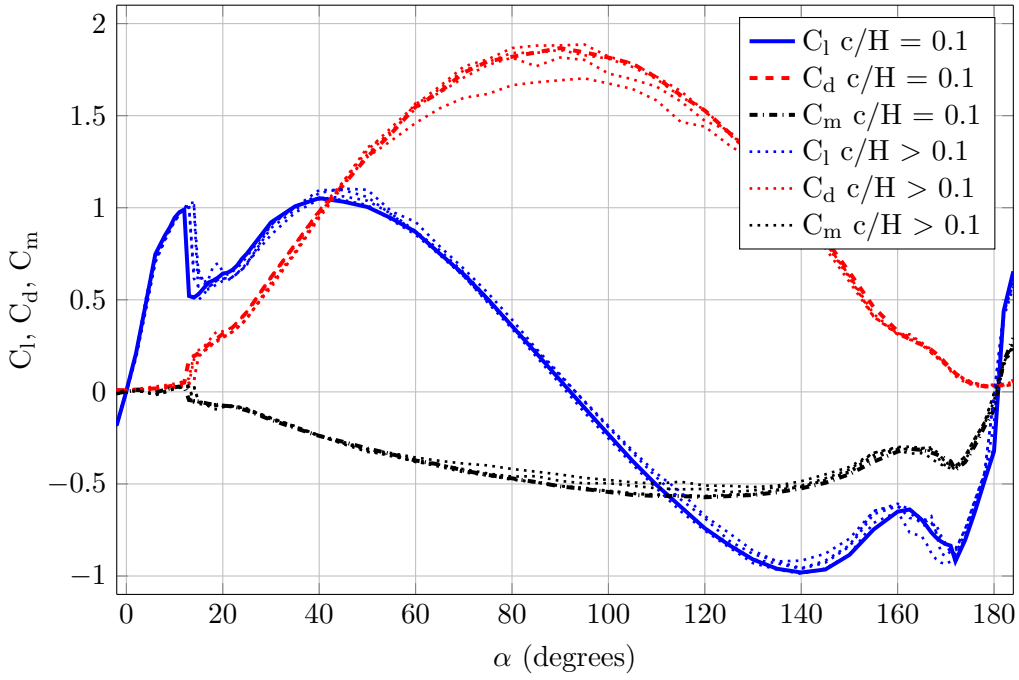


Figure D.14: C_l, C_d and C_m vs α for $c/H = 0.1$, 0.15, 0.2, 0.25 and 0.3 NACA 0015 aerofoils taken in the tolerant tunnel, DS-75 configuration at $Re = 250\,000$.

D.4 Force measurements for the five NACA 0015 aerofoils with solid tunnel walls at $Re = 60\,000$

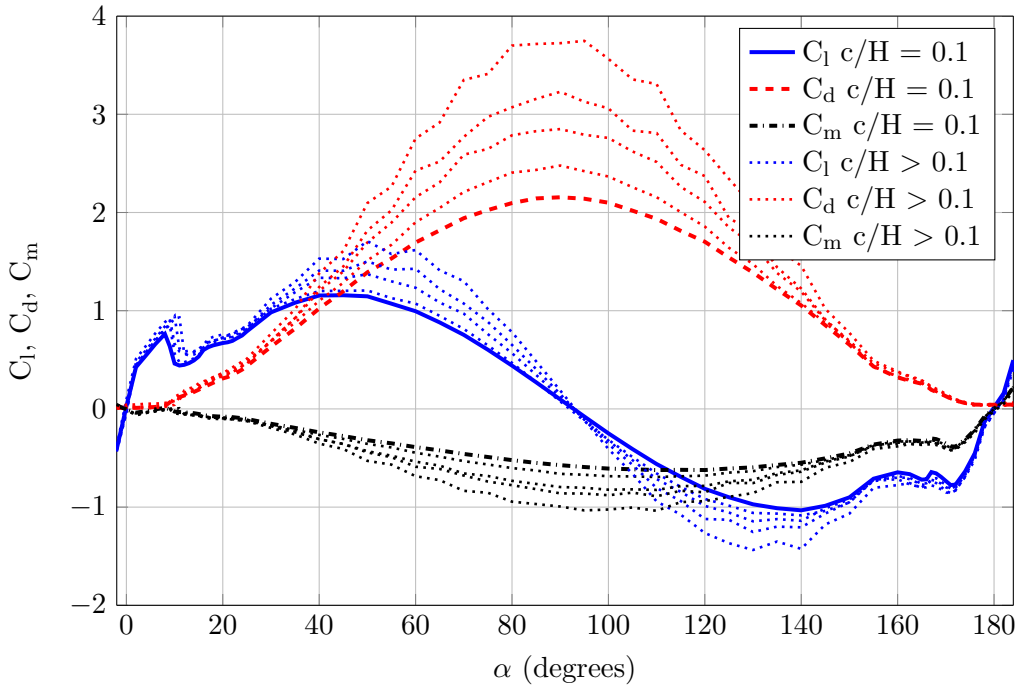


Figure D.15: C_l, C_d and C_m vs α for $c/H = 0.1$, 0.15, 0.2, 0.25 and 0.3 NACA 0015 aerofoils taken in the solid walled tunnel at $Re = 60\,000$.

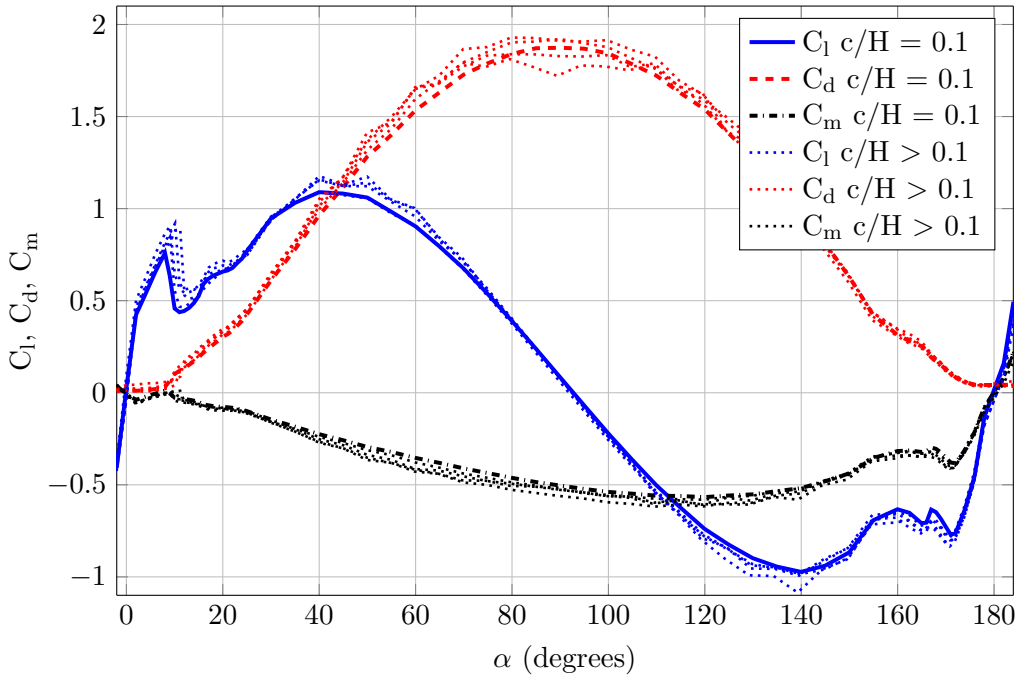


Figure D.16: C_l, C_d and C_m vs α for $c/H = 0.1$, 0.15, 0.2, 0.25 and 0.3 NACA 0015 aerofoils taken in the solid walled tunnel at $Re = 60\,000$, ESDU corrections.

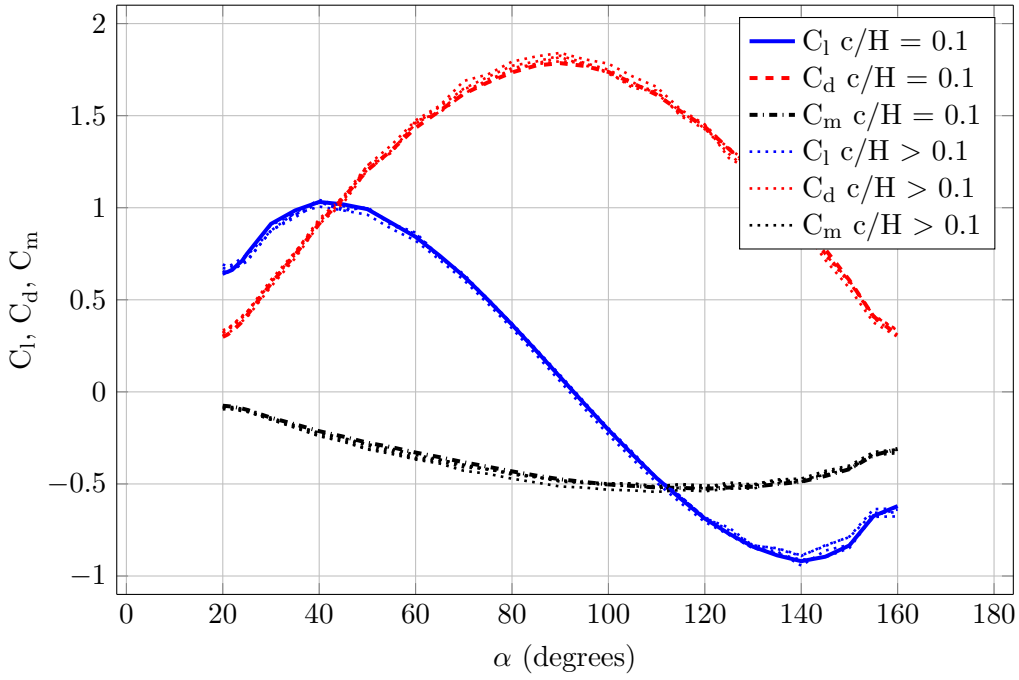


Figure D.17: C_l, C_d and C_m vs α for $c/H = 0.1$, 0.15, 0.2, 0.25 and 0.3 NACA 0015 aerofoils taken in the solid walled tunnel at $Re = 60\,000$, Maskell's corrections.

D.5 Force measurements for the five NACA 0015 aerofoils with solid tunnel walls at $Re = 250\,000$

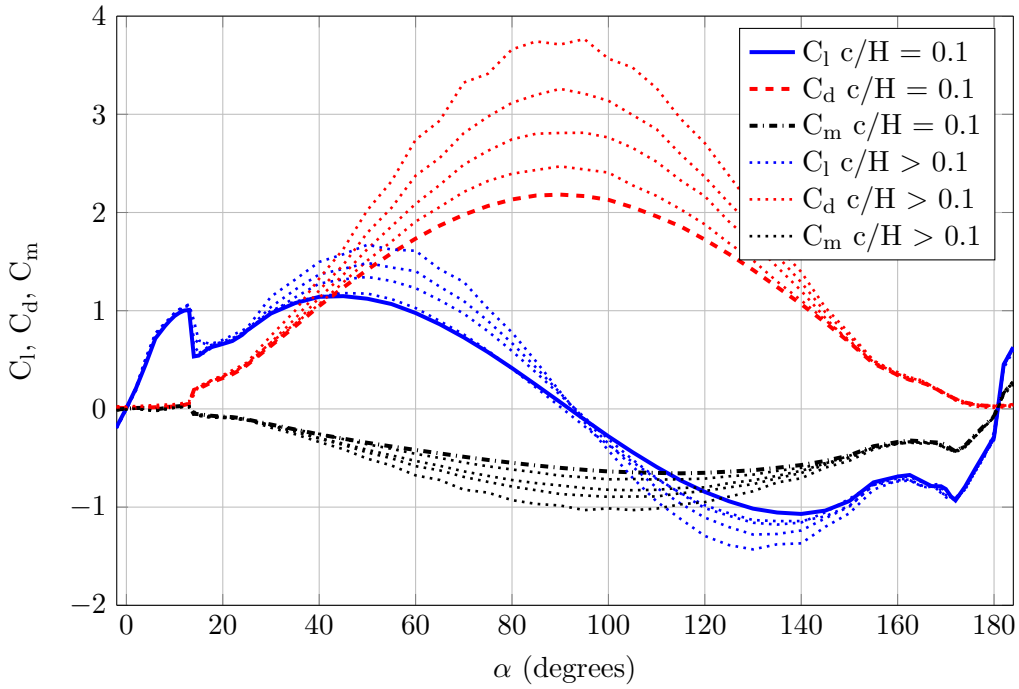


Figure D.18: C_l, C_d and C_m vs α for $c/H = 0.1$, 0.15, 0.2, 0.25 and 0.3 NACA 0015 aerofoils taken in the solid walled tunnel at $Re = 250\,000$.

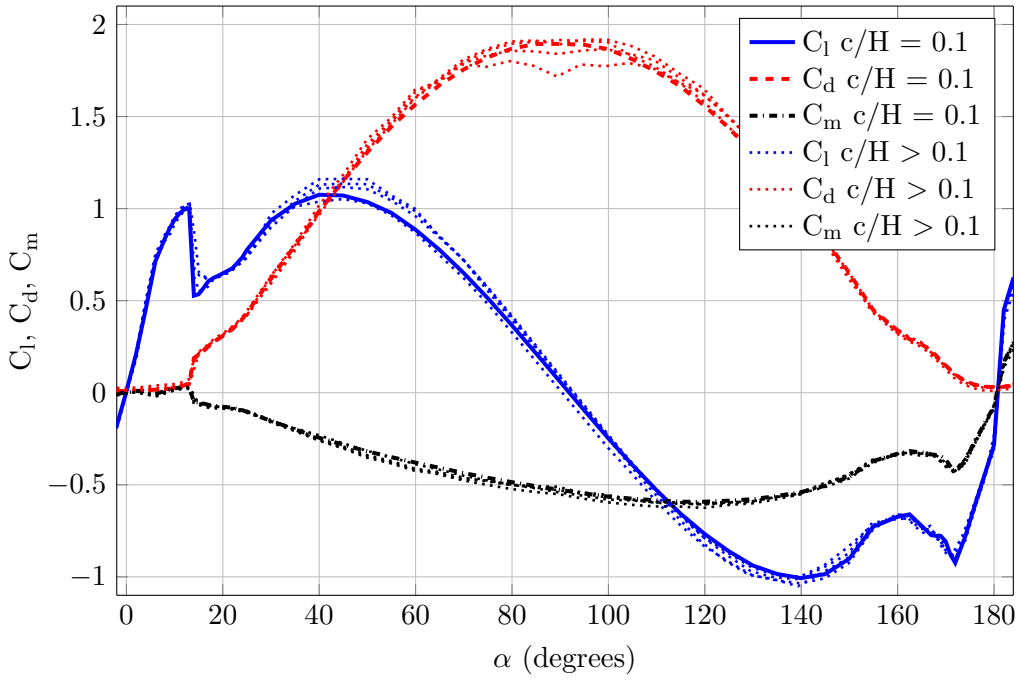


Figure D.19: C_l, C_d and C_m vs α for c/H = 0.1, 0.15, 0.2, 0.25 and 0.3 NACA 0015 aerofoils taken in the solid walled tunnel at Re = 250 000, ESDU corrections.

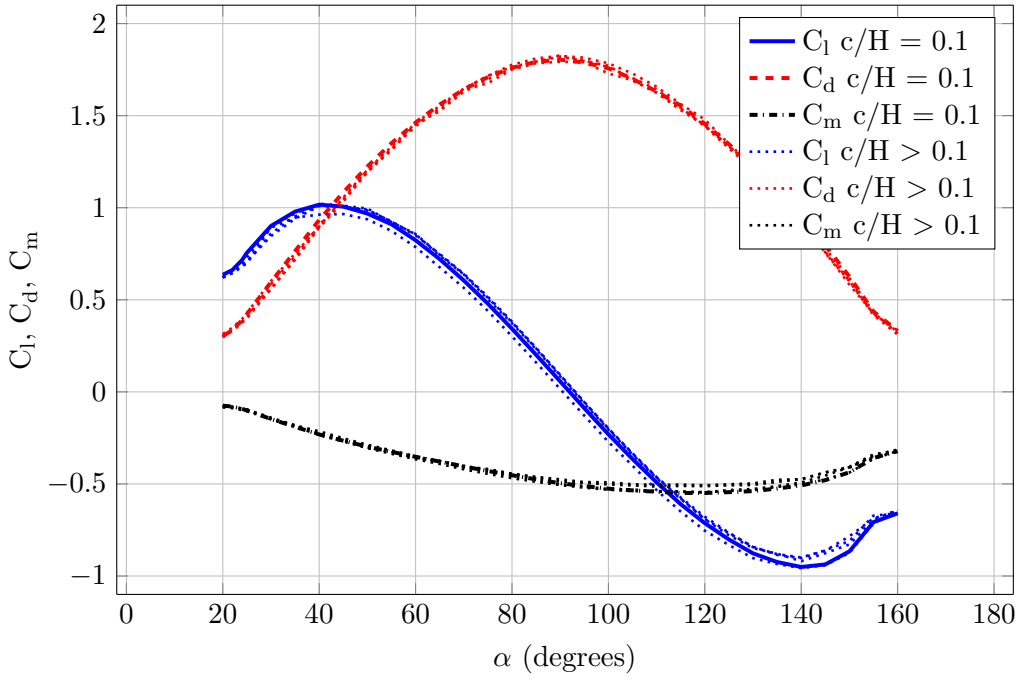


Figure D.20: C_l, C_d and C_m vs α for c/H = 0.1, 0.15, 0.2, 0.25 and 0.3 NACA 0015 aerofoils taken in the solid walled tunnel at Re = 250 000, Maskell's corrections.

D.6 Surface pressures for the two tapped NACA 0015 aerofoils with various tolerant tunnel OARs and solid tunnel walls, at $Re = 150\,000$

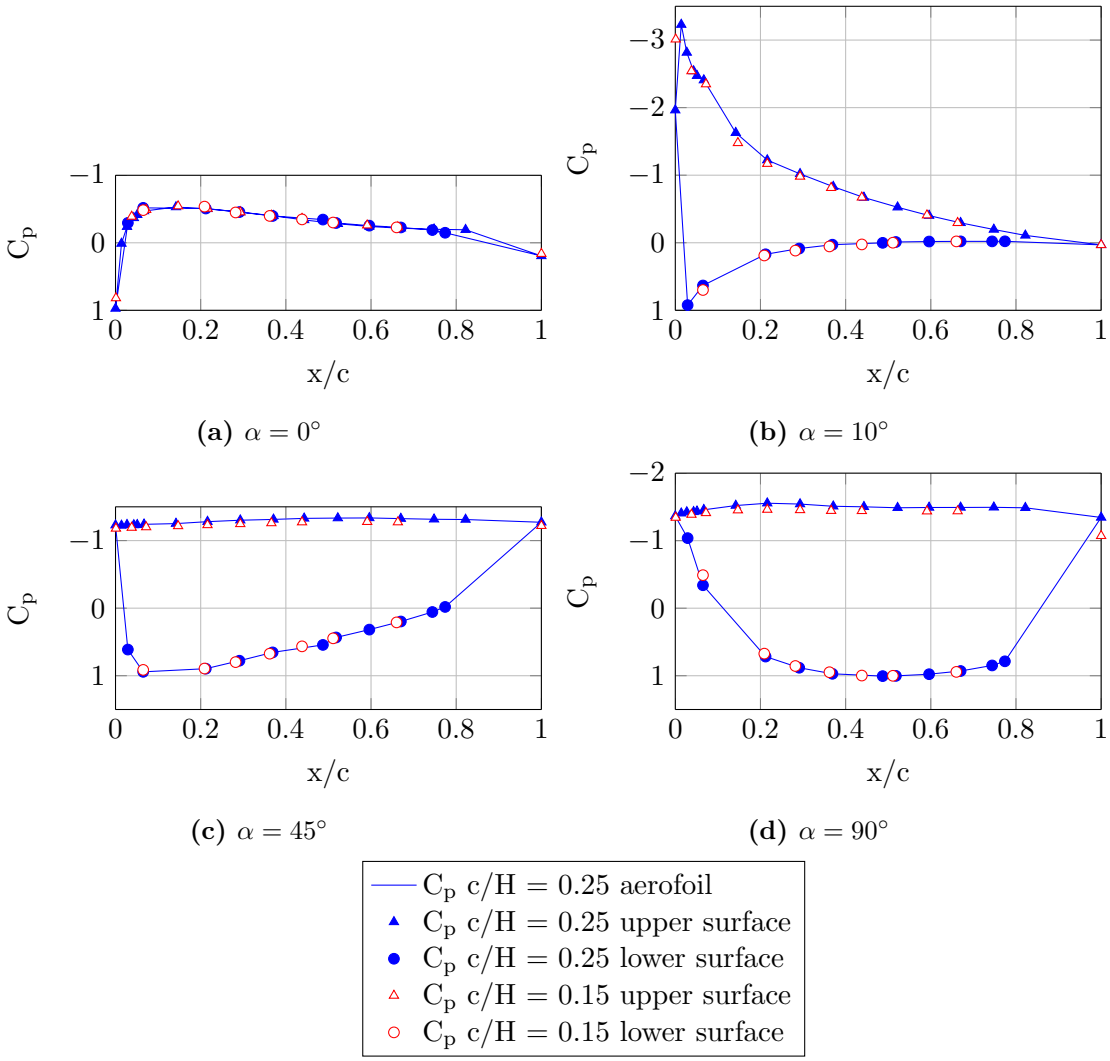


Figure D.21: C_p plotted against normalised chord-wise position for the $c/H = 0.15$ and $c/H = 0.25$ NACA 0015 aerofoils at $Re = 150\,000$ in the DS-67 tolerant tunnel.

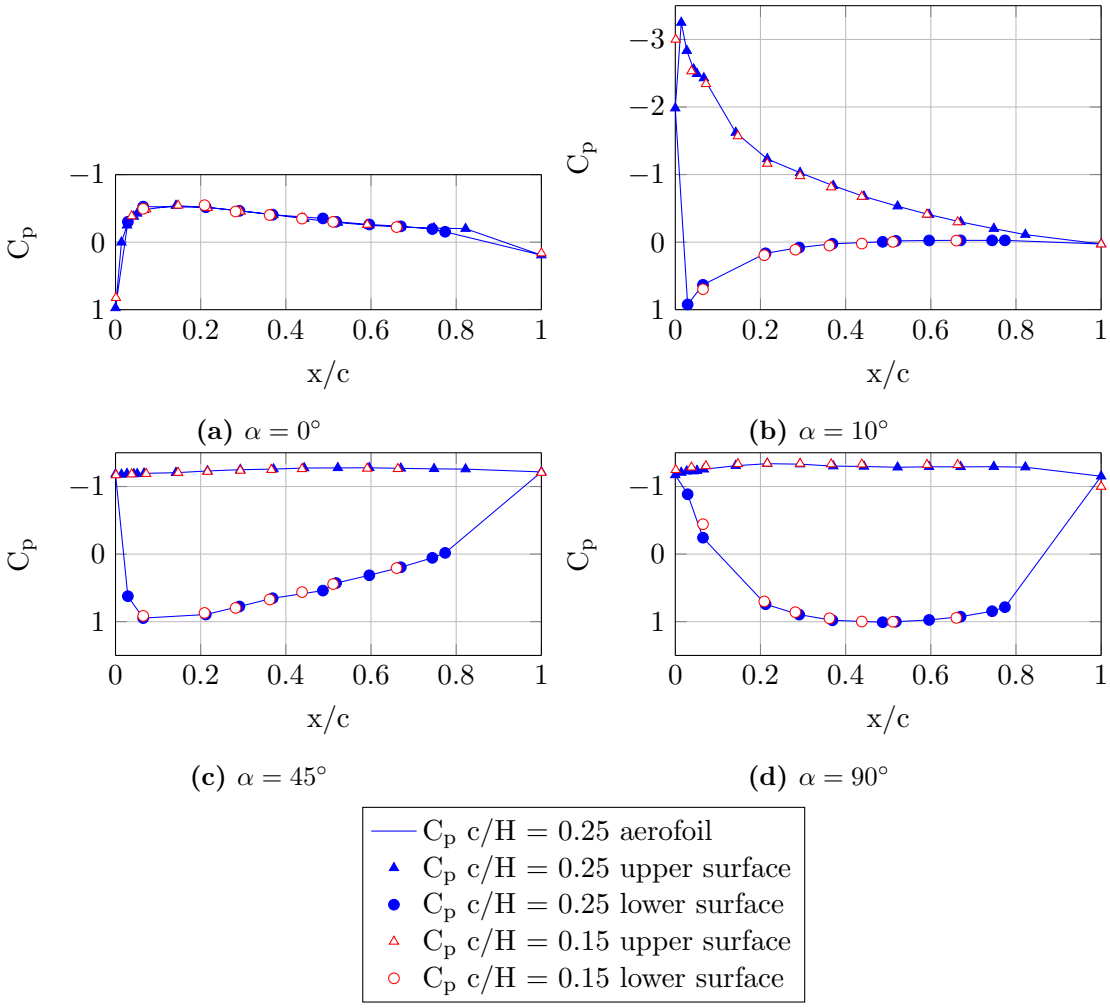
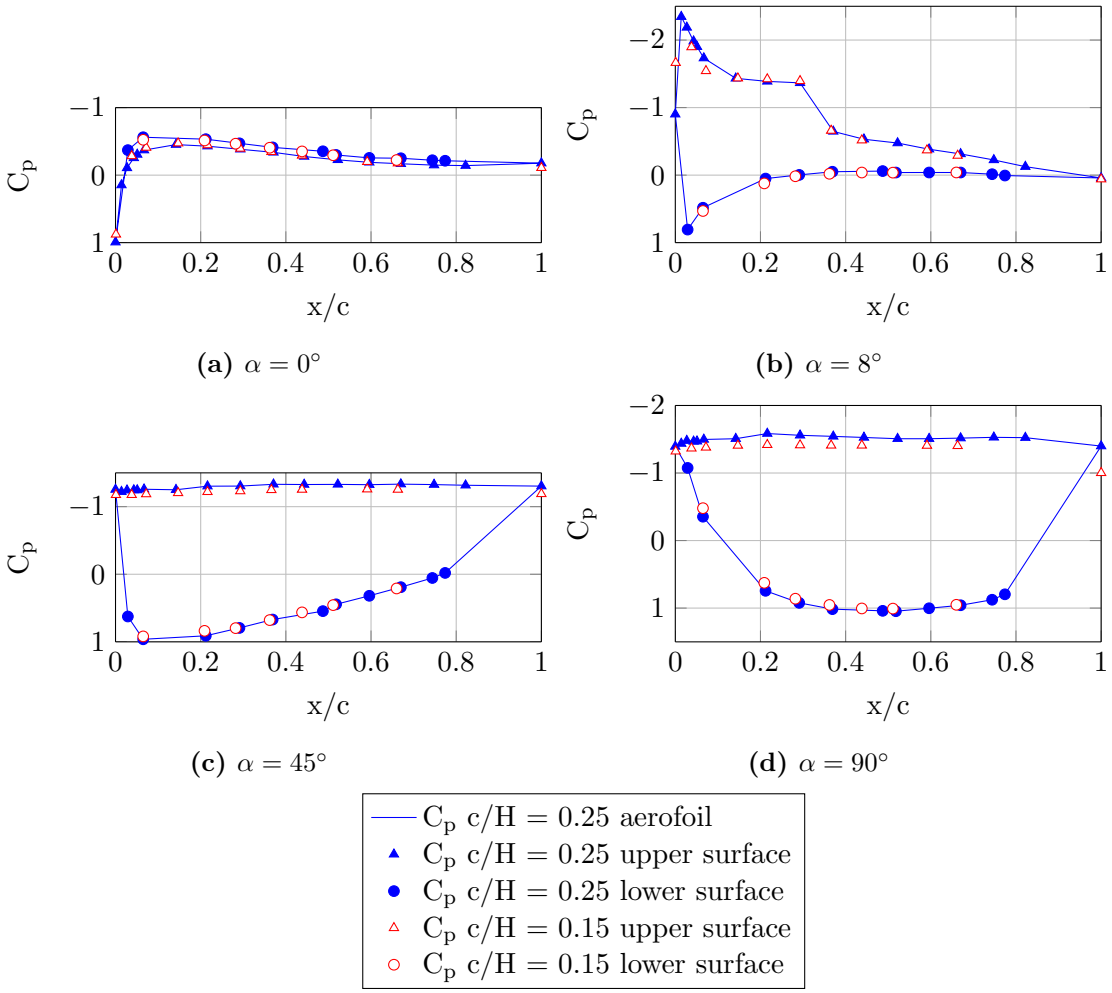


Figure D.22: C_p plotted against normalised chord-wise position for the $c/H = 0.15$ and $c/H = 0.25$ NACA 0015 aerofoils at $Re = 150\,000$ in the DS-75 tolerant tunnel.

D.7 Surface pressures for the two tapped NACA 0015 aerofoils with various tolerant tunnel OARs and solid tunnel walls, at $Re = 60\,000$



(a) $\alpha = 0°$ **(b)** $\alpha = 8°$

(c) $\alpha = 45°$ **(d)** $\alpha = 90°$

Figure D.23: C_p plotted against normalised chord-wise position for the $c/H = 0.15$ and $c/H = 0.25$ NACA 0015 aerofoils at $Re = 60\,000$ in the DS-67 tolerant tunnel.

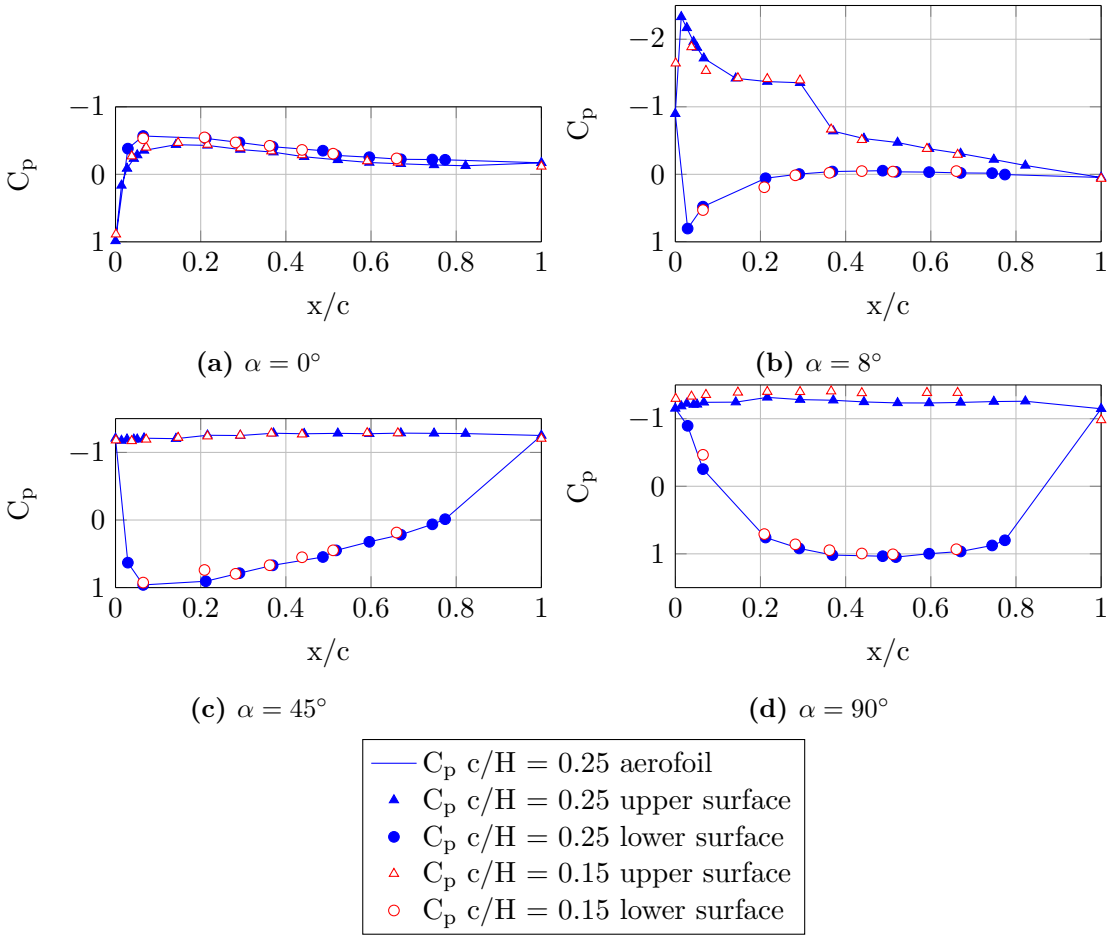


Figure D.24: C_p plotted against normalised chord-wise position for the $c/H = 0.15$ and $c/H = 0.25$ NACA 0015 aerofoils at $Re = 60\,000$ in the DS-71 tolerant tunnel.

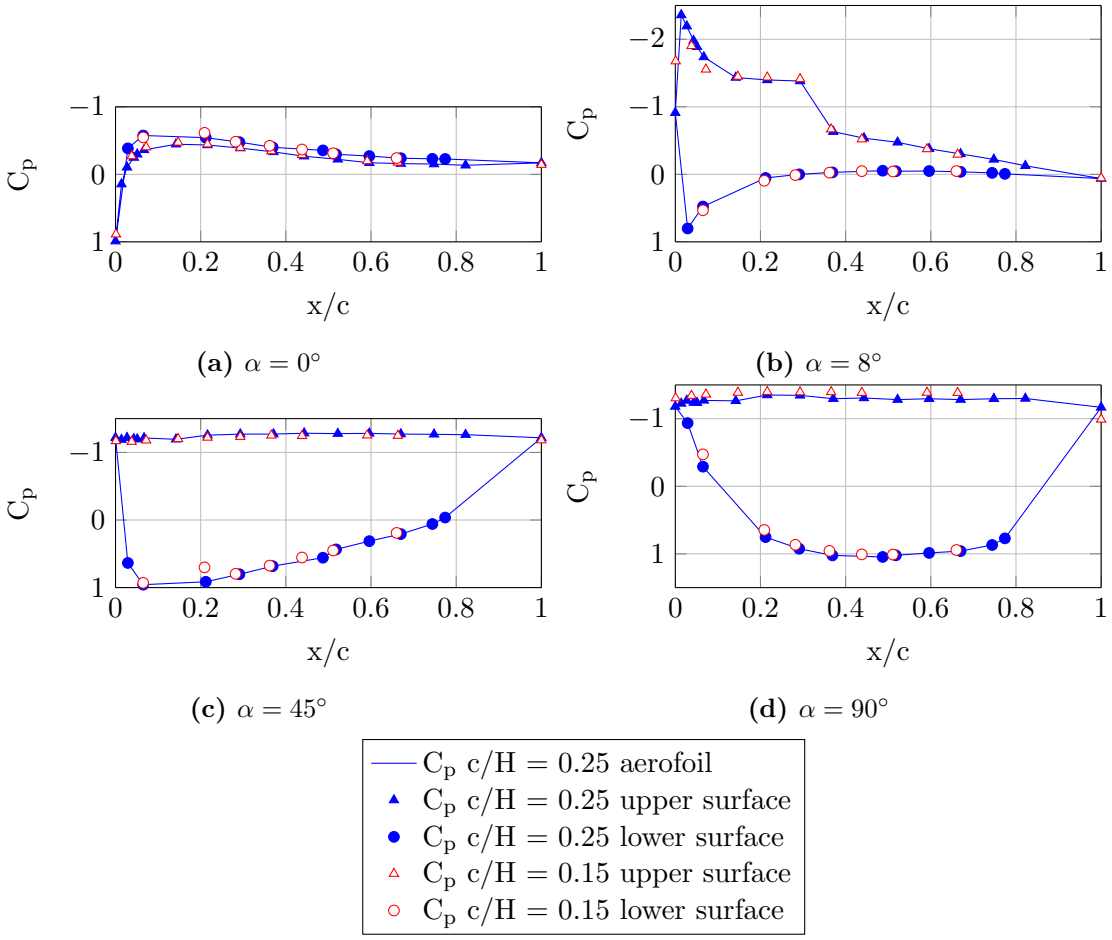


Figure D.25: C_p plotted against normalised chord-wise position for the $c/H = 0.15$ and $c/H = 0.25$ NACA 0015 aerofoils at $Re = 60\,000$ in the DS-75 tolerant tunnel.

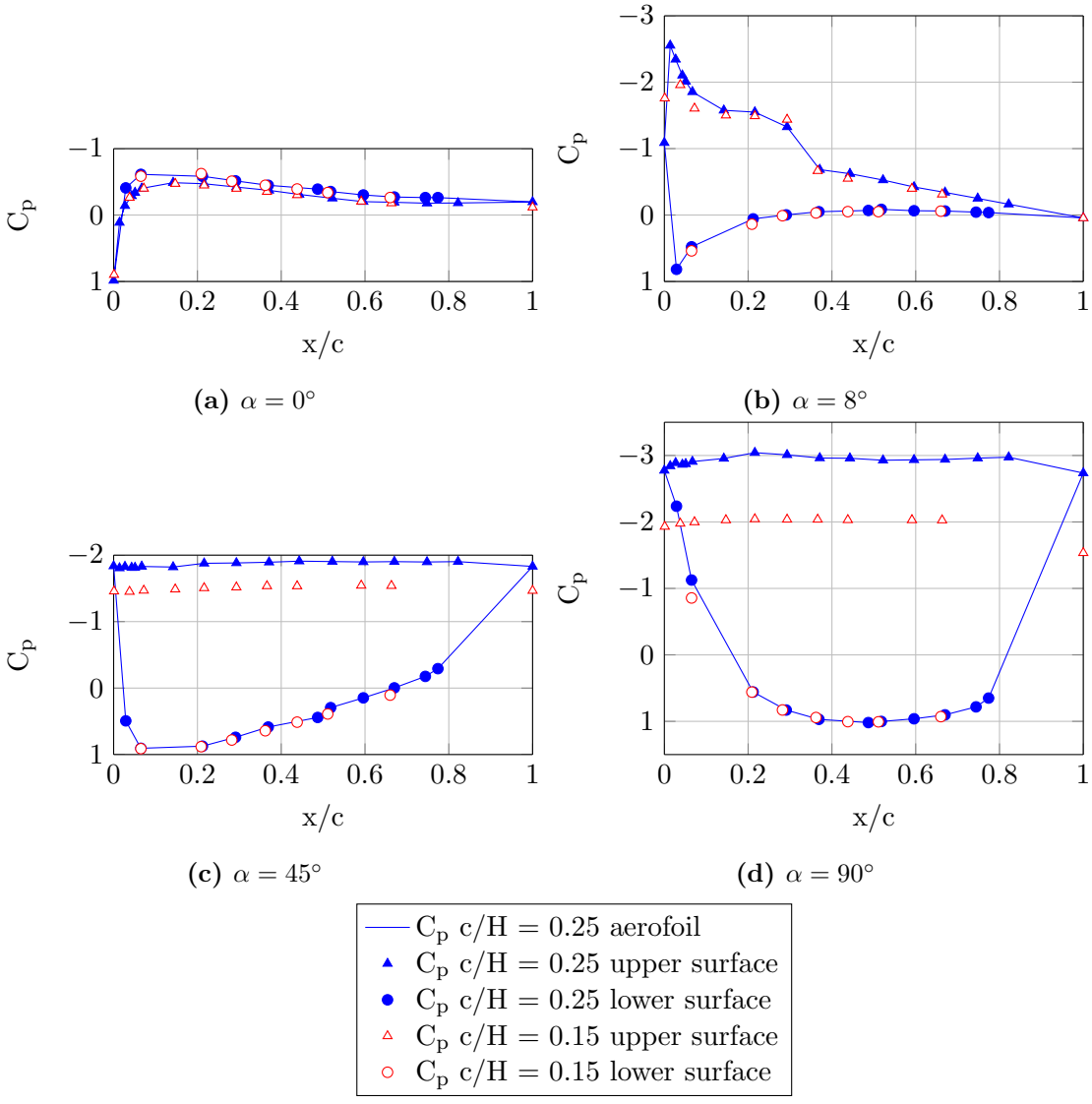
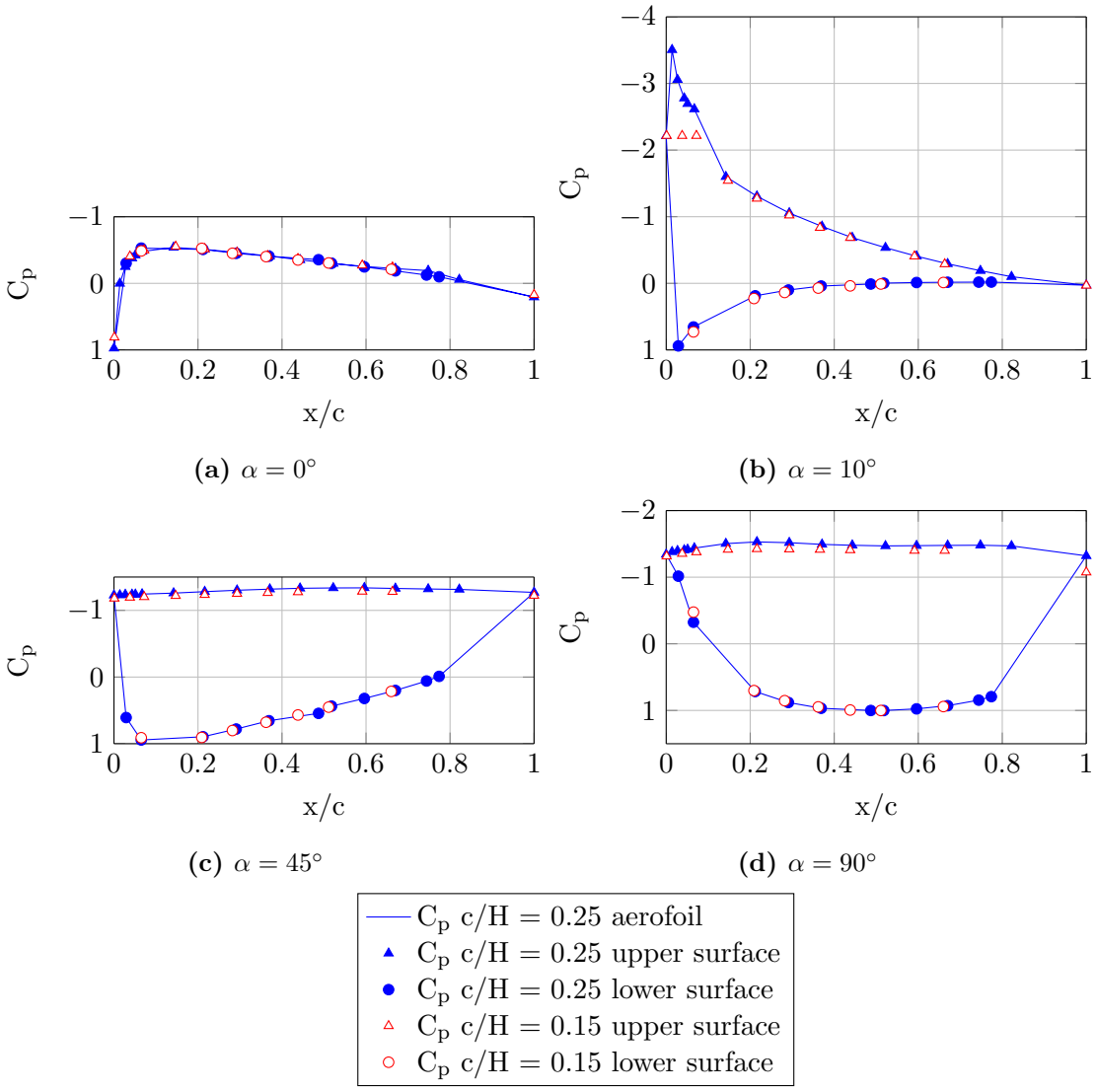


Figure D.26: C_p plotted against normalised chord-wise position for the $c/H = 0.15$ and $c/H = 0.25$ NACA 0015 aerofoils at $Re = 60\,000$ in the solid walled tunnel.

D.8 Surface pressures for the two tapped NACA 0015 aerofoils with various tolerant tunnel OARs and solid tunnel walls, at $Re = 250\,000$



(a) $\alpha = 0°$ **(b)** $\alpha = 10°$

(c) $\alpha = 45°$ **(d)** $\alpha = 90°$

Figure D.27: C_p plotted against normalised chord-wise position for the $c/H = 0.15$ and $c/H = 0.25$ NACA 0015 aerofoils at $Re = 250\,000$ in the DS-67 tolerant tunnel.

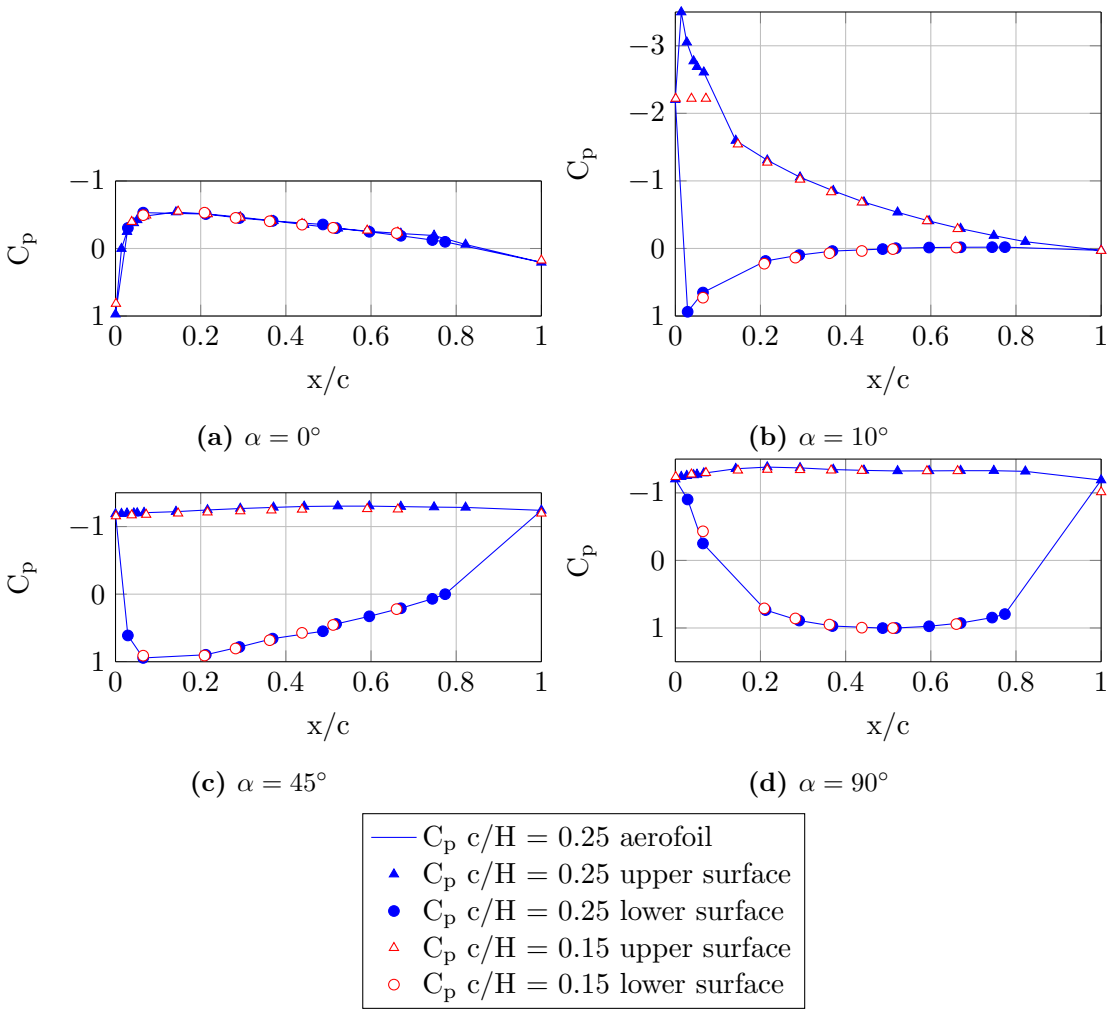


Figure D.28: C_p plotted against normalised chord-wise position for the $c/H = 0.15$ and $c/H = 0.25$ NACA 0015 aerofoils at $Re = 250\,000$ in the DS-71 tolerant tunnel.

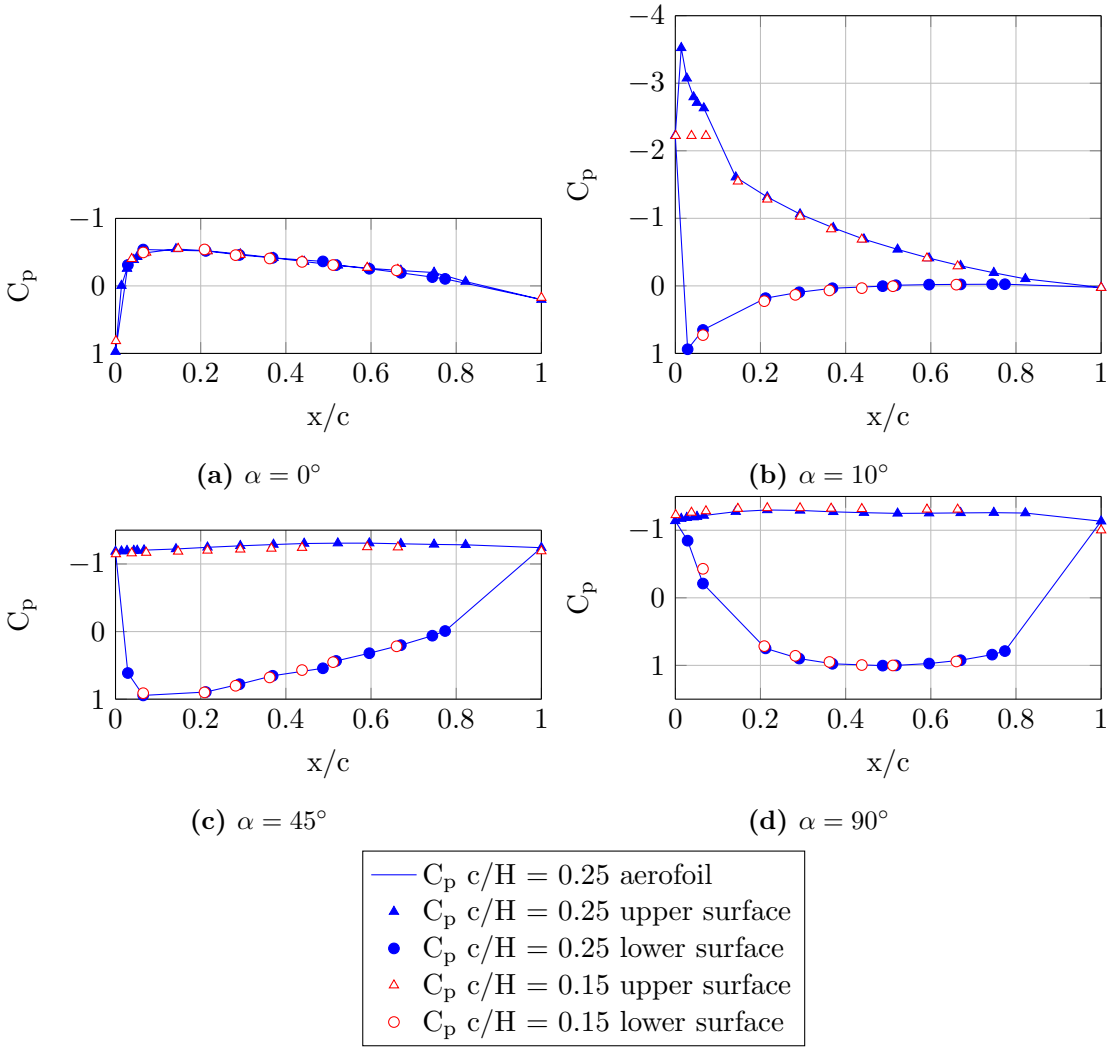


Figure D.29: C_p plotted against normalised chord-wise position for the $c/H = 0.15$ and $c/H = 0.25$ NACA 0015 aerofoils at $Re = 250\,000$ in the DS-75 tolerant tunnel.

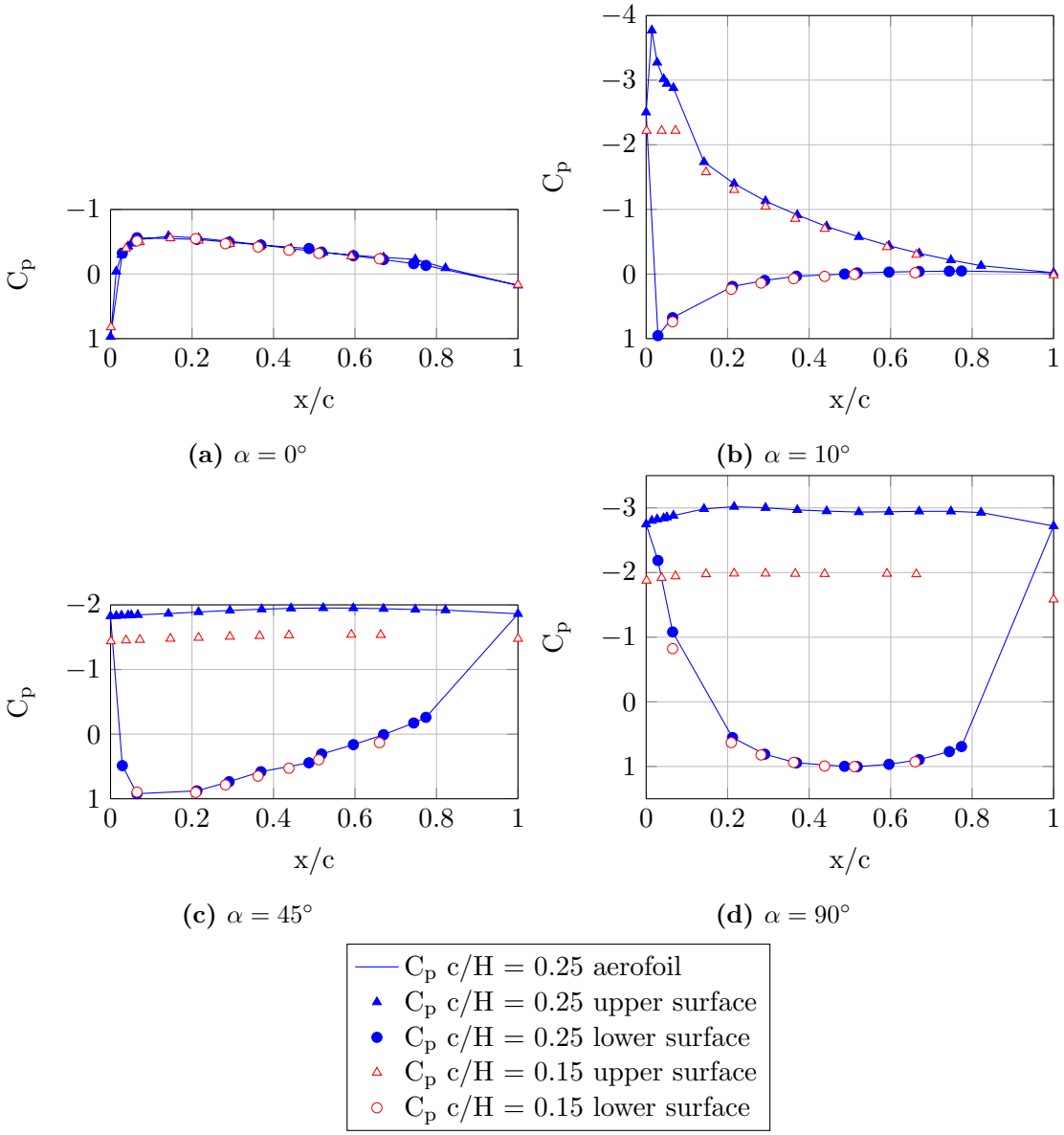


Figure D.30: C_p plotted against normalised chord-wise position for the $c/H = 0.15$ and $c/H = 0.25$ NACA 0015 aerofoils at $Re = 250\,000$ in the solid walled tunnel.